NEURAL CORRELATES OF VISUAL PERCEPTUAL LEARNING AND INHIBITORY NEUROTRANSMITTER IN HUMANS USING MAGNETIC RESONANCE SPECTROSCOPY

---

by
ADRIAN DANTE GARCIA

A thesis submitted to the University of Birmingham
for the degree of DOCTOR OF PHILOSOPHY

PSIBS Doctoral Training Centre
College of Engineering and Physical Sciences
University of Birmingham
April 2016

ABSTRACT

The role of excitatory processes in human visual learning has been well characterised through the use of technologies such as functional magnetic resonance imaging (fMRI). However, established imaging modalities do not distinguish excitatory processes from the inhibitory ones that are also involved. Here we investigate inhibitory processes using magnetic resonance spectroscopy (MRS) and the MEGA-PRESS pulse sequence. We measure concentrations of the inhibitory neurotransmitter gamma-aminobutyric acid (GABA) in different brain regions as functional markers of inhibitory potential. We then investigate the correlations between GABA concentrations and psychophysical learning metrics. We detail a full analysis pipeline that improves the accuracy of *in vivo* GABA quantification and introduce new scaling methods to resolve the grey matter contribution to metabolite measurements. We develop visual learning experiments that are mediated by training difficulty, which we link to inhibitory processes across different time scales. We also present novel evidence for GABAergic inhibitory mechanisms across multiple brain areas using fine and coarse discrimination tasks. Our results support a cooperative top-down and bottom-up model of visual learning in occipital and frontal cortical regions. Our findings reveal chemical interactions with cognition to contribute to our understanding of inhibitory processes in the human learning brain.

DEDICATION

For Julia, Matt, Pooky and Ollie — with love always.

ACKNOWLEDGEMENTS

I would like to thank my supervisors for their generosity with ideas, time and efforts during this research; **Prof. Theodoros Arvanitis, Dr. Nigel Davies, Prof. Zoe Kourtzi** and **Prof. Andrew Peet**. I would also like to acknowledge the **EPSRC** for funding this research and the support of the **PSIBS Doctoral Training Scheme Steering Committee**, in particular **Prof. Michael Hannon**. The project benefitted greatly from the collaboration of the following individuals: **Dr. Tim Yates** for many helpful discussions on scientific and statistical matters; **Dr. Shu-Guang Kuai** for his expertise in psychophysics and perceptual learning; **Dr. Richard Edden** for providing the pulse sequence used in this research; and **Dr. Martin Wilson** for support on the science of MRS acquisition. There are many individuals whose friendship I would like to acknowledge, but especially: **Dr. Rosalind Baker, Dr. Hiroshi Ban, Dr. Dorita Chang, Dr. Nuno Reis Gonçalves, Dr. Dicle Dövencioğlu, Dr. Aimée Goldstone, Dr. Janna Marie Hoogendam, Dr. Roya Jalali, Dr. Xiaoping Li, Dr. Caroline di Bernardi Luft, Dr. Arthur Lugtigheid, Dr. Alan Meeson, Dr. Alexander Muryy, Dr. Matt Patten, Dr. Vassillis Pelekanos, Dr. Hua-Chun Sun, Dr. Rui Wang** and **Dr. Yang Zhang**. This research could not have taken place without the wonderful contributions of my **participants**, I thank you all for your efforts and for loaning me your marvellous brains. Finally, I would like to express my heartfelt gratitude to my mentor **Prof. Ela Claridge**, who proved to be an inspiration in many ways and whose tireless support and good humour will always be appreciated.

TABLE OF CONTENTS

LIST OF FIGURES

LIST OF TABLES

LIST OF CODE SAMPLES

ABBREVIATIONS

Asp	Aspartate
BW	BandWidth
Cho	Choline
Cr	Creatine
CRLB	Cramér-Rao Lower Bounds
CSF	CerebroSpinal Fluid
DA	Divided Attention
DICOM	Digital Imaging and COmmunications in Medicine
EPSP	Excitatory PostSynaptic Potential
FFT	Fast Fourier Transform
FID	Free Induction Decay
fMRI	functional Magnetic Resonance Imaging
GABA	Gamma-AminoButyric Acid (γ-aminobutyric acid)
Gln	Glutamine
Glu	Glutamate
Gly	Glycine
GM	Grey Matter
IPSP	Inhibitory PostSynaptic Potential
Lac	Lactate
LO	Lateral Occipital
LPS	Left Posterior Superior
M1	primary motor cortex
MCI	Mild Cognitive Impairment
MEGA-PRESS	MEsher-GArwood Point REsolved Spectroscopy Sequence
MFG	Mid Frontal Gyrus
mI	myo-Inositol
MM	MacroMolecules
MR	Magnetic Resonance
MRI	Magnetic Resonance Imaging
MRS	Magnetic Resonance Spectroscopy

MT	Middle Temporal
NAA	N-Acetyl Aspartate
OSSS	Orientation-Specific Surround Suppression
ppm	parts per million
PRESS	Point REsolved Spectroscopy Sequence
RAS	Right Anterior Superior
ROI	Region Of Interest
SA	Selective Attention
SNR	Signal to Noise Ratio
STEAM	STimulated Echo Acquisition Method
SVS	Single Voxel Spectroscopy
T	magnetic field strength, Tesla
TE	echo time
TR	repetition time
UFOV	Useful Field of View
VAPOR	VAriable Pulse power and Optimised Relaxation delays
VSTM	Visual Short Term Memory
WM	White Matter

1

INTRODUCTION

The capacity to learn and assimilate knowledge is a remarkable evolutionary feature that allows many species to plan and adapt to the challenges of survival in competitive environments. This capacity has been extensively studied in humans. Despite considerable efforts across numerous scientific disciplines, the processes for how we learn remain largely unknown. In fact understanding the workings of the human brain is still considered as one of the grand challenges of science and advances in this field have potential benefits in many important areas such as health and education.

The reasons why our understanding is incomplete are related to the inherent complexity of our brains and limitations of existing investigative tools. Explanations of the processes behind learning must integrate across multiple levels of analysis (psychological, computational, synaptic, cellular, chemical and molecular) and need to encompass the massively interconnected neuronal structure of the brain. Although this integration of analysis scales has yet to be realised, progress has been made in the mapping of brain activity, largely through the measurement of cerebral blood flow and electrical activity. This has helped us to understand that the firing of neurons in coordinated networks is involved in how we learn, but this remains an incomplete explanation. The electrical activity is dependent on chemical processes,

principally the release of neurotransmitters that modulate the activation or suppression of neuronal activity.

This aspect, the molecular level of analysis, is one that has received less attention in the scientific community and is the focus of the research in this thesis. By investigating chemical interactions with learning we propose that our knowledge of the workings of the human brain might be extended. For example the measurement of particular neurotransmitters might further our understanding of the excitatory and inhibitory balance of neuronal activity, which is not distinguishable through techniques that measure electrical activity alone.

This is the key idea for the research described in this thesis, to investigate aspects of learning in the human brain by examining correlates between neurotransmitter concentrations and learning performance.

1.1 Research Areas

The research areas for this project are interdisciplinary in nature and cover aspects of psychology and physical science. For the life science areas we were interested in learning and in particular focussed on learning in a vision context. We investigated this through experiments where we tasked volunteers to differentiate between shape categories in visual learning psychophysics paradigms. We were also interested in the effect of training difficulty on visual learning performance, especially across different time scales. These experiments were designed to elicit differences in task performance, congruent with the notion that learning differences may be mediated by the effect of dissociable neural mechanisms. The results from psychophysics experiments can be used to suggest that dissociable mechanisms are involved, but they cannot measure neural activity directly and so cannot be used to confirm that this is the case.

The mechanisms involved in visual perceptual learning in humans are most commonly investigated through the application of functional magnetic resonance imaging (fMRI). This technique can only be used to study neural activity through the proxy of blood flow measurements, in contrast to magnetic resonance spectroscopy (MRS), which is capable of measuring neurotransmitter concentrations directly. Of key interest in this thesis is the role that inhibitory processes play in learning. The chief inhibitory neurotransmitter in the human brain is gamma-aminobutyric acid (GABA), and so we propose to use magnetic resonance spectroscopy techniques to measure GABA concentrations. In this way we intend to use the measurements as indicators of inhibitory potential, thereby linking them to inhibitory neural mechanisms.

GABA is present in low concentrations in the human brain and can not be reliably measured using standard MRS techniques. There are specialised MRS techniques designed for this task and we focus on the most common method, which uses the MEGA-PRESS pulse sequence. At the time of this research analysis routines for MEGA-PRESS were not readily available, so we developed a pipeline of processing methods as part of our overall research goals. This investigation into MEGA-PRESS MRS acquisition and analysis techniques form the physical science aspects of our research.

A third aspect of our research is to combine the life science and physical science aspects by linking learning with inhibitory processes. We planned to do this by examining the correlations between visual learning performance metrics and measures of inhibitory neurotransmitter concentrations.

1.2 Aims and Objectives

Our overarching aims are to link GABA measurements from MEGA-PRESS MRS with psychophysics performance metrics to characterise learning as a phenomenon that involves inhibitory mechanisms. Our aims and objectives are framed within the physical and life science areas outlined in the introduction. For the psychology based parts our objectives are:

- To develop psychophysics experimental paradigms in visual learning that suggest dissociable learning performance according to task.
- We intend to test the hypothesis that dissociable learning performance is revealed by increasing the frequency of testing in multi-session psychophysics experiments.

For the physical science based aspects of the research our aims are focussed on the measurement of GABA using the MEGA-PRESS pulse sequence. There are numerous obstacles to obtaining accurate measurements of *in vivo* GABA using this sequence and so we determined to investigate the difficulties and advance solutions:

- A specific objective is to discover appropriate parameter settings and experimental conditions for running successful MEGA-PRESS scans, including a principled way of targeting relevant brain regions of interest.
- We aim to develop analysis routines and strategies to improve the accuracy of measurements of GABA for *in vivo* experiments. These strategies should address sources of error and areas where there is no consensus among the research community.

Our main hypothesis is that inhibitory processes are involved in visual perceptual learning and so we propose to measure inhibitory neurotransmitter as an indicator of inhibitory

potential. We intend to test this hypothesis by bringing the psychophysics and MRS aspects of the research together:

- In particular we propose to conduct correlative studies of visual learning performance versus GABA concentration levels.
- We hypothesise that correlations between psychophysics performance and GABA concentrations may occur in more that one brain region and we aim to investigate this with experiments that target multiple brain areas, to investigate top-down inhibitory processes.
- Our final objective is to investigate tissue segmentation strategies and alternative scaling paradigms to test the hypothesis that grey matter contributions to GABA concentrations might be better predictors for visual learning performance than those from white matter. This hypothesis is based on the observation that connections between cells terminate largely in grey matter and these terminals are the site of GABA production and expression, whereas the bulk of white matter consists of axons that allow the transmission of action potentials.

1.3 Overview of Chapters

We arranged the chapters starting with introductory materials that define the context of our research hypotheses (**Chapter 2: Visual Learning and Magnetic Resonance**). We review key aspects of the neurobiology of the visual system, with respect to the way that neurons function to release chemicals that modulate activity during cognitive processes. We discuss our motivation for using psychophysics and MRS techniques to investigate learning and we survey the state of the art in a literature review for MEGA-PRESS research in visual learning

paradigms.

We set out our research into acquiring MEGA-PRESS spectra and subsequent signal analysis methodologies in **Chapter 3: MEGA-PRESS Acquisition** and **Chapter 4: Post-Acquisition Processing**. These chapters represent the physical science aspects of our research and are complemented by experiments described in **Appendix A: Time Course of MEGA-PRESS**.

Further experimental chapters follow, starting with visual learning experiments where we use psychophysics to characterise dissociable learning performance according to training difficulty (**Chapter 5: Time Course of Training Difficulty Mediated Visual Learning**). This chapter is based on the work of pilot studies, which we describe in **Appendix B: Visual Learning Pilot Studies** and together they represent the psychology aspects of our research.

The physical and life science aspects converge in the next two chapters (**Chapter 6: GABA Versus Training Difficulty Mediated Visual Learning** and **Chapter 7: GABA Versus Coarse and Fine Visual Learning**). In these chapters we investigate correlations between learning performance and GABA concentrations to explore our main thesis aims. In **Chapter 8: Discussion and Conclusions**, we discuss the thesis as a whole in the context of our research hypotheses. We include a section on further work, where we suggest that MRS techniques can be combined with other functional modalities to include information at the molecular level of analysis. This has the potential to extend our knowledge of brain function by supplementing existing measures of activation with chemical measures that point to the excitatory and inhibitory balance that modulates the workings of the learning brain.

2

VISUAL LEARNING AND MAGNETIC RESONANCE

2.1 Introduction

The mechanisms underlying cognition consist of biological processes that involve electrical and chemical transmission of signals through organised networks of specialised cells called neurons. In humans, learning in visual paradigms has been investigated chiefly through behavioural testing and brain imaging modalities. These approaches have been used successfully in inferring the underlying mechanisms, but they do not distinguish between inhibitory and excitatory processes. Our research hypothesis involves the investigation of top-down inhibitory processes associated with learning and we chose to focus on the relationship of inhibitory neurotransmitters in a vision paradigm. This chapter sets the context for this research by surveying the neurobiological basis of the functioning brain, covering the excitatory and inhibitory responses of neurons and describes the architecture and connectivity that characterises learning. We introduce ideas in visual learning and psychophysics and discuss magnetic resonance concepts involved with measuring cognitive processes, in particular the functional aspects of brain chemistry through magnetic resonance spectroscopy.

We define learning in terms of brain plasticity, which can be characterised through behavioural changes as measured through performance metrics, or morphological changes that can be investigated using imaging modalities. Specifically we are interested in the widely shared theory that brain plasticity in learning is related to modulation of lateral interactions and feedback from higher cortical areas (Ahissar & Hochstein, 2004; Kourtzi & DiCarlo, 2006). According to this view learning, including visual learning, is a two-way process involving both bottom-up and top-down streams that employs both excitatory and inhibitory mechanisms. We outline the neurobiology of the visual system by describing the basic functionality of individual neurons and how they connect and communicate in networks across the brain.

We examine aspects of the development of ideas in perceptual learning and introduce the discipline of psychophysics to provide the context for our choices of visual learning paradigms that we use in experimental chapters further on in the thesis. We discuss brain metabolites and our motivation for concentrating on the inhibitory neurotransmitter GABA.

The most common brain imaging modality is functional magnetic resonance imaging (fMRI). We discuss fMRI in the context of perceived limitations with regard to the measurement of inhibitory processes. We then introduce magnetic resonance spectroscopy as the modality that we intend to use for measuring brain metabolite quantities, and we discuss edited pulse sequences as a solution to the difficulties in measuring low concentration metabolites *in vivo*. This introduces the MEGA-PRESS sequence and we link characteristics of the chemical properties of GABA to the physical science of the acquisition process to show how GABA can be resolved from more abundant, overlapping metabolites.

We survey the state of the art in a literature review on MEGA-PRESS and learning experiments to contextualise our topic as one that is a niche, but growing research area.

2.2 Neurobiology of the Visual System

The neurobiology of the visual system is a description of the neuroanatomy, or structure, and the neurophysiology, which can be thought of as the functional aspects of vision. It is common to organise descriptions of neurobiology in terms of different levels of analysis; cellular, molecular, systems and behaviour. Here we will follow this convention by outlining the neurobiology of the visual system starting with a description of the neuron's major structure and function. We will describe the function of neurons in terms of the electrical and chemical transmission of signals. We will also introduce the ways in which neurons are organised into networks of functionally distinct brain regions and discuss the role of excitation and inhibition in learning. This is in line with the idea that the specificity of the synaptic connections is what underlies perception and learning.

2.2.1 Neurons

Structure of the Neuron. The neuron can be described as the basic unit of the brain and each neuron is a signalling unit. A neuron consists of a nucleus, dendrites that receive impulses and an axon that transmits impulses to other cells (**Figure 2.1A**). Neurons can be classified into over 1,000 different types, but in essence they can be reduced to four stages of function; input, integrative, conductive and output stages. These stages cover the electrical and chemical transmission of signal that characterises nerve cells in the brain. In terms of numbers of neurons in the brain, these have been estimated at 86 billion (Azevedo et al., 2009). A signal originating from one neuron is passed to others along a single axon which then splits into many branches. Their terminal points come in close proximity to dendrites of other neurons at synapses. These are sites at which electrical and chemical signals are passed from one neuron to another (**Figure 2.1B**).

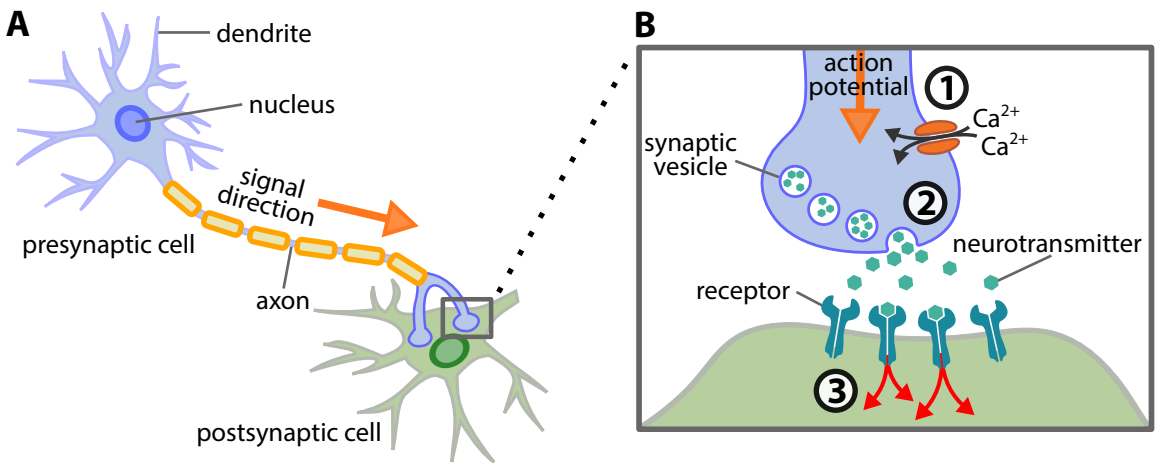

Figure 2.1: Neuronal connections. (**A**) Schematic of neuronal structure with presynaptic and postsynaptic connections. (**B**) Synaptic connection showing neurotransmitter release: (**1**) Action potential arrives and triggers the entry of Ca^{2+}. (**2**) In response to Ca^{2+}, synaptic vesicles fuse with the presynaptic membrane then release neurotransmitter. (**3**) Ion channels open as neurotransmitter binds with receptors, this causes ions to enter and change the postsynaptic cell potential. Image adapted from Splettstoesser (2015).

Synaptic Connections. A typical neuron forms and receives 1,000 to 10,000 synaptic connections. Synapses are characterised as either electrical or chemical. With electrical synapses a direct connection allows charge to be transmitted between presynaptic and postsynaptic cells. In chemical synapses an action potential in the presynaptic cell leads to the release of a chemical transmitter from the nerve terminal. The transmitter diffuses across the synaptic cleft and binds to receptor molecules on the postsynaptic membrane. This leads to changes in the membrane potential of the postsynaptic neuron, through the opening or closing of ion channels, which either excites or inhibits the firing of action potentials. Most synapses in the brain are chemical.

Excitatory and Inhibitory Responses. The diffusion of neurotransmitter release exists as part of a continuum of constantly changing membrane potentials. An excitatory postsynaptic potential (EPSP) is an action potential that increases the likelihood for a postsynaptic neuron to fire an action potential. The excitatory response arises when positively charged sodium ions flow into a cell depolarising its membrane, this cumulative depolarisation can lead to

the firing of action potentials. An inhibitory postsynaptic potential (IPSP) usually causes negatively charged chloride ions to enter a cell, which potentially results in a decrease in firing rate. The excitatory or inhibitory action depends on the neurotransmitter released at the pre-synaptic membrane and the nature of receptors at the post-synaptic membrane. Nearly all fast synaptic actions in the brain are mediated by two main amino acid neurotransmitters; glutamate, which is excitatory, and GABA, which is inhibitory.

Neuronal firing rate is currently thought to be the primary manner in which information is encoded in the nervous system and not the magnitude of the action potentials. The magnitude of an action potential evolves over time but usually reaches the same threshold and therefore can be thought of as firing in a binary fashion. In terms of visual perception, the function of neurons is determined by their tuning to visual stimuli, for example line orientations, directions of movement or responses to colours. A neuron's discriminability in a stimulus space can be measured to determine its 'psychometric' curve (Gilbert & Li, 2013).

Brain Metabolites. Metabolites are the precursors and products of metabolic processes and there have been over 3,000 identified in the human body and 309 in cerebrospinal fluid (CSF). Common brain metabolites include N-acetylaspartate (NAA), creatine (Cr), choline (Cho), myo-Inositol (mI), lactate (Lac), glutamate (Glu), glutamine (Gln), glycine (Gly), aspartate (Asp) and γ-aminobutyric acid (GABA) (Ritsner & Gottesman, 2009). Some metabolites act as neurotransmitters, with the principal ones being Glu and Asp, which are excitatory, and GABA, which is inhibitory. GABA is of prime interest in this work and is discussed in more detail in **Section 2.5.1**.

Plasticity of Neuronal Connections. Neuroplasticity is the term used to describe lasting changes that occur in the brain including changes at the single cell level. Synaptic plasticity

refers to changes in the connections between neurons as apposed to non-synaptic plasticity, which involves changes in the cells' intrinsic excitability. These changes can be either short-term, resulting from modification of existing synaptic proteins, or long-term, which may involve the growth of new synapses, or the elimination of existing ones. Neuroplasticity is at its most active during the development of the neural system at the beginning of life. However it remains active throughout life, playing a central part in learning when the synaptic structure and function are modified in response to experience.

Underpinning synaptic plasticity is modulation of transmitter release. Synaptic strength can be modified presynaptically, by altering the release of neurotransmitter, or postsynaptically by modulating the response to transmitter. Long term changes in these mechanisms are important to learning (Kandel, 2013, p. 284).

2.2.2 Neural pathways

As well as being highly connected individually, neurons are organised into tracts from one structure to another to form pathways or circuits. The complexity of behaviour is linked to the organisation of cells into anatomical circuits with distinct functions, rather than the number of different types of cells. A simple description of the visual pathway might consist of the eye, the optic tract, the lateral geniculate body and the primary visual cortex. This arrangement describes a largely serial pathway that proceeds from input through to low level processing of visual stimuli. This description can be further elaborated to include higher-order sensory areas where more complex processing takes place. Higher-order areas can be processed in parallel and have connections that feed back to earlier areas in the pathway. For example low level visual processing such as edge detection might occur in the visual cortex in cells organised with small receptive fields that are connected mainly to nearby cells. These areas feed

forward to higher-order areas such as the lateral occipital complex, where the edges are constructed into overall shapes by neurons with large receptive fields and which have connections to distant areas in the brain such as the frontal and limbic lobes. As higher-order areas project back to the lower-order areas from which they receive input, areas that are sensitive to global patterns can modulate the activity of areas that are sensitive to local detail.

Retina. The retina is not just a passive sensor, its neurons carry out the earliest stages of the process of visual perception. Light photons that fall on photoreceptors (rods and cones) trigger a change in the photoreceptor's membrane potential. The nerve impulse is then passed to bipolar, horizontal and amacrine cells and then to the retinal ganglion cells. Ganglion cells are involved in the formation of receptive fields, on-centre off-surround and, symmetrically, off-centre on-surround. The receptive fields are of different sizes and have different ratios of the centre and the surround collection area. Ganglion cells integrate the signals from the receptive fields and pass them on to the visual cortex which then makes use of them at the stage of responding selectively to local frequencies and orientations (Hubel, 1988).

Visual Cortex. Signal from the retinal neural cells is transmitted via the optic nerve fibres (via the lateral geniculate body) to the primary visual cortex. The visual cortex forms a part of the cerebral cortex, a 2–4 mm thick outer layer of neural tissue. Anatomically, the cerebral cortex is divided into a number of lobes (**Figure 2.2A**), which have distinct functions; frontal (short term memory, planning future actions, control of movement), parietal (somatic sensation, relating body image to extrapersonal space), occipital (vision), and temporal (hearing, learning, memory and emotion). The lobes can be further divided into motor and sensory regions (**Figure 2.2B**).

The primary visual cortex (area V1), which is anatomically equivalent to striate cortex,

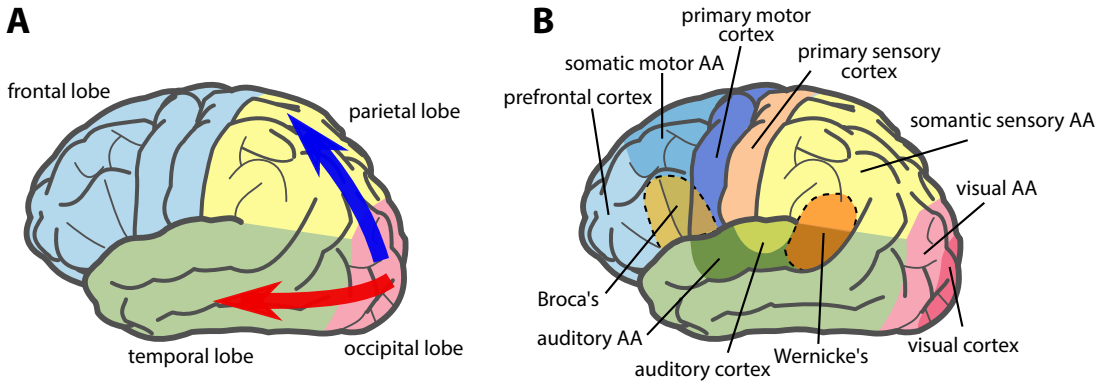

Figure 2.2: Brain areas. (A) Visual cortex lobes, arrows indicate the dorsal stream or "where pathway" (blue arrow) and the ventral stream or "what pathway" (red arrow). **(B)** Motor and sensory regions of the cerebral cortex. **AA** stands for association area. Image adapted from Blaus (2014).

maintains the signal's topographic mapping. Further visual areas, V2–V5, are thought to increasingly correspond to more abstract representations such as local orientations, colour, and frequency (V2), motion (V3), complex shapes (V4) and global percepts (V5). Whereas the direction of signal propagation up until V2 is primarily feed-forward, there is evidence for the existence of feedback pathways into the higher visual areas.

Signals originating from V1 take two distinct pathways: Ventral, going through V2 and V4, is referred to as the "what pathway" and is related to object recognition and long-term memory; and dorsal, going through V2, V5 and V6, referred to as "where pathway", related to motion, object locations and eye control.

Learning Areas of the Brain. Different brain areas and pathways work together to construct and encode the images we see, these processes are what leads to learning in a visual context. The visual cortex is central to these processes with pathways that include the superior colliculus pathway, the middle temporal area pathway, the frontal eye fields pathway and the inhibitory pathway, which regulates activity in the superior colliculus and is responsible for obligatory attention. These are all important to the development of visual attention in humans, but other areas and pathways outside of the occipital lobe are also important in vision

and visual learning. For example the inferior temporal cortex, the superior parietal cortex and the cerebellum are all involved in recognising new visual information. Areas in the prefrontal cortex (and basal ganglia) have been implicated in learning to form visual categories and represent task-relevant features (Duncan, 2001; E. K. Miller & Cohen, 2001; B. T. Miller & D'Esposito, 2005) and Schwarzkopf, Zhang, and Kourtzi (2009) identified a learning network that includes occipito-temporal and fronto-parietal areas using fMRI.

Recognition is predicated on neural plasticity or the brain's ability to reshape itself based on new information (Poldrack, Desmond, Glover, & Gabrieli, 1998). After recognition comes categorisation and the orbitofrontal cortex and two dorsolateral prefrontal regions have been implicated in categorising visual information (Vogels, Sary, Dupont, & Orban, 2002). Following recognition and categorisation comes encoding, which is essential for learning. Several brain areas are involved in this including the frontal lobe, the right extrastriate cortex, the neocortex and the neostiatum. The limbic-diencephalic region is important in transforming perceptions into memories.

Summary. The intention of this section was to give a broad overview of neurobiology of the visual system to set the context for the work of the thesis. It was meant to highlight the facts that learning involves complex interactions at many different levels and across many disparate brain areas, and that these interactions are not yet fully understood. Later on, we will expand on the idea that the locus for inhibition in learning during visual tasks is spread across different areas of the brain, in particular between visual areas and prefrontal cortical areas.

2.3 Visual Learning

This section gives a historical perspective of perceptual learning to set the context for the visual learning paradigms that we selected for the experimental chapters in this thesis. According to

this perspective theories about perceptual learning changed from predominantly feedforward notions to later include top-down mechanisms. The neuro-anatomical substrates underlying learning effects are still an open question, although a growing body of literature has identified the conditions for generalisation of learning across stimuli and tasks (Sagi, 2011).

2.3.1 Historical Perspective

An early view of perceptual learning was that it involved improving the selection of available information that was relevant for the task (Gibson, 1969). At this time training had not been extensively studied and practice was usually employed to familiarise subjects with a task rather than to elicit performance improvement. During the 1970s new understandings of visual cortex led to a shift towards neuronal accounts of learning. Ramachandran and Braddick (1973) were among the first to find learning effects to be orientation selective specifically to oriented lines introduced in training periods. In work on adapting gratings De Valois (1977) reported increased sensitivity following practice and concluded that leaning occurred either by restricting the sample pool to cells most sensitive to gratings, by changing the sensitivity of detectors or by making new connections between existing units. Early studies established that perceptual learning involves improvement of sensitivity of low level visual tasks rather than a change in decisional bias (for example contrast adjustment).

Fiorentini and Berardi (1980) suggested that learning involved modification at the level that integrates the output of orientation-selective neurons in the visual cortex in experiments that showed that learning was selective for stimulus orientation, spatial-frequency and retinal location. Ball and Sekuler (1987) suggested Middle Temporal (MT) as a cortical site for learning effect in motion discrimination paradigms. The 1980s saw a move to acceptance that plasticity occurs in the adult visual system, thus challenging the accepted view that critical

periods were limited to adolescents. Research around this time was concerned with whether perceptual learning involved the rewiring of neurons in early visual areas or if it was driven by improved readout from these (unchanged) neuronal representations. What was established was that different tasks rely on different brain areas and that neurons in the visual system responded to a limited set of stimuli.

During the 1990s a feedforward model of perceptual learning was popular, particularly to explain simple visual features (luminance, colour, motion, orientation). This model posits an architecture with processing layers stacked hierarchically with parallel image analysis of low level features feeding selective read out to higher levels of processing (Dosher & Lu, 1999). This mechanism starts with an input layer and finishes with a decision unit that integrates weighted inputs from neurons earlier in the processing stream.

Towards the end of the decade and into the 2000s top-down models of perceptual learning began to appear to explain more complex visual learning paradigms. In these models early visual areas were thought to become tuned by feedback connections from higher cortical circuits (Roelfsema & van Ooyen, 2005; Roelfsema, 2006). Evidence to support top-down models was provided from fMRI experiments (Kourtzi, Betts, Sarkheil, & Welchman, 2005; Sigman et al., 2005) and cortical anatomy, which revealed that long-range interactions do exist for visual cortex (Gilbert, Li, & Piëch, 2009). **Figure 2.3** shows some of the established ventral pathways concerned with object recognition, including frontal to occipital connections that we explore in later experimental chapters.

The work and ideas outlined above are largely concerned with the locus of perceptual learning in the brain and their supporting circuits. There has been less work specifically on excitation and inhibition, although these two mechanisms are fundamental to the processes of learning. The glutamatergic system is (depending on the receptor system) a fast-signalling

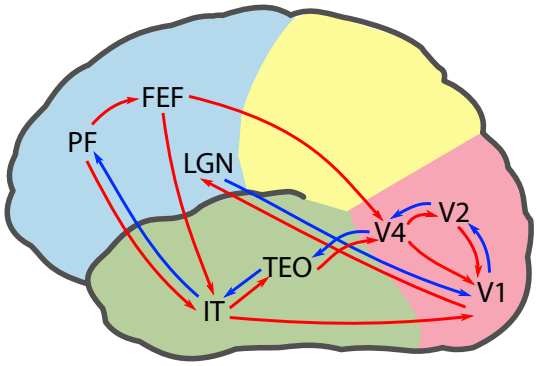

Figure 2.3: Ventral brain pathways. The visual cortical pathways begin in **V1**, which receives input from lateral geniculate nucleus **LGN**. The feedforward connections (blue arrows) proceed through the temporal lobe. Feedback connections (red arrows) provide top-down influences that mediate re-entrant processing. Connections can be direct reciprocal, such as **V2** — **V1**. Alternatively they can cascade over successive of areas, e.g. prefrontal cortex **PF** — frontal eye fields **FEF** — **V4** — **V2** — **V1**. Other areas in the figure are inferior temporal area **IT** and tectum opticum **TEO**. Image adapted from Kandel (2013).

system that is involved in excitation and long-term potentiation (Willard & Koochekpour, 2013). GABAergic processes, which are inhibitory (in addition to other processes such as generating oscillatory responses), ensure that only those neurons with the most support become strongly active. That is, features irrelevant to a task are out-competed and so responses are only to the most relevant features. Distinguishing inhibitory and excitatory mechanisms has received less attention from the perceptual learning research community compared to using measures of brain activation that conflate the two. This is because the dominant brain imaging modalities, fMRI and EEG, can not distinguish inhibitory and excitatory processes directly.

2.3.2 Psychophysics

Psychophysics is defined as the scientific study of perceptual performance through the systematic variation of physical stimuli (Bruce, Green, & Georgeson, 2003). Psychophysics has been used to characterise perceptual learning for many decades and has often been used to demonstrate rapid leaning of difficult tasks. Training has been shown to improve a wide range of visual perceptual skills from low-level feature discrimination, for example orientation (Fiorentini & Berardi, 1980; Matthews, Liu, Geesaman, & Qian, 1999), motion direction

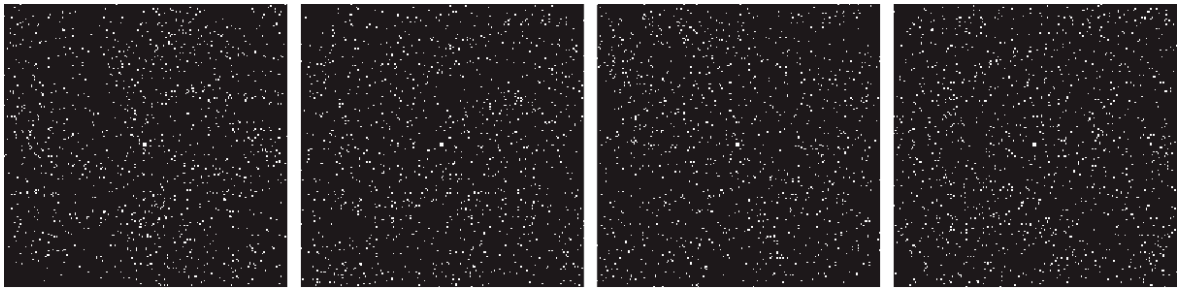

Figure 2.4: Glass pattern stimulus images. Sample images used in psychophysics experiments for this project. From left to right, these samples were created using spiral angles of $35°, 55°, 10°, 80°$ to produce radial and concentric patterns. The classification difficulty of these images can be systematically varied through the manipulation of the spiral angles. The images in this figure were set to 100% signal (no noise).

(Ball & Sekuler, 1987; Z. Liu, 1999; Lu, Chu, & Dosher, 2006), texture (Karni & Sagi, 1991, 1993; Ahissar & Hochstein, 1996) and high-level shape processing and object recognition (Furmanski & Engel, 2000; Golcu & Gilbert, 2009). Research in these areas has demonstrated the remarkable plasticity of the adult visual system (Ahissar, 2001; Fine & Jacobs, 2002; Fahle, 2004; Kourtzi, 2010; Sagi, 2011) and has influenced our own experimental designs. In this section we introduce the stimuli and experimental paradigms that we implemented to investigate our research hypotheses.

The stimuli we chose consisted of dot images, so-called 'Glass patterns' (Glass, 1969), as the visual paradigm for our investigations. These images are created by aligning adjacent pairs of dots to shape templates, for examples see **Figure 2.4**. Glass patterns are flexible tools in vision research as they can be varied in shape and according to noise parameters. Variation by shape allows the difficulty of a discrimination task to be controlled through the parametric alteration of angles between the dot pairs. Altering the noise levels in these visual experiments can be used to create distinct detection versus discrimination experiments.

In typical Glass pattern psychophysics experiments, distinct categories of dot images are shown to subjects. The subjects are then tasked to identify the correct category for each image shown. The difficulty of tasks like this can be controlled by altering experimental parameters.

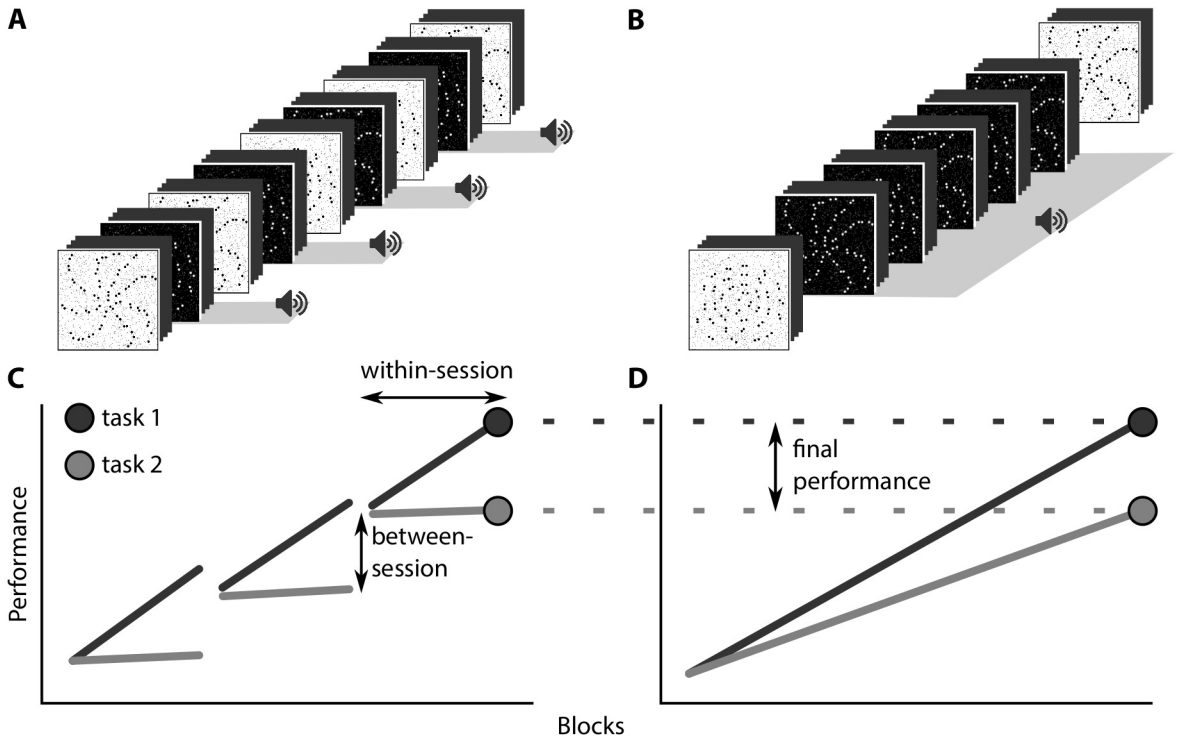

Figure 2.5: Interleaved test and training paradigm. (B) Typical psychophysics design, test blocks (white background) sandwich training blocks (with audible feedback). **(A)** Interleaved design, test and training blocks are alternated. Final performance is the same **(C,D)**, but the different within-session and between-session performance is revealed through the time course of the test blocks.

For example the length of time that the images are displayed for, the levels of additional noise added and the similarity between shape categories can all effect the difficulty of the task. Subject performance is often quantified with a final test that follows numerous training runs. The training runs differ from the test runs as feedback is provided during training runs.

We were interested in the time course of subject performance as we hypothesised that inhibitory processes might interact with learning in distinct ways across different time scales. This led us to design experiments that extended over several sessions and interleaved testing and training runs to improve the resolution of performance measures compared with typical psychophysics paradigms.

A schematic of an interleaved session can be seen in (**Figure 2.5A**). This is different to typical psychophysics experiments where a pre-training test block is often followed by train-

ing blocks and a final post-training test block is used to measure subject learning performance (**Figure 2.5B**). With the more typical psychophysics scheme, comparing performance on different tasks is limited to final performance measures (**Figure 2.5D**). By increasing the frequency of testing over multiple sessions, we can access performance metrics within and between sessions, rather than being limited to overall performance (**Figure 2.5C**). We hypothesised that this paradigm might reveal task mediated performance differences that revealed dissociable learning mechanisms. If dissociative results were indicated then this paradigm could be used in collaboration with MRS experiments to probe the mechanisms behind the different performance for each task.

2.4 Functional Magnetic Resonance Imaging

Functional magnetic resonance imaging (fMRI) is the dominant imaging modality for investigating neural processes in humans (**Figure 2.6**). The contrast in fMRI is arrived at by measuring the spin relaxation properties of the nuclei of atoms within tissues (Webb, 1988), and activated neurons and resting neurons cannot be differentiated by this technique directly.

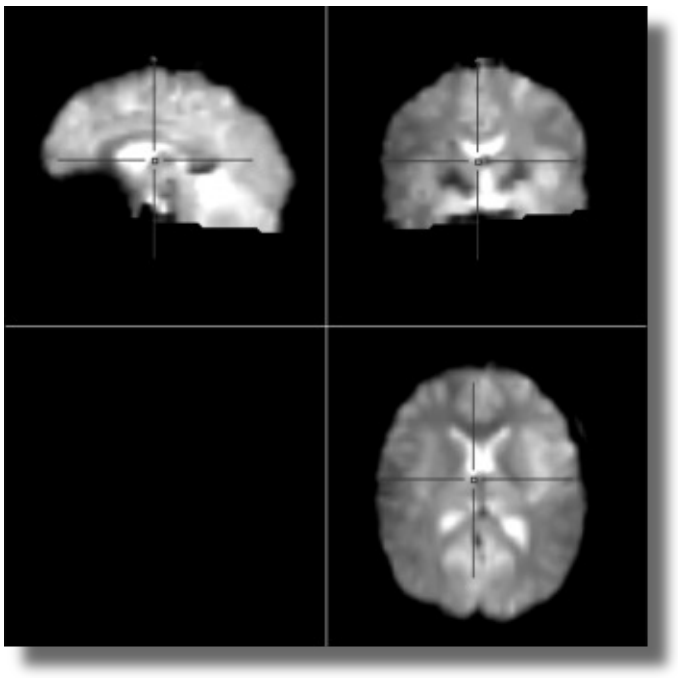

Figure 2.6: Sample fMRI images. Whole brain echo planar images (EPI). We acquired these images during a Glass pattern recognition experiment.

The firing of neurons (excitatory activation) however, involves an energy requirement that is met by an increase in blood flow to the site of activated neurons (Logothetis, 2010; Logothetis, Pauls, Augath, Trinath, & Oeltermann, 2001).

The brain consumes 20% of the oxygen entering the body despite comprising only 2% of the total body mass. Imaging techniques for cognitive neuroscience have therefore concentrated on the metabolic processes associated with neural activity rather than the neural activity directly, and in particular it is increased blood flow that is the process that is measured. The term BOLD (blood oxygen level dependent) signal is used to describe the contrast obtained during fMRI experiments (Ogawa, Lee, Kay, & Tank, 1990). The energy requirements of activated neurons cause a deoxygenation of haemoglobin (Hb). Deoxygenated haemoglobin (dHb) has different magnetic properties than oxygenated Hb (Kherlopian et al., 2008) and this should lead to a decreased signal as the dHb introduces field inhomogeneities that interfere with the MR signal. However, after an initial dip in signal response there is a continued flow of Hb without a commensurate increase in the oxygen consumption rate (Fox & Raichle, 1986; Fox, Raichle, Mintun, & Dence, 1988). The altered balance between Hb and dHb allows a change in image contrast, with typical activation leading to a 1–5% increase in image intensity (Parrish, Gitelman, LaBar, & Mesulam, 2000), which reflects an increase in neural activity.

Typical resolutions for fMRI are 1–2 mm and within this volume one might find 1×10^5 neurons and 1×10^8 synapses in the brain (Menon, 2001). Therefore the BOLD signal represents a large population effect, but the spatial resolution is still far higher than can be achieved in magnetic resonance spectroscopy (MRS) modalities. Despite the enviable spatial resolution of fMRI it is important to note that the BOLD signal does not distinguish between inhibitory and excitatory neuronal activation. This can be seen as a limitation in experiments

that hypothesise the involvement of inhibitory processes for learning. This limitation led us to investigate MRS techniques that could measure brain chemicals associated with inhibitory processes, this area is introduced in the next section. We were keen to view MRS as a complement to fMRI and not as a replacement as there are many uses for MR imaging in MR spectroscopy applications.

2.5 Magnetic Resonance Spectroscopy

Another way of measuring the functioning brain is to use magnetic resonance spectroscopy (MRS) techniques. MRS provides information on the chemical environment within tissue due to resonance frequencies of hydrogen protons (for ^{1}H proton spectroscopy, which is the most common MRS modality used to investigate the human brain).

Nuclei within different chemical functional groups exhibit different resonance frequencies because of unique magnetic shielding of local molecular electrons (Dager, Oskin, Richards, & Posse, 2008). The shielding is based on the bond configuration within the molecules and this

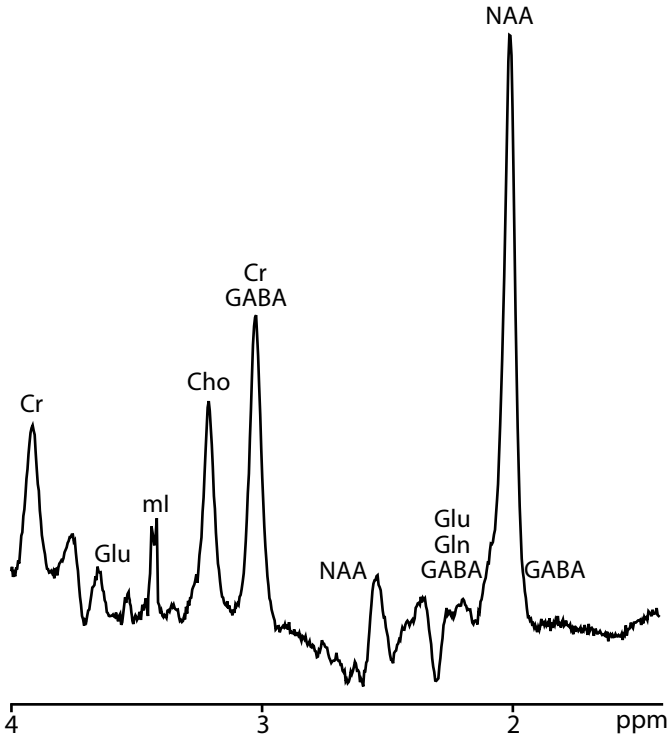

Figure 2.7: Sample MRS spectrum. We acquired this single voxel spectroscopy measurement with a 3 cm^3 volume, centred on the left hemisphere lateral occipital area, using a PRESS pulse sequence. GABA appears at three places along the chemical shift scale and at each place it is dominated by overlapping peaks of other metabolites.

causes a difference in the local magnetic field experienced by each nucleus. This means that the nuclei will resonate at different frequencies depending on the chemical composition of the molecule that the atom resides in. The amount of shift in resonance frequency is termed its chemical shift and this can be measured by an MRS scan to show the chemical environments as peaks along the chemical shift axis (**Figure 2.7**) in units of parts per million (ppm). The position of the peaks corresponds to particular chemicals and the area under the peaks is a measure of the relative amount of the chemical.

Another modulating effect on the spectrum is caused by J-coupling. This is the result of indirect interaction of two spins via the intervening electron structure of a molecule (Blüml & Panigraphy, 2013). Coupling between the nuclei can result in multiplet patterns, which means that a particular chemical may show as several distinct peaks at different points on the chemical shift scale. Some chemicals will also have an overlap of peaks despite being chemically unique. This is because there are limitations in spectral resolution that increase the width of the peaks, causing more highly concentrated molecules to obscure less abundant ones that are adjacent on the chemical shift axis. The range of chemicals measured through MRS can be manipulated through specific acquisition parameters and this allows some molecules to be disambiguated that would otherwise not be separable from masking molecules, this technique is called spectral editing.

Research in a clinical setting makes use of MRS to characterise functional aspects of the brain, for example metabolite differences between normal and diseased tissues can be used as markers for pathology. The use of MRS to study cognitive processes in the healthy brain is more novel and it is this area that we concentrated on for the investigation of inhibitory processes during learning. A benefit of using MRS rather than (or in addition to) fMRI to study the functioning brain is that MRS has the potential to distinguish between excitatory and

inhibitory neurotransmitters, whereas fMRI cannot dissociate inhibitory processes directly.

2.5.1 MRS for GABA Measurements

For the work in this thesis, we concentrated on GABA as we were interested in inhibitory processes during learning and because of its role in synchronising neuronal networks (Cossart, Bernard, & Ben-Ari, 2005). Metabolites are present at different concentration levels in the brain and some require different acquisition parameters in order to resolve them with MRS techniques.

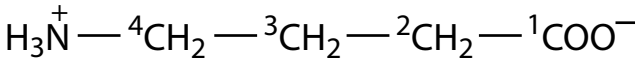

Figure 2.8: Chemical formula of GABA. Coupling results in multiplet lines in the MR spectrum (Govindaraju et al., 2000).

GABA is a metabolite that is difficult to detect *in vivo* using standard MRS. This is because it is found in low concentrations in the brain and also because of spectral overlap with more abundant metabolites. The chemical formulation of GABA (**Figure 2.8**) has implications for interpreting GABA spectra, and leads to splitting of the signal into triplets at 3.01 ppm and 2.28 ppm, and a quintet at 1.89 ppm. These aspects are discussed further in **Section 2.5.2**.

In order to measure GABA it must be available at concentration levels above the limit of detection for the modality in question (Waddell, Avison, Joers, & Gore, 2007). Several studies

Table 2.1: GABA concentration levels *in vivo*. Studies that confirm that GABA exists in concentration levels that are sufficiently high that they can be detected in humans using current technology.

Concentration $mM \cdot kg^{-1}$	**Reference**
1.10	Rothman, Petroff, Behar, & Mattson, 1993
1.60	Keltner, Wald, Frederick, & Renshaw, 1997
1.15	Hetherington, Newcomer, & Pan, 1998
0.80 (with MM nulling)	Terpstra, Ugurbil, & Gruetter, 2002
1.52 (with MM nulling)	Wylezinska, Mathews, & Jezzard, 2003
1.00	Mangia et al., 2006
1.10 (GM), 0.40 (WM)	C. Choi et al., 2007
1.30	Duarte, Lei, Mlynárik, & Gruetter, 2012

have estimated the concentration levels of GABA *in vivo* (**Table 2.1**) at above the detection limits for MRS at 3T.

Our hypothesis about GABA being a marker for inhibitory processes rests on the stability of measurements across time. GABA has been shown to remain constant across different time points in the brain (Evans, McGonigle, & Edden, 2010), therefore we concluded that GABA was suitable for the purposes of testing this research hypothesis. The technology that underpins chemical measurements with MRS consists of programmed manipulations of scanner operational parameters called pulse sequences. Specialised parameter settings are necessary to resolve GABA *in vivo* and so we introduce pulse sequences next to help in understanding how this process works.

2.5.2 Pulse Sequences

In this section we introduce the MEGA-PRESS pulse sequence by firstly outlining the PRESS pulse sequence on which it is based. The chemical bonding arrangement of GABA is briefly mentioned in the context of spectral line splitting as this has consequences for how the MEGA-PRESS sequence works in resolving GABA from more abundant, overlapping metabolites.

In MRS experiments, the signals acquired are manipulated by radio frequency (RF) pulses, which can be tuned to excite particular atoms in different chemical environments and regions of interest through the use of selective gradient pulses. Pulse sequences are used to acquire signals from a volume of tissue in single voxel spectroscopy (SVS) experiments. There are two main types of pulse sequence in SVS experiments; point-resolved spectroscopy (PRESS) and stimulated echo acquisition method (STEAM).

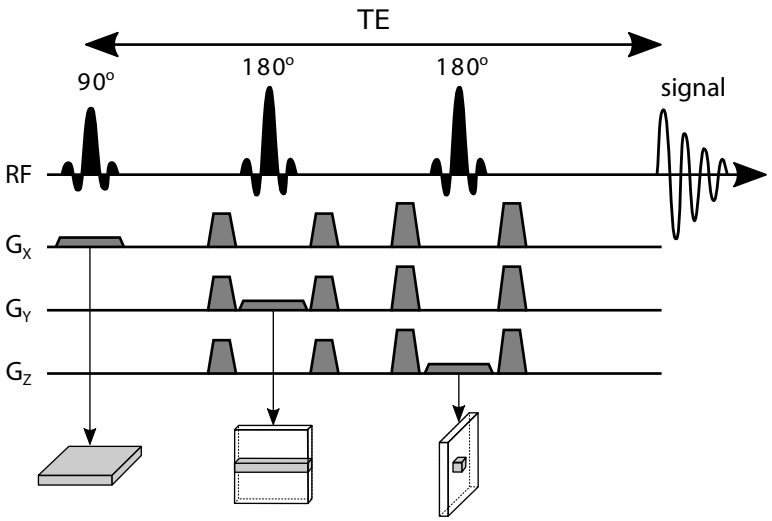

Figure 2.9: PRESS pulse sequence diagram. Sequence shows radio frequency (RF) pulses, gradient waveform and echo time (TE) and gradients (G_X, G_Y, G_Z), which localise the MRS volume.

2.5.3 PRESS Pulse Sequence

In the PRESS pulse sequence (**Figure 2.9**) a 90° and two 180° RF pulses are used to produce an echo, which comprises the free induction decay (FID) signal that is measured. The entire net magnetisation from the voxel is refocussed to produce the echo signal and this means that spectra from PRESS SVS will include signals from any coupled spins (Brown & Semelka, 2010).

This can be considered a disadvantage compared to STEAM, which is unaffected by J-coupled spins, but PRESS has better signal to noise ratio and we considered that this was important for detecting low concentration metabolites such as GABA. In a standard PRESS experiment, all of the signals from GABA are overlapped with the peaks from other more abundant metabolites. This meant that the GABA signal would be effectively hidden under larger peaks of metabolites that were not functionally relevant to the processes we wished to investigate.

2.5.4 MEGA-PRESS Pulse Sequence

To overcome the problems with spectral overlap, we investigated the use of spectral editing strategies and concentrated on the most popular technique for resolving GABA, which is the

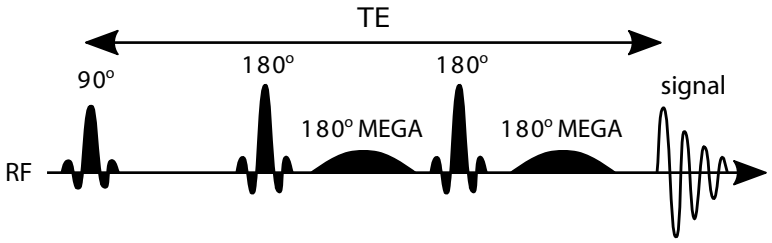

Figure 2.10: MEGA-PRESS pulse sequence diagram. Sequence shows radio frequency (RF) pulses, gradient waveform and echo time (TE), with two identical frequency selective 180° pulses.

MEGA-PRESS (Mescher, Merkle, Kirsch, Garwood, & Gruetter, 1998; Kaiser, Young, Meyerhoff, Mueller, & Matson, 2008) pulse sequence. The MEGA-PRESS sequence is built upon a PRESS foundation, but with the addition of two frequency selective pulses that are designed specifically to resolve GABA from overlapping signals from other metabolites. The position of the frequency selective pulses can be seen in **Figure 2.10** (labelled "180° MEGA") and can be compared with the standard PRESS pulse sequence (**Figure 2.9**).

The GABA molecule (**Figure 2.11**) is arranged in such a way that the bonds between the hydrogen and carbon atoms will result in the hydrogen atoms experiencing different amounts of magnetic shielding due to the interaction of electrons in the molecule. The chemical shifts that result from this differing amount of magnetic shielding are listed in **Table 2.2**, as are the J-coupling constants (Govindaraju et al., 2000), which describe the interaction between the spins of adjacent atoms within a molecule.

The net effect of this chemical arrangement leads to a splitting of the signals for GABA across the chemical shift scale. **Figure 2.12** shows the spectral splitting of GABA achieved under high field *in vitro* conditions. With 3T scanners and *in vivo* conditions, the line shapes

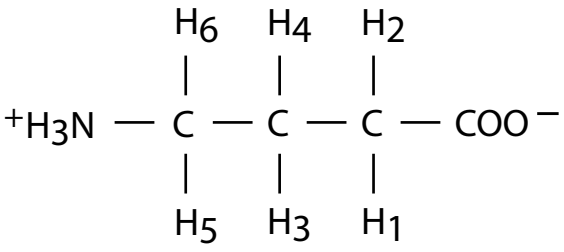

Figure 2.11: GABA bonds. Proton indices correspond to those in **Table 2.2**.

Table 2.2: Chemical shifts and coupling constants for GABA. Chemical shifts relative to DSS-trimethyl singlet resonance at zero ppm.

Resonance	Chemical Shift (ppm)	J-coupling (Hz)
H_1	3.0128	H_1-H_3 (5.37), H_1-H_4 (7.13)
H_2	3.0128	H_2-H_3 (10.58), H_2-H_4 (6.98)
H_3	1.8890	H_3-H_5 (7.76), H_3-H_6 (7.43)
H_4	1.8890	H_4-H_5 (6.17), H_4-H_6 (7.93)
H_5	2.2840	
H_6	2.2840	

are broader due to poorer spectral resolution and this can cause smaller peaks to become obscured under the overlap of larger ones that are adjacent on the ppm scale. The MEGA-PRESS pulse sequence uses the coupling between the GABA spins at around 3.01 ppm and 1.9 ppm. By applying an inversion pulse directed at 1.9 ppm, the edit ON pulse will have an effect on the signal from those spin systems close to 1.9 ppm and any systems that are coupled to them, which includes GABA at 3.01 ppm.

A MEGA-PRESS pulse sequence consists of alternative edit ON and edit OFF acquisitions. The effect of the editing pulse (ON) is to flip the GABA resonance at 1.9 ppm by 180°, which refocusses the J-evolution of the outer triplet peaks of the GABA at 3.01 ppm (Mescher et al., 1998). During the OFF acquisitions the inversion pulse is applied elsewhere and the J-evolution of the GABA resonances 3.01 ppm are allowed to evolve freely through the echo time. The overlapping creatine resonances at 3.03 ppm are not affected in either the ON or

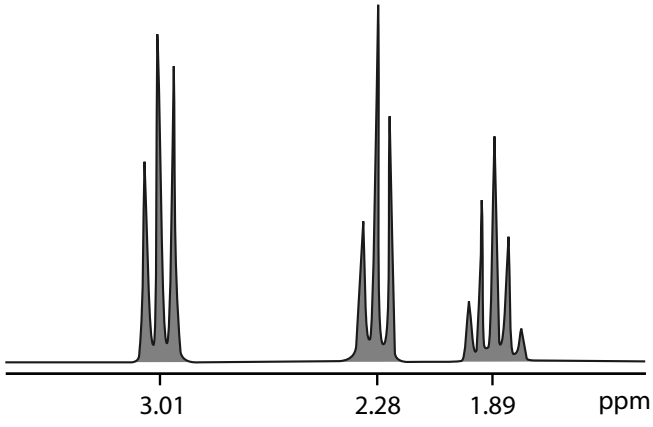

Figure 2.12: *In vitro* GABA spectrum. Position of GABA triplets and quintet along the chemical shift scale (ppm).

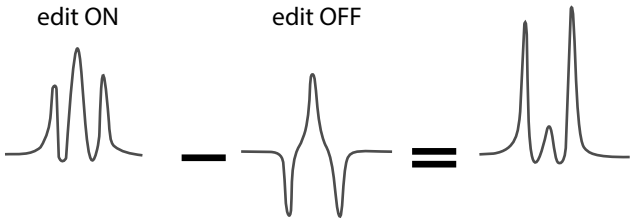

Figure 2.13: MEGA-PRESS combined spectrum. Edit ON with MEGA suppression at 1.9 ppm, edit OFF unsuppressed frequency spectrum and derived GABA peaks by subtraction of OFF from ON.

OFF acquisitions.

Disambiguation of GABA from creatine is achieved through the subtraction of the edit OFF from the edit ON (**Figure 2.13**). In the combined spectrum the outer peaks become more prominent (subtraction of a negative peak adds to the peak value), whereas the centre peak is reduced. The overlapping creatine signal at 3.03 ppm is effectively removed by the subtraction of two identical peaks. At 2.0 ppm the NAA peak becomes negated by the ON minus OFF operation.

The reproducibility of the sequence was an important factor when we decided on the methodology for our research and the MEGA-PRESS sequence has been shown to be strong in this area (Bogner et al., 2010). Having access to the pulse sequence is not in itself sufficient to measure GABA, as there are many operating and experimental parameters that need to be set. The data generated through a MEGA-PRESS experiment must be combined in a particular way and the signals needed to be carefully processed before being analysed with spectral analysis software. Once spectra have been analysed, there are further manipulations that can be applied, for example in scaling measurements according to brain tissue proportions. In this research we examine aspects of the choices that may be made in respect to MEGA-PRESS MRS acquisitions (**Chapter 3: MEGA-PRESS Acquisition**) and also detail an approach to the post-processing of the data obtained (**Chapter 4: Post-Acquisition Processing**), in relation to the physical science aspects of MEGA-PRESS noted in this section.

2.6 Related Work

This section describes the research that motivated our interest in investigating visual learning with spectroscopic techniques and in particular the MEGA-PRESS pulse sequence.

MEGA-PRESS Symposium. Some of the motivation for the work of this project came from a symposium about MEGA-PRESS research that we attended near the start of our project. The symposium discussed the state of the art, the perceived hurdles in obtaining reproducible spectra and was attended by some of the key researchers involved in this area. This meeting confirmed the idea that there was consensus as to what the difficulties were in GABA MEGA-PRESS acquisition, but that there was also a wide variety of approaches to solving the challenges. This meeting provided a stimulus to the direction of our research, for example there was considerable interest in developing best practice in data collection and analysis, with regard to absolute quantification, macromolecule contamination, echo times, phase cycling, frequency alignment procedures and correction of GABA measurements according to tissue fraction. Determining a standardised approach was considered challenging as different approaches were still being debated, however recommendations based on the consensus reached at the symposium were subsequently summarised and published.

Review Articles. The aforementioned symposium formed the basis of a review into current practices in MEGA-PRESS (Mullins et al., 2014). There was another review article that was concerned with GABA MRS acquisition (not just MEGA-PRESS), which usefully summarised current applications in neuroscience and tabulated some key parameters such as experiment duration and region of interest (Puts & Edden, 2012). This review made the observation that individual differences in GABA were not necessarily global across brain regions, this we found particularly interesting and inspired us to investigate multi-ROI experimental designs

(discussed further in **Section 3.4: Regions of Interest**). Another observation made in this review was that increased field strength has been used to increase the signal to noise ratio (SNR) for acquisitions, rather than to decrease the acquisition time for experiments. This led us to investigate the feasibility of shorter acquisition times in a simulation study of the effects of reduced scan time on quality metrics (**Appendix A: Time Course of MEGA-PRESS**). We identified a further review, specifically for GABA and motor cortex, that had some interesting ideas for the mechanisms for GABA and motor plasticity (C. J. Stagg, 2014).

2.6.1 Literature Review

We conducted our own literature review about *in vivo* MEGA-PRESS research and discovered that this area was still novel enough that the key papers could be listed comfortably within a section of a thesis. We were particularly interested in surveying the type of experiments that had used MEGA-PRESS, and therefore tabulated this information, along with the regions of interest and the number of participants (**Table 2.3**).

Table 2.3: MEGA-PRESS experiments. Region of Interest (ROI), participants (n=number, m=number of males, f=number of females, age=average age or age range) and type of experiment. This tables is ordered by publication date.

Reference	ROI	Participants	Experiment
Rothman et al., 1993	Occipital lobe	n=4	Controls for vigabatrin study
Hetherington et al., 1998	Occipital lobe	n=20	Measurement of GABA
Mescher et al., 1998	Occipital lobe	n=8	Water suppression with MEGA
Terpstra et al., 2002	Occipital lobe	n=14, m=6, f=8, age=30	Measurement of GABA *in vivo*
Wylezinska et al., 2003	Occipital lobe	n=5	LCM & MEGA-PRESS
Sanacora, Gueorguieva, & Yu-Te, 2004	Occipital cortex	n=71 incl. 33 clinical	GABA vs. depression
Jensen, deB. Frederick, & Renshaw, 2005	MRSI slice	n=6	Measurement of WM/GM GABA with regression
Floyer-Lea, Wylezinska, Kincses, & Matthews, 2006	Left hand region of motor cortex	n=36	Time course of GABA with motor learning

Continued on next page…

Table 2.3 MEGA-PRESS Experiments. *Continued from previous page.*

Reference	ROI	Participants	Experiment
Gasparovic et al., 2006	Above lateral ventricles parallel to ACPC line	n=14, m=6, f=8	Spectroscopic imaging effect of segmentation strategies
Bhagwagar et al., 2007	Cyngulate gyrus	n=49 incl. 31 clinical	GABA vs. depression
Edden & Barker, 2007	Centrally in posterior WM	n=5, m=2, f=3, age=31	MEGA & Inner Volume Saturation
Kaiser, Young, & Matson, 2007	Parieto-occipital GM	n=3	PRESS+4 & MEGA
Northoff et al., 2007	Anterior cingulate cortex, right hand paracentral cortex (control)	n=12, m=4, f=8, 25 started)	GABA & negative BOLD correlation in ACC (2-D J-resolved)
Waddell et al., 2007	Frontal GM	n=20	Measurement of GABA at rest
Mullins, Chen, Xu, Caprihan, & Gasparovic, 2008	Anterior cingulate cortex GM	n=6 & n=4	TE averaged PRESS vs. PRESS 40 ms
Edden, Muthukumaraswamy, Freeman, & Singh, 2009	Medial occipital lobe	n=13, m=13, f=0, age=33	Visual task, GABA, gamma & orientation selectivity
Muthukumaraswamy, Edden, Jones, Swettenham, & Singh, 2009	Medial occipital lobe	n=12, m=12, f=12, age=35	GABA, peak gamma & fMRI amplitude
C. J. Stagg et al., 2009	Left precentral knob motor cortex	n=16, m=16, age=27.5	Continuous theta burst stimulation & GABA/-NAA
Bogner et al., 2010	Occipital lobe	n=11, m=5, f=6, age=30	Fitting vs. integration
Boy et al., 2010	Supplementary motor area & dorsal medial frontal	n=12, m=12, f=0, age=21-32	Reversed masked priming
Donahue, Near, Blicher, & Jezzard, 2010	Visual cortex	n=12, m=6, f=6, age=30	GABA & haemodynamic measures
Evans et al., 2010	Visual cortex & sensorimotor cortex	n=8, m=7, f=1, age=31	Diurnal stability of GABA
Goto et al., 2010	Frontal & parieto-occipital lobe	n=41, m=21, f=20, age=35	GABA & extroversion
Sumner, Edden, Bompas, Evans, & Singh, 2010	Frontal eye field & visual cortex (control)	n=12, m=12, f=0, age=19-36	GABA & motor decision speed
Waddell et al., 2010	Anterior cingulate & cerebellar vermis	n=19, age=24	Measurement of GABA & Glu in ACC & cerebellar vermis
Yoon et al., 2010	Occipital lobe	n=26 (13 clinical, 13 control)	Orientation surround suppression & GABA
Bhattacharyya, Phillips, Stone, & Lowe, 2011	Motor cortex localised with finger tapping	n=19, 8 were discarded quality, age=38	GM & WM GABA measurements
O'Gorman, Michels, Edden, Murdoch, & Martin, 2011	Left hand dorsolateral prefrontal cortex	n=14, m=7, f=7, age=29, all right handed	Reproducibility GABA & gender effects

Continued on next page…

Table 2.3 MEGA-PRESS Experiments. *Continued from previous page.*

Reference	ROI	Participants	Experiment
Puts, Edden, Evans, McGlone, & McGonigle, 2011	Sensorimotor & occipital	n=16, m=10, f=6, age 27.3	GABA & tactile discrimination
C. J. Stagg, Bachtiar, & Johansen-Berg, 2011a	Motor cortex & occipital lobe (control)	n=12, m=6, f=6, age 21-31	tDCS, GABA & motor learning
Zhu, Edden, Ouwerkerk, & Barker, 2011	MRSI axial slice	n=3, m=0, f=3	MRSI & GABA
Edden, Intrapiromkul, Zhu, Cheng, & Barker, 2012	Occipital lobe	n=5, m=2, f=3, age=40	Measuring T_2
Evans et al., 2012	Right sensorimotor cortex, occipital, right dorsolateral prefrontal cortex	n=18, n=20, n=15 (different experiments)	Investigating alignment strategies
Michels et al., 2012	Left hand dorsolateral prefrontal cortex	n=16, m=9, f=7, age=28, age range=25-38	GABA & working memory
Morgan et al., 2012	Occipital lobe	n=33 incl.16 clinical	GABA vs. insomnia
Muthukumaraswamy, Evans, Edden, Wise, & Singh, 2012	Occipital lobe	n=15, m=15, f=0	GABA & BOLD
Robson, Muthukumaraswamy, Sumner, Evans, & Singh, 2012	Occipital lobe	n=126	GABA, gamma & cortical thickness
Rowland et al., 2012	Anterior cingulate	n=41	GABA & schizophrenia
Aufhaus et al., 2013	Anterior cyngulate cortex	n=48	GABA vs. ageing
Evans et al., 2013	Occipital, sensorimotor, & DLPFC	n=20, f=7, age=20–37	Subtraction artefacts
Foerster et al., 2013	Motor cortex, pons	n=59 incl. 29 clinical	GABA vs. ALS
Gao et al., 2013	Frontal & parietal	n=100, m=49, f=51, age=20-76	GABA & ageing
Puts, Barker, & Edden, 2013	Mesial parietal lobe	n=10, m=5, f=5, age=35	Measuring GABA T_1
Sandberg et al., 2013	Occipital lobe & parietal	n=36, m=36, f=0, age=25	GABA & cognitive failures
Shaw et al., 2013	Left inferior frontal & bilateral visual cortex	n=37, m=0, f=37, age=18-35	GABA & remitted depression
Blicher et al., 2014	Motor cortex	n=41 incl. 21 clinical, age=60	GABA & stroke
Harris et al., 2014	Precuneus	n=11, m=6, f=5, age=27	Frequency drift
C. J. Stagg et al., 2014	Motor cortex	n=12, m=6, age=21-31 & n=16, m=2, age=20-39	GABA & resting state networks
Wiebking et al., 2014	Left insula	n=27, m=17, f=10, age=22	GABA & interoceptive awareness
Riese et al., 2015	Posterior cingulate cortex	n=21 & n=15 MCI, age > 54	GABA & Alzheimer's

Continued on next page…

Table 2.3 MEGA-PRESS Experiments. *Continued from previous page.*

Reference	ROI	Participants	Experiment
Harris, Puts, & Edden, 2015	Visual, auditory, sensorimotor, frontal eye fields & dorsolateral prefrontal cortex	n=16	Tissue segmentation

The earliest published works tended to be concerned with the physical science aspects of the MEGA-PRESS pulse sequence and involved measurement of GABA, often without any particular application other than the validation of the measurements obtained. We found the early work of one group particularly interesting however, as they attempted a time course of GABA acquisitions during a motor learning task (Floyer-Lea et al., 2006). The major findings from this study were that short term GABA modulation was specific for learning, and that this was associated with encoding of the task rather than long term consolidation. Their results showed a decrease in GABA concentration during the learning task that was not evident in a similar, non-learnable task. We have only noted one other attempt to demonstrate a time course of GABA concentrations during a cognitive task, and that was in a study of working memory (Michels et al., 2012). The approach in these two studies represented GABA concentration changes as dynamic functional indicators of inhibitory processes during a task. This is in contrast with all other studies, which characterised GABA as a static marker of inhibitory potential or efficiency and therefore obtained resting state measurements for correlation with separate psychophysics experiments.

It was not until recently (the last five years) that papers started to appear that linked resting state MEGA-PRESS GABA with the performance results of psychophysics experiments. For example there have been papers linking GABA and orientation discrimination (Edden et al., 2009), subconscious motor control (Boy et al., 2010), motor decision speed (Sumner et al., 2010), orientation surround suppression (Yoon et al., 2010), motor learning (C. J. Stagg et al.,

2011a), working memory (Michels et al., 2012), cognitive failure (Sandberg et al., 2013) and interoceptive awareness (Wiebking et al., 2014).

MEGA-PRESS and Visual Paradigms. We identified just five papers that were primarily concerned with visual experiments (Edden et al., 2009; Muthukumaraswamy et al., 2009; Boy et al., 2010; Yoon et al., 2010; Muthukumaraswamy et al., 2012). Although we found that the occipital cortex was the most common region to acquire GABA from (n=18, compared with frontal regions n=9, motor cortex n=9, ACC n=5 and parietal n=3), it should be pointed out that the visual cortex was often used as a control area for experiments, rather than the region of interest that motivated these studies.

In a paper that investigated orientation discrimination with GABA concentrations in the visual cortex (Edden et al., 2009), a negative correlation was found between GABA concentration and performance on the task. The authors concluded that this demonstrated that resting state GABA measurements showed the functional action of GABA and presumed that the measurements would have included both intracellular and extracellular GABA populations. They suggested that GABAergic interneurons mediated neuronal inhibition by one of two mechanisms. Either at a neuronal level, by sharpening the tuning across stimulus contrasts, or at a network level by coordinating neurons. Although the paper cautioned that the actual mechanisms for visual representations were unknown, the idea that mechanisms could be inferred through correlations with inhibitory neurotransmitter influenced us strongly in the direction of our own research. Two of the articles that we identified as being concerned with GABA and visual stimuli were actually predominantly concerned with relating GABA to other physiological responses like the BOLD signal and peak gamma frequency (Muthukumaraswamy et al., 2009; Muthukumaraswamy et al., 2012). However, these articles did conclude that

functional neuroimaging metrics were dependent on the excitation and inhibition balance in the cerebral cortex. This added impetus to our hypothesis that inhibitory processes needed to be investigated in addition to excitatory ones.

In work that looked at the correlation between GABA in the supplementary motor cortex (SMA) and the reversed masked prime effect (Boy et al., 2010), the authors came to the interesting conclusion that the SMA was the site of production of suppression, rather than the site where suppression occurred. This led us to consider GABA correlations in the context of coordinated networks across brain regions. This was not something that we had come across before or since in the GABA literature and was something that we would return to in our conclusions for our own experiments.

The fifth paper that we identified as matching our research area of GABA and visual learning, was a study involving schizophrenic patients and controls, and correlations with orientation-specific surround suppression (OSSS). One of the major findings was a significant positive correlation between GABA levels and the magnitude of OSSS, which by implication suggested the link between inhibition and resting state GABA measurements.

MEGA-PRESS and Physiological Measures. Most of the papers identified in the literature review were more concerned with GABA measurement (n=16) than the link to perceptual learning performance. We did note some interest in connecting GABA concentrations with negative BOLD signal (Northoff et al., 2007; Muthukumaraswamy et al., 2009; Donahue et al., 2010; Muthukumaraswamy et al., 2012) and electrical activity (Muthukumaraswamy et al., 2009; C. J. Stagg et al., 2009), which led us to consider that physiological phenomenon, such as BOLD signal, could be mediated at a chemical as well as a haemodynamic level.

Other Groups. A group centred largely around Cardiff University have been especially visible in publishing MEGA-PRESS research. In addition to publishing their own research interests they have implemented a MEGA-PRESS sequence that runs on all major vendor MRI machines and have allowed other groups to use these implementations. It is from this group that we obtained the MEGA-PRESS pulse sequence that we used in our research. They have also developed a suite of software applications to process MEGA-PRESS data called Gannet (Edden, Puts, Harris, Barker, & Evans, 2014). There are some parallels between Gannet and the physical science aspects of this thesis (see **Chapter 4: Post-Acquisition Processing**), but it should be pointed out that Gannet was at an early stage of development when we began the project and so we were motivated to develop our own analysis pipeline. Another group from the Oxford Centre for Functional Magnetic Resonance Imaging of the Brain have published widely in GABA and motor cortex studies (Bachtiar & Stagg, 2014), this group is also responsible for brain imaging software that is used extensively for tissue segmentation (Jenkinson, Bannister, Brady, & Smith, 2002).

2.7 Discussion

One of our main aims for this project is to investigate the mechanisms behind visual learning with a particular focus on inhibitory processes. We framed the introductory materials around the notion that the usual ways of investigating the learning mechanisms, through psychophysics and fMRI, had limitations: Psychophysical paradigms might infer dissociative learning, but can not reveal the mechanisms directly and fMRI can not distinguish inhibitory activity from excitatory activity. These perceived limitations motivated the direction that we wished to pursue for our research. We discovered that the psychophysics literature had many interesting visual paradigms and selected Glass patterns for our research because of the flex-

ibility that this paradigm offered. This flexibility would allow us finely control parameters to create a variety of experiments based on shape detection and discrimination. The difficulty of the tasks could also be parametrically controlled, which interested us because we had some ideas on closely monitoring the time course of visual learning in multi-session experiments. The limitations of fMRI with regard to inhibitory processes motivated our interest in MRS and the measurement of the inhibitory neurotransmitter GABA. We discovered that GABA is a difficult metabolite to measure through standard MRS pulse sequences and this led us to become interested in investigating the MEGA-PRESS sequence.

Our reading into GABA and MEGA-PRESS research led us to consider that this might be a novel way to approach an investigation into inhibitory processes and visual learning. There had been some interesting experiments described in the literature that used MEGA-PRESS GABA research, but few that had much overlap with our research interests. In fact we identified just four papers that were primary concerned with MEGA-PRESS GABA research and visual learning paradigms. The few papers that were published in this area did inspire some ideas for how we might investigate inhibitory processes and visual learning, however. Our reading also alerted us to some of the difficulties that researchers faced in obtaining good quality spectra from the technology and this led us to make an investigation into processing the MEGA-PRESS signals a further research goal for this project.

The literature review led us to conclude that the investigation of inhibitory processes in visual learning in humans was an area that has hitherto received sparse attention and we therefore suggest that the research context for this thesis is a niche one, but one with great potential for extending our knowledge concerning how the brain learns.

3

MEGA-PRESS ACQUISITION

3.1 Introduction

Standard pulse sequences such as PRESS or STEAM are provided by MR scanner manufacturers and they usually specify default parameter settings that have been optimised to produce reproducible scan results. MEGA-PRESS sequences are experimental sequences. This means that more work is required in the experimental setup and processing of MEGA-PRESS sequences than with standard ones. This is partly because optimised default scan parameter settings are not available for experimental sequences, but also because the scanner software is not designed to process edited scans. One of the aims for this chapter is therefore to describe appropriate parameter settings for MEGA-PRESS. In doing so we will reflect current best practice so that any results will be comparable with other studies.

It is easier to obtain reproducible MR spectroscopic signals from *in vitro* experiments than it is from *in vivo* ones. We therefore decided to test our parameter settings by running MEGA-PRESS experiments on liquid phantoms that we constructed specially for this process. These experiments were designed to investigate the line shape of spectra obtained from the MEGA-PRESS pulse sequence by comparing it to the theoretical line shape of GABA. In one experiment we test the pulse sequence using a high concentration GABA solution and in another

experiment we use a solution with chemical formulations designed to match those found in the human brain.

For *in vivo* MEGA-PRESS experiments it is important to target regions of the brain that are involved with the process that is being investigated. We therefore discuss some strategies for identifying appropriate brain regions based on morphology and fMRI localisers. We also discuss how to maintain consistency in positioning the acquisition voxels, to aid precision and reproducibility in MEGA-PRESS experiments. We describe a novel approach to selecting ROIs based on fMRI BOLD signal measurements and advocate the selection of multiple ROIs for a single experiment; this is in contrast to MEGA-PRESS experiments currently described in the literature.

3.2 Acquisition Parameters

Any pulse sequence will have some parameters whose values are chosen by the researcher to suit a particular experiment. The most important variables for a MEGA-PRESS experiment are the dimensions (volume) of the acquisition region, the repetition time (TR), the echo time (TE) and the number of acquisitions per experiment. The volume of the acquisition should obviously cover the area of the brain under consideration and is expressed in millimetre units. However, there is a linear relationship between the size of the voxel and the signal to noise ratio (SNR) that can be obtained. Larger voxels have higher SNR, so there is an inevitable trade off between localisation and signal quality. The TR will control the time between successive pulse sequences being applied, the unit for this is seconds. The TE (in milliseconds) represents the time between the application of the 90° pulse and the peak of the free induction decay signal. It is varied to optimise the relaxation values of particular metabolites. The SNR of MR acquisitions increases as the square root of the number of scans, therefore more acquisitions

equates to higher SNR. Higher SNR is obtained at the cost of increased scan duration time.

We conducted a review of published MEGA-PRESS experiments in the literature and tabulated the main parameters (**Table 3.1**). This is intended to be used to help inform suitable parameter values for other researchers wishing to conduct experiments that will be most widely comparable with other studies. From this table we can see that the volume for the acquisition voxel was typically $3 \times 3 \times 3$ cm, TR was most commonly 1800 ms, TE mode was 68 ms, field strength mode was 3T and acquisition time ranged between 3–15 min for single voxel spectroscopy experiments.

Table 3.1: Scan parameters. MEGA-PRESS acquisition parameters arranged by publication year. **Volume** (cm unless cc or mL specified), repetition time **TR** (s), echo time **TE** (ms), **System** (Tesla field strength and manufacturer) and acquisition time (s).

Reference	Volume	TR	TE	System	Scan time
Rothman et al., 1993	2x4x3		68	2.1T Oxford Insts.	
Hetherington et al., 1998	13.5 cc	2	72	4.1T	266
Mescher et al., 1998	27 mL	3	34	4T Siemens	240
Terpstra et al., 2002	3x3x3	4	69	7T Magnex, Oxford	
Wylezinska et al., 2003	3x3x3	3	68	3T Varian Inova	
Sanacora et al., 2004	3x3x1.5	2	68	2.1T Oxford Magnet Technology	1200
Jensen et al., 2005	3 cm thick MRSI slice	1.25		4T Varian Unity Inova	2880
Floyer-Lea et al., 2006	2x2x2		68	3T Varian Inova	200
Gasparovic et al., 2006	7.5x9x1.5	1.5-3.0	135	1.5T Siemens Sonata	582
Bhagwagar et al., 2007	3x3x2	3	68	3T Varian Inova	384
Edden & Barker, 2007	3x3x3	2	68	3T Philips Intera	1020
Kaiser et al., 2007	18 mL	2	72	4T Bruker MedSpec	600
Northoff et al., 2007	2.5x2x3	2.5	31–229	3T Philips Intera	960
Waddell et al., 2007	15–40 mL	2.5	70	3T Philips Achieva	640
Mullins et al., 2008	2x2x3	2	30 vs 40 40 vs 80	3T Siemens Tim Trio & 3T Philips Achieva	540
Edden et al., 2009	3x3x3	1.8	68	3T GE Signa HDx	900
Muthukumaraswamy et al., 2009	3x3x3	1.8	68	3T GE Signa HDx	900
C. J. Stagg et al., 2009	2x2x2		68	3T Siemens Varian	200
Bogner et al., 2010	2.5x3x3	1.5	69	3T Siemens Tim Trio	390
Boy et al., 2010	3x3x3	1.8	68		720
Donahue et al., 2010	3x3x3	2	69	3T Siemens Tim Trio	
Evans et al., 2010	3x3x3	1.8	68	3T GE Signa HDx	600
Goto et al., 2010	3x3x3	3	68	3T GE Signa Excite	360
Sumner et al., 2010	3x3x3	1.8	68	3T	600–900

Continued on next page...

Table 3.1 Scan Parameters. *Continued from previous page.*

Reference	Volume	TR	TE	System	Scan time
Waddell et al., 2010	7.32, 6.1 mL	2.5	73	3T	960
Yoon et al., 2010	3.5x3x2.5	1.5	78	3T Siemens Trio	390
Bhattacharyya et al., 2011	2x2x2	2.7	68	3T Siemens Trio	518
O'Gorman et al., 2011	2.5x4x3	1.8	68	3T	600
C. J. Stagg et al., 2011a	2x2x2	3	68	3T Siemens Varian	900–1200
Zhu et al., 2011	21x18	2	68	3T Philips Achieva	1058
Edden, Intrapiromkul, et al., 2012	3x3x3	2	70, 100, 180	3T Philips Achieva	510
Evans et al., 2012	3x3x3	1.8	68	3T GE HDx	
Michels et al., 2012	2.5x4x3	1.8	68	3T GE HDx	
Morgan et al., 2012	3x1.5x3	2.5	68	4T Oxford Magnet Technology	1200
Muthukumaraswamy et al., 2012	3x3x3	1.8	68	SCANNER	900
Robson et al., 2012	3x3x3			3T GE	
Rowland et al., 2012	3.5x3.5x3.5	2	68	3T Philips Achieva	
Aufhaus et al., 2013	4x3x2	3	68	3T Siemens Trio	288
Evans et al., 2013	3x3x3	1.8	68	3T GE HDx	598
Gao et al., 2013	3x3x3	2	68	3T Philips Achieva	660
Puts et al., 2013	3.5cm^3	1, 2, 3 & 5	80	3T Philips Achieva	256–1280
Foerster et al., 2013	3x3x2	1.8	68	3T Philips Achieva	460
Sandberg et al., 2013	3x3x3	2.5	68	3T Siemens Trio	480–1200
Shaw et al., 2013	3x3.5x3.5 & 3x3x3	1.8	68	3T GE Signa HDx	480
Blicher et al., 2014	2x2x2	2.5	68	3T Siemens Trio	930
Harris et al., 2014	3x3x3	2	68	3T Philips Achieva	640
C. J. Stagg et al., 2014	2x2x2	3.0	68	3T Siemens Varian	768
Wiebking et al., 2014	2.3x4.8x2.7	2		3T Siemens Trio	
Riese et al., 2015	3x3x3	1.8	68	3T Philips Ingenia	648
Harris et al., 2015	3x3x3, 4x3x2	2	68	3T Philips Achieva	640

For *in vivo* experiments at 3T we suggest volume sizes of at least 2 cm^3, with 3 cm^3 being preferable in terms of greater SNR. The volume size also needs to be large enough to sufficiently cover the brain area under consideration and we further suggest that the same volume size be used when comparing different brain regions. This is to reduce the chance that variation in metabolite concentration measurements might vary as a factor of volume size, rather than brain region. Echo time of 68 ms has been common since the pioneering papers (Rothman et al., 1993) and has the advantage of being longer than the macromolecule (MM) relaxation time of 40 ms, which should minimise the co-editing of MM contaminants

to the GABA signal (C. Choi et al., 2007). This parameter should only be altered if there are specific hypotheses that needed to be tested, for example with regard to reducing MM contaminants. With TR, a value of 1.8 s has the advantage of being the most commonly used amongst researchers in this field and hence makes results more comparable with the greatest number of other studies. It also means that more repetitions can be acquired in the same experiment time than experiments with longer TR time.

The parameter with the greatest variability was the scan time. Increasing scan time allows for more averages to be acquired and therefore improves the SNR of the measurements. For *in vivo* experiments, subject movement will adversely affect accuracy of the measurements and so scan time is usually chosen by the researcher as a compromise between maximising the scan time, but not making experiments so long as to increase the likelihood of subject movement predicated by discomfort. The number of dynamic averages acquired and phase cycling parameters combine with the TR time to set the scan duration. It is an open question on what the optimal values should be for these parameters (Mullins et al., 2014). Increased phase cycling improves localisation and water suppression but leaves fewer individual signal exports from the scanner, which will impose limitations on post-processing operations. For experiments described later in this thesis, we opted for 32 dynamic averages that consisted of 16 phase cycled acquisitions each. These settings would allow for good localisation within the scanner and also return sufficient free induction decays (FIDs) for post-processing for phase correction (**Section 4.4**) and spectral realignment (**Section 4.5**). These settings led to a total scan duration of approximately 15 min, which was in the upper range of MEGA-PRESS scans from the literature. The experiments described in **Appendix A** confirmed that obtaining more averages resulted in higher SNR, however the results also indicated that shorter scan duration times can produce spectra that is adequate for the purpose of GABA quantitation.

We set the number of samples to 2048 and spectral bandwidth to 2150 Hz. These parameters were less commonly reported in the methods section of MEGA-PRESS literature and so we omitted them from **Table 3.1**. In the publications that did report these parameters, the values of 2048 (samples) and 2150 Hz (bandwidth) were the most common. It is preferable for the number of samples to be a power of two as this facilitates the efficiency of the Fourier transform in subsequent processing (see **Section 4.4** for more on this). The setting for spectral bandwidth should allow sufficient coverage for a range of metabolites including GABA. Further parameter choices that we used in the experiments for this project are detailed in **Table D.1**.

3.3 Phantom Experiments

Detection of GABA *in vitro*, for example in a liquid phantom, is considerably easier than *in vivo*. There are several reasons why this is the case, for example liquid phantoms do not have the complex arrangement of tissues that the human brain has, with the concomitant artefacts that this produces in the magnetic field of the scanner. The artefacts can be visualised with reference to images taken during MRI experiments (Krupa & Bekiesińska-Figatowska, 2015), but they have their analogues as interference in MR spectra for MRS experiments. Examples of MRI artefacts are: Truncation artefacts, which occur near sharp high-contrast boundaries; aliasing artefacts where anatomical structures outside of the field of view become mapped onto the image; and chemical shift artefacts that appear at the lipid-water interface especially in fluid filled structures such as ventricles. Metallic implants, tattoos and even clothing can introduce artefacts in MR experiments and all of these are mitigated when conducting phantom experiments. Phantoms can also be loaded with elevated concentrations of the metabolite of interest, which will also make the task simpler. Humans tend to move during scanning and

this necessitates post-processing of the signals to realign subspectra (**Section 4.5**), this step is not necessary with a phantom. For these reasons it is preferable to conduct experiments using liquid phantoms to test parameter settings as a precursor to *in vitro* experiments.

The phantom experiments described in this chapter were all conducted after we had completed the *in vivo* scans. This was due to technical reasons, such as the availability of materials and subjects. However, we present the *in vitro* experiments first in order to avoid the need to explain post-acquisition processing techniques that are necessary for *in vivo* experiments (these are the substantive content of **Chapter 4: Post-Acquisition Processing**).

What we wished to investigate through the phantom experiments was how close the GABA phantom spectra were compared to the theoretical signal shape (**Section 2.5.2: Figure 2.13**), using the MEGA-PRESS sequence and basic post-acquisition processing steps.

3.3.1 GABA Phantoms

Our first experiment consisted of three scans of a 10 mM solution of GABA (A2129, Sigma Aldritch) in phosphate buffered saline (pH 7.4, P5368, Sigma Aldritch), similar to that reported in (Edden, Puts, & Barker, 2012). We constructed the phantom using a 250 mL glass flask and scanned it using a Philips 3T Achieva scanner (Philips Healthcare, Best, Netherlands). The main scan parameters were TE = 68 ms, TR = 3000 ms, volume = 26 mm^3, samples = 2048, spectral bandwidth = 2150 Hz, scan time = 192 s, other parameters were the same as those in **Table D.1**. We obtained our first scan using 32 dynamic averages with 2 phase cycles. For the second scan we used identical parameters except that we applied the optimisation setting for water. We obtained the third scan with 64 dynamic averages without phase cycling.

We converted the scanner exported signals to frequency domain spectra and the edit OFF spectra and the edit ON spectra were combined and averaged (see **Listing C.1** and **Section 4.4**

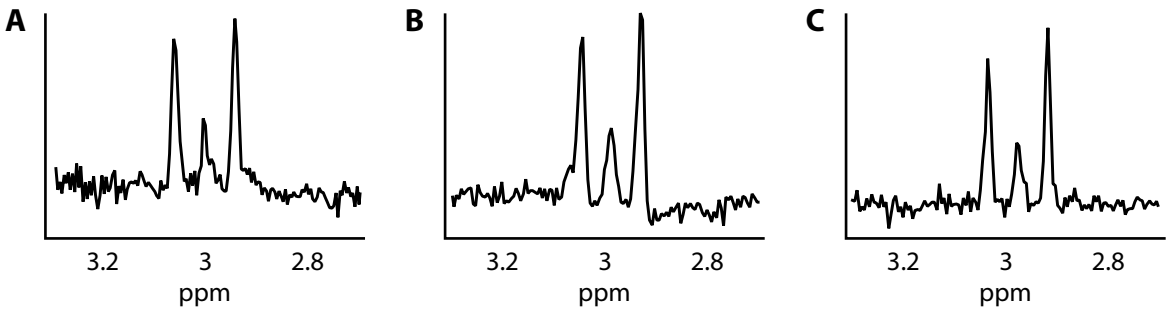

Figure 3.1: GABA phantom triplets. Spectrum from a GABA phantom using the MEGA-PRESS pulse sequence **(A)**, sequence optimised for water **(B)**, no phase cycling **(C)** .

for further details). We plotted the averaged spectra and examined the line shapes between 2.8 and 3.2 ppm (**Figure 3.1**), which is where the GABA signal should appear in a MEGA-PRESS experiment. We compared the plots with the theoretical line shapes (**Section 2.5.2: Figure 2.13**) and concluded that the spectra did match the expected shape with the reduced central peak compared with the outer peaks of the GABA triplet at 3.01 ppm. The GABA concentration of 10 mM is higher than *in vivo* concentrations. This concentration was chosen to improve the chances of unambiguous detection of GABA in the phantoms.

The water optimisation setting (**Figure 3.1B**) did not not make appreciable differences to the line shapes of the spectra, neither did the changes made to the phase cycling (**Figure 3.1C**). These changed settings might effect the line shapes more with *in vivo* scans. The phase cycling for example can help with problems that are related to subject movement and this is not relevant with a static phantom scan.

We concluded from this experiment that the MEGA-PRESS pulse sequence resolved the GABA triplet at 3.01 ppm, using the acquisition parameters that we chose in a phantom with 10 mM concentration of GABA. This represented a useful validation of the sequence and parameter settings, but it did not test the disambiguation of creatine from GABA, which is the main innovation of the MEGA-PRESS sequence.

3.3.2 GABA and Brain Metabolite Phantoms

To address the limitations of the GABA phantom experiments we created phantoms that included additional metabolites that mimic those found in the human brain (**Table 3.2**). The additional chemicals would tell us about the efficacy of the GABA inversion in the edited pulse sequence, in particular the effect of creatine subtraction on the line shape. We chose two concentrations of GABA to represent lower (2.8 mM) and higher (8.8 mM) concentration phantoms. These were still both above *in vivo* concentrations (see **Table 2.1**).

We used a combination of phosphate buffered saline (NaCIKCI), mono basic dihydrogen phosphate (KH_2PO_4) and dibasic mono hydrogen phosphate (K_2HPO_4) to raise the pH of the phantom solution to 7.1. We also added sodium azide $(NaN_3, 15\ \text{mM}, 65.01\ \text{u}, 0.9751\ \text{g})$ to act as an anti-microbial, this was to minimise the possible side effects of organic contaminants over time. As before, we constructed the phantoms using 250 mL glass flasks.

We set the values of the main scan parameters to; volume = 30 mm^3, TR = 1800 ms, TE = 68 ms, samples = 2048, spectral bandwidth = 2150 Hz, water suppression = VAPOR, phase cycles = 16, dynamic scans = 32, scan duration = 921.6 s (15 min 21.6 s) for a spectral

Table 3.2: Brain phantom metabolites. List of chemicals used to simulate brain metabolite concentrations in MR phantoms with two elevated concentrations of GABA. **Conc.** is the desired concentration in milli molars, **MW** is the molecular weight and **Mass** is the weight of the substance needed to create the desired concentration in a 1 dm^3 phantom. All ingredients were sourced from Sigma Aldritch.

Metabolite	Chemical Formula	Conc. mM	MW g/mol	Mass g
GABA	$NH_2(CH_2)_3COOH$	2.8	103.12	0.2887
GABA	$NH_2(CH_2)_3COOH$	8.8	103.12	0.9075
NAA	$C_{12}H_{10}O_1$	12.5	186.21	2.3276
Creatine	$H_2NC(=NH)N(CH_3)CH_2CO_2H$	10.0	131.13	1.3113
Choline	$C_{11}H_{21}NO_8$	2.5	295.29	0.8859
Myo-Inositol	$C_6H_{12}O_6$	7.5	180.16	1.3512
Glutamate	$NaOOCCH_2CH_2CH(NH_2)COOH{\cdot}H_2O$	12.5	186.13	2.3266
Glutamine	$C_5H_{10}N_2O_3$	6.0	146.14	0.8768
Lactate	$C_3H_5NaO_3$	5.0	187.13	0.9357

resolution of 1.05 Hz/point. These parameters were identical to those we planned to use for *in vivo* experiments.

We combined and averaged the frequency domain signals as before (**Section 3.3.1**). This involved the minimum of processing steps necessary to produce the frequency domain averages. More sophisticated processing is required for *in vivo* experiments, for example phase correction and alignment, these are explained in detail in **Chapter 4: Post-Acquisition Processing**. For the purposes of this section we wished to take advantage of the simpler experimental paradigm that *in vitro* scanning provides and plotted the spectra obtained from the two phantom experiments without additional post-processing of the signals (**Figure 3.2**). The higher GABA concentration phantom showed a convincing GABA peak at the expected ppm range, as well as the expected inverted NAA peak at 2 ppm and GLX signal at 3.7 ppm. The lower concentration spectrum showed a smaller GABA peak, as was also expected.

We concluded from these scans that the sequence and parameter selections were suitable

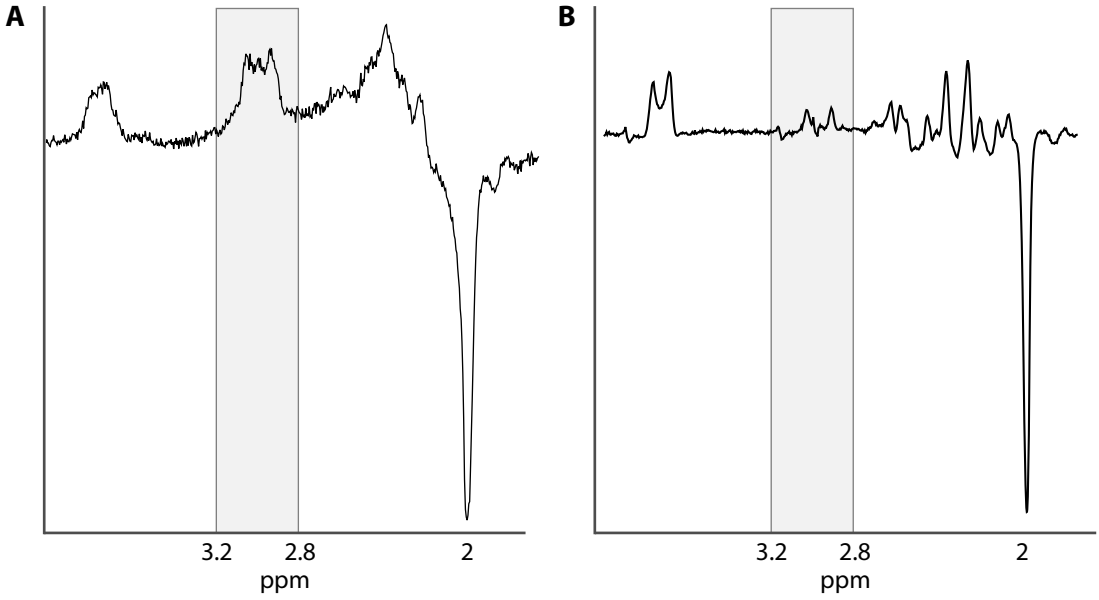

Figure 3.2: GABA brain phantom spectra. Spectra from brain phantoms with two concentrations of GABA. **(A)** had GABA at a concentration of 8.8 mM and **(B)** had GABA at 2.8 mM. The shaded boxes represent the range on the chemical shift scale for the GABA signal.

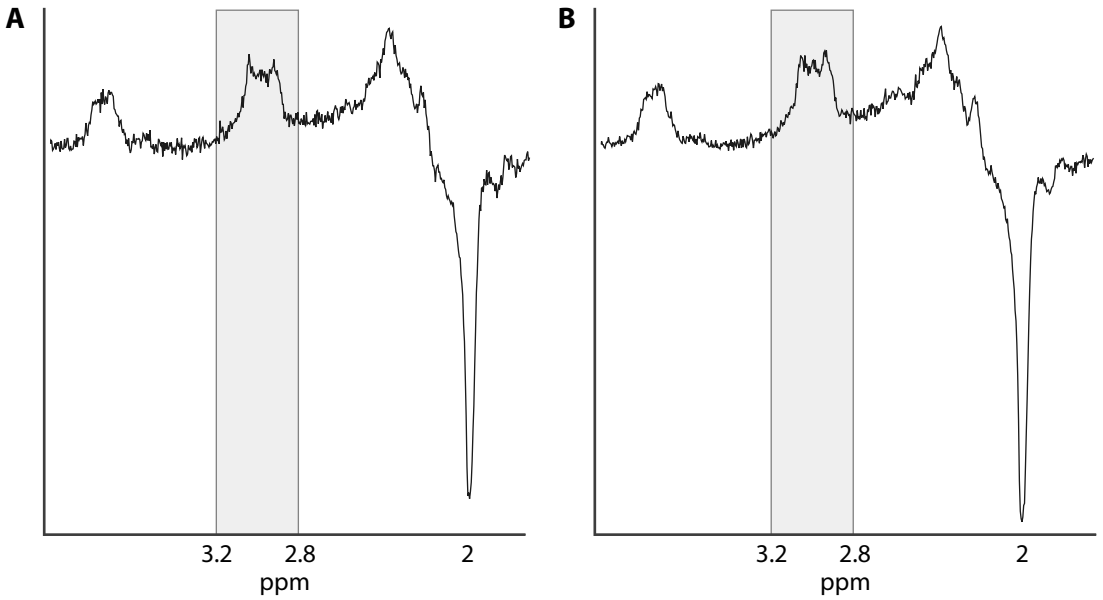

Figure 3.3: GABA brain phantom spectra, different scan durations. Spectrum obtained from **(A)** scan duration of 460.8 s (7 min 40.8 s) versus **(B)**, which was acquired in a scan lasting for 921.6 s (15 min 21.6 s).

for resolving GABA in a brain-like phantom and that effective GABA inversion at 3 ppm in the edited sequence had occurred. This conclusion came with the caveat that phantoms represent fewer challenges for MR techniques than those with human brains and that the GABA concentrations were relatively high. However, we also noted that good visual agreement with the theoretical line shape was achieved, even with a rudimentary processing method.

We conducted a further phantom experiment where we sought to see what effect a reduced scan time would have on the higher concentration phantom. For this we compared two scans; the parameters were identical in both scans, except for the duration of the scan. In **Figure 3.3A** we have plotted the spectra where the dynamic scans were reduced from 32 to 16, which halved the duration of the scan to 460.8 s (7 min 40.8 s). **Figure 3.3B** was plotted from the data acquired in a scan that lasted for 921.6 s (15 min 21.6 s). These plots were not intended to be quantitative (hence we omit values on the y axes), but we noted that the outer peaks of the GABA triplet at 3 ppm were still in evidence in the shorter duration scan.

We concluded from this that it might be worthwhile investigating the possibility of using

shorter scans in subsequent experiments (see **Appendix A: Time Course of MEGA-PRESS** for more detail on this idea).

3.4 Regions of Interest

It is very important to choose appropriate regions of interest (ROIs) and accurately position MRS acquisition voxels, whether the scans are for clinical practice or for research purposes. If a clinician is trying to characterise the metabolite profile of a brain tumour for example, it would be crucial that the position of the ROI correspond accurately with the tumour in question. Misplacing the acquisition voxel outside of the tumour or using inappropriate voxel dimensions would not help at all in such a case. Similarly in research situations the placement of the acquisition voxel is important. Not only does the placement of the voxel need to be chosen with regard to the hypothesis under investigation, it also has to be positioned consistently so that MRS measures can be compared across subjects. Care must taken to acquire MRS measurements from tissue only, as bone, fat, ventricles and air cavities can all introduce artefacts into the scan results.

This section discusses some strategies to help with consistent voxel placement that use MR imaging techniques. These techniques can be simple, for example using reference brain images or they can be more sophisticated, such as using localiser scans to identify ROIs. We introduce the idea of using fMRI BOLD signal brain maps to guide the choice of ROI, which is a novel practice in the field. We also discuss the merits of using multiple ROIs in visual learning experiments, again this has not been widely attempted by other research groups.

3.4.1 MRS Planning, Morphological Features

Some ROIs are readily identifiable through an inspection of morphological features that are visible on brain images. For example the motor cortex can be seen on a sagittal image as lying

between somatosensory cortex and the supplementary motor cortex. In order to position an acquisition voxel at a scanner, which is referred to as planning the experiment, the acquisition voxel is manipulated into position by the operator using a graphical display that has 3-D MR anatomical images of the subject on it.

A virtual acquisition voxel, represented by a wireframe cube, can be manipulated into position with a mouse, directly over the anatomical images. If the region under investigation can be identified visually on the anatomical images then this represents the simplest planning case. The motor cortex is an example of this type of planning, and can be approximately located with reference to the anatomical images alone (**Figure 3.4**). Note that the voxel is rotated in the coronal and sagittal views (**Figure 3.4B,C**), this is to ensure that the voxel covers the greatest amount of grey matter while keeping within the tissue boundaries. The positioning of this ROI is deliberately not centred on the motor hand knob. This is because the ROI is intended to be used as a control region in experiments that may be extended to include concurrent psychophysics testing. In such experiments GABA concentrations in the motor hand area could conceivably be a factor, for example if the subjects were required to press buttons during tasks. We therefore placed the control ROI away from the motor hand knob to avoid this potentially confounding factor.

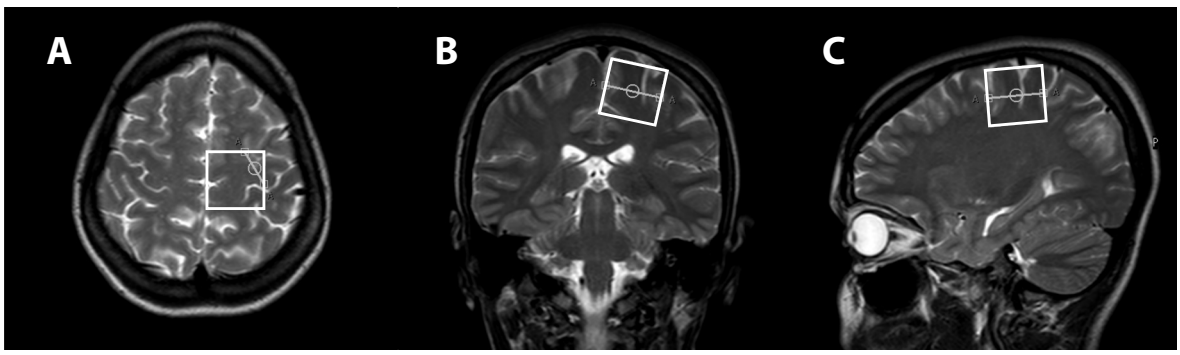

Figure 3.4: Motor cortex planning. MR planning voxel (white box) for motor cortex in (**A**) axial, (**B**) coronal and (**C**) sagittal views.

3.4.2 MRS Planning, Talairach Coordinates

In the case of brain regions that are larger than the acquisition voxel, the challenge is to identify a particular part of the region to acquire from. This could be the central point of the region or the part of the region with the most grey matter, depending on the hypothesis under consideration. The mid frontal gyrus is an example of such a region. The approach we took to identifying this ROI, was to take average Talairach (Talairach & Tournoux, 1988) coordinates reported in the literature (Pernet et al., 2004; Vogels et al., 2002; Heekeren, Marrett, Bandettini., & Ungerleider, 2004). We then plotted these coordinates onto MRI images that had been transformed into Talairach space (**Figure 3.5A,B**). We then used these images as references whilst planning mid frontal gyrus scans.

During the planning of MEGA-PRESS experiments, we acquired T_2 brain images in three orthogonal planes and used these images to visually position the acquisition voxel at the scan-

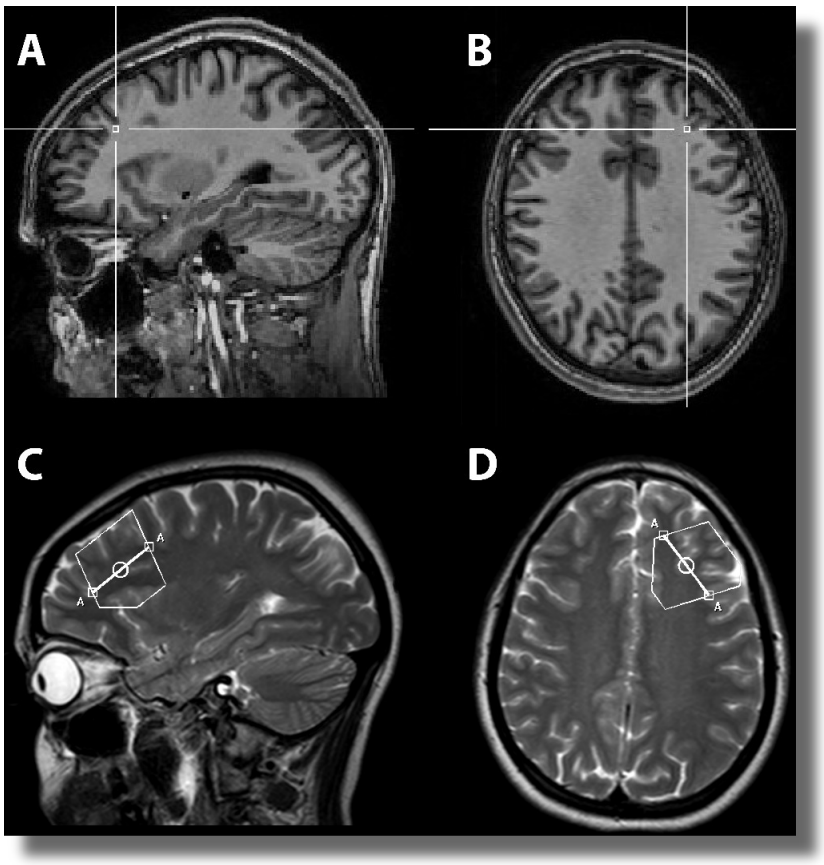

Figure 3.5: ROI planning for MRS acquisition. Sample T_1 images (**A, B**) marked with average Talairach coordinates for mid frontal gyrus. Scanner console T_2 images (**C, D**) with bounding box for the MRS voxel.

ner console. We compared the Talairach reference images (**Figure 3.5A,B**) with the scanner console planning images (**Figure 3.5C,D**) to obtain a consistent positioning for the acquisition. Achieving this consistency is very important, especially if comparisons between subjects is intended. The scout T_2 images that were used to plan the voxel position were acquired at the beginning of each experiment and we found that a slice gap of 4 mm gave the best compromise between resolution and scan duration time, which was less than 1 min per plane. This slice gap meant that we typically acquired between 24 and 36 slices per axis. The T_2 images were also useful when we performed across session alignment of brain images, which became important for segmentation (**Section 4.7**).

3.4.3 MRS Planning, Localiser Scans

Some ROIs do not have specific morphological identifiers, nor is there consensus on their position among the research community. This means that the approaches outlined above could be problematic. Lateral occipital (LO) areas such as the lateral occipital complex or the kinetic occipital (KO) are examples of ROIs that are difficult to identify with standard methods. Lateral occipital areas are involved in shape recognition (Altmann, Bülthoff, & Kourtzi, 2003). This is relevant to the Glass pattern stimuli that we planned to use (**Section 2.3.2: Psychophysics**) as the stimuli can be manipulated to create distinct shapes. A method that can be used to locate this region is to use localiser scans. These use specially designed visual stimuli to evoke a BOLD response in the relevant ROI of the subject who views the stimuli. The BOLD response is quantified by brain imaging software and this can be visualised as an activation map on a brain image. In the absence of consensus for the location of lateral occipital areas we decided to conduct our own fMRI localiser scans.

We localised lateral occipital areas of five participants with a procedure that used intact

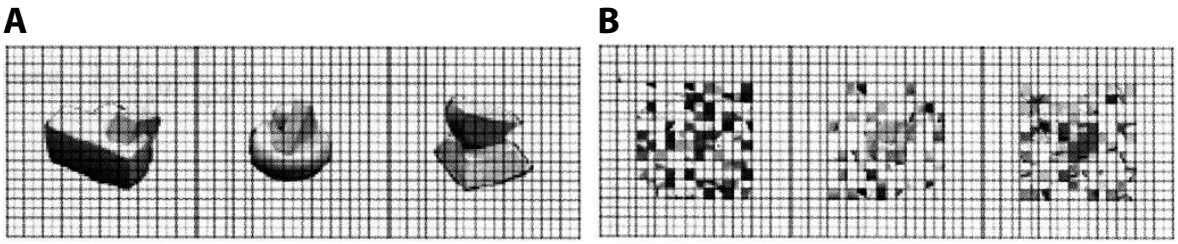

Figure 3.6: Intact versus scrambled localiser. Examples of intact (**A**) versus scrambled (**B**) localiser images.

versus scrambled images (**Figure 3.6**), with identical experimental details to that described in Kourtzi and Kanwisher (2000), apart from the scanner, which was a 3T Philips Achieva scanner (Philips Healthcare, Best, Netherlands). The stimuli were 300×300 pixel images of objects, including line drawings, modelled objects and photographs. Scrambled versions were created by dividing the images into grids of 20×20 pixels and randomly reordering them. A blocked presentation design was used with 16 stimulus epochs of 16 s duration, interleaved with fixation periods. Presentation time was 200 ms with 600 ms blank interval between each presentation. The order of conditions was balanced. During the scan, participants were required to take part in a one-back-matching task to identify two or more consecutive repetitions in each epoch. This task was simply to engage the observers' attentions during the scans. Scan duration time was 336 s (5 min 36 s).

We visualised the brain areas that responded with the greatest BOLD signal change between rest and the stimulus images using Brainvoyager QX (Brain Innovation, Maastricht, the Netherlands). We supplied the design matrix, which specified the time course for each stimulus condition (predictor) and the software automatically fitted the predictors with the haemodynamic response function. A model was created in the software for the time course of each predictor at each voxel location. The software plotted those voxels that showed the most significant differences in the stimulus conditions compared to the rest conditions (**Figure 3.7**). These images showed consistent activation in areas lateral to the early visual cortex and we

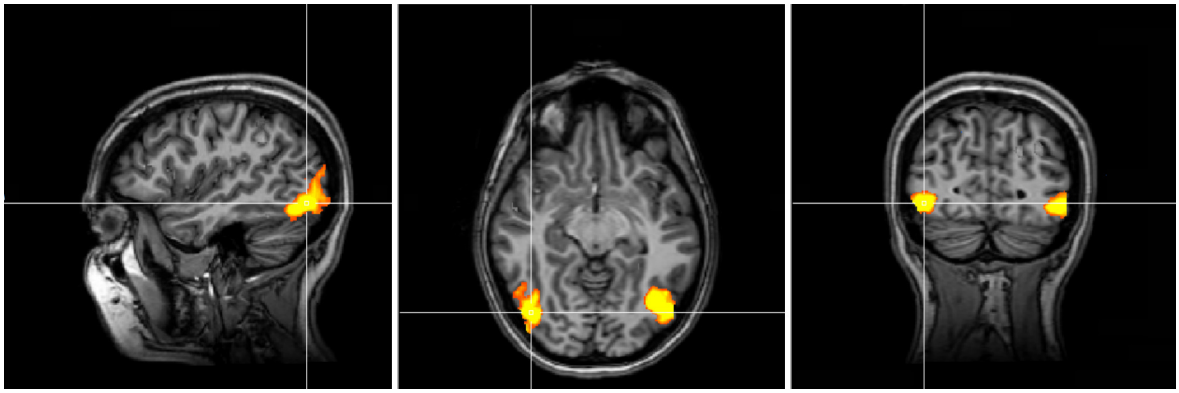

Figure 3.7: Lateral occipital localiser. Colour map of voxel responses during shape-based stimuli localiser, warm colours (yellow through to red) signified greatest differences between stimulus and rest images.

used them as reference images to plan subsequent MEGA-PRESS experiments.

3.4.4 FMRI Guided ROI Selection

Previous MEGA-PRESS experiments described in the literature were generally limited to a single region of interest (ROI), sometimes accompanied by a secondary ROI as a control region (see **Section 2.6.1: Table 2.3**). The rationale behind the choice of ROI was not always explicitly described, but the choices were usually intuitively understandable. For example the ROI in a haptic motor driven experiment might be centred on the motor cortex (e.g. Floyer-Lea et al., 2006) or in a visual task the ROI would likely be in the occipital lobe (e.g. Edden et al., 2009). Motor cortex and occipital lobe were common choices for ROI selection in published studies, this was the case in the choice of control area as well as the region under investigation.

We wondered whether there might be a more principled method of selecting ROIs. This led us to consider what fMRI BOLD activation might tell us about inhibitory activity. The relationship between the BOLD signal and inhibitory processing is largely unknown, but it is reasonable to suppose that a relationship exists. Inhibitory processing might contribute to the BOLD signal in the same way that excitatory activation has been shown to do. If so, we

could expect an *increase* in BOLD signal in areas where GABA is being released and recycled. Equally, it is also feasible that inhibitory processes might *lower* BOLD response, as the release of GABA might reduce excitatory activation and hence decrease the energy requirements of neurons local to the GABA release. In either case, we thought that fMRI guided ROI selection was worth investigating.

To do this we designed experiments that characterised the BOLD response from Glass patterns, to match the psychophysics paradigm that we wished to investigate further. However, we did not wish to compromise the psychophysics elements by exposing participants to identical stimuli in the BOLD response experiments. We therefore designed a stimulus space that used hyperbolic Glass patterns (**Figure 3.8**), in contrast with the concentric and radial patterns that we had planned for the psychophysics (**Section 2.3.2: Figure 2.4**). Details for the stimuli parameters are provided in **Section 5.2.2**.

Five participants (4 male, 1 female, mean age 22) participated in the hyperbolic Glass pattern BOLD response scans. All of the participants were agnostic to the study protocol and

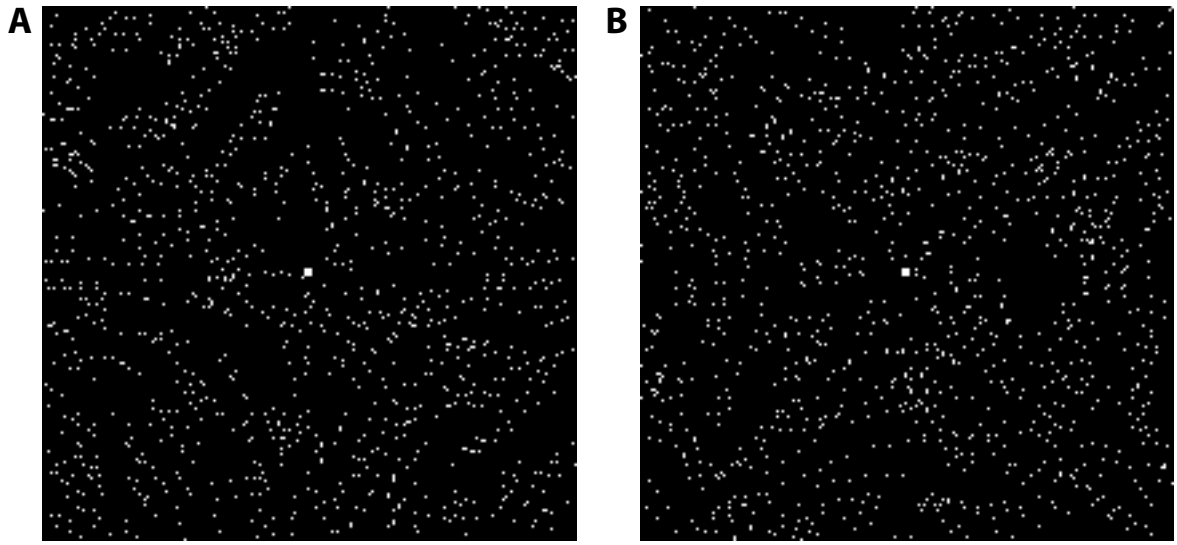

Figure 3.8: Hyperbolic Glass pattern stimuli. (**A**) Sample hyperbolic image that looks like a '**+**' character. (**B**) Sample hyperbolic image, rotated 45° that looks like an 'x' character. The larger, central white dot is the fixation point.

stimuli and had normal, or corrected-to-normal, vision. The University of Birmingham Ethics Committee approved the study. We conducted all scans on a 3T Philips Achieva scanner (Philips Healthcare, Best, Netherlands) and the participants gave written, informed consent to participate in the procedure.

We used a blocked presentation design with 18 blocks of 16 s duration, interleaved with fixation periods (**Figure 3.9**). Each block consisted of 20 trials with a presentation time of 200 ms and 600 ms blank interval between each presentation. The total run time was 318 s and each subject took part in 4×318 s runs during a single scanning session. The subjects were tasked to classify each stimulus image as belonging to one of two categories, although the task was largely included to ensure that participants attended to the stimuli.

We acquired echo planar imaging (EPI) data from BOLD signals using an 8 channel head coil. The main scan parameters were: Number of dynamics = 159, TR = 2 s, slice thickness = 3 mm, slice gap = 0 mm, and TE = 35 ms.

The results were consistent with previous work that identified areas responsive to Glass pattern stimuli (Ostwald, Lam, Li, & Kourtzi, 2008). This prior work defined three Glass pat-

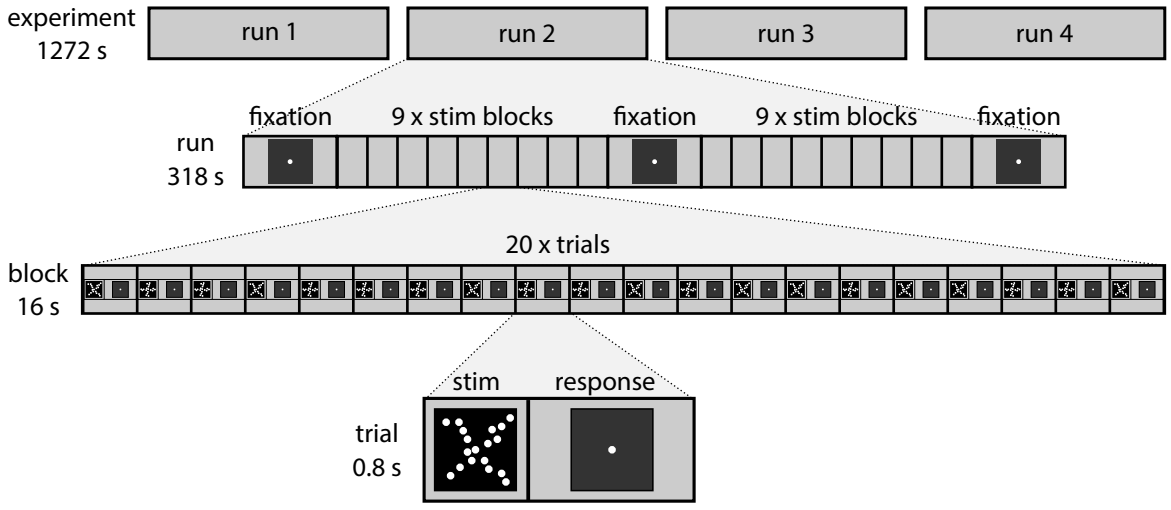

Figure 3.9: Glass pattern localiser design. Participants took part in four runs of 318 s each. A run consisted of two, 9×16 s stimuli blocks and 3×10 s fixation blocks. A block was made up of 20×0.8 s trials. Each trial consisted of a 0.2 s stimulus presentation and a 0.6 s response period.

tern response regions: One that was dorsal to occipital complex and inferior to V3a, another that was ventral and lateral to occipitotemporal cortex and a third that was ventral and medial in occipitotemporal cortex. That work used classifiers to characterise the fMRI data and concluded that lateral occipital areas were better for predicting learning performance than early visual areas.

Our own observations confirmed that there was less activation for higher cortical areas (**Figure 3.10C,D**) and greater activation for occipital areas (**Figure 3.10A,B**). Increased activation is usually associated with increased excitatory processes, but increased activation is also

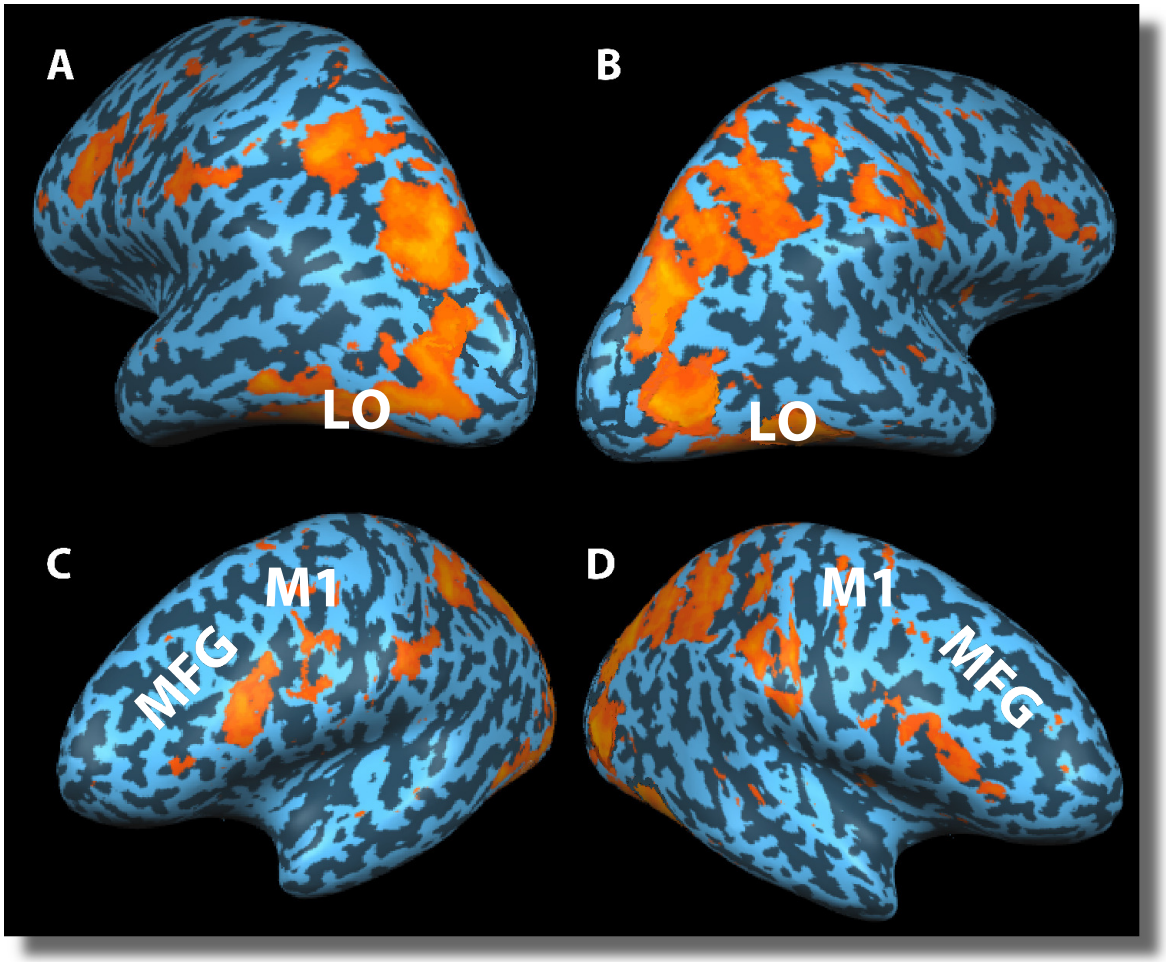

Figure 3.10: Glass pattern activation maps (inflated brain). Posterior left hemisphere (**A**), posterior right hemisphere (**B**), anterior left hemisphere (**C**), anterior right hemisphere (**D**). Approximate positions of brain areas labelled in white: Lateral occipital (**LO**), motor cortex (**M1**), mid frontal gyrus (**MFG**). Cool colours (blue) represent the morphology of the brain (sulci and gyri), warm colours (yellow/orange) represent BOLD signals that responded more to the hyperbolic stimulus images than the rest condition.

needed to overcome inhibitory processes and therefore might indicate high baseline GABA concentration (Donahue et al., 2010). Based on the activation that we saw we therefore decided to investigate lateral occipital areas and frontal areas centred on the mid frontal gyrus. We were also motivated to implement a multi-ROI experimental design as it has been previously observed that individual differences in GABA concentrations are not necessarily global across the brain (Puts & Edden, 2012). We hypothesised that selecting multiple ROIs on the basis of increased and decreased fMRI activation might be a way to test this observation. We also required a control area and decided that primary motor cortex would be an appropriate area to act as a control as we reasoned that this area was unlikely to be involved with visual learning experiments.

3.5 Discussion

The aim of this chapter was to create the foundation for *in vivo* MEGA-PRESS experiments by introducing the options in setting scanning parameters and we demonstrated a method to target brain regions likely to be involved in visual learning experiments. We suggested that adopting the scan parameter values that were most commonly used in the literature would lead to results that would be most generally comparable, apart from scan duration time, which we suggested should be at the upper end of extant experiments in order to maximise SNR. Acquiring GABA measurements *in vivo* is considered challenging, however our *in vitro* experiments showed that the GABA triplet around 3 ppm was well resolved at high metabolite concentration, with minimal post-processing of data. The brain metabolite phantom also showed a convincing GABA signal at high concentration and evidence of one at a lower concentration too. These *in vitro* experiments are meant to illustrate a suggested route for researchers preparing for their first *in vivo* MEGA-PRESS acquisitions.

We wanted to choose the brain regions for our in vivo experiments in a principled way. We therefore conducted fMRI experiments that used visual stimuli that were similar to those we planned to use in correlative studies of GABA concentration and visual learning. The brain activation that was observed through these fMRI experiments was then used as a guide to MRS acquisition voxel placement. We used fMRI to localise activity and hence identify particular brain regions, but also used the BOLD pattern of activity to target regions of interest for subsequent MRS experiments. As there is no agreed model on the contribution that inhibitory processes make to the overall BOLD signal, we used our results to select both highly activated and less activated areas. The use of BOLD signal to guide MRS placement is not something that is discussed much in the MEGA-PRESS literature, and the use of multiple regions is similarly rare. These ideas will be explored in subsequent experiments in later chapters and represent novel approaches to MEGA-PRESS research.

4

POST-ACQUISITION PROCESSING

4.1 Introduction

The raw signals from a MEGA-PRESS experiment consist of two sets of interleaved acquisitions referred to as edit ON and edit OFF. These signals need to be processed to account for potential artefacts and problems with data quality before being combined for subsequent metabolite quantitation. The aim of this section is to investigate the source of noise and errors in MEGA-PRESS experiments and to describe our research into implementing techniques that account for these problems and lead to improved metabolite quantitation.

There are several challenges with obtaining *in vivo* MRS measures of GABA. These challenges are partly to do with the anatomy of *in vivo* specimens and may be seen as a contrast with the *in vitro* conditions that we described in **Section 3.3: Phantom Experiments**. The human head has scalp, bone, ventricles and air cavities, which all contribute to creating field inhomogeneities in the scanner during an MR experiment. These inhomogeneities result in artefacts and noise in the signals. The brain is composed of different tissue types, such as white matter, grey matter and cerebrospinal fluid and these have different water relaxation properties that can affect the signals in MR spectroscopy. GABA is present in low concentrations in the brain and its resonance frequencies are overlapped by more abundant metabolites. The

low concentration levels make it difficult to resolve from background noise (i.e. it has low signal to noise ratio) and MR experiments are typically run over many averages to improve the signal to noise of the spectra. The development of the edited pulse sequences in MEGA-PRESS was a direct response to the problem of disambiguating GABA from the larger, overlapping creatine peaks in standard PRESS MRS sequences. The existence of interleaved sequences leads to the problem of how to combine the signals in a MEGA-PRESS experiment. Theoretically this is straightforward and is described as a subtraction of the edit OFF from the edit ON sequence (**Section 2.5.4**). However the signals derived from *in vivo* experiments exhibit errors and noise related to phenomena such as out of phase acquisitions and poorly aligned subspectra. These errors can be visualised by plotting the frequency domain spectra of the edit ON and edit OFF data, with minimal post-acquisition processing as in **Figure 4.1**.

Here a general problem with the phase of the spectra can be seen by comparing the slope of the spectra in **Figure 4.1C** (ascending baseline) with **4.1E** (descending). Ideally the baseline should be flat, with peaks appearing only above the baseline, rather than a combination of peaks and troughs that can be seen in this figure. Presumably advances in scanning technology will lead to more consistently phase aligned signals in the future, but the state of the art at the present means that researchers have no practical control over the phase of signals in MEGA-PRESS experiments. However there are options to correct this post-acquisition. We discuss these options in this chapter.

The poorly aligned subspectra can also be seen in this figure, for example in **Figure 4.1B** the arrowed peaks have become misaligned. One effect of averaging such spectra, without accounting for shifted spectra could be a widening of the peak profile that can cause an overestimation of the metabolite volume. Another problem could be the appearance of pseudo-peaks, where misaligned spectra become interpreted as separate components of a peak. This

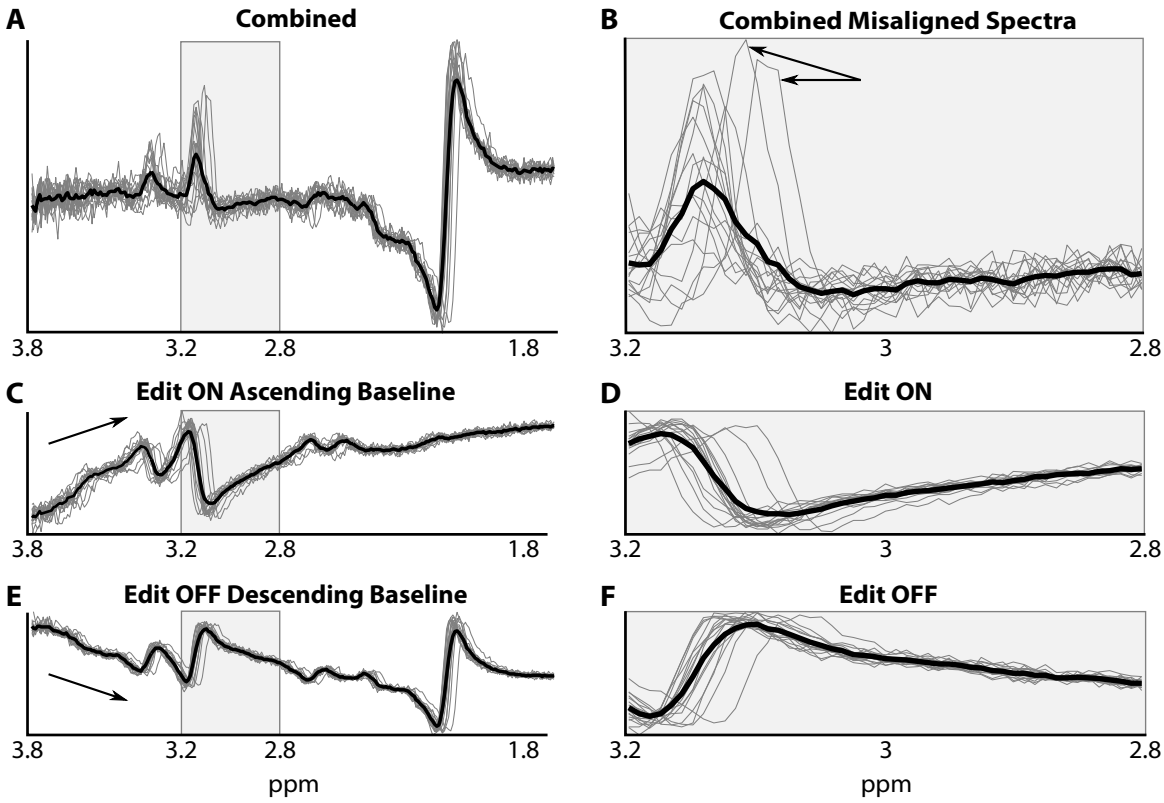

Figure 4.1: Sample misaligned subspectra. Light spectral lines represent individual acquisitions, thicker lines represent the averaged spectra. The left hand plots (**A, C, E**) show the spectra along the range 1.8–3.8 ppm. The right hand plots (**B, D, F**) show corresponding areas across the range indicated by the grey boxes (2.8–3.2 ppm). Arrows indicate misaligned spectra (**B**) and phase error effect of the baseline slope; (**C**) ascending baseline and (**D**) descending baseline.

has particular significance for the GABA resonance at 3.01 ppm (and is discussed further in **Section 4.6: Peak Modelling**). In situations where alignment is particularly poor it may become a challenge to distinguish misaligned peaks from genuinely different peaks, for example choline and creatine peaks near 3 ppm. We discuss how to overcome this challenge by using a method that employs offsets from prominent metabolite peaks that are unlikely to be misidentified, for example the large NAA peak at 2.1 ppm (see **Section 4.5: Subspectral Shifting**).

We begin this chapter with a description of some MRS tools that are useful for metabolite quantitation. These are general purpose MRS tools that can be used for measuring GABA, but they can be made more accurate by performing the post-acquisition processing steps described in this chapter. We introduce these steps, starting with the time domain characteri-

sation of the FIDs from a MEGA-PRESS experiment, as this illuminates the phase alignment problems particular to those pulse sequences.

We discuss remedies to phase alignment and advocate an automatic phase correction step to enhance the reproducibility of measurements. We also describe the nature of sub-spectral misalignment and explain a method of realignment that uses an independent alignment scheme for edited and non-edited spectra.

Segmentation is an important topic as variable proportions of white matter, grey matter and CSF can skew metabolite measurements in MRS experiments. We describe how to translate the problem from the spectral domain of MRS into the imaging domain, where brain segmentation has been successfully solved and we detail how to retrieve tissue proportions using MRI image analysis software.

The chapter ends with a discussion on aspects of scaling options for MEGA-PRESS acquisitions. One of our main research hypotheses was that cortical grey matter GABA concentrations are involved with learning in visual paradigms. White matter GABA concentrations might also be involved, but we hypothesised that the white matter would mainly consist of axons whose role is more to do with routing signals, rather than as the site of GABA expression. We therefore concentrate our efforts on grey matter tissue segmentation and propose a scheme to apply this to scale GABA measurements.

The aim for this chapter is to discuss the data processing challenges that are inherent with MEGA-PRESS acquisitions and to suggest solutions to these based on a pipeline of software that we developed during our experiments. This pipeline covers aspects of spectral manipulations that need to be applied before metabolite quantitation is attempted and also covers rescaling operations on the quantitated results.

4.2 Signal Quantification

Signal quantification is the process of obtaining measures of the abundance of specific metabolites from spectra. At its simplest, this usually involves fitting a model of the metabolite peaks to the data and then integrating the area under those peaks, accounting for the number of protons that contribute to the metabolite of interest. There are several tools available for this process including LCModel (Provencher, 2001), Tarquin (Reynolds, Wilson, Peet, & Arvanitis, 2006; M. Wilson, Reynolds, Kauppinen, Arvanitis, & Peet, 2011), jMRUI (Stefan et al., 2009) and Gannet (Edden et al., 2014). The test-retest reproducibility of each of these approaches has been reported as being very similar (O'Gorman et al., 2011), and it is therefore preferable to use these validated tools instead of bespoke peak integration methods (Bogner et al., 2010). There are complexities relating to relaxation constants of reference signals (water or creatine for example) that need to be taken account of as a minimum (Alger, 2010). Also, any changes in the metabolite model will alter concentration estimates, so we suggest that the standard basis sets are used unless there is a compelling reason to change them. We suggest that using the specialised spectroscopy analysis tools in their default configurations is likely to be lead to more accurate and comparable measurements across groups. A further advantage of using these tools is that they provide spectral quality metrics that can assist in determining the reliability of the metabolite measurements (Mullins et al., 2014).

This is important because any manipulation, such as subspectral realignment or changes to the peak model, might negatively impact on the quality of the data. Therefore we suggest that care is taken to monitor the quality of data at each stage of post-processing. In our research we were closely involved with the developers of the Tarquin spectroscopy software, who implemented a MEGA-PRESS analysis routine after we requested the option. Tarquin software can automatically calculate various quality metrics including SNR max, SNR residual, Q value

and Cramér-Rao lower bounds (CRLB). We found that scrutinising the quality metrics and visually inspecting the model fit against the raw spectra at each stage of spectral manipulation helped in determining the optimal parameters for post-processing MEGA-PRESS signals. For these reasons we used Tarquin for all signal quantification in our experiments.

4.3 Time Domain Signals

The data acquired from a MEGA-PRESS experiment consists of edited and non-edited time varying free induction decay (FID) signals. These signals are usually Fourier transformed so that they can be visualised in the frequency, as apposed to the time, domain. The same information is held in both the time domain and the frequency domain, but the interpretation of the frequency domain spectra is usually considered more intuitive. For this reason, it is rare to see time domain plots of the FIDs in MEGA-PRESS research. The FIDs can be visualised however, by plotting the real and the imaginary part of the complex numbers that make up the FID. If the edit ON and edit OFF FIDs are plotted individually (i.e. not combined and then plotted), then it becomes apparent that they are distinct from one another and this is due to the different phase of the edited versus the non-edited FIDs. For example if the real

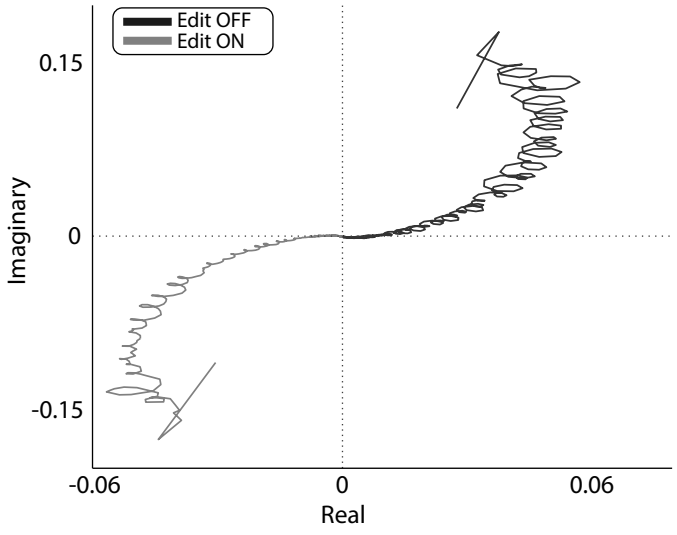

Figure 4.2: Time domain, edit OFF versus edit ON. Edit OFF FID (top right quadrant) and edit ON (bottom left quadrant). Plot lines represent averaged FID values (n=16). The edit OFF FID starts at a point on the positive side of the x and y axes and subsequent points show the oscillating, descending decay towards zero. The edit ON begins from a point on the negative side of the axes and also oscillates and decays towards zero. This plot is meant to show that there is a phase difference between edited and unedited spectra that is apparent from the time domain signals.

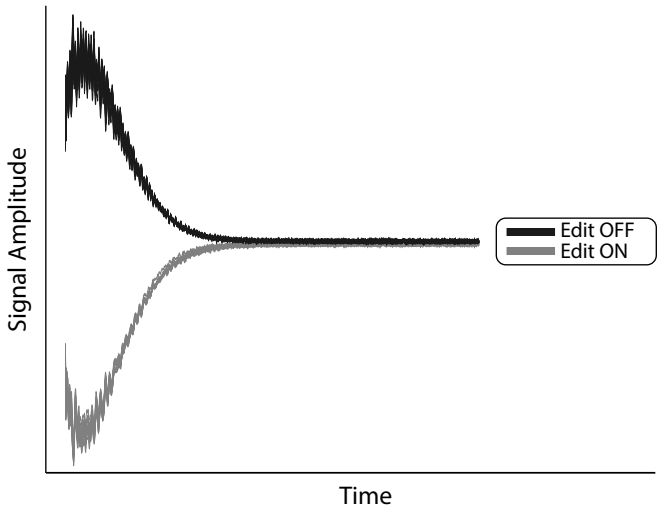

Figure 4.3: Time domain plots, exponential decay. The inverted nature of the edit ON FIDs, compared to the edit OFF ones, is caused by the signals being out of phase with respect to one another.

components are plotted against the imaginary components (**Figure 4.2**) then the edit ON FIDs appear inverted compared with the edit OFF ones.

The FIDs can also be visualised separately as a function of time and this reveals the exponential decay characteristic of the FIDs and the inverted nature of the edited FIDs compared with the unedited ones (**Figure 4.3**). The opposition of phase that can be seen in the time domain signals has an important consequence for combining the edited and non-edited data and is discussed further in the next section (**4.4: Phase Correction**).

4.4 Phase Correction

The FIDs can be transformed into frequency domain signals through the use of the fast Fourier transform (FFT). Metabolite signals can then be identified by their peaks on the chemical shift scale, but peak positions are dependent on signals that have been phase corrected. The FIDs acquired directly from the scanner are not typically phase corrected, as was shown in **Figure 4.3**, where the edited signals were out of phase alignment. Phase correction of spectra is often achieved through the use of software such as jMRUI (Stefan et al., 2009) and involves the manual adjustment of the phase-zero and phase-one components. This requires some expertise and is usually done by an experienced MR physicist. For this project we sought

an automatic solution to phase correction to increase the reproducibility of our experiments. The algorithm that we used was developed by Chen, Weng, Goh, and Garland (2002) and was based on entropy minimisation. Here we demonstrate the data transformation steps necessary to integrate the algorithm into a Matlab workflow.

This phase correction algorithm required the frequency domain spectra, sample frequency and the synthesiser frequency as input parameters. On the Philips system that we used, these data were retrieved from the parameter and data files (the `.SPAR` and `.SDAT` files respectively). We applied the FFT with the Matlab function `fft`. The phase alignment algorithm did not take account of the wrap around effect of the high values (peaks) at the low and high ends of the spectrum. This discontinuity meant that the frequency domain signals required that the zero-frequency component be moved to the centre of the data structure and we used another Matlab function, `fftshift`, to achieve this (**Listing C.2**). These frequency domain, frequency-shifted data, were passed to the phase correction algorithm and the phase-

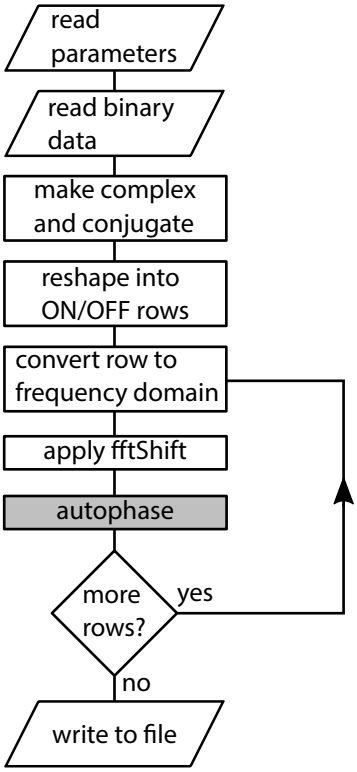

Figure 4.4: Phase correction flowchart. Input data to the system were supplied from text parameter files (.SPAR) and binary FID files (.SDAT). Each data row was processed iteratively through the phase correction algorithm so that the final data structure represented frequency domain, phase corrected spectra. The process box marked 'autophase' (shaded) represents the algorithm developed by Chen et al. (2002).

corrected data were written out to file. The process is shown diagrammatically in **Figure 4.4**.

In order to plot the phase corrected spectra we took the non-conjugate transpose of the output from the phase correction algorithm and plotted the real component of the complex signal. Typical raw spectra would often have an uneven baseline (**Figures 4.5A,B**) and the edit OFF spectra were out of phase by 180° compared with the edit ON spectra. This meant that the peaks were inverted (**Figure 4.5B**) and this could lead to processing errors if not taken account of. For example, a typical brain MR spectrum should have a large NAA peak at 2 ppm, this is clearly identifiable on phase corrected edit OFF spectra (**Figure 4.5D**), but was less clear on uncorrected spectra (**Figure 4.5B**). Also, the theory for combining MEGA-PRESS acquisitions is to subtract the edit OFF spectrum from the edit ON (see **Section 2.5.2: Pulse Sequences**), if this operation was applied to spectra where the edited and non-edited spectra were out of phase by 180°, then the averaged spectrum would not have a peak around

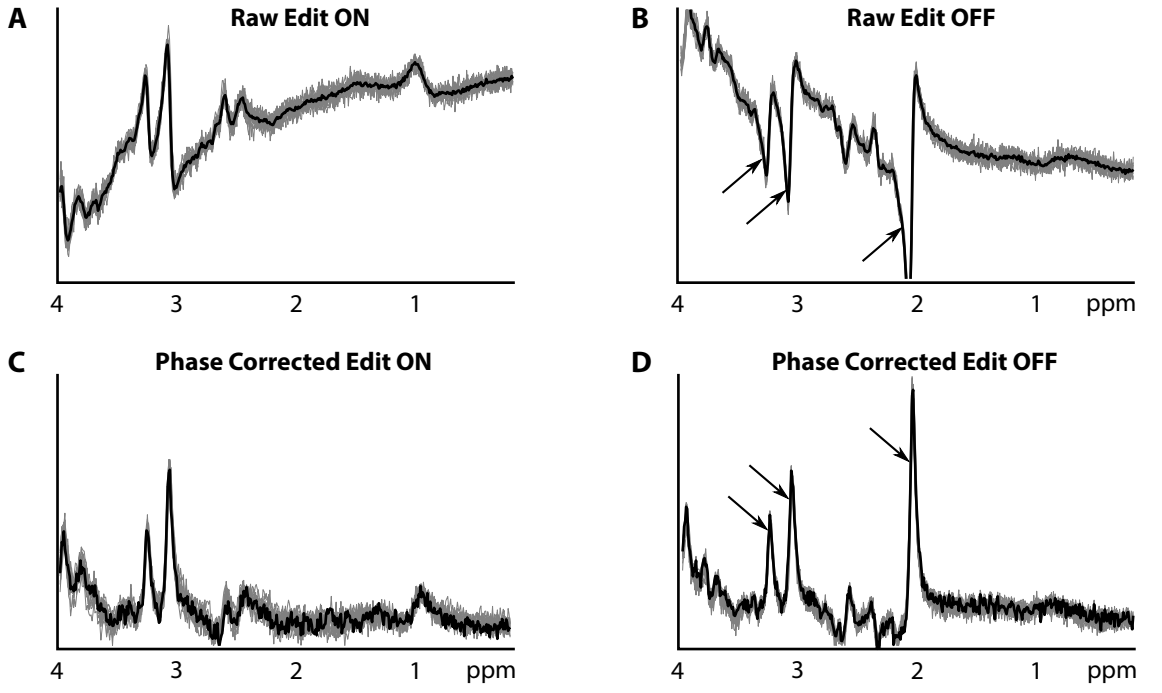

Figure 4.5: Sample raw and phase corrected spectra. Edit ON spectra on left hand side (**A, C**), edit OFF on right hand side (**B, D**). Raw spectra above (**A, B**) and phase corrected spectra below (**C, D**). Lighter chart lines represent subspectral components (n = 16) and the darker lines represent the averaged spectra. Arrows on the raw edit OFF (**B**) show inverted peaks that are realigned on the phase corrected edit OFF (**D**).

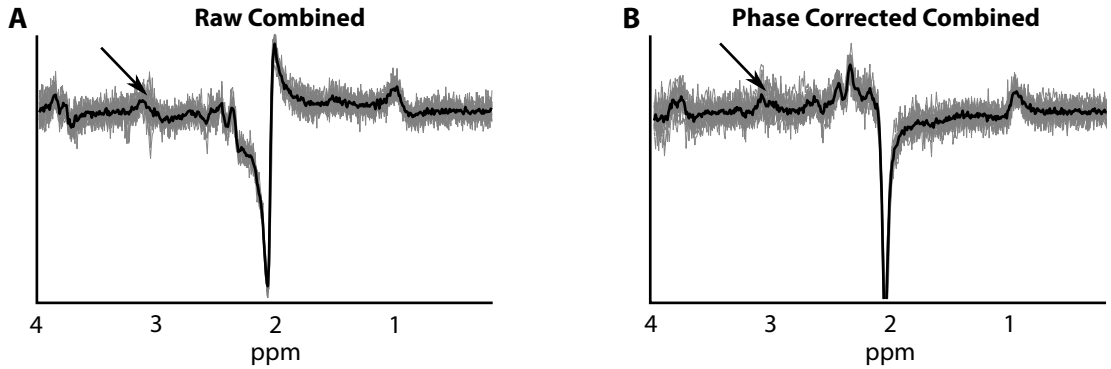

Figure 4.6: Combined edit ON and edit OFF spectra; raw signal and phase corrected. The raw spectra have been combined by adding the edit ON and edit OFF spectra (**A**). The phase corrected spectra have been combined by subtracting the edit OFF from the edit ON spectra (**B**). Arrows indicate approximate expected position for GABA peaks.

3.02 ppm, which is where we expect to measure GABA. Therefore the combination operator would need to become edit ON *plus* edit OFF (**Figure 4.6A**) for non-phase corrected signals. Phase corrected spectra do not exhibit this problem and can be combined using the subtraction operator as dictated by theory (**Figure 4.6B**).

We compared the spectra from the automatic approach outlined above with manual manipulations using jMRUI and concluded that the automatic phase correction was a suitable solution that had the advantages of reproducibility and could fit into an automated processing pipeline. We used the automatic approach to phase correction of the frequency domain signals in all operations that required phase correction, for example subspectral shifting.

4.5 Subspectral Shifting

The number of edit ON and edit OFF FIDs that are acquired in a MEGA-PRESS experiment is dependent on the acquisition parameters chosen by the researcher and is set for each experiment. Specifically, the number of dynamic scans will govern how many FIDs are retrieved. The dynamic scans parameter is set along with the phase cycling parameter to mediate between the localisation performed by the scanner and the number of raw FIDs that is thought

appropriate for optimal post-processing manipulation. With the parameters chosen in **Section 3.2: Acquisition Parameters** the scanner will run the pulse sequences 512 times, with 256 edit ON end 256 edit OFF sequences. As there are two distinct pulse sequences, the number of dynamic scans can be set in powers of two (2, 4, 8, 16, 32, 64, 128, 256, 512) and the number of phase cycles will then determine how many FIDs are combined for each dynamic scan acquisition (the product of the number of dynamic scans and the number of phase cycles will need to total the number of pulse sequences that are run by the scanner). Maximising the number of dynamic scans results in the greatest flexibility in post-processing terms, but the increased number of FIDs also increases the complexity of the task. Decreasing the number of dynamic scans means that more processing of the FIDs is handled by the scanner, which results in less complexity in post-processing. The optimum number of dynamic scans therefore depends on how well phase cycling combines the FIDs in the scanner compared with how well the task is completed with post-processing tools. The performance of phase cycling in the scanner is an unknown quantity as the pulse sequence is an experimental one. At the onset of this project we had yet to develop post-processing tools, so obviously the performance of these tools was also unknown.

In the absence of performance metrics for phase cycling versus post-processing algorithms, we selected the median value from the range of possible values for dynamic scans in experiments of 512 pulse sequence runs. This was 32 dynamic scans per ROI. This means that each exported FID is created from 16 phase cycles ($32 \times 16 = 512$). We reasoned that this would provide sufficient scans to improve through post-processing if needed, whilst keeping the size of data files from becoming unwieldy. We transformed the FIDs to frequency domain spectra and we plotted and overlaid them individually to see if there was good alignment of the spectra or not (an example of this type of plot was given in the **Section 4.1: Introduction,**

Figure 4.1). We found it useful to plot all of our spectra this way and ran the plots as animated sequences, with one second intervals between the appearance of each subspectral component. The point to viewing the plots in an animated fashion was to see, across time, whether or not the spectra moved systematically in one direction or if misaligned spectra occurred more randomly. That is, whether the spectra shifted along the positive and negative axes of the ppm scale in one direction only throughout the acquisition (systematic scanner drift as a function of time), or if they shifted in both directions with random frequency.

Analysis of the time course of our acquisitions, led us to conclude that subspectral movement was more random than systematic and the size of the shift also varied within individual experiments. We assumed that subject movement was the main culprit that produced misaligned spectra (Jansen, Backes, Nicolay, & Kooi, 2006). Another feature of the shift that we identified through this process was that where misalignment occurred, it happened across the whole spectrum. For example It was not the case that a peak around 2 ppm would be shifted in one direction and another peak at 3 ppm was shifted in the opposite direction. This was helpful because it meant that to move the spectra back into alignment, we need to identify a single peak that was out of alignment and move the entire spectrum by the offset of the

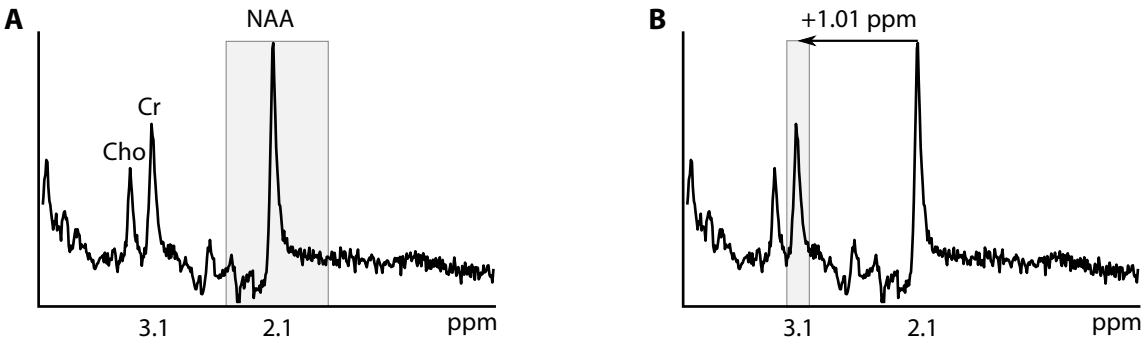

Figure 4.7: Disambiguating creatine from choline. A two step process was employed to disambiguate the creatine (Cr) peak from the choline (Cho) peak in misaligned spectra. **(A)** The NAA peak was identified with a window (shaded box) centred around 2.1 ppm. **(B)** The creatine was identified in a narrow window (shaded box) around an offset of +1.01 ppm from the identified NAA peak.

individual peak.

In order to programmatically identify a particular metabolite peak, we thought it sensible to focus on the peaks around 3 ppm, which is the approximate position of creatine and GABA (see **Figure 4.7**). These peaks are in close proximity to the choline peak and could potentially be misidentified in the case of poorly aligned spectra. We therefore first identified the NAA peak around 2.1 ppm in the OFF spectra with a peak identification algorithm. This is a large peak without any similar peaks nearby and is therefore easily identified even in the case of poorly aligned spectra. From the identified NAA peak, a narrow window can be searched that was centred on the distance between NAA and creatine peaks (approximately 1.01 ppm).

Using this method (**Listing C.4**) the creatine and GABA peaks are more readily identified without misidentifying any out of alignment choline peaks (**Figure 4.7**). We did the final peak identification by using a weighted average (**Listing C.5**) of the maximum of the data points around the window identified from the offset from the NAA peak. An alternative to

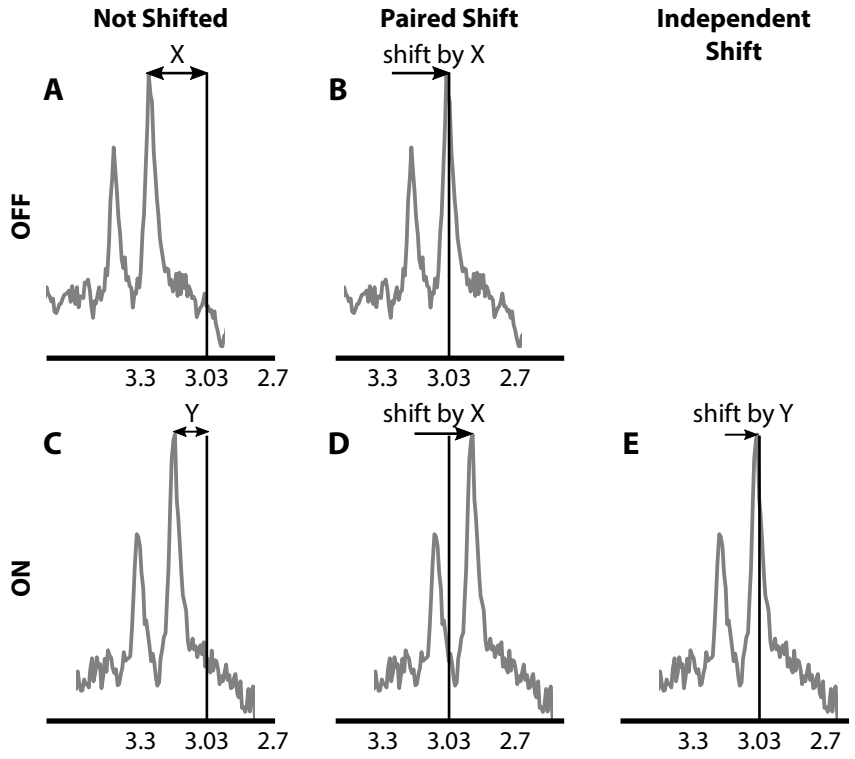

Figure 4.8: Paired and independent alignment. The edit OFF **(A)** is shifted according to the offset of the creatine peak from 3.03 ppm **(B)**, labelled 'X' on the figure. The edit ON **(C)** is shifted according to the same 'X' offset in the paired alignment scheme **(D)**, but by the ON offset, labelled 'Y' in the independent scheme **(E)**.

the weighted average is to use median point of the maximum peak values, we found that this method had more peak misidentification errors with our data.

A further choice when realigning spectra was whether realignment should be applied independently or based on pairs of ON and OFF spectra (**Figure 4.8**). The paired alignment approach involves applying the same realignment to the the subspectra in the edit ON pairing that is applied to the edit OFF pairing. In the independent scheme the edit OFF and edit ON subspectra are realigned irrespective of the shifts applied to the other.

A paired approach has been shown to produce less subtraction artefacts than independent alignment for data acquired on a GE HDx 3T scanner (Evans et al., 2012). Our analysis differed in that we found that independent realignment produced the better results.

For example the correlation coefficient for the paired alignment spectra in **Figure 4.9B** was $r = 0.82\,(\mathrm{p} < 0.01)$ compared with $r = 0.96\,(\mathrm{p} < 0.01)$ for the independent alignment spectra in **Figure 4.9E**. We have visualised the correlation matrices for these data in **Fig-**

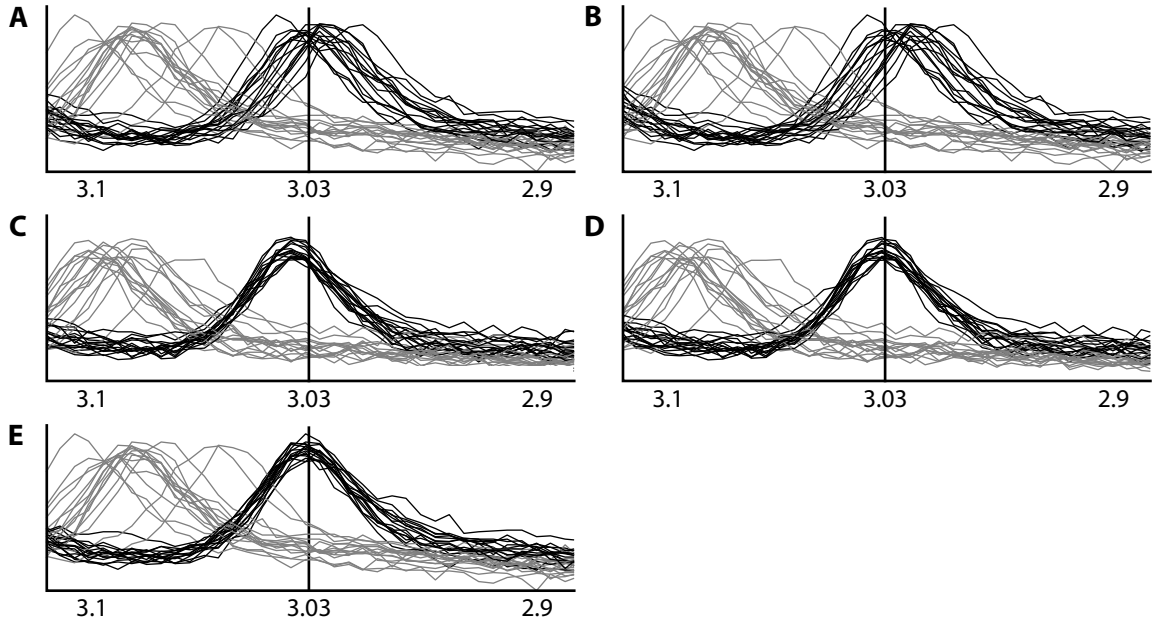

Figure 4.9: Shifting based on NAA and Cr reference peaks for edit ON and edit OFF, independent (IA) and paired (PA) alignment. Grey lines are the phase-corrected raw spectra, the black lines are the shift-corrected spectra: (**A**) edit ON, NAA, PA; (**B**) edit ON, Cr, PA; (**C**) edit OFF; NAA, IA; (**D**) edit OFF, Cr, IA; (**E**) edit ON, Cr, IA. The units for the x-scale are ppm.

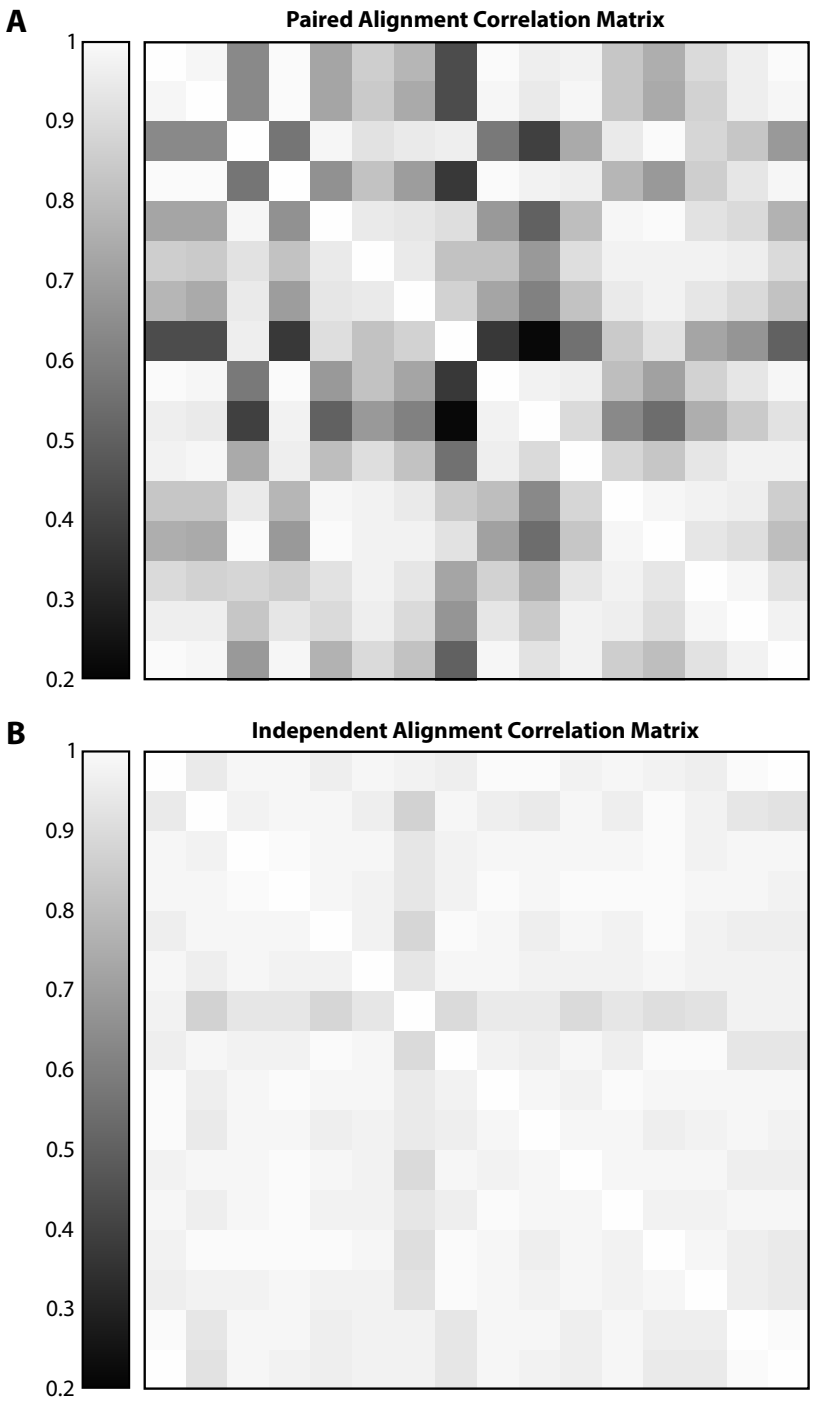

Figure 4.10: Paired and independent alignment correlation heatmaps.
We computed two correlation matrices to calculate the Pearson's *r* values for the two alignment strategies (paired and independent). The data for the correlations consisted of the data points from the 16 spectral lines.
We then visualised each matrix with a grey scale heat map.
Plot **(A)** represents the *r* values from the matrix correlating the spectra after the paired alignment strategy.
Plot **(B)** represents the independent alignment strategy.
The independent alignment strategy **(B)** spectra were more highly correlated, as represented by the lighter shaded matrix compared with the paired alignment **(A)**.

ure 4.10. The corresponding scatter plots can be found in **Appendix E : Post-Acquisition Supplementary** (**Figures E.2** and **E.3**).

We compared the effect of paired and independent alignment on 221 MEGA-PRESS acquisitions. We acquired the data set from ROIs situated in frontal, lateral occipital, early visual and motor cortex areas. Each FID was transformed into the frequency domain, where it was

phase-corrected and then the individual components of the subspectra were aligned using paired and independent realignment schemes.

We calculated metrics specifically for the GABA signal at 3.01 ppm and also for the wider spectrum (**Table 4.1**). For the GABA specific metrics, the GABA peaks were constrained to values between 2.8–3.2 ppm and the noise spectrum was constrained to 0–2 ppm. The SNR for the GABA peaks was calculated by dividing the maximum value of the GABA signal by the root mean square of the noise (**Listing C.6**).

Table 4.1: Independent versus paired alignment. Spectral quality metrics for shift-corrected data according to independent alignment and paired alignment schemes. **SNR** = signal to noise ratio across the whole spectrum, **Q** = spectral quality metric across the whole spectrum, lower values (down to unity) represent higher quality, **CRLB** = Cramér-Rao lower bounds across range 2.8–3.2 ppm, expressed as %SD, lower values indicate higher quality, **SNR GABA** = signal to noise ratio across range 2.8–3.2 ppm.

Alignment Scheme	SNR	Q	CRLB GABA	SNR GABA
Independent	38.37 ± 8.28	2.38 ± 0.65	5.49 ± 6.21	12.56 ± 3.37
Paired	37.49 ± 10.00	2.50 ± 0.81	7.61 ± 11.70	12.26 ± 3.37

From these metrics independent alignment produced better quality values than paired alignment (higher SNR, lower Q and lower CRLB). We speculated that this might be due to hardware differences (GE versus Philips) as we noted a small systematic tendency for the edit OFF acquisitions to be shifted to the negative x-axis compared with the edit ON acquisitions. This would render paired alignment unsuitable in the majority of our acquisitions acquired on Philips hardware.

We compared the effect that the independent realignment scheme had on quality metrics versus no realignment. This confirmed that the shifted spectra had on average better SNR (2.5% higher), Q (3% lower) and CRLB values (3% lower) than the uncorrected data. In addition to improving the quality on average, we noted that individual cases could be dramatically improved, and could lead to the rescue of some data that would otherwise have been

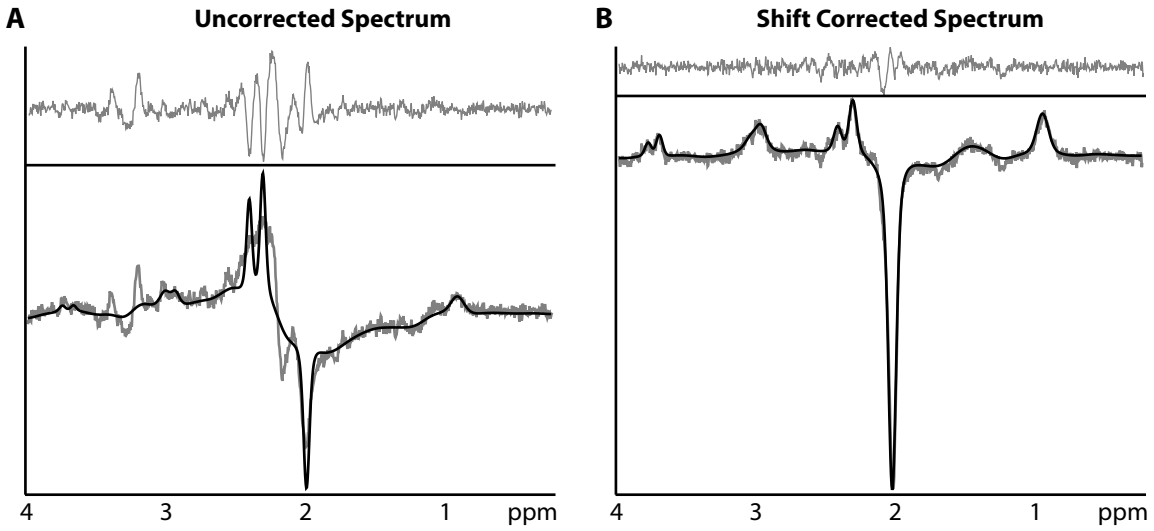

Figure 4.11: Sample raw and shift corrected spectra. (**A**) Tarquin (Reynolds et al., 2006; M. Wilson et al., 2011) processed spectrum without shift correction (see **Section 4.2**). Note the large residuals (top) and poor fit of model (black line) against the raw averaged subspectra (grey line). (**B**) After subspectral shifting, the spectrum's shape is more typical for a MEGA-PRESS experiment. The SNR values of this sample increased from 4.14 to 32.1 after shift correction.

discounted from analysis as being too poor for quantitation (**Figure 4.11**). We also considered that the improved quality metrics were likely to lead to a reduction in the occurrence of subtraction artefacts (**Section 4.6**).

4.6 Peak Modelling

The theoretical shape of the GABA peak around 3 ppm that should result from a MEGA-PRESS experiment is that of a doublet (**Section 2.5.2**: **Figure 2.13**). However, limitations such as the inhomogeneity of the magnetic field with 3T scanners, have caused some researchers to doubt whether doublets do in fact reliably occur in the data. Pseudo-doublets can also occur where misaligned subspectra are averaged to give the appearance of a doublet peak (**Figure 4.12**), or during the subtraction of the edit OFF spectra from the edit ON spectra where subtraction artefacts can produce a pseudo doublet.

At a symposium for GABA researchers organised by Cardiff University (Mullins et al.,

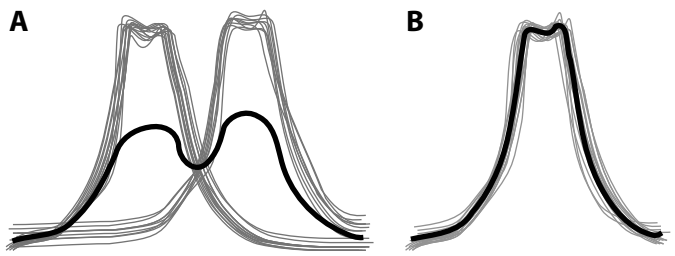

Figure 4.12: Pseudo doublet. (**A**) Schematic showing two groups of misaligned subspectra (grey lines) being modelled as a single pseudo doublet (thicker black line) after averaging. (**B**) Well aligned subspectra (grey lines) being modelled correctly as a doublet (thick black line).

2014), there was some discussion where Philips users reported the appearance of doublets more frequently than Siemens and GE users. Analysis of the raw spectra in our own acquisitions, acquired using Philips hardware, seemed to suggest that doublets were reliably detected and so we investigated singlet and doublet models of the GABA peaks. The data points that make up a peak in a spectrum are usually fitted with a curve fitting model, for example a Gaussian function (Weisstein, 2017) such as that in **Equation 4.1**.

$$P(x) = \frac{1}{\sigma\sqrt{2\pi}} e^{-(x-\mu)^2/2\sigma^2} \tag{4.1}$$

After applying the subspectral shifting techniques (**Section 4.5**), we analysed the model fit against the raw spectra using a double Gaussian model of the GABA peaks and a single peak model (**Figure 4.13**).

In order to compare the two models we integrated the area under the GABA peaks for both single and double peak models for 140 MEGA-PRESS scans and plotted the measurements

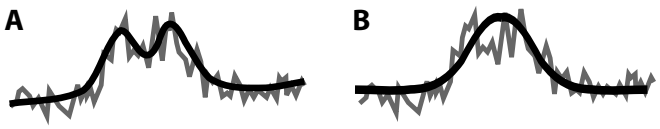

Figure 4.13: Double and single peak modelling. (**A**) Double Gaussian model fit (black) to the raw GABA peaks (grey). (**B**) Single Gaussian model.

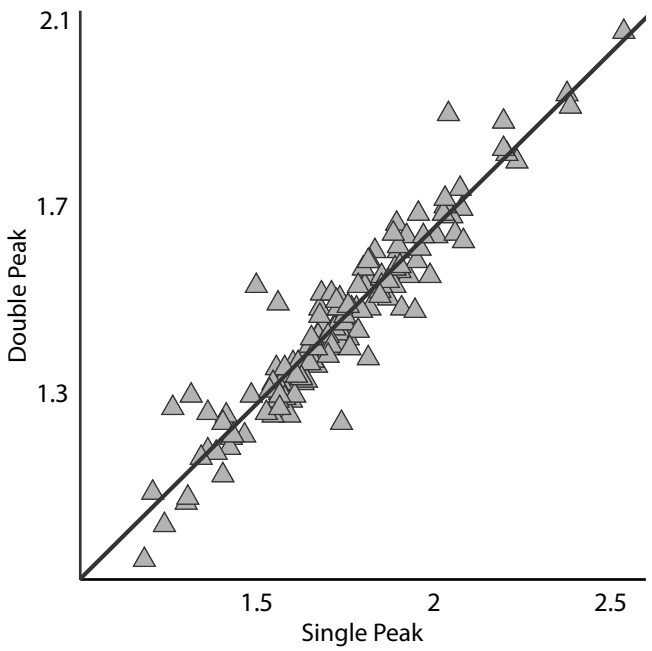

Figure 4.14: Measurements of GABA using two peak model versus one peak model. Triangles show the intersection between GABA measurements calculated with a two peak (Gaussian) model and a one peak model. The least squares fit line was calculated with the equation $0.75\,x + 0.13$ and the Pearson value was $R^2 = 0.89$ $(n = 140)$.

against each other (**Figure 4.14**). The single peak model gave higher absolute values for the measurements, but the closeness of fit of the least squares line suggested that a linear scaling existed between the measurements obtained from the two models that would probably make little difference in practical terms to correlative studies. This is in agreement with similar analysis completed by other researchers (Edden et al., 2014).

4.7 Segmentation

Segmentation in the context of brain imaging is the process of separating different tissues in a given brain area. It can be important to know the tissue proportions within an MRS voxel as the tissue environment can affect quantitative aspects of metabolite concentrations, for example water relaxation constants are different in white matter compared to grey matter. In MEGA-PRESS experiments voxel volumes are commonly 3 cm^3 and therefore contain grey matter (GM), white matter (WM) and cerebrospinal fluid (CSF). GABA is measured from the entire volume, but as CSF does not contain GABA in any appreciable amounts, then the potential exists that different proportions of CSF in the acquisition voxels might skew the

measurements. We therefore investigated the amounts of each tissue in our acquisitions to account for possible tissue driven effects. There have been reports of different densities of GABA in white matter compared to grey matter (Jensen et al., 2005; Petroff, Spencer, Alger, & Prichard, 1989) and a further argument for accurate segmentation of the acquisition voxels is that it allows the potential to scale voxels separately for white and grey matter.

Segmentation of tissue types in the brain is achieved through imaging techniques, but MRS is not an imaging modality. We therefore needed to construct images based on the geometry of the MRS acquisition voxels as a first step towards segmenting the tissue proportions of our acquisition voxels. These fabricated images can then be registered to high-resolution anatomical images. Once the registration had been correctly applied, the proportion of different tissues can be calculated using appropriate, existing software such as FSL (Jenkinson, Beckmann, Behrens, Woolrich, & Smith, 2012) or Freesurfer (Fischl et al., 2002; Dale, Fischl, & Sereno, 1999).

Whole brain segmentation can be achieved by supplying appropriate software with a high resolution 3-D T_1 MRI anatomical and the software will create the segmentation with little manual intervention. This is the case for several alternatives that can also achieve whole brain segmentation; for example SPM (Frackowiak, Friston, Frith, Dolan, & Mazziotta, 1997), Bioimage Suite (Duncan et al., 2004) or Brain Suite (Shattuck, Sandor-Leahy, Schaper, Rottenberg, & Leahy, 2001). Whole brain segmentation is a straight forward operation when using such software. However we found that methods to accurately register acquisition volumes with segmented MRI images required further detailed work to account for differences in coordinate systems.

Here we detail our approach to solving the issue of how to calculate the proportions of white matter, grey matter and CSF from the region targeted during an MRS experiment

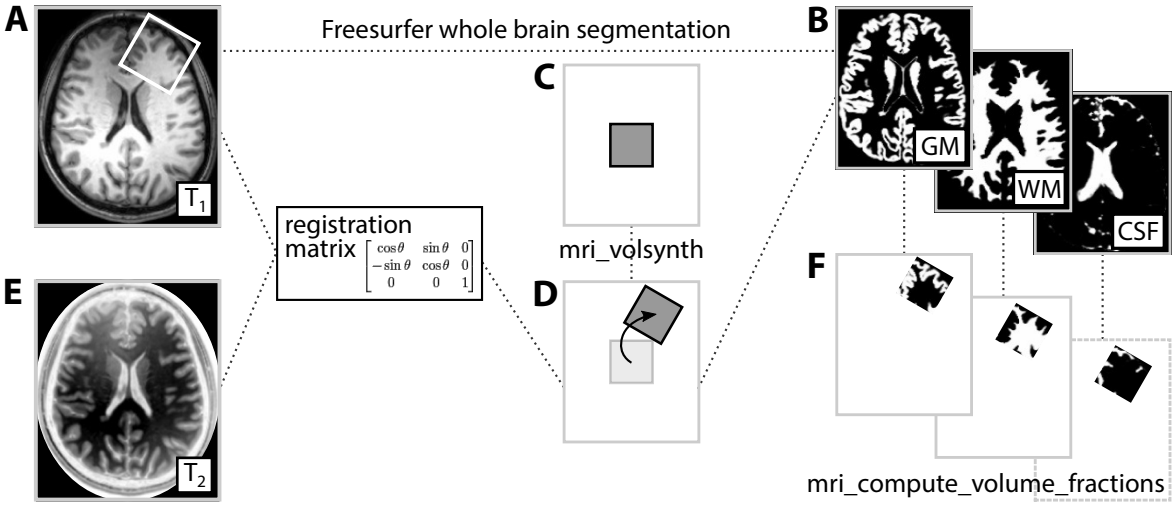

Figure 4.15: Segmenting MRS acquisitions. (**A**) DICOM files containing T_1 anatomical and MRS acquisition coordinates. (**B**) Automatic whole brain segmentation into GM, WM and CSF with Freesurfer. (**C**) Simulated fMRI created with mri_volsynth. (**D**) Simulated fMRI volume registered to anatomical. (**E**) T_2 manually registered with T_1 across sessions. (**F**) Simulated fMRI volume used as a mask to obtain MRS segmentation information with mri_compute_volume_fractions.

(**Figure 4.15**). The location of the acquisition voxel in scanner coordinate space is stored in parameters within the Digital Imaging and Communications in Medicine (DICOM) files associated with an acquisition. The rotation and translation information is most usefully processed from the direction cosines (the cosines of the angles between the three coordinate axes), but these data are not available from the standard exported data in `.SPAR` files associated with the Philips set up. Therefore we exported DICOM format files from the scanner from all of our scans. The specific tags that contain the relevant information are `ImageOrientationPatient`, which stores the row and column direction cosines and `ImagePositionPatient` that has the offset information (**Listing C.7**). The slice direction cosines are not stored in the DICOM files, but they can be calculated as the cross product of the row and column direction cosines (**Listing C.8**). It is worth noting that DICOM used the LPS (left, posterior, superior) coordinate system and that might differ from the software used to synthesise a MRI volume image for segmentation purposes. In our case, we used a Freesurfer program called `mri_volsynth` (**Listing C.9**) that requires parameters to be organised in RAS (right, anterior,

superior) coordinates. The DICOM coordinates needed to be converted before segmentation for our particular experiments (**Listing C.10**).

The files that are produced from `mri_volsynth` can be used as proxies for fMRI voxels in brain imaging software like Freesurfer. However when they are first produced they do not contain information on the coordinates and orientation of the associated MRS acquisitions. To position the newly fabricated fMRI proxies, we can use registration matrices (rigid transformations) to orientate the image files to the high resolution anatomical scans that were taken as part of the MRS scanning procedure (**Listing C.11**). For situations where the MRS scan and the anatomical MRI scan occur in the same session, the registration matrix is simply the identity matrix. For cases where the anatomical scan was acquired in a separate session then a transform matrix must be generated from the manual registration of images obtained in the separate sessions. The transform matrix obtained from this process can then be used to register and orient the fMRI proxy to the anatomical scan.

A visual comparison between screenshots taken during scanning and the visualisation of the registered fMRI volume can be made to ensure that the process has been correctly applied (**Figure 4.16**).

The problem of registration between MRI images is familiar to researchers in image analysis and computer science and there are software tools available to assist with this. However the particular use case that requires the creation of proxy MRI images for MRS experiments was less well supported, particularly in areas such as psychology. Due to an absence of tools that specifically addressed this use case, we needed to adapt our own approach, as described below.

Our approach to segmenting the tissue proportions of our MRS acquisition voxels was to register the fMRI proxies to their respective anatomical scans, which had already been seg-

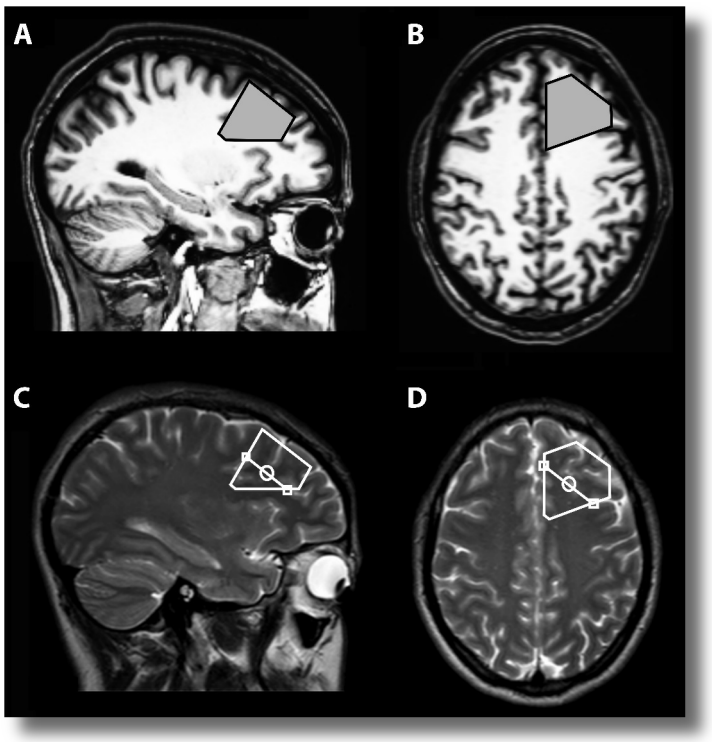

Figure 4.16: Visualised fMRI volume. The grey shapes represent the simulated fMRI volumes (**A,B**), displayed over a T_1 anatomical scan. The white wire shapes (**C,D**) are the acquisition voxels selected on the scanner console, displayed on a T_2 anatomical scout scan. Accurate alignment of the simulated voxels compared to the actual scanner screenshots can be seen in this figure.

mented into the tissue types through the automated processing in Freesurfer. To conduct the whole brain segmentation we used the Freesurfer software package, in combination with the function `mri_compute_volume_fractions`. Freesurfer has automatic brain segmentation routines, that are lengthy to run, typically over 13 hours to complete per anatomical image, but they have the advantage that they provide consistent tissue segmentation results that utilise validated procedures that are based on anatomical mapping information as well as image intensity models. The software uses volumetric and surface based algorithms to achieve whole brain segmentation (and brain region labelling). The `mri_compute_volume_fractions` function works by producing grey scale images with the same dimensions, orientation and spatial location as the simulated fMRI images that were produced using `mri_volsynth` (**Listing C.12**). By using the segmentation information that had been calculated for the whole brain, the function extracts segmentation information that coincides with the boundaries of the simulated fMRI image. The function outputs three data files that can be visualised as im-

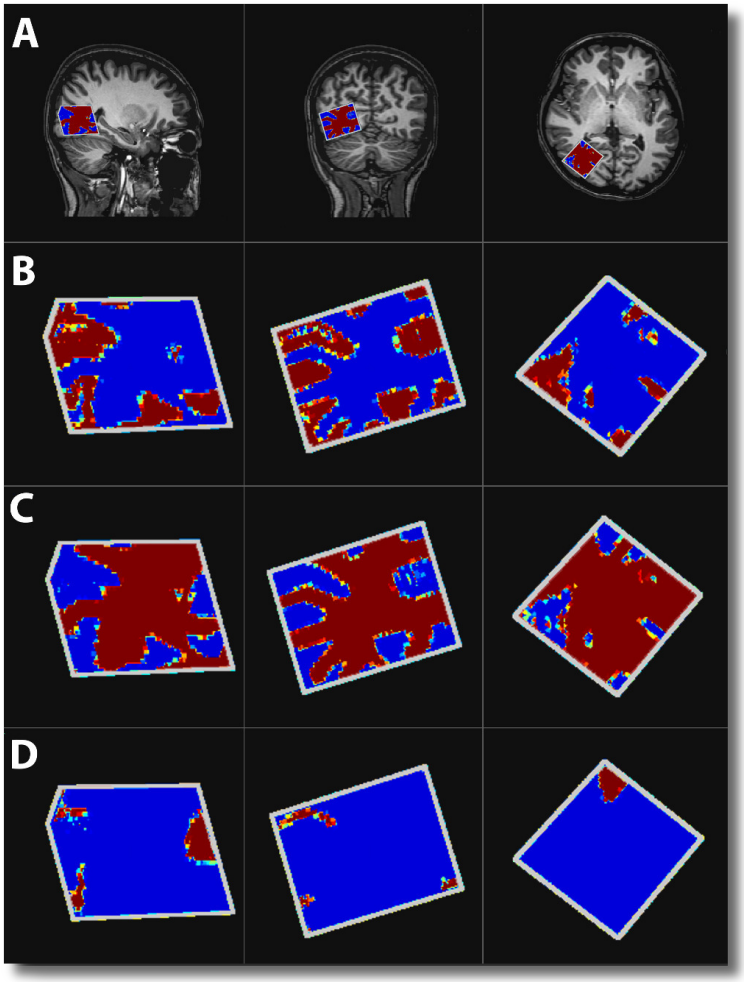

Figure 4.17: Sample segmented MRS acquisition. For colour bar see **Figure 4.18**. For monochrome version see **Appendix E.1**.
(**A**) Visualisation of a MRS segmentation mask. A colour gradient has been applied to map the highest matrix values to red and the lowest to blue. These sample images (sagittal, coronal and axial) are of a lateral occipital acquisition taken in the left hemisphere.
(**B**) Grey matter segmentation images corresponding with the MRS acquisition. Red tones indicate higher probability that the voxel is identified as GM.
(**C**) White matter segmentation images. Red tones indicate higher probability that the voxel is identified as WM.
(**D**) Cerebrospinal fluid segmentation images. Red tones indicate higher probability that the voxel is identified as CSF.

ages (**Figure 4.17**); one for the white matter (WM), one for the grey matter (GM) and one for the cerebrospinal fluid (CSF).

The segmented image files consist of 3-D matrices. The matrix values of each file represents the probability that each sub voxel consists of the particular tissue types defined by the file (WM, GM, CSF). For example a sub voxel that has been identified clearly as WM has a value of one in the WM file and zero in the equivalent sub voxel in the GM and CSF files. If a voxel was identified as being equally likely to be WM or GM, but definitely not CSF then it might have value of 0.5 in the WM and GM matrices and zero in the CSF one. Each sub voxel has a corresponding sub voxel in the other two files, and the sum of the three related sub voxel values is always one. Each individual sub voxel can have any decimal value between zero and

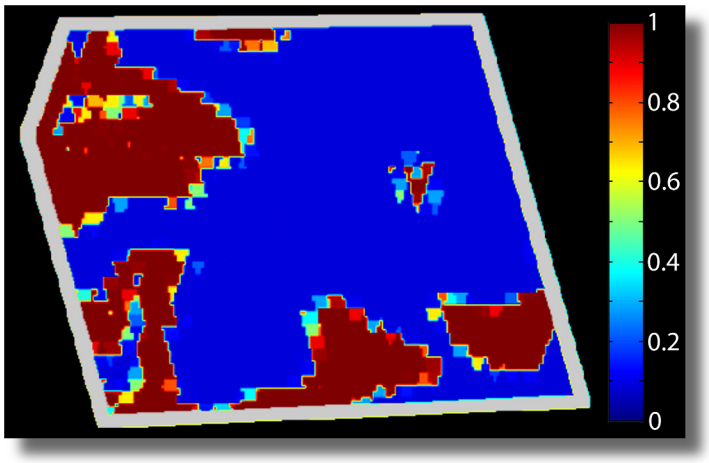

Figure 4.18: Sample segmentation image.
Colour visualisation of a segmentation matrix. This image is an enlarged version of the leftmost image from **Figure 4.17: B**. The range of colours, between red and blue shades, shows probability from zero to one.

one (**Figure 4.18**), this means that when the masks are visualised they are not binary images.

The probabilistic assignment of tissue type to each sub voxel struck us as an improvement over the binary assignment of FSL and was the deciding factor in choosing Freesurfer over FSL. However, all of the tools mentioned for segmentation are likely to produce more accurate segmentation than bespoke 'in house' schemes. The number of sub voxels in the image files is related to the MRS acquisition voxel dimensions. For example in the experiments that we conducted, with acquisition dimensions of 30 mm^3 and a resolution of 1 mm^3 per sub voxel, there were 27,000 sub voxels in each image. A summation of all the values in all of the sub voxels in each file can be used to calculate the percentage of tissue type.

We conducted segmentation analysis on 212 MRS acquisitions obtained from 31 subjects. We tabulated our tissue ratios according to brain region and the variability between subjects by tissue type was approximately 10% (**Table 4.2**).

This raised an interesting question as to whether or not scaling was necessary in all cases, because if the proportions of WM, GM and CSF were the same in every acquisition, then a linear scaling would alter the measurements by the same proportion. We noted that the tissue proportions that we measured were similar for a variety of brain regions and had low standard deviations. That is with the exception of early visual area (centred on V1, but overlapping

Table 4.2: Proportion of tissue type by ROI. The proportion and standard deviations of grey matter, white matter and cerebrospinal fluid in regions of interest related to lateral occipital, motor cortex, mid frontal gyrus and early visual areas. Separate measurements for left and right hemispheres (except for early visual, which was acquired medially across both hemispheres). There were 212 MRS acquisitions from 31 subjects.

ROI	GM	WM	CSF
Lateral occipital left hemisphere	0.33 ±0.03	0.61 ±0.04	0.06 ±0.02
Lateral occipital right hemisphere	0.32 ±0.04	0.63 ±0.04	0.05 ±0.02
Motor cortex left hemisphere	0.28 ±0.02	0.63 ±0.05	0.09 ±0.04
Motor cortex right hemisphere	0.27 ±0.03	0.64 ±0.06	0.09 ±0.03
Mid frontal gyrus left hemisphere	0.27 ±0.04	0.65 ±0.05	0.08 ±0.03
Mid frontal gyrus right hemisphere	0.27 ±0.03	0.65 ±0.05	0.08 ±0.03
Early visual cortex	0.39 ±0.03	0.49 ±0.04	0.12 ±0.03
Mean	**0.30**	**0.61**	**0.08**
Mean without early visual cortex	**0.29**	**0.64**	**0.08**

with V2 and V3). We acquired this area by placing the acquisition voxels medially over both hemispheres and therefore included a greater proportion of CSF from the gap between the two hemispheres (**Figure 4.19A**). The early visual region also had greater proportions of grey matter than other regions, again this was probably related to the medial positioning. These results suggest that lateral occipital, motor cortex and mid frontal gyrus areas could all be compared with or without rescaling the measurements, but that comparisons involving early visual areas would need to be scaled. As the proportions of tissue and CSF cannot be known exactly for each acquisition in advance, we suggest that calculating the tissue proportions of all voxels be done as a matter of course in MEGA-PRESS experiments. The tissue proportions can then be used to rescale the measurements to take account of different tissue proportions,

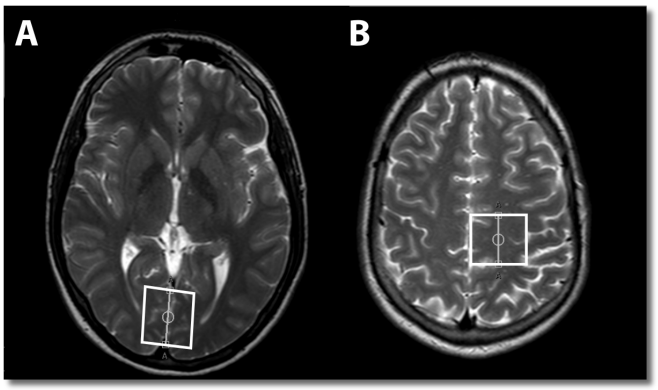

Figure 4.19: Across hemisphere positioning for occipital region.
(**A**) Acquisition voxel (white box) showing the position covering both halves of the brain. This may explain the increased grey matter proportions measured in this brain region compared to regions acquired in one hemisphere only.
(**B**) Motor cortex contained in one hemisphere only.

or be used to justify not rescaling the measurements if that is appropriate for a particular experiment.

There are certain conditions where scaling by tissue proportions becomes important even in the case where the proportions are similar across acquisitions. For example if absolute quantitation is attempted, if the contribution from particular tissues was sought or if there is a hypothesis that the metabolite of interest (GABA for example) was at different densities in white matter and grey matter. We explore these conditions over the next few sections.

4.8 Scaling and Reference Metabolites

Scaling of measured GABA according to tissue proportion in the acquisition voxel is an aspect of processing for which there is no current consensus. Some groups dismissed tissue scaling altogether, others thought it necessary (Michels et al., 2012; Puts et al., 2011) and those that scaled their measurements did so using different algorithms (Bhattacharyya et al., 2011) and according to different rationales. Different groups also reported their GABA measurements in different ways, for example as ratios to other metabolites such as NAA (C. J. Stagg, Bachtiar, & Johansen-Berg, 2011b), creatine (Bhattacharyya et al., 2011; I.-Y. Choi, Lee, Merkle, & Shen, 2006; Goto et al., 2010; Jensen et al., 2005; McLean et al., 2002; Waddell et al., 2010; Wylezinska et al., 2003) and water (Bogner et al., 2010; Puts et al., 2011).

The principle behind reporting GABA as a ratio is that the reference metabolite concentrations should be considered stable. This stability refers to inter-subject variability (i.e. this should be low) and also that the reference metabolite is not functionally relevant to the phenomena being investigated. In the case of creatine, it has been shown that creatine varies more than water during visual stimulation paradigms (Mumuni et al., 2012) and we concluded that this could adversely effect our results. Another potential problem that has been identified

with creatine is that grey matter density increases of 84% over white matter have been reported (Wang & Li, 1998). This led us to conclude that the interpretation of GABA/creatine ratios would be complicated unless we accounted for the different concentrations within the tissue proportions. Another difficulty that we identified with creatine was that it has been shown to be in different concentrations according to brain region (Pouwels & Frahm, 1998). This would make comparisons across brain areas difficult as the GABA quantity (measured as a ratio to creatine) could vary based on the concentration of the reference metabolite, rather than actual variation in GABA concentration.

Creatine concentrations have also been associated with working memory (Ozturk et al., 2009), and this could have a confounding effect on our experiments if working memory was part of the learning mechanism for our visual learning experiments. Similarly, the other popular reference metabolite, NAA, has been linked with verbal intelligence (Pfleiderer et al., 2004), cognitive performance (Jung, Gasparovic, Chavez, Caprihan, et al., 2009; Jung et al., 2005) and creativity (Jung, Gasparovic, Chavez, Flores, et al., 2009). These factors led us to conclude that the assumptions that these reference metabolites were not functionally relevant were unsafe.

4.8.1 Water Scaled GABA

As there are potential difficulties with confounds related to reference metabolites, we decided to concentrate on water in place of the other reference metabolites (Ernst, Kreis, & Ross, 1993; Kreis, Ernst, & Ross, 1993). The use of internal water as a reference has been considered advantageous because the water densities and signal relaxation times of grey matter, white matter and CSF could be reliably estimated and were assumed to not change significantly between subjects (Gasparovic et al., 2006).

Spectroscopy analysis software often uses simplified assumptions concerning the water concentration constants when calculating metabolite concentrations. These assumptions can have a distorting effect on the concentration values calculated. For example, both LCModel and Tarquin spectroscopy software use a water concentration value of 35,880 — which is actually a white matter water concentration constant. As neither software has the facility to specify the proportion of tissue types before quantification, the metabolite quantification will not be accurately scaled according to the actual water concentration value constants for grey matter and CSF. The equation used by Tarquin for example is reproduced in (**Equation 4.2**).

$$
\begin{aligned}
water_{WM} &= 35{,}880\,\text{mM} \\
signal_{conc} &= \frac{signal_{amp} \times water_{WM} \times water_{att} \times 2}{water_{amp}}
\end{aligned}
\tag{4.2}
$$

We therefore rescaled the Tarquin output (**Equation 4.3**) to take account of the tissue proportions and water concentration constants for GM ($water_{GM}$) and CSF ($water_{CSF}$), using the values tabulated in Gasparovic et al. (2006).

$$
\begin{aligned}
water_{GM} &= 43{,}000\,\text{mM} \\
water_{CSF} &= 53{,}474\,\text{mM} \\
rescaled &= signal_{conc} \times \frac{pGM \cdot water_{GM} + pWM \cdot water_{WM} + pCSF \cdot water_{CSF}}{water_{WM}}
\end{aligned}
\tag{4.3}
$$

A further simplification in the quantification calculations for LCModel and Tarquin is the assumptions made with the water attenuation factor (**Equation 4.4**). In both software suites,

the factor assumes a TE (echo time) of 30 ms and a field strength of 1.5 T.

$$water_{att} = \frac{exp(-t/T_2^{water})}{exp(-t/T_2^{signal})}$$
$$water_{att} = \frac{exp(-30/80)}{exp(-30/400)} \approx 0.7 \tag{4.4}$$

The default values would lead to an overestimation for the metabolite concentrations (Yamamoto et al., 2015) in experiments that used TE times of 68 ms. However, contrary to the findings in that paper, the fix is simple and can be applied to Tarquin by setting the value directly after calculating with the correct TE. We can substitute the appropriate TE time (68 ms for the experiments described in this thesis) to calculate the correct water attenuation factor (which is ≈ 0.5), thus circumventing the overestimation. T_2 relaxation times have been found to be independent of field strength (Stanisz et al., 2005), unlike T_1 relaxation times, which increase with the strength of the magnetic field. We can therefore use the T_2 constants for water and metabolites from **Equation 4.4**, which are approximations that are suitable for 1.5 T and 3.0 T.

The value calculated from this scaling operation represented the GABA measurement, scaled to water in the different compartments and the unit of measurement is milli molar (mM), in contrast to the often quoted institutional units that is used when this scaling is not used. There were further scaling operations that could be applied, for example to account for the CSF proportion or to report values as ratios to other metabolites.

4.8.2 Tissue Scaled GABA

The measurements that we derive from the signals in MRS experiments come from voxels that contain grey matter, white matter and CSF. However, metabolites are present in CSF in only negligible amounts compared with tissue. This means that when comparing measurements across different subjects or brain regions the measurements should be scaled so that they are per unit of brain tissue (McLean et al., 2002; Michels et al., 2012; Puts et al., 2011), to reflect the proportion of CSF in the ROI. The most straightforward way to do this is to divide the metabolite measurement by the proportions of GM and WM (**Equation 4.5**).

$$D = \frac{metabolite}{pGM + pWM} \tag{4.5}$$

Implicit in **Equation 4.5** is the idea that the concentration of the metabolite within GM and WM are the same, and D is meant to represent a notional density. However, it has been reported that GABA is twice as concentrated in GM compared to WM (Jensen et al., 2005). To test this assumption we completed a regression analysis using the same method as that reported by Bhattacharyya et al. (2011). The regression analysis predicts metabolite densities in GM and WM from measurements where the tissue fractions have been calculated. This is done by extending the regression line to zero (WM) and one (GM).

We measured GABA+ from four brain areas for a total of 199 voxels and calculated the tissue scaled GABA+ quantitation (**Table 4.3**).

We plotted the tissue scaled GABA+ quantitation versus the proportion of grey matter divided by the proportion of tissue and performed a regression analysis on the pooled data (**Figure 4.20**).

Table 4.3: Mean GABA+ values by region of interest. Mean tissue scaled GABA+ values for lateral occipital, motor cortex, mid frontal gyrus and early visual cortex.

Region of Interest	N	Mean	SD
Lateral occipital	58	1.64	±0.18
Motor cortex	53	1.53	±0.15
Mid frontal gyrus	60	1.53	±0.22
Early visual cortex	28	1.75	±0.17
Totals / averages	**199**	**1.59**	**±0.20**

The regression showed that for every institutional unit of tissue scaled GABA+, grey matter weighted measurements increased by 1.27, which represented 0.4 of a standard deviation. 95% confidence intervals were 0.86 to 1.68. F(1,197)=37.4, p=<.01 showed that the results were unlikely to have arisen through sampling error, assuming the null hypothesis to be true.

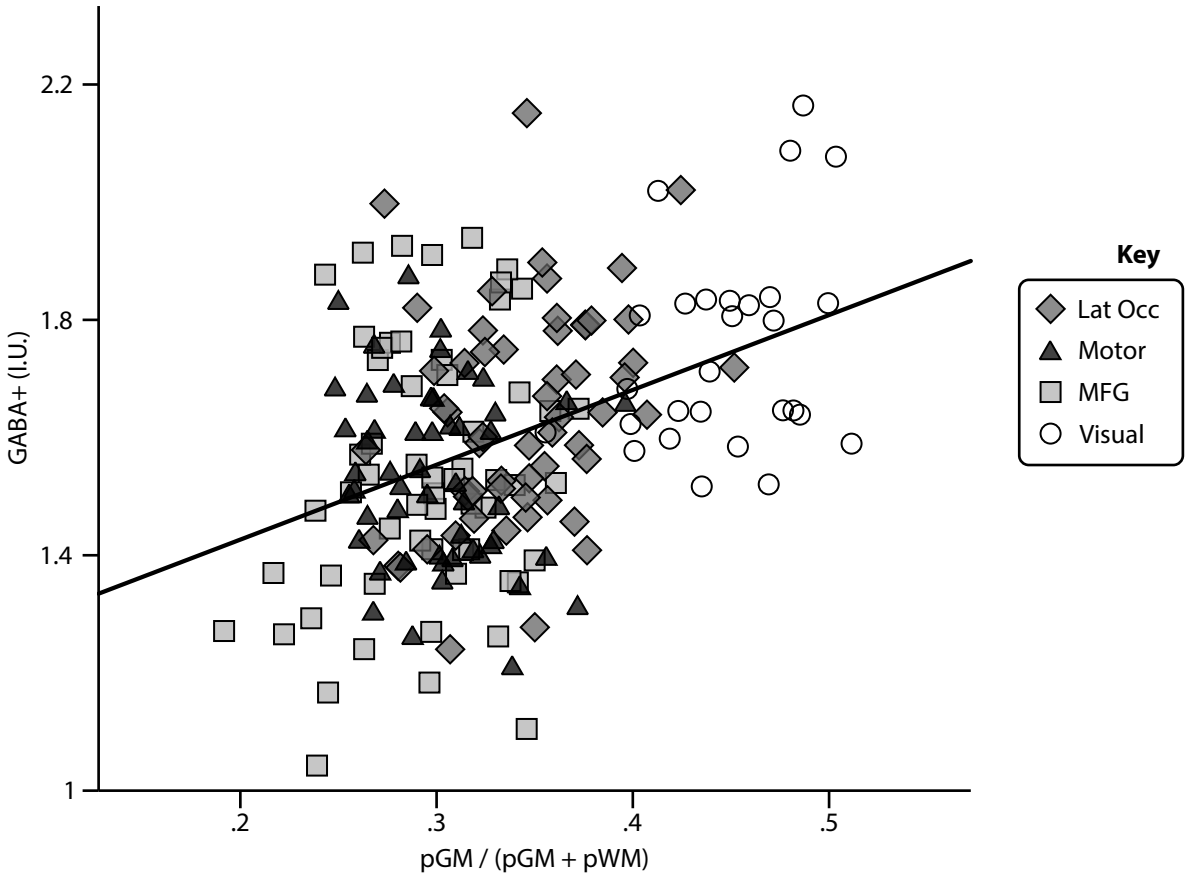

Figure 4.20: Grey matter concentrations regression analysis. Linear fitting to determine the grey matter and white matter GABA+ concentrations (r=.4, p=<.01, standard error=0.19). Extrapolating the line to **pGM / (pGM + pWM) = 0**, resulted in a white matter value of **1.17**. Extrapolating the line to **pGM / (pGM + pWM) = 1**, resulted in a grey matter value of **2.44**, which represented a twofold increase in concentration.

Table 4.4: ROI and grey matter fraction. Linear regression model for the interaction between ROI and grey matter fraction (**GM-fraction**). Only **GM-fraction** (pooled data) has a statistically significant effect. The ROIs (**Motor, MFG, Visual**, relative to Lateral Occipital) have no significant effect on the intercept, and the interaction coefficients (**Motor:GM-fraction, MFG:GM-fraction, Visual:GM-fraction**) indicate no significant effect of ROI on the gradient.

Name	Estimate	SE	tStat	DF	pValue	Lower	Upper
Intercept	1.12	0.24	4.71	191	0.00	0.65	1.59
Motor	0.12	0.34	0.35	191	0.73	-0.55	0.79
MFG	0.07	0.31	0.22	191	0.83	-0.55	0.68
Visual	-0.01	0.53	-0.01	191	0.99	-1.04	1.03
GM-fraction	1.50	0.69	2.18	191	0.03	0.14	2.86
Motor:GM-fraction	-0.38	1.05	-0.37	191	0.72	-2.46	1.69
MFG:GM-fraction	-0.33	0.97	-0.34	191	0.74	-2.23	1.58
Visual:GM-fraction	-0.08	1.25	-0.07	191	0.95	-2.55	2.38

Extending the regression fit line to zero and unity gave the GABA+ values for grey matter and white matter as 2.44 and 1.17 respectively. We calculated the grey matter to white matter GABA+ ratio as 2.09, confirming the twofold concentration increase in grey matter reported in the literature.

The data in **Figure 4.20** is pooled across voxels from different brain regions and there appears to be some clustering shown here. We tabulated the results from a linear regression model so that the interaction between ROI and grey matter fraction could be examined (**Table 4.4**). This shows that ROI is not a significant predictor as a main effect or as an interaction with the fraction of grey matter. The fraction of grey matter is the only variable that was statistically significant in this table, this suggests that pooling the data makes sense. We plotted the predicted mean and 95% confidence interval from the mixed effects model for each voxel type and also performed a simple linear regression by fitting just the data for each voxel type (**Figure 4.21**). The variation within each region is the same as that between regions (the mean for any region lies within the 95% confidence interval of the predictions for all other regions in **Figure 4.21: A**), showing consistency across regions. A benefit of pooling the data is that this gives narrower 95% confidence intervals at zero and one (**Figure 4.21: B**).

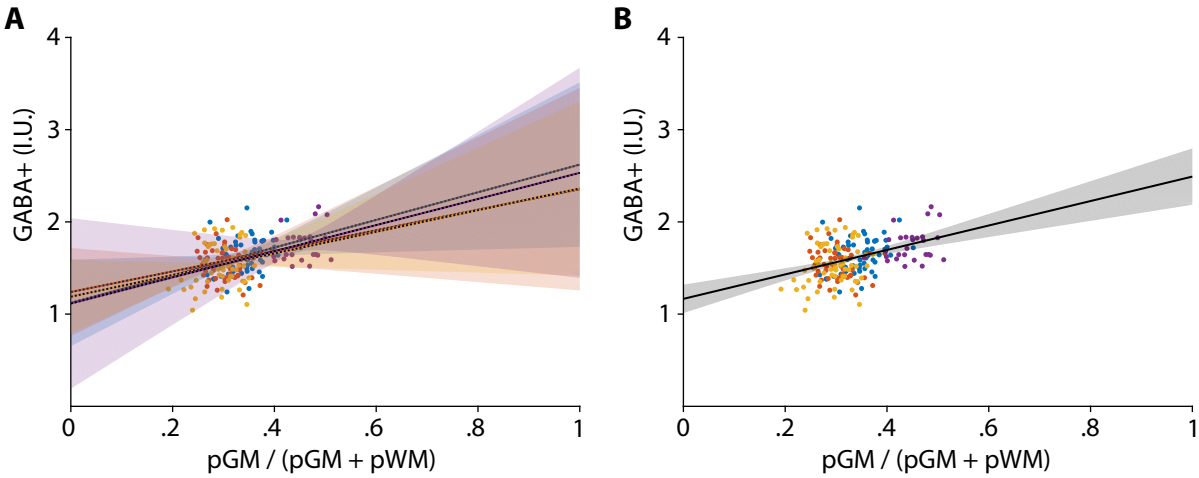

Figure 4.21: Grey matter concentrations pooling ROIs. (**A**) Predicted mean and 95% confidence intervals from two regression models; a mixed effects model and a simple linear model. The simple linear model is represented by dotted lines that appear almost identically to the mixed effects model, over which they are superimposed. Shaded areas represent the 95% confidence intervals for the mixed model regression lines. The 95% confidence intervals are narrower for pooled data (**B**), when extended to zero and one on the GM-fraction axis.

The different concentrations of GABA according to tissue type, led us to propose an amendment to the standard scaling, which includes a term for a scaling factor to account for any differences in concentration between GM and WM (**Equation 4.6**).

$$D = \frac{metabolite}{pGM \cdot sGM + pWM \cdot sWM} \tag{4.6}$$

In **Equation 4.6**, sGM and sWM refer to the scaling factors for GM and WM. If these were set to 1, then it would be equivalent to **Equation 4.5**. However, if we wished to simulate the double GABA density in GM, then we could simply set sGM to a value that was twice that of sWM. For example sGM could be set to 1 and sWM set to 0.5, this would scale the values according to the density assumptions and keep the magnitude of the values similar to the original unscaled values.

We were interested in the interaction between inhibitory processes and visual percep-

tual learning and this led us to become interested in investigating the GM contribution to the measured GABA. It is an open question whether WM GABA concentrations are functionally relevant in learning experiments (Angulo, Le Meur, Kozlov, Charpak, & Audinat, 2008; Fields, 2008), but given that fMRI analysis usually precludes WM from the analysis we thought it worth trying to separate the WM and GM contributions to the signal. This would also be consistent with the hypothesis that grey matter GABA concentrations modulated the efficiency of visual learning rather than those in the white matter. We therefore split the notional density measurement D into the GABA grey matter (gGM) and GABA white matter (gWM) contributions to the signal (**Equations 4.7,4.8**).

$$gGM = D \times \frac{pGM \cdot D \cdot sGM}{GABA} \tag{4.7}$$

$$gWM = D \times \frac{pWM \cdot D \cdot sWM}{GABA} \tag{4.8}$$

$$D = gGM + gWM \tag{4.9}$$

The sum of gGM and gWM would be equal to the original value of D (**Equation 4.9**), but when we separated the GM and WM components like this we could account for variations in GM proportion with the GABA density assumptions chosen with the scaling factors (sWM and sGM). These scaling factors could be used with other metabolites. In fact it might be advantageous when reporting GABA values as ratios, where the reference metabolite was also known to vary in density in GM compared to WM. Creatine has been used as a reference metabolite in GABA studies, but this metabolite has been shown to differ in density across tissue types (Kreis et al., 1993).

It would not make sense to use these scaling factors in the case where the GABA was being

reported as a ratio to another metabolite that had the same scaling factors for GM and WM as GABA. In this case the ratio would be the same whether **Equation 4.5** or **Equation 4.6** were used.

We tabulated the effect of applying these equations to various tissue proportions (**Tables 4.5,4.6**), including boundary cases and proportions that we calculated from our *in vivo* experiments. The reason for this was to provide illustrative examples so that the effect of using the equations could be seen in various scenarios (for example cases where there was elevated grey matter content versus white matter and vice versa). The bottom row, highlighted, has tissue proportions that were calculated from our *in vivo* experiments. When we compared the values between **Tables 4.5** and **4.6** (where the scaling constants for GM were twice that of WM) we concluded that this scaling method elevated the GM contribution (gGM) compared to the WM contribution (gWM) from approximately half of WM (3.54 versus 7.32) to almost the equivalent value (8.06 versus 8.33).

In correlation studies between GABA measurements and perceptual learning, where the hypothesis involved grey matter inhibition, this had the potential to distinguish the contribution of GM GABA that might otherwise be masked by the influence of the WM GABA contribution. We investigated this in the experiments described in **Chapter 6: GABA Versus Training Difficulty Mediated Visual Learning** and **Chapter 7: GABA Versus Coarse and Fine Visual Learning**.

Other researchers have applied different approaches to separating the GM and WM contributions. For example one group (C. J. Stagg et al., 2011a) has used the scheme in **Equation 4.10**. In this scheme the GABA measurement was calculated as a ratio to creatine, however both GABA and creatine were multiplied by tissue proportions and while GABA was scaled using the proportion of grey matter, creatine was scaled using the proportion of both

Table 4.5: Grey matter scaling. Sample scaled values where the scaling factor for WM and GM was the same (sGM = sWM = 1), sCSF was set to 0.001. Calculations for typical tissue proportions (mean) are shown in the highlighted row. **gTOT** the measured GABA quantity (set to 10 in all cases); **pGM** proportion of GM; **pWM** proportion of WM; **pCSF** proportion of CSF;

D = $\frac{\text{gTOT}}{(\text{pGM}\times 1+\text{pWM}\times 1+\text{pCSF}\times 0.001)}$ nominal density (see **Equation 4.6**);

gGM = $\text{D}\times\frac{\text{pGM}\times\text{D}\times 1}{\text{gTOT}}$ GABA from the GM contribution (see **Equation 4.7**);

gWM = $\text{D}\times\frac{\text{pWM}\times\text{D}\times 1}{\text{gTOT}}$ GABA from the WM contribution (see **Equation 4.8**);

gCSF = $\text{D}\times\frac{\text{pCSF}\times\text{D}\times 0.001}{\text{gTOT}}$ GABA from the CSF contribution.

gTOT	pGM	pWM	pCSF	D	gGM	gWM	gCSF
10	1.00	0.00	0.00	10.00	10.00	0.00	0.00
10	0.00	1.00	0.00	10.00	0.00	10.00	0.00
10	0.00	0.00	1.00	$1\cdot10^4$	0.00	0.00	$1\cdot10^4$
10	0.50	0.50	0.00	10.00	5.00	5.00	0.00
10	0.40	0.40	0.20	12.50	6.25	6.25	0.00
10	0.10	0.30	0.60	24.96	6.23	18.69	0.04
10	0.30	0.10	0.60	24.96	18.69	6.23	0.04
10	0.60	0.20	0.20	12.50	9.37	3.12	0.00
10	0.30	0.62	0.08	10.87	3.54	7.32	0.00

Table 4.6: Grey matter scaling, accounting for different density in GM compared to WM. Differences in the formulas with **Table 4.5** are highlighted in light grey.

D = $\frac{\text{gTOT}}{(\text{pGM}\times 1+\text{pWM}\times \boxed{0.5}+\text{pCSF}\times \boxed{0.0005})}$;

gGM = $\text{D}\times\frac{\text{pGM}\times\text{D}\times 1}{\text{gTOT}}$; **gWM =** $\text{D}\times\frac{\text{pWM}\times\text{D}\times \boxed{0.5}}{\text{gTOT}}$; **gCSF =** $\text{D}\times\frac{\text{pCSF}\times\text{D}\times \boxed{0.0005}}{\text{gTOT}}$.

gTOT	pGM	pWM	pCSF	D	gGM	gWM	gCSF
10	1.00	0.00	0.00	10.00	10.00	0.00	0.00
10	0.00	1.00	0.00	20.00	0.00	20.00	0.00
10	0.00	0.00	1.00	$2\cdot10^4$	0.00	0.00	$2\cdot10^4$
10	0.50	0.50	0.00	13.33	8.89	4.44	0.00
10	0.40	0.40	0.20	16.66	11.11	5.55	0.00
10	0.10	0.30	0.60	39.95	15.96	23.94	0.05
10	0.30	0.10	0.60	28.55	24.45	4.07	0.02
10	0.60	0.20	0.20	14.28	12.24	2.04	0.00
10	0.30	0.62	0.08	16.39	8.06	8.33	0.00

grey matter and white matter.

$$scaled\_GABA = GABA \times \frac{pGM}{pGM + pWM + pCSF}$$
$$scaled\_Cr = Cr \times \frac{pGM + pWM}{pGM + pWM + pCSF}$$
$$GABA\_ratio = \frac{scaled\_GABA}{scaled\_Cr} \tag{4.10}$$

Although this scaling scheme was markedly different to the one we employed and used different assumptions, the scaled measurements obtained from it were still strongly correlated with scaled measurements calculated according to our equations. When we examined the correlations for the GABA measurements calculated with **Equation 4.10** versus those calculated with **Equation 4.5** we found them to be strongly correlated, $r(201)=.71$, $p=<.01$ (**Figure 4.22**).

It might be considered surprising that the different scaling schemes produced such highly correlated results. However, when we considered that there was a low variability in tissue proportions then this made sense. The consistency of voxel placement resulted in there being similar tissue proportions and thus the scaling made a large difference in the magnitude of

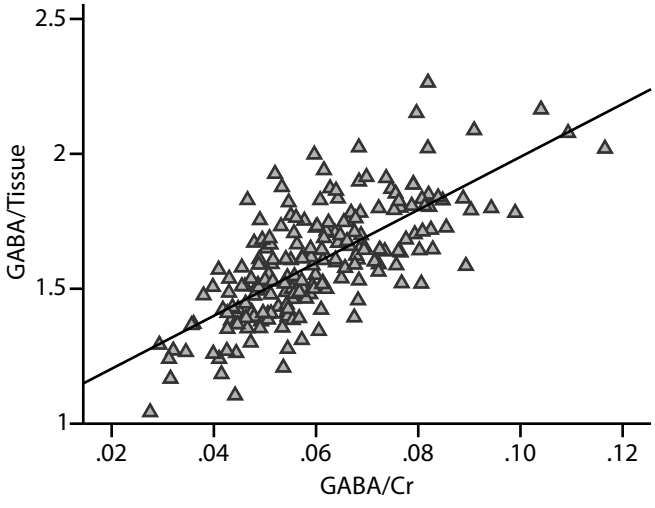

Figure 4.22: Comparison of scaling methods, creatine versus tissue. Correlations between two scaling schemes that use different assumptions about GABA densities in tissue. GABA/Cr scaling that used a tissue proportion multiplier (x-axis) versus a water scaled scheme that divided by tissue proportion (y-axis). Despite the different methods these schemes produced strongly correlated results, $r(201)=.71$, $p=<.01$.

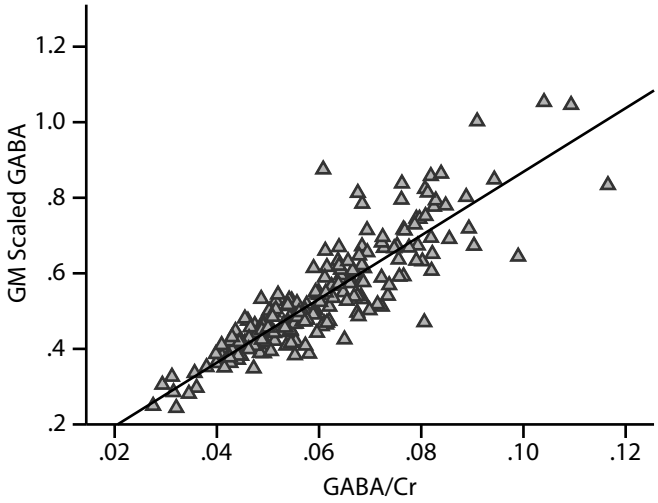

Figure 4.23: Comparison of scaling methods, creatine versus grey matter. Correlations between two scaling schemes that use different assumptions about GABA densities in tissue. GABA/Cr scaling that used a tissue proportion multiplier (x-axis) versus a water scaled scheme that accounted for grey matter proportion (y-axis). Despite the different methods these schemes produced very strongly correlated results, $r(201)=.88$, $p=<.01$.

the scaled values, however they still produced metrics that were well correlated.

In **Equation 4.10** the measured metabolite quantities are multiplied by the proportion of tissue. In our scheme (**Equation 4.7**) the measured GABA concentration is divided by the proportion of the tissue of interest. Both operations are intended to emphasise the grey matter contribution, but do so using equations that one might expect to have very different results. Interestingly, when we examined the correlations between this scheme and our scheme, the correlations were even stronger, $r(201)=.88$, $p=<.01$ (**Figure 4.23**).

4.8.3 Correlations Between Scaling Methods

We examined the correlation coefficient from GABA measurements taken from Tarquin versus the same measurements scaled according to **Equation 4.6**, which essentially scaled by tissue (GM and WM) and accounted for the CSF proportion in the voxels. The results were very strongly correlated, $r(201)=.97$, $p=<.01$ (**Figure 4.24**).

The scaling factors for GM and WM are the same in this scheme, but the slight variation accrued from the different proportions of CSF in the voxels. We also looked at the comparison where the GM scaling factor was set to twice that for WM. This showed a similarly strong correlation, $r(201)=.95$, $p=<.01$ (**Figure 4.25**).

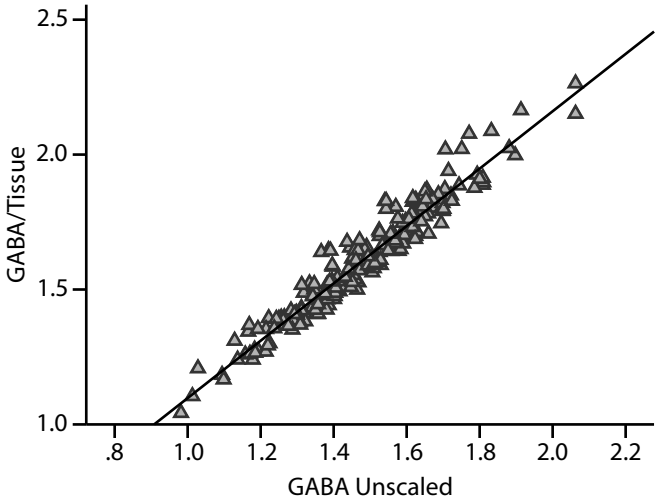

Figure 4.24: Correlations, unscaled versus tissue scaled. $r(201)=.97$, $p=<.01$.

As expected the magnitude of the scaled values increased (as the GM values were effectively doubled), but this lead to scaling that was almost linear and therefore resulted in very similar correlations to those in **Figure 4.24**.

Next we investigated the correlations between unscaled GABA measurements and grey matter scaled measurements (**Equation 4.7**). This effect size was less strong, $r(201)=.61$, $p=<.01$ (**Figure 4.26**) and this suggested that correlations between learning metrics and GABA measurements scaled in this way were likely to be different to correlations between learning metrics and unscaled GABA measurements.

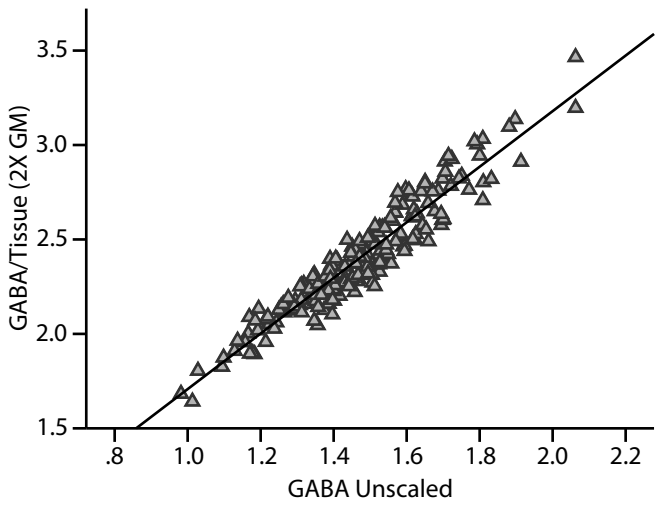

Figure 4.25: Correlations, unscaled versus tissue scaled, grey matter scaling factor twice that of white matter. $r(201)=.95$, $p=<.01$.

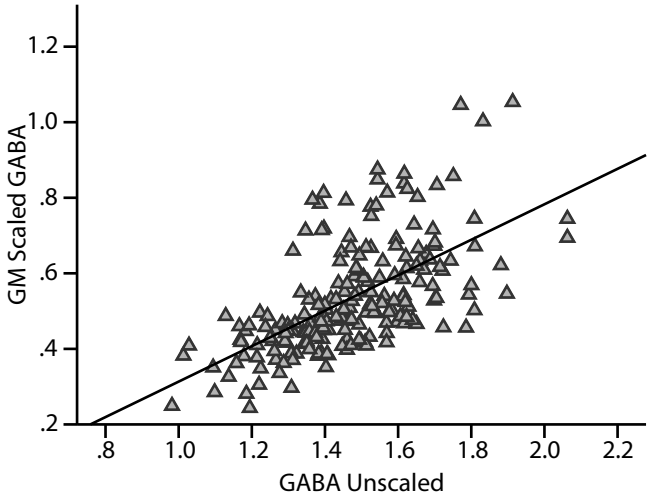

Figure 4.26: Correlations, unscaled versus grey matter scaling. $r(201)=.61$, $p=<.01$.

We also examined the correlations between the unscaled GABA measurements and the GM scaled values from **Equation 4.7**, but where the GM scaling factor was set to twice the WM scaling factor (**Figure 4.27**). This resulted in a correlation of $r(201)=.79$, $p=<.01$, which indicated a slightly stronger effect size.

The final correlation that we examined was that between the two GM scaled values, which differed only in the scaling factor, which was set to twice that of WM in one of the variables. This was expected to be very strongly correlated, as the scaling factor should be approximately linear and so it proved to be, $r(201)=.96$, $p=<.01$ (**Figure 4.28**).

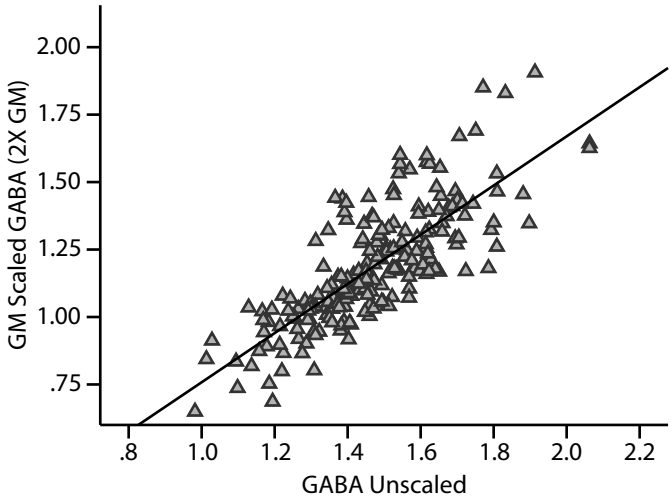

Figure 4.27: Correlations, unscaled versus grey matter scaling, grey matter scaling factor twice that of white matter. $r(201)=.79$, $p=<.01$.

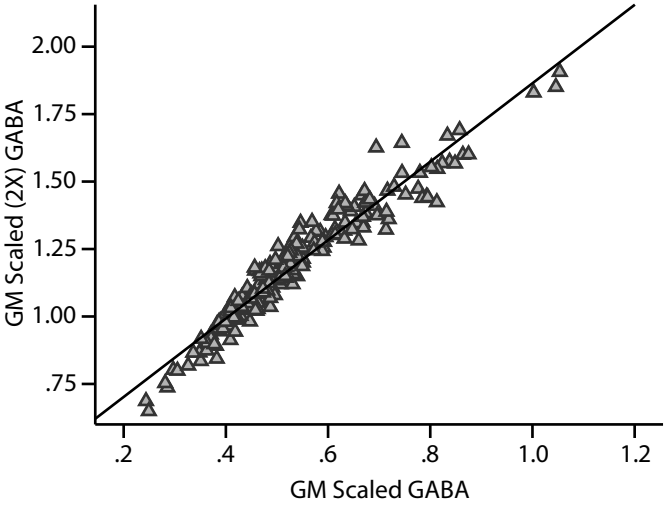

Figure 4.28: Correlations, grey matter scaling versus grey matter scaling with scaling factor doubled. $r(201)=.96$, $p=<.01$.

The conclusions that we drew from these correlations were that scaling according to the CSF proportion is necessary to align it to the known fact that CSF contributes negligible amounts to the overall measured GABA total. However, in cases where absolute quantitation is not attempted (the majority of MEGA-PRESS experiments) and where the CSF ratio is consistent (this should normally be the case when comparing the same region of interest and where voxel positioning is consistent) then the scaling would generally be linear and should therefore not alter the findings in correlational studies. Where GM scaled correlations are concerned we concluded that the scaling introduced some variability into the correlations. This we interpret as potentially helpful in highlighting the contribution of GM GABA over the dominating contribution of WM GABA, which was found to be in approximate proportions of 2:1 compared to GM in our acquisitions (**Section 4.7: Table 4.2**). The correlations between the GABA scaled with a twofold increased density assumption compared to WM scaled GABA were so strong that we suggest that it would not make much difference which scheme is used in correlational studies, however we preferred the twofold GM scheme as it matched the findings from our regression analysis. We therefore conclude that the GM GABA scaling scheme, with double GM scaling factor, would best suit our hypothesis that inhibitory

mechanisms in cortical grey matter would mediate performance in visual learning tasks. We applied this scaling scheme to all subsequent correlative studies.

4.9 Discussion

Once data has been obtained from the scanner for a MEGA-PRESS experiment there are various approaches that can be employed to quantify and improve the quality of the MRS data. This chapter discussed these approaches and introduced a sequential pipeline of steps that went from initial time domain characterisation of MEGA-PRESS phase difficulties through to rescaling techniques; with spectral correction, tissue segmentation, peak modelling and quantification approaches all described along the way.

It is unusual to see time domain plots in research for MEGA-PRESS related work. This is in part because of an assumption that time domain data are difficult to interpret visually, compared to frequency domain plots. However this section showed that differences in phase between edited and non-edited sequences are unambiguously evident in time domain plots, where the exponential decay of the edited FID is inverted compared to the non-edited FID. This is not necessarily the case with frequency domain plots that tend to obfuscate spectral peaks and troughs in out-of-phase data. Having prior knowledge that one half of the MEGA-PRESS data are out-of-phase by 180° can facilitate optimisations in automatic phase correction algorithms. This is because a typical phase correction algorithm will sweep through a range of angles and cease as the phase correction approaches its optimum. If it is known that a spectrum is approximately 180° out of phase then an initial guess of the phase correction can be provided, thus reducing the time taken to reach the optimum solution.

In the section on phase correction we demonstrated how to integrate an automatic algorithm for each FID acquired. The point to this approach was to improve the processing speed

and reproducibility of the results data obtained (compared to manual phase correction). We also showed that this approach leads to consistency in combining edited and non-edited spectra, as edit OFF scans are always subtracted from edit ON ones. Subspectral shifting is another way of realigning spectra that would otherwise lead to erroneous quantitation and other potential artefacts such as pseudo doublets. We went into some detail here as this process receives scant attention in most of the MEGA-PRESS literature. We demonstrated significant improvements that this technique can make to poorly aligned data and reported an improvement with independent alignment versus paired alignment strategies, which contrasted with previous findings.

We concluded that doublet models of GABA peaks would produce data that functioned similarly to singlet models in correlative studies, based on the strong correlations between the measurements obtained by integrating the peaks of the two models. However we still preferred the doublet model as it matched the theoretical line shape of the GABA spectrum and we believe it more closely matches the raw data that we observed (while accepting that other researchers, using different equipment might observe data more suitably modelled with a singlet model). This suggests the importance of checking widely held assumptions and the need to have a flexible pipeline of analysis tools.

An important step in the post-acquisition processing of metabolite signals for correlative studies is to take account of the volumes of tissue and CSF in the acquisition voxel. The main obstacle to calculating these volumes is in converting the coordinates, offsets and dimensions of the acquisition voxel to an image that can be registered to a high resolution MRI scan. We demonstrated a method that we hope has been explained in sufficient details so that it may help shorten the learning curve for other researchers wishing to implement this step.

The reasons why the segmentation step is considered important were outlined in the sec-

tion on scaling and reference metabolites. Here we discussed the different approaches that researchers have taken and proposed a method to concentrate on the grey matter contribution to the measured signal. This is a novel approach that fits with a hypothesis on the role of GABA in perceptual learning that we develop in later chapters of this thesis. We also show through several correlative plots that differently scaled GABA measurements produce similar (highly correlated) results. Our conclusions for this are that scaling methods are unlikely to make large differences where the tissue proportions are similar across brain regions and subjects. However, we do note that different scaling operations might be important where there are specific hypotheses regarding density differences of metabolites of interest in different tissue types or if absolute quantitation is attempted.

Since developing our analysis routines other groups have also developed MEGA-PRESS analysis software, with Gannet (Edden et al., 2014) being the most comprehensive. This software has some similarities to our pipeline; both are script based, command line driven interfaces that interact with other software. Gannet is Matlab based and aims to support GABA-edited data acquired from Philips, GE and Siemens scanners. Gannet modules apply frequency and phase correction in a pairwise manner, they apply outlier rejection and fit a single Gaussian peak to GABA and quantitate it using either water or creatine as a reference metabolite. In the most recent version, Gannet interacts with SPM software to calculate tissue fractions using T_1-weighted images taken at the same time as the MRS acquisitions. Our software uses Matlab and Python scripts to support Philips acquired data, we use independent alignment strategies and quantitate using Tarquin software instead of internal algorithms. Our segmentation dependency is on Freesurfer, rather than SPM, the major difference being that SPM produces binary masks and Freesurfer produces masks with variable grey scale values to represent probabilities of tissue type. Gannet aims to be the more complete analysis suite as

it supports more vendors and processes more of the analysis steps automatically using internal algorithms. Our approach was focussed on producing the most appropriate analysis for our particular experimental settings and this has allowed us to process our data using options that were not available elsewhere at the time we ran our experiments. This situation is subject to change however, as we note that some analysis options that were previously absent from Gannet have now been introduced and we would expect that further flexibility with regard to processing steps is likely to follow as the user base increases. At the time of writing there were still tasks and methodological choices that were easier to implement with our software, compared with Gannet. For example segmentation using MRI images acquired in different sessions was not possible using Gannet's automatic approach, which assumes that the subject is in the same physical position with regard to the scanner coordinate space.

We found that it was instructive to challenge some commonly held assumptions about how to approach the post-acquisition processing stages, as such assumptions were likely to form the default settings of alternative software suites. We therefore suggest that there is benefit in creating a pipeline such as the one outlined here that is flexible enough to test alternative processing approaches. For example, for work in later chapters, we will process our MEGA-PRESS scans using the automatic phase correction and independent alignment techniques mentioned above; we will use a double peak model for the quantitation stages, we will reference the water signal (taking account of the relaxation values appropriate for the tissue proportions) and we will concentrate on the grey matter GABA contribution to suit our hypothesis that grey matter GABA concentrations are involved in perceptual learning. All of these choices can be made because the testing that we have done suggests they are appropriate approaches to the data we have collected and the hypotheses we wish to test.

5

TIME COURSE OF TRAINING DIFFICULTY MEDIATED VISUAL LEARNING[1]

The main aim for this thesis is to investigate the neural correlates of inhibitory neurotransmitter and perceptual learning, we therefore sought a psychophysics paradigm that would evince dissociable learning as a step towards this aim. We reasoned that if we could design psychophysics paradigms that elicited dissociable learning, then we could use learning metrics from these experiments in correlative studies with MRS.

We prepared for the experiments described in this chapter by making some key decisions about a suitable experimental paradigm and then used a series of pilot experiments to optimise parameters to evoke dissociable learning performance in participants (see **Appendix B: Visual Learning Pilot Studies**). The first decision we made was to select Glass patterns as the stimulus type. Glass patterns are comprised of dots that can be manipulated to produce global shape patterns. This was important to us because we were particularly interested in cortical areas such as lateral occipital complex, which is involved with shape processing. In our pilot experiments we manipulated image parameters such as spiral angles and noise and found that we could parametrically alter the task difficulty of discrimination experiments through these

[1]This chapter is based on Garcia, Kuai, and Kourtzi (2013).

manipulations.

This led us to consider the effect of training difficulty on performance. We ran experiments where we compared learning performance as a function of training difficulty. We discovered that training schemes that subjects found more difficult elicited higher learning performance than training that was easier. We also varied the length of the tasks and extended them into multi session experiments so that we could better characterise the time course of learning. Results from these changes suggested that training difficulty evoked differences in performance over different time scales, for example *across* a single session compared with *between* sessions. We were interested in the time course of subject performance as we hypothesised that inhibitory processes might interact with learning in distinct ways across different time scales.

Learning is known to facilitate performance in a range of perceptual tasks. Behavioural improvement after training is typically shown after practice with highly similar stimuli that are difficult to discriminate (*Hard-Training*), or after exposure to dissimilar stimuli that are highly discriminable (*Easy-Training*). However, little is known about the processes that mediate learning after training with difficult compared to easy stimuli. Here we investigate the time course of learning where observers discriminated similar global form patterns after *Hard* versus *Easy-Training*. *Hard-Training* requires observers to discriminate highly similar global forms, while *Easy-Training* involves clearly discriminable patterns.

The aim for this chapter is to describe a multi-session, interleaved psychophysics paradigm that evokes dissociable learning performance as a function of training difficulty. In subsequent chapters we will use variations of this paradigm to investigate the correlations between psychophysics performance metrics versus concentration levels of GABA to probe the main hypothesis of the thesis.

5.1 Introduction

Training task difficulty has been identified as one of the main factors that contributes to training outcome (Ahissar & Hochstein, 1997; Z. Liu & Weinshall, 2000; J. Liu, Lu, & Dosher, 2012). It is widely believed that supervised training (i.e. training with feedback) on difficult tasks that require discrimination of highly similar stimuli improves participants' performance (Ball & Sekuler, 1987; Shiu & Pashler, 1992; Fahle & Edelman, 1993; Herzog & Fahle, 1997; Dwyer, Hodder, & Honey, 2004; Seitz, Nanez, Holloway, Tsushima, & Watanabe, 2006; Aberg & Herzog, 2012). However, there is accumulating evidence that training on *Easy* discrimination tasks, when stimuli are clearly discriminable, may also facilitate better performance in perceptual judgments (Ahissar & Hochstein, 1997; Rubin, Nakayama, & Shapley, 1997; Z. Liu & Weinshall, 2000; Jeter, Dosher, Petrov, & Lu, 2009; J. Liu, Lu, & Dosher, 2010; J. Liu et al., 2012).

Although these studies have suggested that *Hard* versus *Easy-Training* may relate to different learning processes, previous work has focused on assessing the final outcome of training rather than the time course of learning. Investigating the time course of learning-dependent improvements is important for understanding the processes that underlie learning based on *Hard* versus *Easy-Training*.

To address this question, we designed a stimulus space and a paradigm that allowed us to compare the time course of behavioural improvement during training on *Hard* versus *Easy* shape discrimination tasks. We used parametric manipulations of Glass patterns that comprised oriented dot dipoles. For these stimuli, small local changes to dot patterns have a predictable influence on the perception of global forms. We manipulated the difficulty of the training task by varying the similarity between global forms, using linear morphing between concentric and radial patterns. *Hard-Training* involved training on similar patterns, while

Easy-Training involved training on highly discriminable patterns. We assessed training outcome by testing observers on the discrimination of similar patterns without feedback. To monitor improvement of behavioural performance during *Hard* versus *Easy-Training* we interleaved training and test blocks within each session.

5.2 Materials and Methods

5.2.1 Participants

Thirty-six observers (16 male, 20 female, mean age 24 ± 6) participated in four experiments. None of the participants had prior experience with the stimuli or the study protocol. All of the participants had normal or corrected-to-normal vision, gave written informed consent and were paid for their participation. The study was approved by the University of Birmingham ethics committee.

5.2.2 Psychophysics

Stimuli. Glass pattern stimuli (Glass, 1969) were used, as previously described (Li, Mayhew, & Kourtzi, 2009). In particular, stimuli comprised of white dot pairs displayed within a square aperture ($7.7^\circ \times 7.7^\circ$) on a black background with 100% contrast. Each dipole comprised two dots (2.3×2.3 arc min^2) with 16.2 arc min separation between them. These parameters were chosen based on pilot psychophysical studies (**Appendix B: Visual Learning Pilot Studies**) and in accordance with previous work (H. R. Wilson & Wilkinson, 1998) that showed coherent form patterns were reliably perceived for these parameters.

We created *Easy-Training* and *Hard-Training* versions of radial and concentric shapes. We defined these by placing dipoles with respect to the circumference of a circle that was centred on a fixation dot (**Figure 5.1**). The angle between the dot dipole orientation and the radius, from the centre of the dipole to the centre of the stimulus aperture, defined the spiral

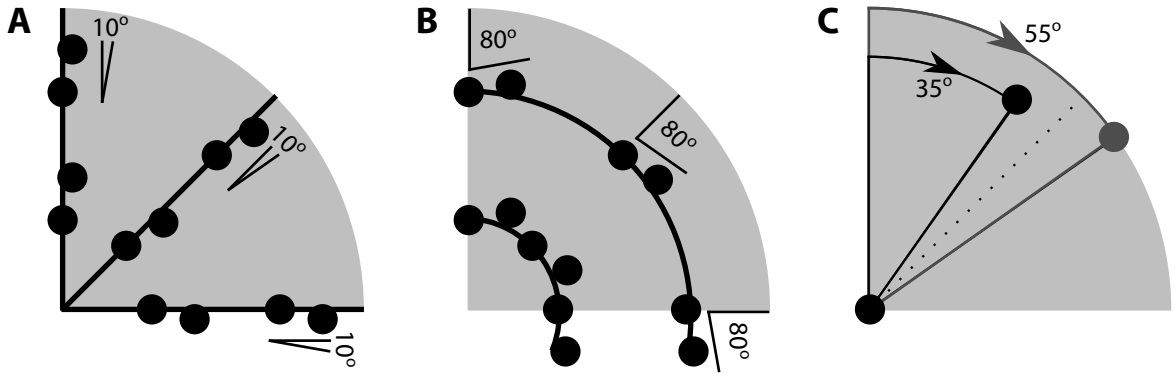

Figure 5.1: *Easy-Training* and *Hard-Training* spiral angles. (A) Radial, easily discriminable pattern (black lines), dipoles arranged with angles of 10° to the circumference. **(B) Concentric**, easily discriminable pattern, (black arcs), dipoles arranged with angles of 80°. **(C) *Hard-Training* radial and concentric**, less discriminable patterns, dipoles arranged with angles of 35° (radial) and 55° (concentric). Each pattern is 10° from the boundary between radial and concentric (dotted line).

angle. We parametrically altered the spiral angle to generate shapes that were characteristically more radial (spiral angles closer to 0°, **Figure 5.1A**) or concentric (spiral angles closer to 90°, **Figure 5.1B**). Sample *Easy and Hard* stimulus images are reproduced in **Figure 5.2**.

A 21-inch CRT monitor (1280×1024, 85 Hz frame rate) was used to display the images and all psychophysics experiments were conducted in low light conditions. We fixed the viewing distance at 47 cm with a chin rest. Stimulus images were generated and presented using Matlab (The MathWorks, Inc., Natick, Massachusetts, USA) and Psychtoolbox version 3 (Brainard, 1997; Pelli, 1997).

Procedure. We conducted four experiments. In *Experiment 1*, we randomly assigned 16 participants to an *Easy* or a *Hard-Training* group. In the *Hard-Training* group, observers were trained to discriminate Glass patterns with spiral angles of 35° (radial) and 55° (concentric). In the *Easy-Training* group, observers were trained to discriminate Glass patterns with spiral angles of 10° and 80°. Participants in both the *Hard* and *Easy-Training* groups were tested with spiral angles of 35° and 55°. Observers participated in three sessions conducted on consecutive days. Each session comprised four test blocks without feedback and three training blocks

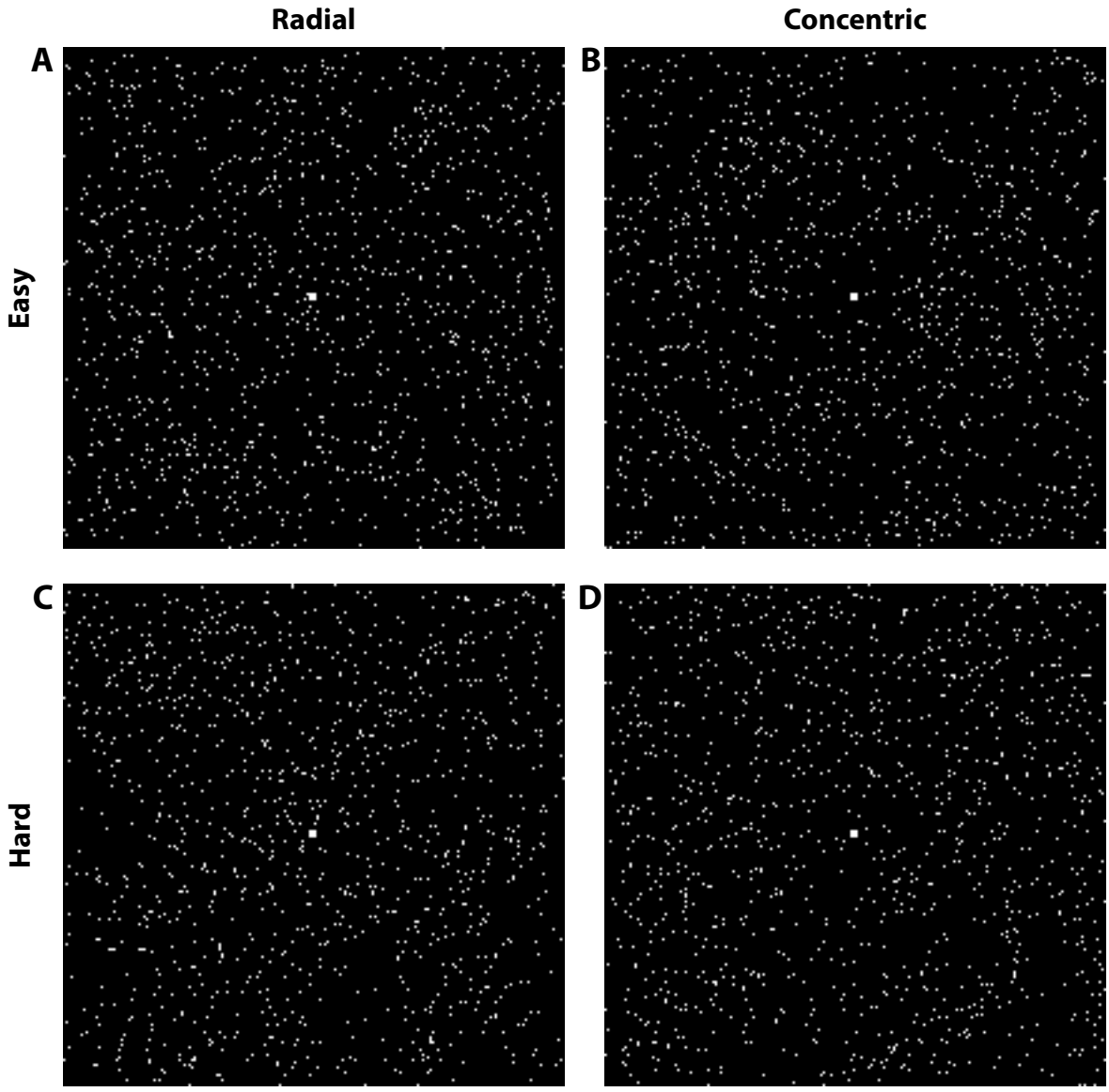

Figure 5.2: Stimulus images *Easy-Training* versus *Hard-Training*.[2] *Easy-Training* images: **(A)** radial 10°, **(B)** Concentric 80°. *Hard-Training* images: **(C)** radial 35°, **(D)** concentric 55°. The perceived size of these images when presented on screen was 70mm^2, this is the size that this figure is intended to reproduce if it is printed on standard A4 sized paper.

with auditory error feedback. The test and training blocks were interleaved during the session and the session started and ended with a test block. This design allowed us to characterise the time course of learning during each session rather than measure performance only before and after training. Each block consisted of 200 trials. In each trial, a stimulus image was presented for 200 ms and participants were required to judge whether the stimulus was radial, with a left mouse click, or concentric using a right mouse click. All experiments were self-paced, so non

responses were not possible as subsequent stimulus presentation was dependent on subject response. To avoid participant fatigue, participants took breaks of a minimum of 60 s after each 100 trials with a longer break of 180 s half way through the session. These precautions were introduced as a result of our observations from previous pilot studies.

In *Experiment 2* we tested whether lower performance after *Easy-Training* was due to the limited number of training sessions. Eight participants were trained for six to eight consecutive sessions. The same protocol and stimulus parameters were followed as in *Experiment 1*. For each individual participant, training stopped after performance had saturated. We defined performance saturation as the point at which performance levels in the learning metrics stopped increasing, whereas they had previously been rising.

For *Experiment 3* (n = 5) we controlled for the possibility that performance differences between the *Hard* and *Easy-Training* groups in *Experiment 1* were due to the fact that participants in the *Hard-Training* group were trained and tested with stimuli presented at the same spiral angles (35° vs. 55°). Participants were trained with stimuli presented at spiral angles of 40° vs. 50° and tested with stimuli presented at spiral angles 35° vs. 55°. That is, the training stimuli were more difficult to discriminate than the test stimuli.

In *Experiment 4* (n = 7), we controlled for the possibility that improved performance could result from learning during the test blocks rather than from supervised training. Participants were tested on stimuli presented at spiral angle of 35° vs. 55° (four test blocks as in *Experiment 1*) but were not trained with feedback on any additional blocks.

5.3 Results

5.3.1 *Experiments 1 and 2*: Behavioural Improvement Following *Hard* Versus *Easy* Training

In *Experiment 1*, we compared learning between *Hard-Training* (training to discriminate patterns at spiral angles of 35° vs. 55°) and *Easy-Training* (training to discriminate patterns at spiral angles of 10° vs. 80°). An Analysis of variance (ANOVA) of the training blocks (**Figure 5.3A**) showed that performance for the *Hard* task improved significantly across training sessions [F (1.2, 8.1) = 23.8, $p < 0.01$, Greenhouse-Geisser corrected], while performance for the *Easy* task was already at ceiling for the first training session and did not improve significantly across sessions [F (1.1, 7.5) = 3.6, $p = 0.09$, Greenhouse-Geisser corrected]. These results confirmed that discriminating patterns at spiral angles of 10° vs. 80° constituted an *Easy* task, while discriminating patterns at spiral angles of 35° vs. 55° constituted a *Hard* task that required additional training. Further, analysis of the test blocks (**Figure 5.3B**) showed that for both groups (*Easy* versus *Hard-Training*) participants improved significantly in discriminating between similar Glass patterns presented at spiral angles of 35° vs. 55° (test blocks) after three sessions of training. In particular, a repeated-measures ANOVA showed a significant main effect of session [*Pre-* vs. *Post-Training* session, F (1, 14) = 76.2, $p < 0.01$]. However, behavioural improvement was stronger following *Hard* rather than *Easy-Training* as was shown by a significant interaction [F (1, 14) = 9.8, $p < 0.01$] between-session (*Pre-* vs. *Post-Training*) and training task (*Easy* vs. *Hard*). According to the Student's t-distribution test, no significant differences [t (14) < 1, $p = 0.8$] in performance were observed before training in the first test block, which suggested that differences in post-training performance between *Easy* and *Hard-Training* could not be due to differences in baseline performance. These findings suggested that for the same amount of training, training on a *Hard* discrimination resulted in better performance than training on an *Easy* discrimination.

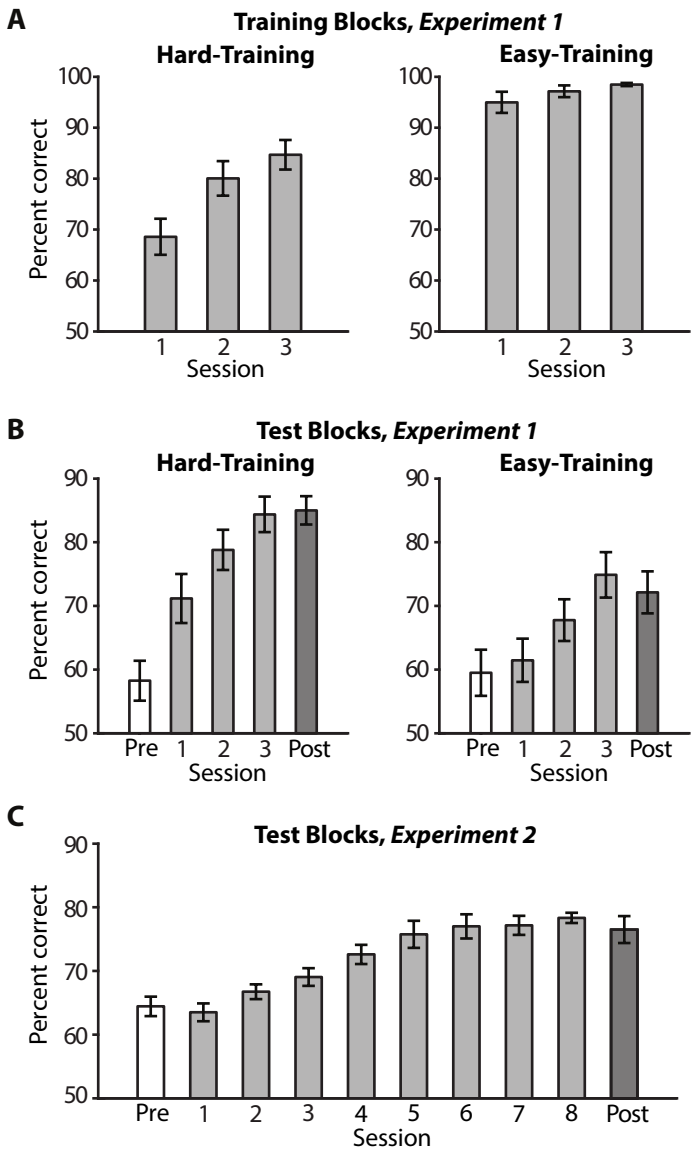

Figure 5.3: *Experiments 1 and 2* mean behavioural performance across participants for (A) training blocks in *Experiment 1*, (B) test blocks in *Experiment 1*, (C) test blocks in *Experiment 2*. (**A**) A post hoc t-test on the session means showed that performance was higher in the third session than first for *Hard-Training* [t (14) 3.52, $p < 0.01$], but this was not the case for *Easy-Training* [t (14) 1.67, $p = 0.06$].
(**B**) Comparing the performance in the Post and Pre runs showed that performance increases were significant in *Easy-* [t (14) 3.22, $p < 0.01$] and *Hard-Training* [t (14) 6.01, $p < 0.01$]. However, by comparing the difference of Post and Pre we confirmed that *Hard-* produced higher performance than *Easy-Training* [t (14) 2.52, $p < 0.01$].
(**C**) Performance increased significantly between Pre and Post [t (14) 4.01, $p < 0.01$], however performance did not increase significantly between session 5 and Post [t (14) –0.33, $p = 0.63$].

To test whether the lower improvement for *Easy* compared to *Hard-Training* was due to the limited amount of training (three sessions), we trained participants (n = 8) on the *Easy-Training* task for six to eight sessions (*Experiment 2*). Participants improved across sessions [F (2.1, 8.4) = 16.2, $p < 0.01$, Greenhouse-Geisser corrected] but performance flattened out on average after the fifth session (**Figure 5.3C**). Comparing post-training performance for shorter (*Experiment 1*) and longer (*Experiment 2*), *Easy-Training* protocols did not show any significant differences [t (14) = 1.11, $p = 0.28$]. Further, performance after longer *Easy-Training* was significantly weaker than performance for *Hard-Training* [t (14) = 2.8, $p = 0.02$],

which suggested possible limits in behavioural improvement for *Easy-Training*.

5.3.2 Learning Time Course for *Hard* Versus *Easy* Training

We investigated the time course of learning for *Hard* versus *Easy-Training* by plotting the participants' performance across test blocks in *Experiment 1* (**Figures 5.4A,C**). We observed different time courses for the two training procedures. For *Hard-Training*, discrimination performance increased within each of the first two sessions before reaching a plateau during the last session. In contrast, for the *Easy-Training* condition, there was no significant improvement within a session. However, performance increased between training sessions.

To quantify these observations, we defined *Within-* and *Between-Session* learning indices. The *Within-Session* learning index was calculated by subtracting mean performance in the first test block from mean performance in the last test block in each session. The *Between-Session* learning index was defined as the mean performance difference between the last block in the preceding session and first block in the subsequent session. We calculated the *Within-*

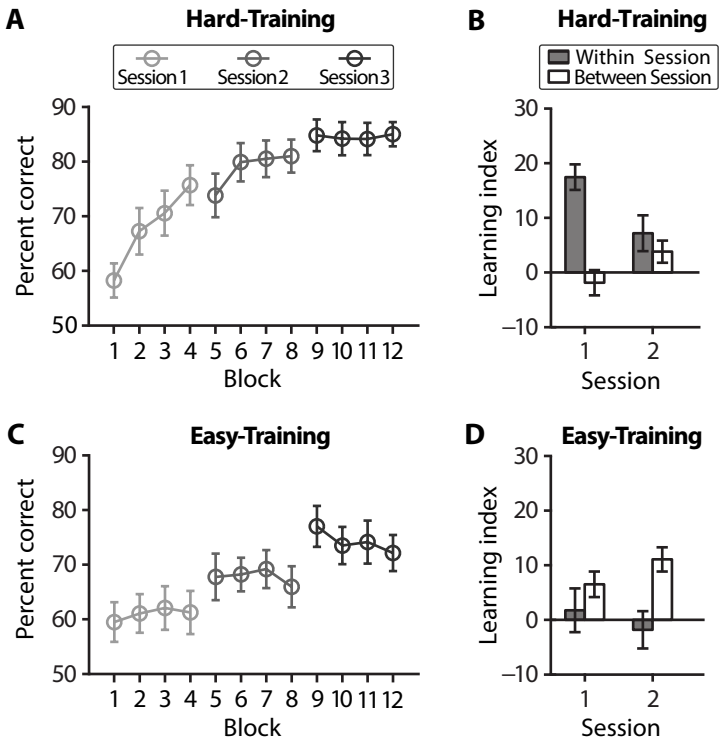

Figure 5.4: *Experiment 1* time course of learning. Mean behavioural performance across participants per block for **(A)** *Hard* and **(C)** *Easy-Training*. We calculated *Within-* and *Between-Session* learning indices **(B)** *Hard* and **(D)** *Easy-Training*. The *Within-Session* index was calculated by subtracting the mean performance in the first test block from the last test block in a session. The *Between-Session* index was calculated as the mean performance difference between the last test block in the preceding session and first test block in the subsequent session. Error bars indicate the standard error of mean across participants.

and *Between-Session* learning indices for the first two sessions, as there was no subsequent session to calculate this index for the third session (**Figures 5.4B,D**). A repeated measures ANOVA showed a significant interaction [F (1, 14) = 10, $p < 0.01$] between learning index (*Within-* vs. *Between-*) and training task (*Easy* vs. *Hard*), consistent with stronger *Within-Session* learning for *Hard-Training* [F (1, 14) = 10.7, $p < 0.01$] and stronger *Between-Session* learning for *Easy-Training* [F (1, 14) = 7.7, $p = 0.02$].

ANOVA is usually used to show differences in means and so some explanation may be required to explain why we think it addresses hypotheses about the temporal evolution of participant performance (where regression analyses might be more commonly applied). While ANOVA does not take into account explicit ordering of independent variables, in this analysis the temporal ordering is implicit in the learning index, which is a measure of the temporal evolution of participant performance. The ANOVA does not compare means of performance, but compares means of temporal evolution, with independent variables of *Within-* and *Between-Session* learning and training difficulty.

To support the use of ANOVA described here, we also conducted regression analyses using the blocks to predict gradients for *Within-* and *Between-Session* performance. The *Within-*

Table 5.1: Regression *Within* sessions, *Hard* and *Easy* training. The (**Within 1**) is fitted to blocks 1 through to 4, (**Within 2**) uses blocks 4 to 9, and (**Within 3**) uses blocks 8 to 12. The metrics tabulated are the estimated **Gradient** of the regression using the relevant blocks, the 95% confidence intervals (**CI**) and the significance (**p**). The regression analysis showed improvement for *Hard Training* **Within 1** and **Within 2** but no significant improvement for the first two sessions in the *Easy Training*. Predictions from the **Within 1** model extrapolated to block 5 overlap with predictions from the **Within 2** model for *Hard* training but not *Easy* training (and likewise for the **Within 2** models extrapolated to block 9). The gradients and extrapolations of performance support the ANOVA findings for the *Within-Session* index in **Figure 5.4**.

	Hard Training			**Easy Training**		
	Gradient	**CI**	**p**	**Gradient**	**CI**	**p**
Within 1	5.56	[4.41, 6.98]	< 0.01	0.63	[-1.32, 2.57]	0.52
Within 2	2.22	[0.68, 3.76]	< 0.01	-0.44	[-2.09, 1.21]	0.59
Within 3	0.05	[-0.91, 1.01]	0.92	-1.40	[-2.38, -0.42]	< 0.01

Table 5.2: Regression *Between* sessions, *Easy* and *Hard* training. In the *Easy Training* the gradients were positive and statistically significant for both **Between 1–2** (fitted to blocks 4 and 5) and **Between 2–3** (fitted to blocks 8 and 9). The regressions for *Hard Training* were not significant between sessions. These results support the ANOVA findings for the *Between-Session* index in **Figure 5.4**.

	Hard Training			Easy Training		
	Gradient	**CI**	**p**	**Gradient**	**CI**	**p**
Between 1–2	-1.88	[-6.52, 2.77]	0.40	6.50	[1.81, 11.19]	0.01
Between 2–3	3.81	[-0.25, 7.87]	0.06	11.06	[6.62, 15.50]	< 0.01

Session gradients (**Table 5.1**) are overall more positive for *Hard-* than for *Easy-Training*, while the *Between-Session* gradients (**Table 5.2**) are overall more positive for *Easy-* than for *Hard-Training*. These findings are consistent with differences in simple effects that contribute to the significant interaction indicated by the ANOVA analysis. The regression analysis reveals which sessions contribute more to the difference in *Within-Session* simple effects (i.e. positive/neutral changes in performance for *Hard-Training* compared with negative/neutral changes for *Easy-Training*). Likewise the *Between-Session* gradients reveal which pairs of sessions contribute more to the difference in *Between-Session* simple effects.

5.3.3 *Experiment 3*: *Hard* Training With Different Stimuli Than Testing

In *Experiment 3*, we trained and tested participants in a *Hard* discrimination but with stimuli presented at different spiral angles. The aim of this experiment was to control for the possibility that performance differences between *Hard* and *Easy-Training* in *Experiment 1* were due to the fact that participants in the *Hard-Training* group were trained and tested with stimuli presented at the same spiral angle (35° vs. 55°), while participants in the *Easy-Training* group where trained and tested with stimuli presented at different spiral angles. In particular, we tested participants with stimuli presented at spiral angles of 40° vs. 50° and tested with stimuli presented at spiral angles of 35° vs. 55°. We observed a similar pattern of results (**Figure 5.5**) as for *Hard-Training* in *Experiment 1* (**Figure 5.4**). That is, behavioural

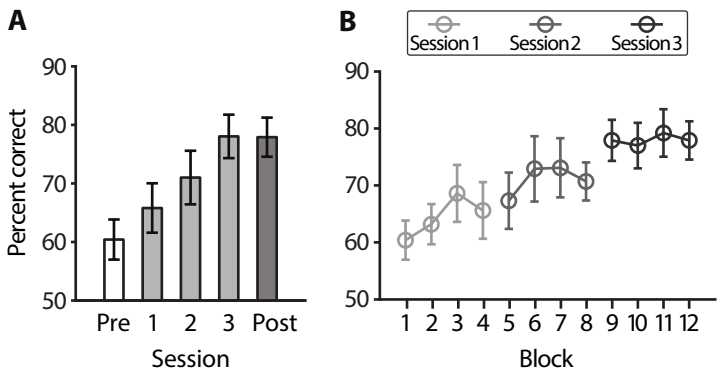

Figure 5.5: *Experiment 3*. Mean performance across participants per **(A)** session and **(B)** block when participants were trained with stimuli at spiral angles of 40° vs. 50° that differed from the test stimuli (35° vs. 55°). Error bars indicate the standard error of mean across participants.

performance improved within sessions 1 and 2 and appeared to have reached its maximum in session 3. In particular, a repeated measures ANOVA showed no significant interaction [F (1, 11) = 2.6, p = 0.14] between learning index (*Within-* vs. *Between-Session*) and Experiment (*Experiment 1* vs. *3*). These results suggested that differences in the time course of learning for *Easy* vs. *Hard-Training* were due to differences in the difficulty of the training rather than the similarity of the stimuli used for these two training protocols.

5.3.4 *Experiment 4*: Learning Without Feedback

To control for the possibility that improved performance resulted from exposure to the test stimuli rather than training with feedback, we tested participants on the same number of test blocks (n = 7) as in *Experiment 1* (participants were presented with stimuli at spiral angle of 35° vs. 55° without feedback) but did not expose them to any training blocks with feedback (**Figure 5.6**).

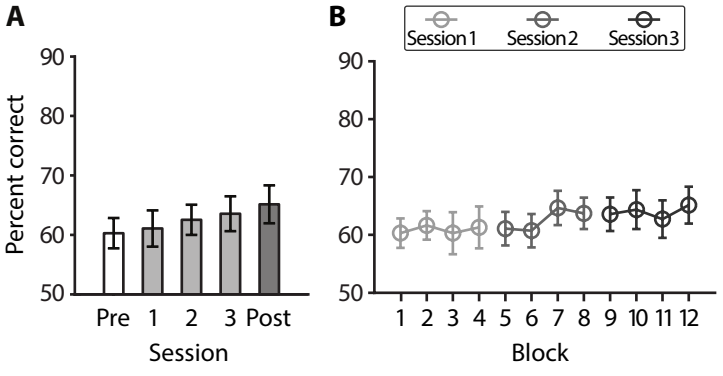

Figure 5.6: *Experiment 4* no training blocks. Mean performance across participants per **(A)** session and per **(B)** block when only test but no training blocks were included in each session. Error bars indicate the standard error of mean across participants.

Our results showed that the observers' performance did not improve significantly across sessions [F (4, 24) = 1.8, p = 0.17] and that post-training performance was significantly lower without (*Experiment 4*) than with (*Experiment 1*) training [t (13) = 5.2, $p < 0.01$]. These results suggested that training with feedback rather than mere exposure to the stimuli was required for improvement in the discrimination of similar global form patterns.

5.4 Discussion

Our results demonstrated differences in the time course of learning for *Hard* versus *Easy-Training*. In particular, training on a *Hard* discrimination resulted in stronger behavioural improvement than training on an *Easy* discrimination. Interestingly *Hard-Training* performance improved within the time course of a single session, while for *Easy-Training* performance improved across but not within sessions. These findings suggested differences in the processes that underlie learning based on *Hard* versus *Easy-Training*. Training on a difficult task supported continuous and strong improvement in the discrimination of specific features that were similar between training and test (i.e. observers were asked to discriminate highly similar stimuli in both the training and test). However, training on an *Easy* task required transfer of learning, as stimulus features differed between the stimuli used for training (highly discriminable) and test (highly similar). As a result, behavioural improvement was lower following *Easy* compared with *Hard-Training* and may have required consolidation across sessions.

Underlying the explanations in this discussion are the actual mechanisms, that is the low-level neurobiological responses that occur during learning. These mechanisms entail excitation and suppression of activation through the chemical modulation of excitatory and inhibitory neurotransmitters. The experiments described in this chapter did not measure any

of these mechanisms directly and so any attempts to link them to the psychophysics results would be purely speculative. However, these results suggest dissociable learning performance and so we hypothesise that the experimental paradigm described in *Experiment 1* might be suitable for further investigations of the mechanisms. For example by measuring inhibitory neurotransmitter concentration in brain regions associated with the task we might be able to discover a link between inhibitory mechanisms and between-session learning.

These psychophysics results suggest that the experimental paradigm should be suitable to further probe the mechanisms responsible by correlating the results with measurements of neurotransmitter concentration. This is the subject of **Chapter 6: GABA Versus Training Difficulty Mediated Visual Learning**.

6

GABA VERSUS TRAINING DIFFICULTY MEDIATED VISUAL LEARNING

6.1 Introduction

We have previously demonstrated dissociable learning performance under *Easy and Hard-Training* conditions using psychophysics experiments over several sessions (**Chapter 5: Time Course of Training Difficulty Mediated Visual Learning**). Specifically a between-session learning mechanism based on consolidation and transfer was suggested for the *Easy* condition and a within-session online learning mechanism was suggested for the *Hard-Training* condition.

Here, we investigate the dissociable learning mechanisms further by measuring the GABA concentration levels of participants who undertook the same psychophysics training as in the main experiment in the previous chapter. Our hypothesis was that learning performance would be correlated with GABA concentrations in visual shape processing regions and higher cortical regions of the brain, and that this would infer the dissociable learning mechanisms to be GABAergic inhibitory processes.

6.2 Materials and Methods

6.2.1 Participants

Sixteen subjects (10 male, 6 female, mean age 21 ±3) participated in visual shape learning tasks and resting state MR scans. All of the participants were agnostic to the study protocol and visual stimuli patterns and each had normal, or corrected-to-normal vision. The University of Birmingham ethics committee approved the study. All participants gave written, informed consent and were paid for their participation. Participants completed questionnaires to ascertain nicotine, alcohol and pharmaceutical levels. We reviewed all questionnaire responses and concluded that the MRS and performance results were unlikely to be affected by these factors.

6.2.2 Psychophysics

The stimuli consisted of *Easy-Training* and *Hard-Training* versions of radial and concentric Glass patterns, which we created using identical methods to those described in **Section 5.2.2**, in the previous chapter (**5: Time Course of Training Difficulty Mediated Visual Learning**).

Procedure. The participants were randomly assigned to either an *Easy-Training* or a *Hard-Training* shape learning task. This resulted in eight participants on the *Easy* and eight on the *Hard* learning paradigms.

We arranged the psychophysics element of the experiment over three sessions, which we conducted on consecutive days. Individual sessions consisted of four test blocks without feedback and three training blocks with feedback (**Figure 6.1**). The feedback consisted of audible error warnings after each trial. We interleaved the test and training blocks in pairs to allow the time course of learning to be monitored. Each block consisted of 200 trials and stimulus presentation lasted for 200 ms. Subjects were required to categorise the visual stimuli as

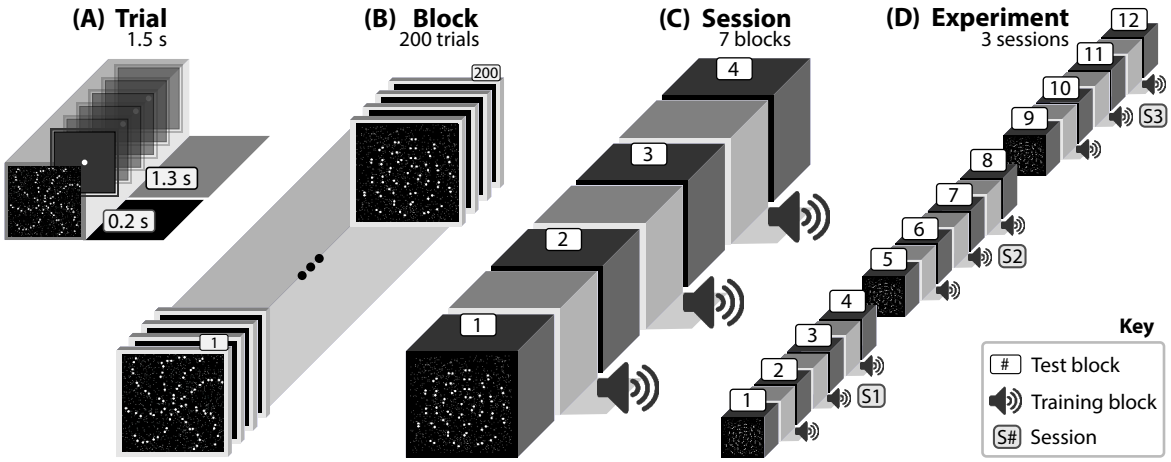

Figure 6.1: Psychophysics design *Easy* versus *Hard-Training*. A single trial **(A)** consisted of stimulus presentation for 200 ms followed by subject response. The next trial cannot start until a subject has made a response, and will wait for a minimum of 1.3 s. Trials were arranged in groups of 200, which constituted a block **(B)**. We interleaved 4 test blocks and 3 training blocks (with feedback) to make a session **(C)**. Three sessions were run over consecutive days **(D)**.

radial or concentric shapes after each stimulus presentation with mouse clicks; left for radial and right for concentric. After each block and half way through each block, subjects were given breaks from the task. The duration of the breaks was determined by the participants, but minimum breaks of one minute were enforced to help ameliorate the effects of fatigue on the subjects' performance.

Behavioural Indexes. Each trial i within block j elicited a correct or incorrect response from the participants, evaluated as c_j^i.

$$c_j^i = \begin{cases} 1, & \text{if response to trial } i \text{ of block } j \text{ is correct} \\ 0, & \text{if response to trial } i \text{ of block } j \text{ is incorrect} \end{cases}$$

From this we calculated the percent correct metric PCB_j, for block j, comprising n_j stimulus presentations (**Equation 6.1**). When used across all subjects, this metric simply represents

the mean correct response scores for a block.

$$PCB_j = 100 \times \frac{1}{n_j} \sum_{i=1}^{n_j} c_j^i \tag{6.1}$$

All blocks comprised 200 trials, so for the kth session comprising a set of blocks S_k, we calculated the percentage correct per session PCS_k using the unweighted average of the percentage correct per block (**Equation 6.2**). When used across all subjects, this metric simply represents the mean correct response scores for a session.

$$PCS_k = \frac{1}{|S_k|} \sum_{j \in S_k} PCB_j \tag{6.2}$$

Using *PCB* and *PCS* we calculated three behavioural indexes through which we investigated the psychophysics findings of the previous chapter: *Between Session Index, Overall Learning Index and Normalised Mean Index*.

Between Session Learning Index. This metric replicates the one used for measuring the *Easy-Training Between-Session* learning effect reported in Garcia et al. (2013). We calculated it (**Equation 6.3**) by subtracting the percent correct in the last test block of the second session (block 8, **Figure 6.1D**) from that in the first test block from the third session (block 9).

$$BetweenSessionIndex = PCB_9 - PCB_8 \tag{6.3}$$

In Garcia et al. (2013) we concluded that the performance increases between sessions involved consolidation learning away from the stimuli, possibly requiring sleep between sessions. Our rationale for using the *Between Session Learning Index* was to use it to represent

this observed learning performance difference between the *Easy* and *Hard* training conditions. Another reason for using this metric is that it represents the largest between-session learning effect that the *Easy-Training* condition produced in the previous experiments.

The Overall Learning Index. We used this metric to characterise the learning effect over all three sessions. It made use of the performance in the first and last test blocks (numbered 1 and 12 in **Figure 6.1D**). By using the first and last test blocks in the calculation, our intention was to represent the difference between the pre-training test block and the post-training test block. We used this metric, rather than the simple difference between post and pre blocks, to account for differences in starting performance. We reasoned that low starting performance might unduly accentuate the magnitude of performance increase. As starting performance is not influenced by the training we divided the difference of post and pre by the sum of post and pre (**Equation 6.4**) to ameliorate the apparent increased performance that low initial scores might engender.

$$OverallLearningIndex = \frac{PCB_{12} - PCB_1}{PCB_{12} + PCB_1} \tag{6.4}$$

Normalised Learning Index. We used the percent correct metric in test block one (PCB_1) to represent the pre-training performance. We calculated the *Normalised Learning Index* by subtracting the percent correct in the first session $S_1 = \{B_2, B_3, B_4\}$ from the percent correct of the last session $S_3 = \{B_9, B_{10}, B_{11}, B_{12}\}$, where B_j denotes block j. Note that S_1 does not include block B_1 as this is used to evaluate pre-training performance. We divided both mean

session values by the pre-training performance PCB_1 (**Equation 6.5**).

$$NormalisedMeanIndex = \frac{PCS_3 - PCS_1}{PCB_1} \tag{6.5}$$

Our rationale for using this metric was to represent the higher learning performance in the *Hard-Training* condition that we observed, compared with the *Easy-Training* condition, but using whole session, rather than just the post and pre blocks.

6.2.3 MRS Acquisitions

Regions of Interest. We selected ROIs for the MRS acquisitions to correspond with lateral occipital areas and higher cortical areas (mid frontal gyrus), in addition to a control voxel in the motor cortex region (**Figure 6.2**). These ROIs were selected following pilot fMRI experiments that showed interesting activation patterns during Glass pattern localiser sessions, which we described in **Section 3.4: Regions of Interest**. As the activation patterns showed symmetry across the hemispheres, we obtained two MRS acquisitions per ROI (one in each hemisphere). For each subject the final quantitated GABA measurement was the mean of the two measurements.

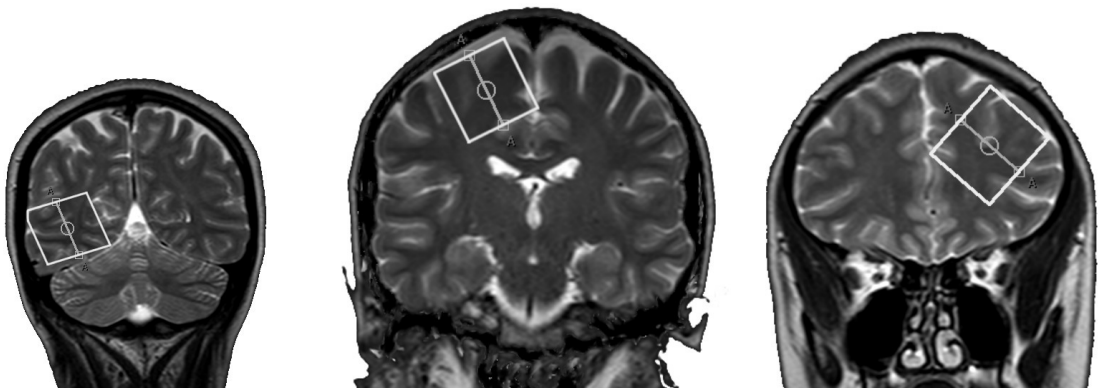

Figure 6.2: Regions of interest. MRS acquisition voxels (highlighted boxes) for lateral occipital, motor cortex and mid frontal gyrus, respectively. Coronal view T_2 weighted images.

MRS Parameters. The main MRS parameters (**Section 3.2: Acquisition Parameters**) were: TR = 1800 ms, TE = 68 ms, volume = 30 mm^3, samples = 2048, spectral bandwidth = 2150, dynamic scans = 32, phase cycles = 16, water suppression = VAPOR. This led to a scan duration time of 921.6 s (15 min 21.6 s) per acquisition. We also obtained a water unsuppressed acquisition with a standard PRESS pulse sequence for each MEGA-PRESS acquisition; phase cycles=8, dynamic scans=1. We used a 3T Philips Achieva scanner (Philips Healthcare, Best, Netherlands) to obtain the MRI and MRS data.

MRS Scans Sequence. Voxel planning was completed using T_2 anatomical images acquired in three planes (24-36 slices per plane), we also obtained 3-D high resolution (1 mm) T_1-weighted images for each subject. The scans were at resting state so there was no task to perform during scanning. We randomised the order in which we acquired the regions of interest. Scanning took place over two to three sessions, which occurred after the psychophysics testing. PRESS acquisition used identical voxel positioning as the MEGA-PRESS acquisitions and automatic shimming was performed for all scans.

MRS Processing. We converted the time domain signals to frequency domain spectra using the fast Fourier transform (**Section 4.3: Time Domain Signals**). We phase corrected the spectra using an automatic algorithm (**Section 4.4: Phase Correction**) and applied subspectral realignment based on an independent alignment scheme (**Section 4.5: Subspectral Shifting**). We used segmentation techniques (**Section 4.7: Segmentation**) on the high resolution T_1 anatomical MRI images to obtain tissue proportion estimates for each scan. We averaged the realigned subspectra and combined them by subtracting the edit OFF spectra from the edit ON spectra (**Section 2.5.4: MEGA-PRESS Pulse Sequence**). We used Tarquin to quantify the processed spectra (Reynolds et al., 2006), which used a double peak model (**Section 4.6: Peak**

Modelling) for the GABA signals centred at 3.01 ppm to produce a GABA+ measurement scaled to the unsuppressed water acquisition. We applied a correction factor (**Equation 4.3**) to the measurements and a scaling factor to account for the grey matter contribution to the measured GABA+ (**Equation 4.7**).

6.3 Results

We arranged our results in the following order: We assessed the MRS measurements by examining the signal to noise ratio (SNR) and Cramér-Rao lower bounds (CRLB) of the spectra. We also inspected the scans for identifiable peaks around 3.01 ppm in the combined (edit ON minus edit OFF) sequences.

We compared the subjects' performance on the *Easy* versus *Hard* experiments by examining the correlations between the GABA measurements and the psychophysics performance metrics, which we defined in **Section 6.2.2: Behavioural Indexes**. We set the significance level for rejecting the null hypothesis to $p < 0.05$ for all correlations and calculated 95% confidence intervals using a bootstrapping procedure with 1000 resamples.

6.3.1 MRS Spectra

Two subjects failed to complete the full scan schedule and therefore the sample size for two of the results were reduced from eight to seven. We assessed the quality of each spectrum by examining the signal to noise ratio (SNR) and the Cramér-Rao lower bounds. Mean values by region of interest are listed in **Table 6.1**.

Table 6.1: Mean signal to noise ratio and Cramér-Rao lower bounds. Mean values for acquisitions measured from the lateral occipital, mid frontal gyrus and motor cortex (control) regions.

Measurement	Lateral Occipital	Mid Frontal Gyrus	Motor Cortex
SNR	35.6	45.3	37.6
CRLB	3.6	4.7	4.7

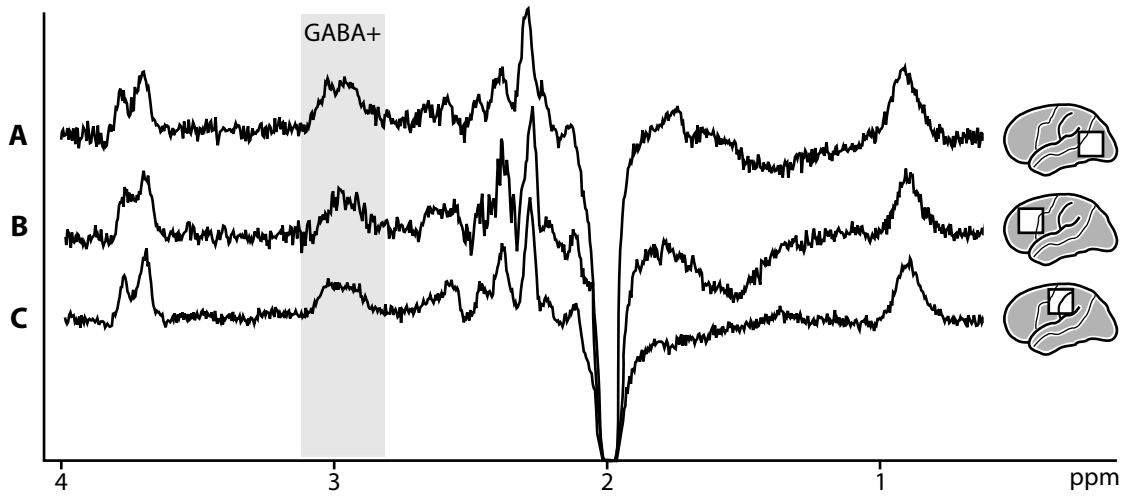

Figure 6.3: Representative spectra from three scans. (**A**) lateral occipital, (**B**) mid frontal gyrus, (**C**) motor cortex. GABA+ peaks highlighted on chart. Approximate ROIs shown as white shapes on the sagittal view brain cartoons.

GABA peaks at 3.01 ppm were reliably observed in the acquisitions, with representative spectra reproduced in **Figure 6.3**.

6.3.2 Correlates of GABA and Training Difficulty

In **Chapter 5: Time Course of Training Difficulty Mediated Visual Learning**, the interesting findings for psychophysics performance results for this paradigm were the between-session learning for the *Easy-Training* condition and stronger overall performance for the *Hard-Training* condition. We therefore concentrated on metrics that reflected those findings for the correlation study.

The psychophysics metrics were the *Between Session Index* for the *Easy-Training* experiment and for the higher performance in the *Hard-Training* we used the *Overall Learning Index* and the *Normalised Mean Index*.

In the *Easy-Training* condition we examined the correlation between GABA+ in the lateral occipital region and the *Between Session Index* (**Figure 6.4**). This showed a very strong correlation (r=.96, p=<.01), which was not evident in the *Hard-Training* condition for the

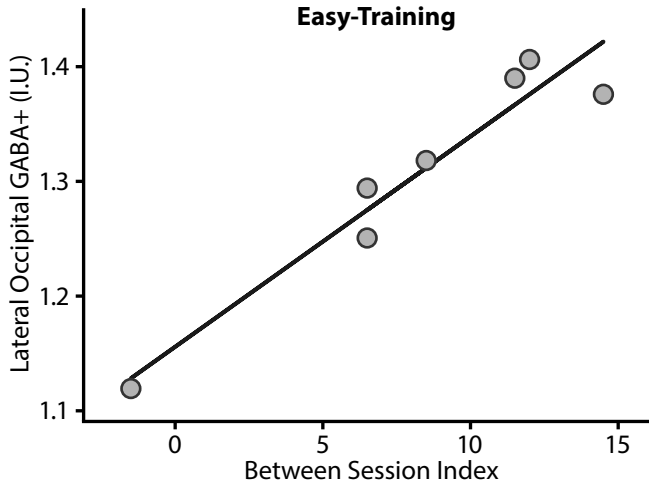

Figure 6.4: *Easy-Training* condition: Correlation between lateral occipital GABA+ versus *Between Session Index*. Strong positive correlation (r=.96, 95% CI=[.76 .99], p=<.01). The GABA measurement was expressed as GABA+ to indicate that it contained contributions from macromolecules and was scaled in institutional units.

same ROI (r=.43, p=.29). The correlation indicated that the dissociable learning mechanism inferred by the previous psychophysics learning results were connected with the GABAergic processing that was shown in the *Easy-Training*, but absent from the *Hard-Training*. The correlation for the control voxel (motor cortex) and GABA+ was not significant in the *Easy-Training* condition (r=.54, p=.28) or the *Hard-Training* condition (r=.12, p=.65).

In the *Hard-Training* condition we examined the correlation between the frontal region GABA+ and the Overall Learning Index (**Figure 6.5**). This showed a strong correlation (r=.72, p=.04) that did not exist in the *Easy-Training* condition for the same ROI (r=.42, p=.31). This suggested that GABA+ mediated the overall learning in the *Hard-Training* as higher concentrations of frontal cortex GABA+ predicted improved performance in visual learning. The

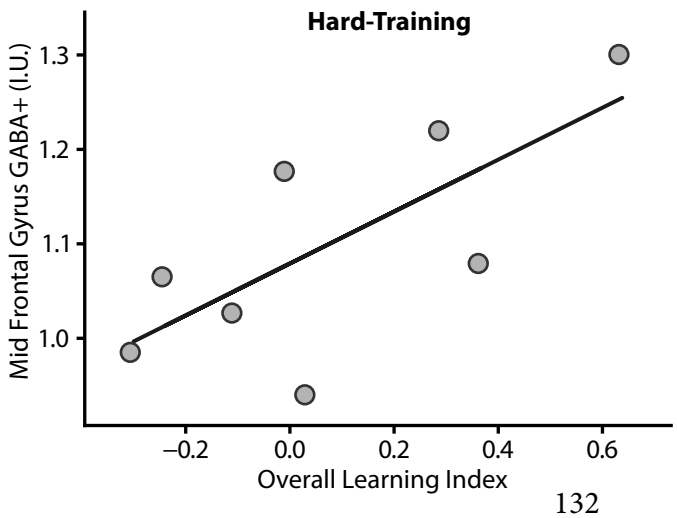

Figure 6.5: *Hard-Training* condition: Correlation between frontal region GABA+ versus *Overall Learning Index*. Strong positive correlation (r=.72, 95% CI=[.15 .97], p=.04). The GABA measurement was expressed as GABA+ to indicate that it contained contributions from macromolecules and was scaled in institutional units.

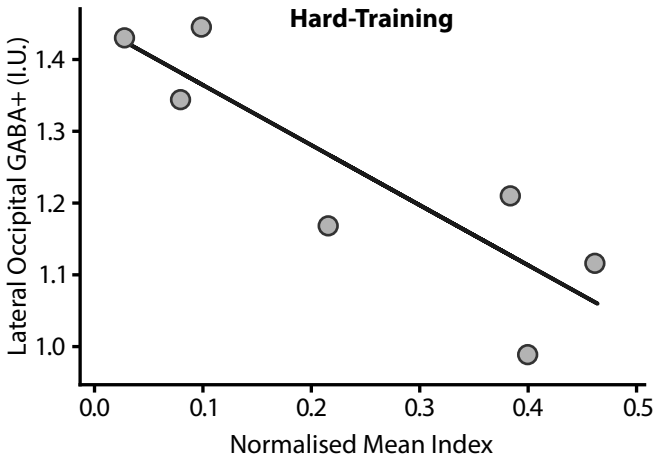

Figure 6.6: Correlations *Hard-Training* condition: Lateral occipital region GABA+ versus *Normalised Mean Index*. Strong negative correlation (r=–.87, 95% CI=[–.97 –.27], p=.01). The GABA measurement was expressed as GABA+ to indicate that it contained contributions from macromolecules and was scaled in institutional units.

correlation for the control voxel (motor cortex) was not significant in the *Easy-Training* condition (r=.52, p=.24) or the *Hard-Training* condition (r=.49, p=.28).

We also investigated the correlation between the GABA+ measurements and the *Normalised Mean Index* (**Figure 6.6**). This revealed a strong, negatively correlated relationship (r=–.87, p=.01) in the *Hard-Training* condition. In the *Easy-Training* condition for the same ROI we could not reject the null hypothesis (r=.30, p=.56). This was also the case in the control voxel (motor cortex) in the *Easy-Training* condition (r=.19, p=.72) and the *Hard-Training* condition (r=–.48, p=.28).

The negative correlation in lateral occipital region (**Figure 6.6**) contrasted with the positive correlation in the frontal region (**Figure 6.5**) for the visual learning metrics in the *Hard-Training* condition. The negative correlation also contrasted with the positive correlation for the lateral occipital region versus the *Between Session Index* in the *Easy-Training* condition (**Figure 6.4**).

6.4 Discussion

The psychophysics learning results from the previous chapter showed that for *Easy-Training* there was a transfer consolidation for between-session learning. For the *Hard-Training*, higher

final performance indicated better visual learning than was achieved for *Easy-Training*. We investigated the correlations between psychophysics metrics that characterised the different performance versus GABA+ measurements. This was to see if a link might exist between inhibitory neurotransmitter concentrations and learning performance according to *Easy and Hard* training.

We considered how these hypothesised links might be consistent with theories concerning the competition between bottom-up and top-down mechanisms. In these theories it has been suggested that bottom-up attention is organised by occipital visual stimuli representations and that top-down attention is mediated through the inhibition of irrelevant stimuli in prefrontal areas (Desimone, 1998). Accordingly, increased GABA concentrations would indicate a greater inhibitory potential and decreased GABA concentrations would suggest less inhibition and the possibility that more signal is propagated through the relevant cortical circuits. In this way we hypothesised that feedforward models of cognition would be supported by evidence of reduced GABA in visual areas and top-down models would correspond with increased GABA in higher cortical areas, such as frontal cortex.

Bottom-up processing represents a central idea of sensory information processing and is based on the transmission of signal through a hierarchy of cortical areas traversing progressively more complex aspects of the visual scene in a feedforward manner. These cortical circuits begin in the primary visual cortex and ascend through two main pathways; one is dorsal and involves attentional control and the other is ventral and is linked to object recognition.

Superimposed on these bottom-up pathways is the top-down, re-entrant pathway that conveys higher order information to antecedent cortical areas. These feedback pathways set up countercurrent streams of processing, with resulting percepts reflecting the set of functional states of all the areas in the visual cortical hierarchy (Gilbert & Li, 2013). As we men-

tioned in the introduction to this thesis, the functional properties of neurons are not fixed, instead they can be characterised as adaptive processors that modulate their function according to behavioural context and the demands of different perceptual tasks. Top-down therefore refers to the influence exerted by higher-order representations on earlier stages in the processing of visual information. In the context of our work higher-order refers to frontal cortical regions and the earlier stages are the visual cortex. Additionally, top-down modulation has a role in the encoding and recall of learned information.

Discussions of bottom-up and top-down mechanisms in learning, linked to *in vivo* GABA measurements have started to appear in the literature. Edden et al. (2009) speculated that individuals with higher GABA may have increased inhibitory control on feedback processes for example. Sandberg et al. (2013) have suggested that GABA is involved in the selective suppression of irrelevant information, or alternatively that it influences the specificity of neural representations in the visual cortex to improve attentional modulation.

One consequence from the accumulating body of literature on plasticity in the visual system is that there is not an exclusive locus for this plasticity. Rather, learning is distributed across cortical circuits using recurrent mechanisms that support adaptive processing, according to task context and demands (Kourtzi & DiCarlo, 2006). This, combined with the oft stated comment that the neural mechanisms that mediate experience dependent plasticity remain largely unknown gives scope to use MEGA-PRESS experiments to suggest both locus and mechanism to explain observed learning effects and GABA correlations.

6.4.1 Occipital Transfer Effects for *Easy-Training*

For *Easy-Training* the lateral occipital (visual processing) region GABA was very strongly, positively correlated with the *Between Session Learning Index* (**Figure 6.4**), but not in the

Hard-Training condition. This indicated that the dissociable mechanism was linked to a higher concentration of GABA+ in a visual processing region. Easy training has been suggested to generalise more to new stimuli than hard training does (Ahissar & Hochstein, 1996) and we hypothesised that learning transfer effects might be involved in the learning mechanism. This could explain why in the *Easy-Training* paradigm learning did not occur within-session, but did so across-session. The idea of across-session transfer suggests consolidation during sleep. This has been shown to enhance perceptual learning (Karni, Tanne, Rubenstein, Askenasy, & Sagi, 1994; Mednick, Nakayama, & Stickgold, 2003) and in particular to modulate learning specificity (Yotsumoto et al., 2009). We suggest therefore that the results for the *Easy-Training* condition inferred a GABAergic inhibitory modulation in occipital regions that promoted a between-session learning effect based on consolidation and transfer effects.

6.4.2 *Hard-Training*: Occipital Bottom-Up and Frontal Top-Down Correlates

For the *Hard-Training* condition the GABA+ concentrations in two ROIs were strongly correlated with performance indices that showed the total learning effect. The first was the strong positive correlation between the frontal region versus the *Overall Learning Metric* (**Figure 6.5**). There was no correlation for the same ROI and learning metric in the *Easy-Training* condition. The second strong correlation, this time negative, was between GABA+ in the lateral occipital region versus the *Normalised Mean Index* (**Figure 6.6**). Again, we did not detect a correlation for these variables in the *Easy-Training* condition.

This is an interesting observation as it shows a very strong negative correlation in the lateral occipital region in the *Hard-Training* overall learning, which contrasts with the strong positive correlation in the same ROI for the *Easy-Training* within-session learning. We suggest that this indicates that inhibitory processes mediate learning using different mechanisms

that are task dependent. This is in addition to the finding that inhibitory processes meditate learning in a region of interest dependent manner; as was shown by the contrast in correlations between GABA concentrations in occipital and frontal areas versus the learning metrics. The higher learning performance in the *Hard-Training* paradigm may have occurred through real-time weight adjustment from feedback in the training sessions, where the stimuli were the same as the testing sessions (Petrov, Dosher, & Lu, 2005). The strong positive correlation between GABA concentrations in mid frontal gyrus and the higher learning performance would seem to indicate a plausible locus for this re-weighting feedback mechanism.

6.4.3 Inhibitory Correlates in *Easy-* Versus *Hard-Training*

For the *Easy-Training* between-session learning that was shown in the psychophysics results, we suggest that the learning mechanisms are linked to inhibitory, bottom-up processing in lateral occipital (shape discriminating) visual areas.

For the overall learning effect that accrued from the *Hard-Training* paradigm the picture was a little more complicated as there was both a positive correlation with performance metrics and mid frontal gyrus GABA+ and a negative correlation with lateral occipital GABA+.

With the positively correlated GABA+ in mid frontal gyrus we might be tempted to conclude that this indicated a top-down inhibitory mechanism. This would allow us to contrast the bottom-up visual region processing in the *Easy-Training* with the top-down frontal regions processing in the *Hard-Training* experiments. However, we would also need to take account of the negative correlation found for lateral occipital in the *Hard-Training*. We could contrast this finding with the positive correlation found in the same region for the *Easy-Training* experiment. This line of argument could then be used to support the idea that the learning mechanisms were different between the two tasks because in the *Easy-Training* we

found evidence of bottom-up inhibitory processing, which explained the between-session learning effects that were not evident in the *Hard-Training*. This was the case for both the psychophysics results and the correlations with the learning performance and the GABA+ concentrations. However, the fact that the correlation in the *Hard-Training* was strongly negative, led us to speculate that there may be some cooperative process occurring in the *Hard-Training* learning that involved the visual and frontal areas.

Accordingly we suggest that it is the combination of less GABA in the visual areas and more GABA in the frontal areas that explaines the inhibitory learning mechanism that we were investigating. For this cooperative model of the learning mechanism, the lower concentration of occipital GABA indicates a lower potential for inhibition of visual signal and this directly facilitates the top-down inhibitory processing in the frontal region. The idea being that the frontal cortex might process the information from the visual stimuli more efficiently if more uninhibited signal was passed to it from the visual cortex.

In summary these results suggest three conclusions; firstly that GABAergic processes mediate learning in *Easy* compared to *Hard-Training* visual tasks, secondly that increased occipital GABA+ concentrations mediate between-session consolidation learning for *Easy-Training* visual paradigms, and thirdly, that a combination of reduced occipital GABA+ concentrations and increased frontal GABA+ concentrations mediate visual learning in *Hard-Training* visual paradigms. This represents the first time that a dual-dissociable mechanism (for brain area and training difficulty mediated task performance) has been stipulated in a visual learning paradigm with the use of MEGA-PRESS spectroscopy. These results provide novel evidence of inhibitory learning processes that support theories concerning cooperative top-down and bottom-up learning mechanisms.

7

GABA VERSUS COARSE AND FINE VISUAL LEARNING

7.1 Introduction

We have shown in **Chapter 6: GABA Versus Training Difficulty Mediated Visual Learning** that GABA concentrations are associated with visual perceptual learning metrics. In those experiments the psychophysics metrics that were correlated with GABA concentrations were different in the two training conditions; for *Easy-Training* the performance metric was for between-session learning and for *Hard-Training* it was for across-session improvements. We were also interested in investigating whether GABAergic correlations mediated visual learning performance in different *tasks*, rather than different *training conditions*. We hypothesised that different tasks, that have dissociable psychophysical performance results, might correlate in distinct ways with GABA concentrations in visual cortex and frontal cortical regions.

We therefore designed a visual learning experiment where the stimuli were different in the training *and* the testing conditions to create a *Fine* condition and a *Coarse* condition. We measured GABA concentrations using the methods outlined in **Chapters 3: MEGA-PRESS Acquisition** and **4: Post-Acquisition Processing**, to create a correlative study through which we tested this hypothesis.

7.2 Materials and Methods

7.2.1 Participants

Thirty-two subjects (15 male, 17 female, mean age 24 ±6) participated in visual shape learning tasks and magnetic resonance spectroscopy (MRS) scans. All of the participants were agnostic to the study protocol and stimuli and had normal, or corrected-to-normal, vision. The University of Birmingham Ethics Committee approved the study. All participants gave written, informed consent and were paid for their participation.

7.2.2 Psychophysics

Stimuli. The stimulus images consisted of Glass patterns (Glass, 1969), which we arranged in concentric and radial configurations (Li et al., 2009). We defined shape patterns by placing dipoles with respect to the circumference of a circle that was centred on a fixation dot. The angle between the dot dipole orientation and the radius, from the centre of the dipole to the centre of the stimulus aperture, defined the spiral angle (**Figure 7.1**). We parametrically altered the spiral angle to generate shapes that were characteristically more radial (spiral angles closer to 0°, **Figure 7.1A**) or concentric (spiral angles closer to 90°, **Figure 7.1B**).

***Coarse* Task.** Spiral angles that are far apart produce shapes that are easily detected in the absence of image noise, but are hard to detect when embedded in noisy images. We created the noise condition images to represent a *Coarse* task. We set the spiral angle for radial shapes to 10° and the angle for concentric shapes to 80°. We added noise by replacing 65% of the signal dot dipoles with randomly oriented dots (**Figure 7.1C**). We based the noise ratio on staircase procedure pilot experiments, which we previously ran to optimise the learning performance.

***Fine* Task.** Spiral angles that are close together represent *Fine* tasks. Previous experiments have shown that *Fine* tasks are challenging (e.g. **Chapter 5: Time Course of Training Dif-**

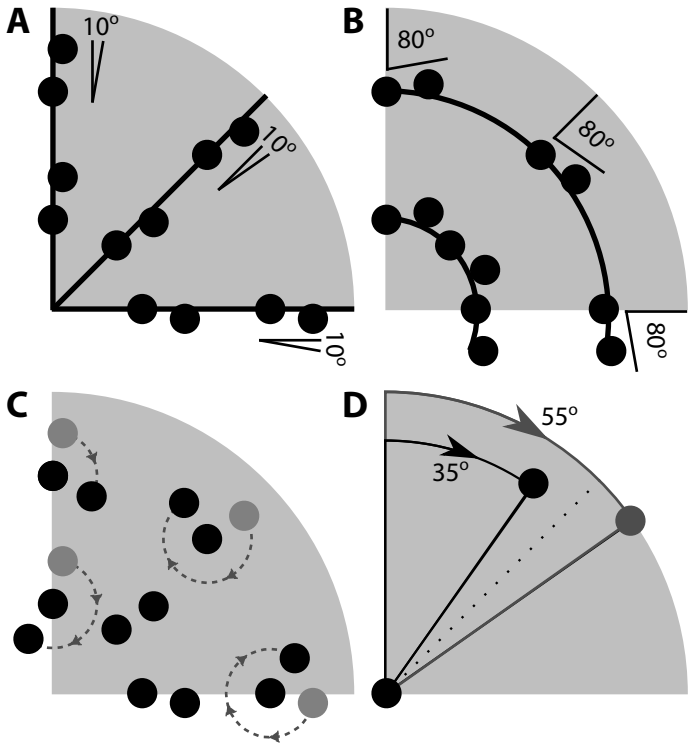

Figure 7.1: *Coarse* and *Fine* spiral angles.
(A) *Coarse* radial pattern (black lines), dipoles arranged with angles of 10° to the circumference.
(B) *Coarse* concentric pattern, (black arcs), dipoles arranged with angles of 80°.
(C) *Coarse* radial noise pattern, dipoles arranged with angles of 10° to the circumference. 65% have spiral angles changed (grey circles show original position, dotted arc indicates random spiral angle change).
(D) *Fine* radial and concentric patterns. Dipoles arranged with angles of 35° (radial) and 55° (concentric). Each pattern is 10° from the boundary between radial and concentric (dotted line).

ficulty Mediated Visual Learning), even in the absence of noise in the stimulus images. We therefore set the spiral angles for radial images to 35° and the concentric angles to 55° (**Figure 7.1D**). No noise was added to the *Fine* condition stimulus images.

***Coarse* and *Fine* Stimuli Parameters.** We randomly jittered the magnitude of the spiral angle ±2.5° in both the *Coarse* and the *Fine* conditions. This was in order to reduce the effect of local features and ensure that learning of shapes was based on global patterns. We generated a unique pattern for each stimulus presentation.

The patterns were formed from white dipoles (dot pairs) on a black background to give 100% contrast between foreground and background. The perceived size of each dipole was 2.3 arcmin² and the distance between dots in a dipole was 16.2 arcmin. The images were projected such that they extended over a square aperture $7.7° \times 7.7°$. Representative stimulus images are shown in **Figure 7.2**.

A 21-inch CRT monitor (1280×1024, 85 Hz frame rate) was used during the psycho-

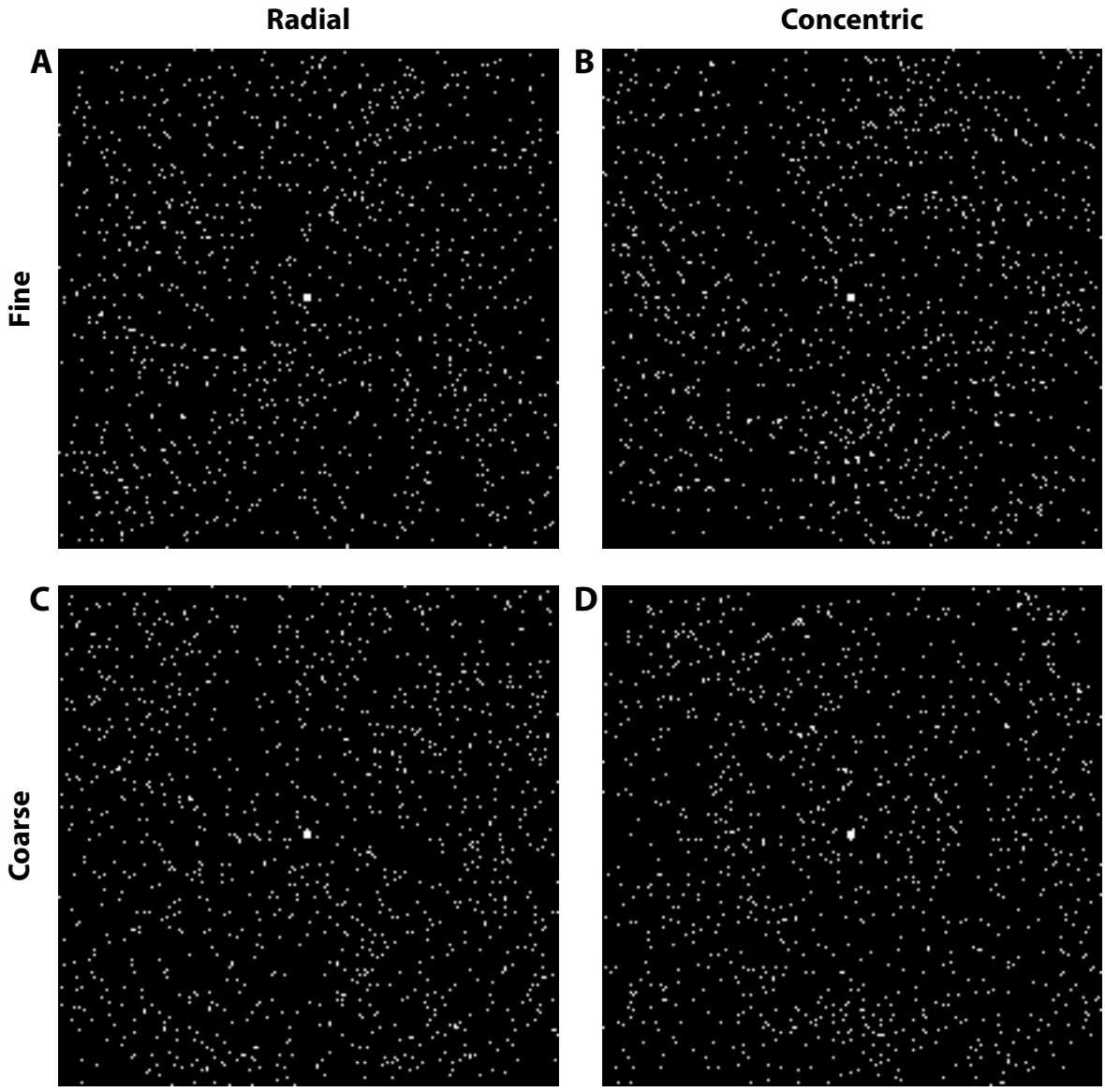

Figure 7.2: Stimulus images *Fine* versus *Coarse*. *Fine* images: **(A)** radial 35°, **(B)** concentric 55°, noise 0%. *Coarse* images: **(C)** radial 10°, **(D)** concentric 80°, noise 65%.

physics experiments and all psychophysics experiments were conducted in low light conditions. A chin rest was used to fix the viewing distance at 47 cm. We generated and presented stimulus images using Matlab (The MathWorks, Inc., Natick, Massachusetts, USA) and Psychtoolbox version 3 (Brainard, 1997; Pelli, 1997).

Procedure. The participants were randomly assigned to either a *Fine* or *Coarse* shape learning task. This resulted in 17 participants on the *Fine* task and 15 on the *Coarse* task.

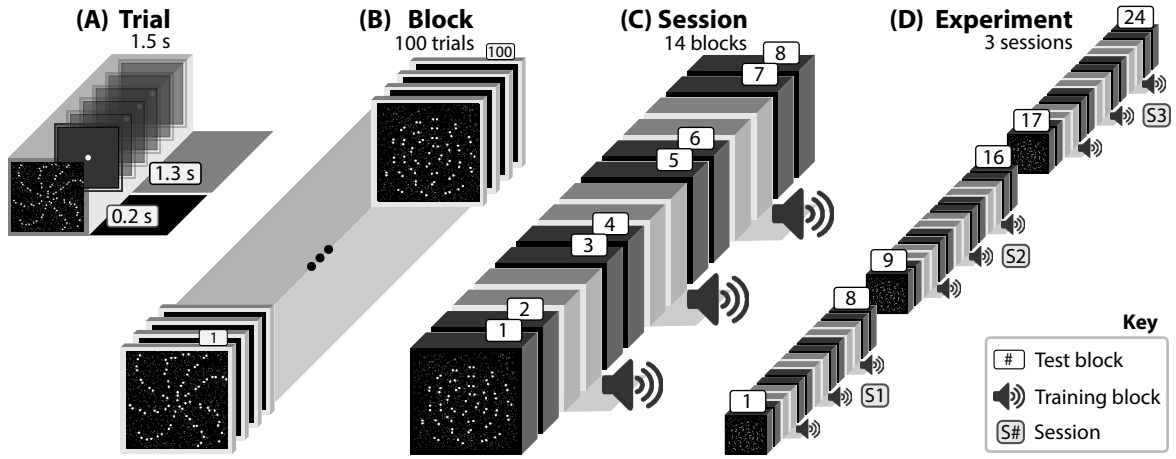

Figure 7.3: Psychophysics design coarse versus fine. A **trial (A)** consists of a stimulus image presentation (200 ms), subject response during a fixation block (minimum 1300 ms) and an audible error beep for incorrect responses on training blocks (there was no feedback on testing blocks). A **block (B)** consists of 100 trials. A **session (C)** consists of 14 blocks, starting with test blocks (shown as darker shapes) and interleaved training (indicated with lighter shaded shapes with audio icons) and more testing blocks. The whole **experiment (D)** consists of three sessions **(S1, S2, S3)**, which the participants completed on consecutive days. The numbers on **(C)** and **(D)** represent sequential test block numbers to help identify particular blocks in the text.

Each subject participated in three psychophysics sessions that took place on consecutive days (**Figure 7.3**). Individual sessions consisted of eight test blocks without feedback and six training blocks where sound, in the form of error beeps, was used to provide feedback on each trial. We interleaved the test and training blocks in pairs to allow the time course of learning to be monitored. Each block consisted of 100 trials and stimulus presentation lasted for 200 ms. After each stimulus presentation, participants were required to categorise the image as radial with a left mouse click, or concentric with a right mouse click. The next stimulus presentation would not occur until the participant had made a choice. Breaks of at least 60 s were mandated after each block and we encouraged observers to take longer breaks if they became fatigued during the experiments.

The participants also took part in control experiments away from the main shape learning experiments. These were designed to assess the participants' threshold for discriminating stimuli and their visual short term memory. The stimulus thresholds were assessed with

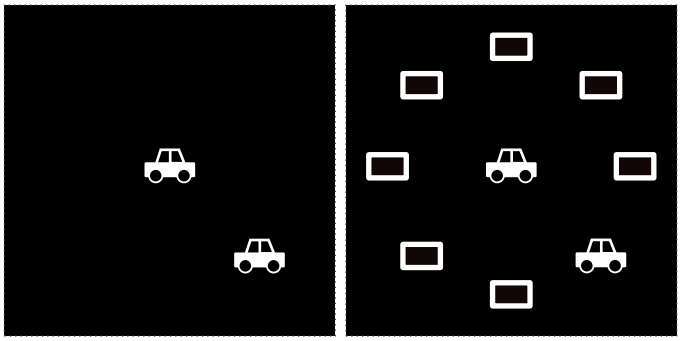

Figure 7.4: Useful field of view.
Sample stimuli of vehicle surrounded by eight radial placeholders.

useful field of view (UFOV) experiments (Edwards et al., 2006). The procedure involved a central stimulus image of motor vehicles surrounded by radial placeholders in eight positions (**Figure 7.4**). The participants were tasked with firstly identifying the type of vehicle in the central image and also the position of a secondary image that appeared at one of eight placeholder positions. This tested the participants' visual awareness and was referred to as the *Divided Attention (DA)* index. A second index, *Selective Attention (SA)*, involved the same procedure, but with added distractor images that obscured the subjects' view of the central stimulus image (47 triangles). The participants' visual short term memory (*VSTM*) was tested with a procedure described in Luck and Vogel (1997) and involved identifying the colour of circle shapes that changed with random frequency between stimulus presentations.

Behavioural Indexes. The visual awareness and memory control experiments provided three behavioural metrics: *Visual and Short Term Memory (VSTM), Divided Attention (DA)* and *Selective Attention (SA)*.

From the *Fine* versus *Coarse* experiments we calculated a further three metrics from the testing blocks only: *Pre-Training Index, Normalised Accuracy Index* and the *Normalised Mean Index*. These metrics were based on the percent correct responses in particular blocks (*PCB*) and sessions (*PCS*), which we defined in the previous chapter (**Equation 6.1** and **Equation 6.2**). The block numbers refer to **Figure 7.3**.

Pre-Training Index. This consisted of the performance in block one, we therefore considered this to represent a baseline measure that indicated pre-training performance.

$$PreTrainingIndex = PCB_1 \tag{7.1}$$

Our rationale for using this metric was to compare starting (unlearned) performance between the *Fine* and *Coarse* tasks, and to use this metric as a normalising factor across the two experiments.

Normalised Accuracy Index. We selected this metric to investigate the time course of performance over all sessions. We calculated it (**Equation 7.2**) by normalising the percent correct score in each block by the percent correct score in the *Pre-Training Index* block.

$$NormalisedAccuracyIndex_b = \frac{PCB_b}{PCB_1} \tag{7.2}$$

Our rationale for using this metric was to show block-by-block, learning performance changes in the *Fine* and *Coarse* tasks. This metric is similar to that used in Garcia et al. (2013), except that in the current chapter we have added a normalising factor. The experiments in the paper had identical experimental methods for the first block in both *Easy-* and *Hard-Training* conditions. This was reflected in similar performance scores in the first block by both sets of subjects. The current experiment has different stimuli for *Coarse* compared to *Fine* conditions. This means that differences in starting performance might affect the potential performance gains depending on how high one groups' starting performance was compared with the others'. The normalisation step was performed to account for any differences in starting performance between the two tasks.

Normalised Mean Index. We used percent correct in test block one (PCB_1) to represent the pre-training performance. We calculated the *Normalised Mean Index* by subtracting the percent correct in the first session $S_1 = \{B_2, B_3, ..., B_8\}$ from the percent correct of the last session $S_3 = \{B_{17}, B_{18}, ..., B_{24}\}$, where B_j denotes block j. Note that S_1 does not include block B_1 as this is used to evaluate pre-training performance. We divided both mean session values by the pre-training performance PCB_1 exactly as we did in **Chapter 6, Equation 6.5**. Our rationale for using this metric was to represent differences in the *Fine* condition, compared with the *Coarse* condition across the entire span of the experiments. This metric has the advantages that it builds on the work of the previous chapter, it takes account of potential differences in initial starting performance across the different conditions and it uses all of the blocks in the first and third sessions.

7.2.3 MRS Acquisitions

Regions of Interest. We chose regions of interest to cover visual areas including lateral occipital complex and higher cortical areas encompassing mid frontal gyrus (**Figure 7.5**). We also selected a control area covering motor cortex. We chose the ROIs based on our hypothesis that GABA mediated inhibition would lead to different correlations in visual cortex compared to higher cortical areas. We also used the results from our fMRI experiments (**Section 3.4.4**), which showed interesting activation patterns for these regions, to inform our selection of these brain areas.

MRS Parameters. For each ROI we acquired a GABA edited acquisition using the MEGA-PRESS method (Edden & Barker, 2007; Mescher et al., 1998; Mullins et al., 2014). The main MRS parameters were: TR = 1800 ms, TE = 68 ms, volume = 30 mm^3, samples = 2048, spectral BW sample frequency = 2150, water suppression = VAPOR, dynamic scans (rows) = 32, phase

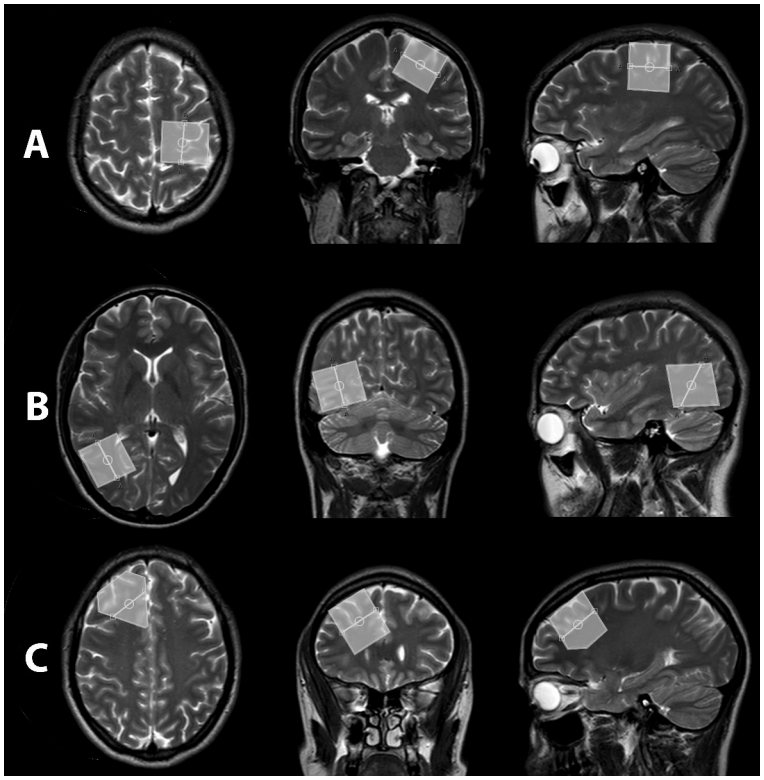

Figure 7.5: Regions of interest. Anatomical MRI images, from left to right, axial view, coronal view, sagittal view. ROIs indicated by highlighted wireframe shapes:
(**A**) Motor cortex (control region).
(**B**) Lateral occipital.
(**C**) Mid frontal gyrus.

cycles = 16. We also performed a single PRESS acquisition for each ROI so that the water concentration could be used in the post-processing stages: Phase cycles = 8 and dynamic scans = 1. We used a 3T Philips Achieva scanner (Philips Healthcare, Best, Netherlands) to obtain the MRI and MRS data. We set the parameters in accordance with the literature review that we conducted in **Chapter 3: MEGA-PRESS Acquisition**. Each MEGA-PRESS acquisition took 921.6 s (15 min 21.6 s). We selected this duration to maximise the accuracy and spectral quality of the data acquired, in accordance with our findings in **Appendix (A): Time Course of MEGA-PRESS**.

MRS Scans Sequence. We acquired a 1 mm^3 isotropic resolution T_1-weighted anatomical scan for each participant and we planned the MRS acquisitions using three orthogonal T_2 scout scans (slice gap 4 mm, 24–36 slices per scan). The order in which the ROIs were acquired was randomised and there was no task to perform during the scans. Alcohol, nicotine and caffeine intake never exceeded each subjects' usual levels, which we determined through self-

reported questionnaires. We randomly varied the time of day for the scans, although we did not expect this to have an effect on the MRS signals (Evans et al., 2010). All MRS scanning was performed after behavioural testing had been completed.

MRS Processing. The detail for the MRS processing pipeline are described in **Chapter 4: Post-Acquisition Processing**. Here we briefly outline the processing stages and refer to the sections from that chapter where a more detailed description is given.

We converted the free induction decay signals (**Section 4.3: Time Domain Signals**) that we obtained from the MEGA-PRESS scans using the fast Fourier transform. We phase corrected the spectra (**Section 4.4: Phase Correction**) and realigned to correct for subspectral misalignment (**Section 4.5: Subspectral Shifting**), no data was removed during this process. We averaged the realigned subspectra and combined them by subtracting the edit OFF spectra from the edit ON spectra. We obtained GABA quantities from Tarquin (Reynolds et al., 2006) and we subsequently rescaled the measurements to calculate the grey matter contribution (**Section 4.8: Scaling and Reference Metabolites**). We obtained tissue proportions (grey matter, white matter and CSF) from high resolution T_1 anatomical scans (**Section 4.7: Segmentation**), using Freesurfer (Dale et al., 1999; Fischl et al., 2002). Each GABA measurement used in this study was the average of two acquisitions per subject, one from each hemisphere. We used GABA+ designation to indicate the contribution of macromolecules in the GABA signal, which we quoted as institutional units (I.U.) to indicate that we did not attempt absolute quantitation.

7.3 Results

We arranged our results in the following order: We assessed the MRS measurements by examining the signal to noise ratio (SNR) and Cramér-Rao lower bounds (CRLB) of the spectra.

We also inspected the scans for identifiable peaks around 3.01 ppm in the combined (edit ON minus edit OFF) sequences. We compared the subjects' performance on the *Fine* versus *Coarse Normalised Accuracy Index* by block. We compared the the *Normalised Mean Index* in the *Fine* versus *Coarse* experiments. We tabulated the correlations between GABA+ versus the control experiments (*VSTM, DA* and *SA*). We also tabulated the correlations between GABA+ versus the *Pre-Training Index*. The main results that we present here are the correlations between GABA+ in two ROIs versus the *Normalised Mean Index* in the *Fine* and *Coarse* experiments. We set the significance level for rejecting the null hypothesis to $p < 0.05$ for all correlations.

7.3.1 MRS Spectra

Mean SNR values for the spectra were: Lateral occipital 37.8 ±10.1; mid frontal gyrus 45.0 ±6.5 and motor cortex 34.6 ±7.4. Mean CRLB values for the GABA peaks at 3.01 ppm were: Lateral occipital 3.9 ±1.1, mid frontal gyrus 4.3 ±1.1, motor cortex 4.8 ±1.5. GABA peaks were reliably observed in the acquisitions (**Figure 7.6**).

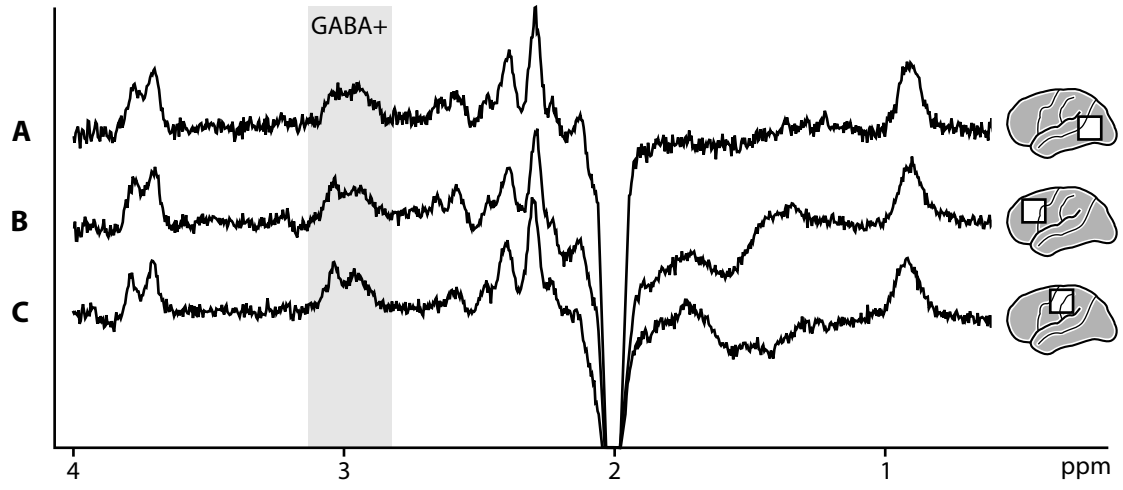

Figure 7.6: Representative spectra. (**A**) lateral occipital (mean SNR=37.8 ±10.1, CRLB=3.9 ±1.1), (**B**) mid frontal gyrus (mean SNR=45.0 ±6.5, CRLB=4.3 ±1.1), (**C**) motor cortex (mean SNR=34.6 ±7.4, CRLB=4.8 ±1.5).

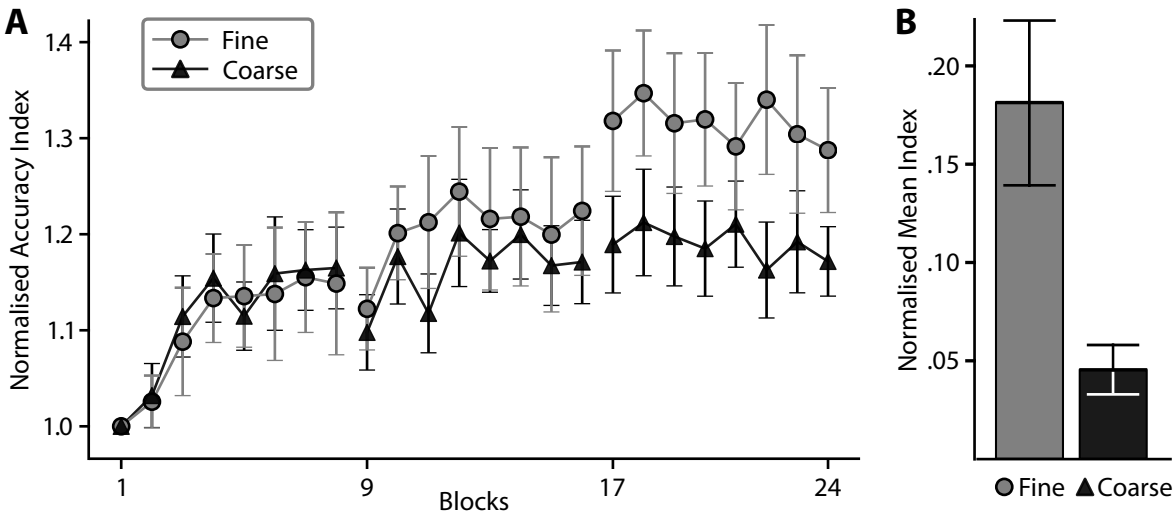

Figure 7.7: *Fine* versus *Coarse Normalised Accuracy* and *Normalised Mean* indices. (A) Accuracy on the test blocks was calculated as the percentage of correct trials per block and the results were normalised to the performance in the first block. *Fine* (circular markers) versus *Coarse* (triangular markers). **(B)** *Fine* (n=17) versus *Coarse* (n=15) *Normalised Mean Index*. The grey bar represents the *Fine* task average performance, the black bar represents the *Coarse* task average performance. Error bars are standard error of mean.

7.3.2 Dissociable Learning for Coarse Versus Fine

We plotted the *Normalised Accuracy Index* for the two tasks (**Figure 7.7A**). Performance results on the *Fine* versus *Coarse* test runs were quite similar for the first session (blocks 1 to 8) across subjects. However, by the end of the third session, subjects on the *Fine* task had improved more than subjects on the *Coarse* task. Further, the difference in performance was most striking between the end of the second session and the beginning of the third session (blocks 16 and 17). For the *Fine* task there was a between-session improvement that was not evident in the *Coarse* task.

We averaged the *Normalised Mean Index* by *Fine* versus *Coarse* task and plotted the results to show the difference in learning effect for the two experimental conditions (**Figure 7.7B**).

7.3.3 GABA Does Not Predict Attention and Short Term Memory Effects

We compared the correlations of the GABA+ measurements with the *Visual Short Term Memory (VSTM), Selective Attention (SA)* and *Divided Attention (DA)* psychophysics metrics. These

Table 7.1: GABA+ versus memory and attention metrics. In the correlations between GABA+ measurements and *Visual Short Term Memory (VSTM), Selective Attention (SA)* and *Divided Attention (DA)* metrics, there were no significant correlations in this analysis.

Performance Index	Lateral Occipital	Motor Cortex	Mid Frontal Gyrus
Fine VSTM	(r= –.42, p= .07)	(r= .14, p= .57)	(r= –.14, p= .56)
Fine DA	(r= .14, p= .56)	(r= .17, p= .49)	(r= .10, p= .70)
Fine SA	(r= .11, p= .63)	(r= .29, p= .22)	(r= –.21, p= .36)
Coarse VSTM	(r= .25, p= .39)	(r= –.15, p= .59)	(r= .20, p= .48)
Coarse DA	(r= .13, p= .67)	(r= .21, p= .49)	(r= –.25, p= .40)
Coarse SA	(r= –.10, p= .76)	(r= .25, p= .42)	(r= .03, p= .93)

were control experiments designed to exclude short term memory and attention effects as potential mediators in the experiments. The results from these controls (**Table 7.1**) showed low r-values and p-values that were higher than our significance threshold. We did not correct for false positives in this table because we did not report any correlations that were statistically significant.

7.3.4 GABA Correlates in *Coarse* and *Fine*

We wished to control for variation in starting performance and so we correlated the GABA+ measurements with performance on the *Pre-Training Index* (**Table 7.2**). The r-values were low and the p-values were higher than our significance threshold. This suggested that the untrained performance scores at the beginning of the *Fine* and *Coarse* experiments could be discounted as predictors for any dissociable learning that we observed.

Table 7.2: GABA+ versus *Pre-Training Index*. The r-values were all low and the p-values were above our level of significance, therefore we could not reject the null hypothesis for any of these correlations.

Experiment	Lateral Occipital	Motor Cortex	Mid Frontal Gyrus
Fine	(r= –.04, p= .85)	(r= .19, p= .33)	(r= .10, p= .58)
Coarse	(r= .20, p= .35)	(r= .07, p= .76)	(r= .04, p= .86)

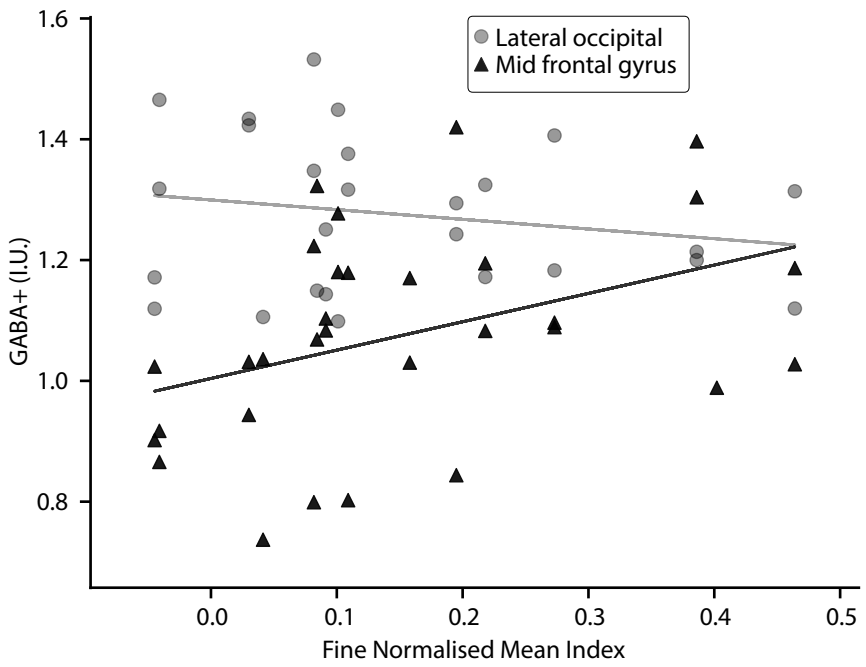

Figure 7.8: Mid frontal gyrus GABA+ versus *Normalised Mean Index* in the *Fine* experiment. GABA+ in mid frontal gyrus (triangular markers) was moderately, positively correlated (r = .40, p = .03) with the *Normalised Mean Index*. GABA+ in lateral occipital (circular markers) was not correlated (r = –.19, p = .35).

We investigated the Pearson correlation coefficient between the *Fine* versus the *Coarse Normalised Mean Index* and the GABA+ concentrations in the lateral occipital versus frontal regions of the brain. For the *Fine* experiment we found a moderate positive correlation between the *Normalised Mean Index* versus GABA+ in the higher cortical areas (r=.40, p=.03), which was not evident (r=–.19, p=.35) in the occipital region (**Figure 7.8**). In the correlation between the motor control region versus the *Normalised Mean Index*, we could not reject the null hypothesis (r=.23, p=.25).

For the *Coarse* experiment we found a strong negative correlation between the GABA+ in the occipital region versus the *Normalised Mean Index* (r=–.63, p <.01), which was not evident (r=.11, p=.62) in the frontal region (**Figure 7.9**). We could not reject the null hypothesis for GABA+ in the motor cortex region versus the *Normalised Mean Index* ($\mathrm{r} = -.27, \mathrm{p} = .22$).

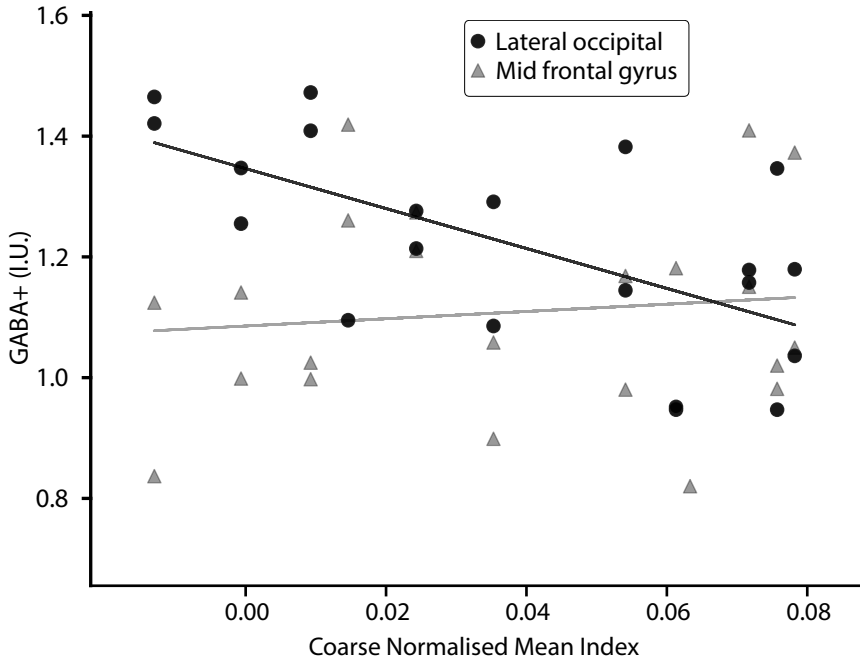

Figure 7.9: Lateral occipital GABA+ versus *Normalised Mean Index* in the *Coarse* experiment. GABA+ in lateral occipital regions (circular markers) was strongly, negatively correlated ($r = -.63$, $p < .01$) with the *Normalised Mean Index*. GABA+ in mid frontal gyrus (triangular markers) was not correlated ($r = .11$, $p = .62$).

7.4 Discussion

The psychophysics results for the *Normalised Accuracy Index* suggested a dissociable learning mechanism between *Fine* and *Coarse* tasks, as the performance of subjects on each task was different (**Figure 7.7A**). The differences in performance were most noticeable for the third session where the *Normalised Mean Index* highlighted the apparent dissociable learning mechanism between the two tasks. We hypothesised that the mechanism is based on inhibitory processes in grey matter in specific regions of the brain.

Both tasks involved visual awareness, as the stimuli required careful attention to discriminate between the radial and concentric shapes, which only appeared briefly (200 ms presentation time). Short term memory might also be involved with performance, as subjects would need to remember shape features from the training blocks (i.e. the blocks that had the feedback). We investigated the correlations between the GABA+ versus the *Visual Short Term Memory (VSTM)*, the *Divided Attention (DA)* and the *Selective Attention (SA)* metrics. This was to see if we should be interested in inhibitory mechanisms for memory and atten-

tion. The *p*-values for the correlations between GABA+ and memory versus attention metrics (**Table 7.1**) were all too high for us to be able to reject the null hypothesis. We therefore concluded that inhibitory processes for short term memory and visual awareness did not explain the dissociable performance we saw in the psychophysics results.

The *Coarse* and *Fine* tasks were different from one another; the *Coarse* task involved the detection of discriminable shapes that were embedded in noise, whereas the *Fine* task involved the discrimination of similar shapes in the absence of noise. As the tasks were different we were concerned that any differences in baseline performance might mediate performance. We therefore controlled for differences in difficulty between the two tasks by investigating the correlations between the *Pre-Training Index* versus GABA+. The *p*-values were once again above the significance threshold (p=.05) and so we could not reject the null hypothesis (**Table 7.2**). We interpreted this to show that initial scores on the tasks were not mediated by inhibitory processes in any of our ROIs.

When we turned our attention to the correlations between GABA+ versus the *Normalised Mean Index* we found that they were different for the *Fine* and *Coarse* tasks, both in terms of brain region and whether the *r*-values were positive or negative (**Figures 7.8, 7.9**).

7.4.1 Less Occipital GABA Predicts Learning in *Coarse*

For *Coarse* tasks, less GABA+ in the lateral occipital area was correlated with increased performance on the task (**Figure 7.9**), this observation was supported by the negative sign of the *r*-value. This inverse relationship with visual areas and GABA was consistent with other work in this area as a negative correlation in occipital areas in an orientation selectivity experiment has been previously reported (Edden et al., 2009). In a motor decision speed experiment a negative correlation with GABA and frontal eye field has also been reported (Sumner et al.,

2010). Further, in regard to negative correlations, it has been hypothesised that simpler mechanisms, such as low level visual processing, are likely to have inverse relationships with GABA (C. Stagg & Rothman, 2014).

Indeed, we have previously found a negative correlation in visual cortex (**Chapter 6: GABA Versus Training Difficulty Mediated Visual Learning**), which we suggested may have played a role in a cooperative model of inhibitory processing between visual and frontal cortex. The frontal cortex GABA+ correlations in the *Coarse* experiment described here were positive, but did not reach statistical significance.

7.4.2 More Frontal GABA Predicts Learning in *Fine*

For the *Fine* task we found that more GABA+ in frontal areas predicted better performance on the task (**Figure 7.8**), as was evidenced by the moderate positive correlation that we discovered. This finding is consistent with top-down theories of neural processing in which suppression of irrelevant stimuli in prefrontal areas is the key mechanism (Desimone, 1998). The task was a discrimination one that relied on the evaluation of fine differences in the absence of noise. We suggest therefore that top-down theories fitted as plausible explanations to match our finding that increased GABA+ in frontal areas correlated with overall learning improvement. This is consistent with other work that has shown that the amount of GABA reflects the potential capacity for selective suppression of irrelevant information (Sandberg et al., 2013). The results were also consistent with our findings (**Section 6.4**) on the *Hard-Training* paradigm, which also showed positively correlated frontal region GABA+ and negatively correlated visual region GABA+ concentrations. The *Fine* task is similar to the *Hard-Training* paradigm described in **Chapter 6: GABA Versus Training Difficulty Mediated Visual Learning**, in terms of the parameter settings of the stimuli used. We therefore suggest

that these results further support the conclusions that we made in that chapter.

7.4.3 GABAergic Inhibitory Mechanisms in *Coarse* Versus *Fine*

When we compared the correlations between the *Coarse* experiment versus the *Fine* one, the most obvious difference was in the sign of the *r*-values (**Figures 7.8, 7.9**). In the *Coarse* experiment, the learning index was negatively correlated with visual GABA+ concentrations. In the *Fine* experiment the learning index was positively correlated with frontal GABA+ concentrations. This was an interesting finding by itself, because we found that there is dissociable learning performance between the two paradigms and this can be explained by the different correlations (i.e. positive and negative) that we found in the different brain regions. However, we also noted that in addition to these (statistically significant) correlations, the trend for the sign of the *r*-values in visual regions was consistently negative and the sign of the *r*-values for frontal areas was positive, regardless of whether the paradigm was *Coarse* or *Fine*. For the *Fine* experiments, we observed that the correlations in the two brain regions were consistent with the *Hard-Training* results from **Section 6.4**, which suggested a top-down cooperative model that included less inhibitory potential in the visual cortex. Although the visual cortex GABA correlations were negative in the *Fine* paradigm, they were not statistically significant. We interpreted this to mean that the same cooperative model might apply to the learning mechanisms for the *Fine* learning as the previous *Hard-Training* learning. However, in the *Fine* task, the top-down processing in frontal cortex was the key discriminator in performance, rather than the amount of inhibitory potential in the visual cortex. In the *Coarse* task, we suggest that the lower inhibitory potential in visual cortex is the key factor for better performance, rather than the top-down inhibitory processing in frontal areas.

The observation that the inhibitory mechanisms are located in different brain regions

shows the importance of targeting specific brain regions as apposed to inferring global changes from GABA concentrations in one region. The importance of targeting specific ROIs has been discussed in work that showed correlations between GABA versus reversed masked priming task performance (Boy et al., 2010). Here we not only show a regionally specific effect, but also that there might be cooperation between different ROIs that leads to better performance.

In summary, these results represent evidence for GABAergic inhibitory mechanisms for visual learning, which are dissociable by brain region and task. Moreover, they demonstrate the dissociable mechanism through correlations with the same psychophysics performance metric versus GABA+ concentrations in both lower (visual processing) and higher (frontal) grey matter cortex. This suggests that GABAergic processing is involved in cooperative top-down and bottom-up mechanisms in visual learning.

8

DISCUSSION AND CONCLUSIONS

This concluding chapter is organised as follows: Firstly we summarise our research, organised by the different disciplines that comprised our research context. Next we evaluate the key aims and objectives to discuss the contributions that we made. Following this we identify limitations that we found in our methodological approaches. We have a section on our recommendations for how this research could be extended and we finish with some concluding remarks about what the thesis as a whole represents.

8.1 Introduction

Understanding the mechanisms that drive learning in the human brain is a key research aim in science and progress in this area is expected to hold important benefits, particularly in terms of long term health. Current knowledge of how the brain learns has been advanced through behavioural experimentation and measures of brain activity. In humans, the measures of activity are usually indirect measures and further advances are expected to rely on technological improvements in the tools that are used for the measurements. In our research we identified that the chemical aspects involved with learning were less fully explored than those aspects that focussed on brain activation such as electroencephalography or fMRI. Techniques for

measuring brain chemicals in humans must rely on non-invasive modalities and MRS is a mature technology for this application that is used primarily in the detection of pathology, but less so for the healthy brain. Our main research questions revolved around the idea that using MRS to characterise the learning brain had the potential to supplement the more common modalities with new information on brain function. Recent advances in MR technology have allowed researchers to begin measuring GABA concentrations with the MEGA-PRESS pulse sequence and we took advantage of this to design experiments to link inhibitory neurotransmitter with learning performance, thereby suggesting the involvement of inhibitory mechanisms in learning.

8.2 Summary

In the pursuance of our main research goal we explored and made contributions to three different disciplines: Psychophysics, physical and computational sciences, and neuroscience as follows.

Starting from the hypothesis that learning performance results that were dissociable by task would be most likely to be based on dissociable learning mechanisms, we designed psychophysics experiments that evoked performance differences. This led to research into the time course of learning and our first contribution, which involved novel interleaved testing and training paradigms that were spread over multiple sessions.

The MEGA-PRESS technique presented several challenges for the researcher, principally due to a dearth of established tools for processing the MR signals and a lack of consensus on analysis methodologies, such as scaling by tissue type. We therefore developed a set of tools and methodologies to address these challenges. We offer that our efforts will have benefits for other scientists wishing to conduct research with the MEGA-PRESS sequence. This aspect of

our work represents our contribution to the physical science aspect of the research.

We brought the behavioural and MR strands together in correlative studies that were designed to probe the links between inferred inhibitory mechanisms and dissociable learning performance. There were several novel features to these experiments such as the methods for targeting MR acquisition voxels, the use of multiple ROIs and our use of new scaling methods. Our results showed correlations that were consistent with our hypothesis that inhibitory mechanisms, that were invisible to other modalities, can be inferred through MRS experiments. Our results were congruent with our main research aim that was to suggest MRS as a supplementary tool for probing inhibitory mechanisms in the healthy learning brain.

8.3 Evaluation

The research question addressed in this interdisciplinary project involved the measurement of inhibitory neurotransmitter in humans as a probe for investigating inhibitory mechanisms in visual learning.

Our first objective was to develop visual learning experiments that would engage different brain areas in two groups of observers. We developed interleaved, multi-session visual learning experiments that showed dissociable performance according to training difficulty. By increasing the frequency of testing we revealed visual learning performance that was different for within and between sessions. Investigations into training regimen are important aspects of psychological enquiry with consequences in areas such as education. Our work on this represented represents a new finding for the project and led to a publication (Garcia et al., 2013).

Other research questions were related to physical science areas of the project, such as approaches to post-acquisition processing methods and how to target brain regions in MRS

learning experiments. One way of evaluating this work is to examine the quality of the spectra obtained before and after applying any signal processing methods developed. We demonstrated improvements across a range of quality metrics after applying correcting algorithms for phase, spectral alignment and peak modelling. We also drew conclusions from this work, including that independent alignment strategies improved over paired alignment and demonstrated that fMRI guided ROI selection showed promise in MEGA-PRESS experiments. This has the potential to make the targeting of relevant brain areas in neurobiological studies more efficient and thus add a methodological improvement to MRS experimental paradigms.

Our further objectives were to investigate grey matter scaling approaches. The significance of this is that grey matter is often considered to be important in cognitive processes – often more so than white matter. This has caused researchers involved with fMRI analysis to routinely segment grey matter from the white matter so that only grey matter BOLD signals are figured in their results. This segmentation is not commonly applied in MRS experiments, but the same arguments about the efficacy of grey matter processing versus white matter processing should apply just as they do in fMRI. We have demonstrated in this thesis how to apply segmentation in MRS experiments and have provided some of the first examples of neural correlates of GABA and learning that have been scaled by grey matter proportion.

8.4 Limitations

Our work was planned as a multidisciplinary project from the start. As such there is always the danger that the research areas may become spread too thinly and will fail to satisfy any one discipline with regard to the methodological rigour employed. For example the metrics that we used to measure performance might attract criticism for not adhering to standard approaches in psychology. Similarly our contributions to the psychological areas were largely

based on correlations and it is a well known scientific mantra that correlations do not imply causation. These are limitations that we acknowledge, but suggest that there is value in simplicity, particularly for nascent research areas. Our approach of reporting correlations with GABA concentrations and percent correct learning metrics has the advantage of demonstrating inhibitory mechanisms in intuitively comprehensible terms, which might encourage researchers from other neuroscience disciplines to engage with MRS techniques.

We hypothesised that GABA in grey matter might be a better predictor of learning performance than white matter GABA pools and we presented evidence to support this idea. However, this is a novel approach and would need to be further validated before being advocated as a standard approach for MRS studies, as it is in the case of fMRI research.

8.5 Further Work

Part of the work in this thesis showed time courses for the psychophysics of learning and the feasibility of shorter scan times than the current norm. We would like to extend this idea to investigate time courses for MEGA-PRESS acquisitions. If we could optimise the time taken for reliable GABA measurements, then we would like to focus future research on a time course for GABA metabolism during a learning experiment. This could follow similar lines to the motor learning experiment in Floyer-Lea et al. (2006) or the working memory experiments in Michels et al. (2012), but we anticipate shorter, more frequent time points that would lead to a high temporal resolution characterisation of inhibitory processes in perceptual visual learning. A high temporal resolution GABA experiment could help to characterise GABA as a functionally dynamic metabolite whose real time fluctuations might lead to a better understanding of cortical inhibitory processes. We have made tentative steps towards this goal with work showing that shorter scan times than the current average are feasible with minimal

negative effects on the quality of spectra obtained.

The focus of the research in this thesis was on the inhibitory neurotransmitter GABA. However further investigations into excitatory neurotransmitters such as glutamate and aspartate would certainly be of interest. This would be particularly so if methods of measuring the excitatory and inhibitory balance could be developed. This has the potential to greatly advance our understanding of the workings of the human brain.

8.6 Conclusions

The key idea for the research described in this thesis was to investigate inhibitory neurotransmitter concentrations in the human brain and how these might relate to visual learning. Our primary contribution is to reveal that GABA is a correlate of learning and a potential predictor of performance. We achieved this through a combination of improving MEGA-PRESS post-acquisition signal processing and developing experimental methods that target grey matter inhibitory processes in multiple brain areas. The detailed methods of how to accurately measure and process MEGA-PRESS signals are still being refined and critical consensus on how GABA concentrations explain behavioural improvements have only recently begun to emerge. By addressing both the methodological details of GABA measurement and linking these to inhibitory mechanisms in task specific brain areas means that our research is therefore timely.

Through the development of robust MEGA-PRESS post-acquisition processing methods we achieved improved GABA signals. This meant we were able to draw confident conclusions concerning links for GABAergic processes in frontal and occipital brain areas to support feedforward and top-down models of visual learning. Specifically we have suggested that less GABA in lateral occipital areas and more in frontal areas explain performance increases

in visual learning tasks modulated by training difficulty. For *Easy-Training* we have found a novel connection between higher concentrations of GABA in lateral occipital areas and *Between-Session* learning. Our results from *Coarse* and *Fine* visual learning experiments support cooperative feedforward and top-down mechanisms that are dissociable by brain region and task.

Taken as a whole this thesis represents an investigation of aspects of chemical interactions of learning that have received less attention in the scientific community than those based on electrical activation. This approach has the potential to contribute to our understanding about the chemical level of analysis in neuroscience generally and for inhibitory processes of learning in particular. Our integrative approach to both methodological and experimental research areas provides a pattern that we hope other researchers will use to add MEGA-PRESS techniques to their existing fMRI and EEG experiments, to further our knowledge of inhibitory processes in the human learning brain.

A

TIME COURSE OF MEGA-PRESS

A.1 Introduction

Researchers have taken advantage of increasing field strengths (3T and higher) to improve signal to noise ratio (SNR) rather than to reduce acquisition time (Puts & Edden, 2012). However, a reduction in acquisition time would have advantages for experiments that involve the quantification of GABA. For example more regions of interest (ROIs) could be investigated during a scanning session of the same length. Also, experiments that track changes in GABA during an experiment, such as the motor learning experiment described in (Floyer-Lea et al., 2006), should benefit from the increased time resolution of shorter duration acquisitions. For these reasons we planned to investigate the time course of MEGA-PRESS acquisitions to see if shorter than typical acquisition times were feasible.

To investigate this we compared measures of spectral quality, such as SNR and Cramér-Rao lower bounds (CRLB), at 16 time points from 210 MEGA-PRESS scans.

A.2 Materials and Methods

The time course of a MEGA-PRESS experiment is shown in **Figure A.1**, for a hypothetical scan of 16 min duration, with 512 dynamic averages and phase cycling set to 16. This illus-

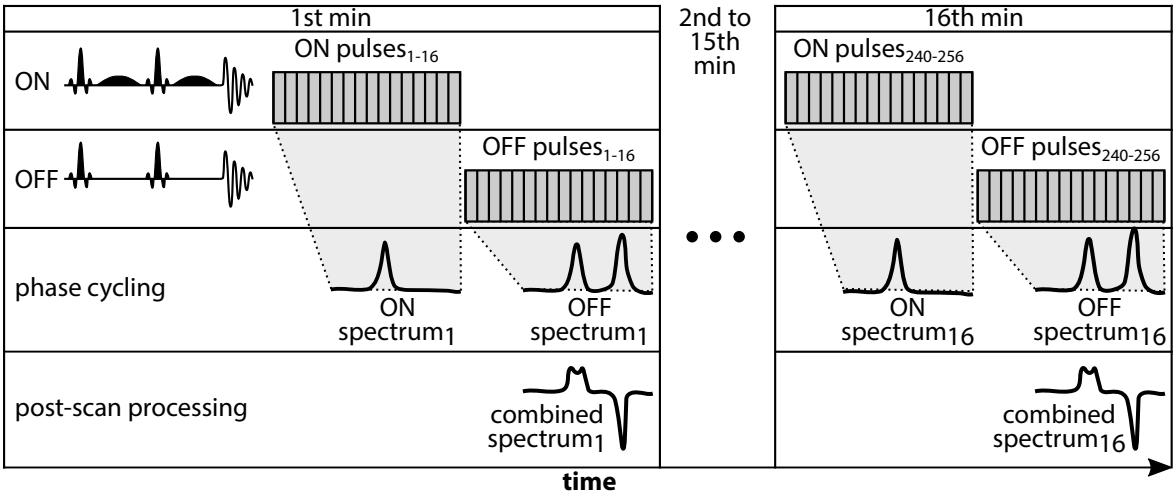

Figure A.1: Time course of a single MEGA-PRESS experiment. Time increases along the x-axis in the direction of the arrow. Interleaved edited (ON) and unedited (OFF) pulses are phase cycled to produce 16 pairs of serially acquired data from 512 (256 edit ON, 256 edit OFF) individual pulses.

trates the interleaved application of MEGA-PRESS (ON) and PRESS (OFF) pulse sequences. In the figure, time increases along the x-axis in the direction of the arrow. During the first minute, the MEGA-PRESS pulse sequence (ON) runs 16 times, followed by the unedited sequence (OFF). The ON and OFF data are phase cycled in the scanner to produce the first exportable data sets, labelled "ON spectrum$_1$" and "OFF spectrum$_1$". These sets are displayed as frequency domain spectra for illustrative purposes, although the data will actually consist of time domain signals in the scanner. This pattern repeats for a further 15 times so that 16 edit ON and 16 edit OFF FIDs are produced for export from the scanner. These acquisitions are produced from 512 (256 edit ON, 256 edit OFF) individual pulses.

Altering the phase cycling parameter will change the number of exported data sets. For example setting the phase cycling to 1 for the hypothetical experiment in **Figure A.1** would result in 512 sets, each one representing a time point of 1.9 s.

To investigate the time course of MEGA-PRESS experiments we acquired data from 210 scans, which covered 7 ROIs. Each MEGA-PRESS scan used the following MRS parameters: TR = 1800 ms, TE = 68 ms, volume = 30 mm^3, samples = 2048, spectral BW sample frequency

= 2150, water suppression = VAPOR, dynamic scans = 32, phase cycles = 16. We used a 3T Philips Achieva scanner (Philips Healthcare, Best, Netherlands) to obtain the MRS data. Scan duration was 921.6 s (15 min 21.6 s) per ROI.

We separated the data for each scan according to the 16 phase cycled data sets and plotted

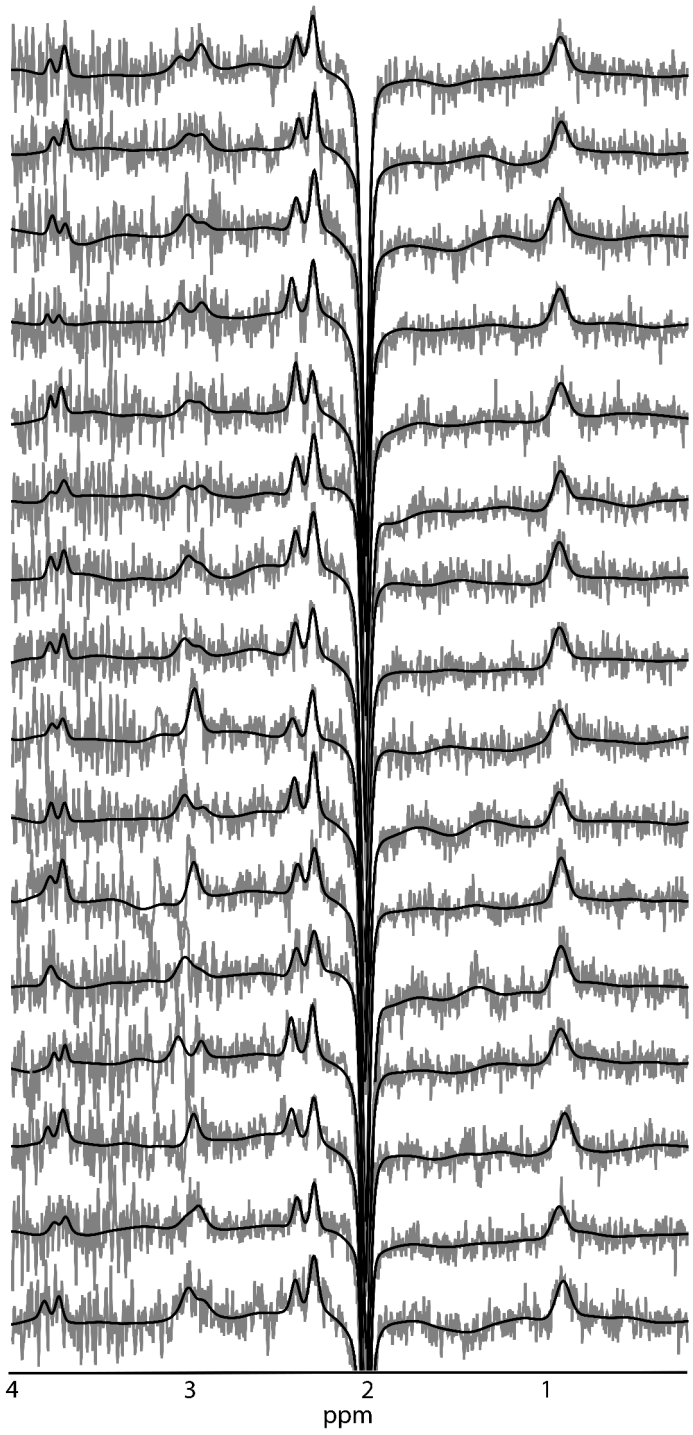

Figure A.2: Representative spectra, time course. Each spectrum represents a time point in 57.6 s increments during a 921.6 s MEGA-PRESS scan, ordered top to bottom, first acquired to last. Grey lines represent the raw spectra with metabolite model fit superimposed in black. The ROI in this example was from the right hemisphere of the motor cortex.

each as a spectrum to represent the time course of MEGA-PRESS (**Figure A.2**). Each spectrum in this figure represents 57.6 s of scanning. The topmost spectrum was the first acquired during the scan and the bottom spectrum was acquired at the end of the scan.

As shown in the figure, there is a mismatch between the fit lines and the raw spectra. There are also some noticeable differences in the line shape of the model fit of GABA at 3 ppm in each spectrum displayed. This indicates noise in the system and explains why MEGA-PRESS, indeed all MRS techniques, typically average multiple acquisitions to increase the SNR of the acquisitions.

We can investigate the improvement that this averaging produces in the fit between the model and the raw data by cumulatively adding the data acquired from each time point according to **Equation A.1**.

$$CS(t_n) = \frac{1}{N}\sum_{i=1}^{n} S(t_i) \quad \text{where n} = 16, \text{t} = \text{time} \tag{A.1}$$

The cumulative addition of spectra in **Equation A.1** improves the alignment between the raw data and the model fit with each successive time point (**Figure A.3**). This provides us with a model of the effect of shorter scan times. By truncating the data at a particular time point we can omit all of the scan data that came after the selected time point. With the scan parameters that were chosen for this project that means that we can simulate MEGA-PRESS experiments for 16 different durations from the 15 min 21.6 s experiments that we actually ran.

Our plan was to analyse spectral quality metrics for each simulated experiment. In this way we expected to characterise the changes in the metrics as a function of time. The reason

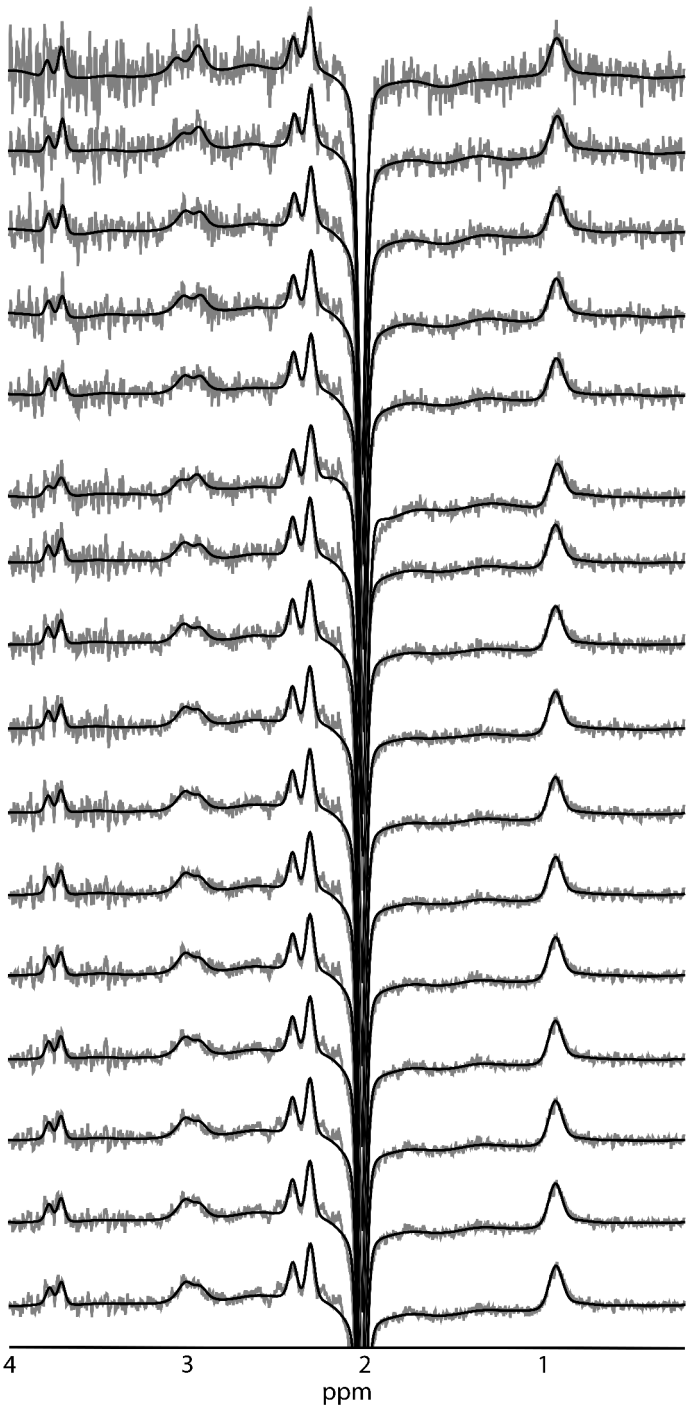

Figure A.3: Representative spectra, cumulative averages. The data in this figure comes from the same scan acquisition as **Figure A.2**. In this figure successive spectra are cumulatively added to the spectra of previous time points. The improvement in fit between the metabolite model in black and the acquired signal in grey becomes apparent towards the bottom of the figure, which represents the longest time point and hence greatest amount of signal averaging.

for doing this was to see if scan durations might be shortened, without compromising the scan data quality.

A.2.1 Regions of Interest

The ROIs from our scans covered four brain regions; lateral occipital cortex (covering lateral visual areas including those responsible for processing shape recognition and movement), motor cortex, frontal areas centred on the mid frontal gyrus and early visual cortex including V1 (**Table A.1**).

Table A.1: Number of samples by region of interest. The ROI refers to the brain area that the acquisition voxel was centred on, the early visual cortex voxels were acquired medially between the two hemispheres. Total number of samples = 210.

ROI	N
Lateral occipital, left hemisphere	28
Lateral occipital, right hemisphere	30
Motor cortex, left hemisphere	27
Motor cortex, right hemisphere	27
Mid frontal gyrus, left hemisphere	31
Mid frontal gyrus, right hemisphere	31
Early visual cortex, medial	36
Total	**210**

We calculated the mean GABA+ quantities (**Figure A.4**) for each ROI and the Cramér-Rao lower bounds (**Figure A.5**) so that we could decide whether to characterise all the acquisitions together or whether we needed to treat each ROI separately.

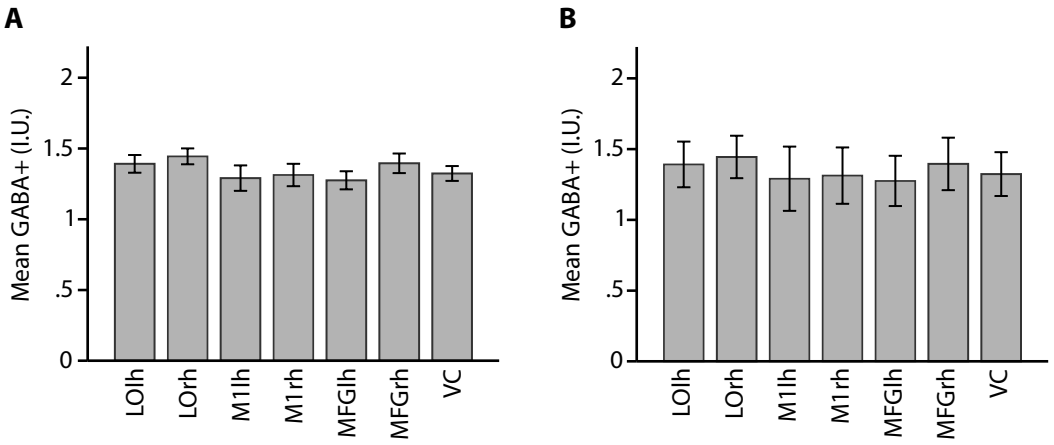

Figure A.4: GABA+ by region of interest. Mean GABA+ measurement (n = 210) by ROI; LO=lateral occipital, M1=motor cortex, MFG=mid frontal gyrus, VC=early visual cortex, lh=left hand, rh=right hand. (**A**) bars are 95% confidence intervals. (**B**) bars are one standard deviation. GABA+ quoted in arbitrary units.

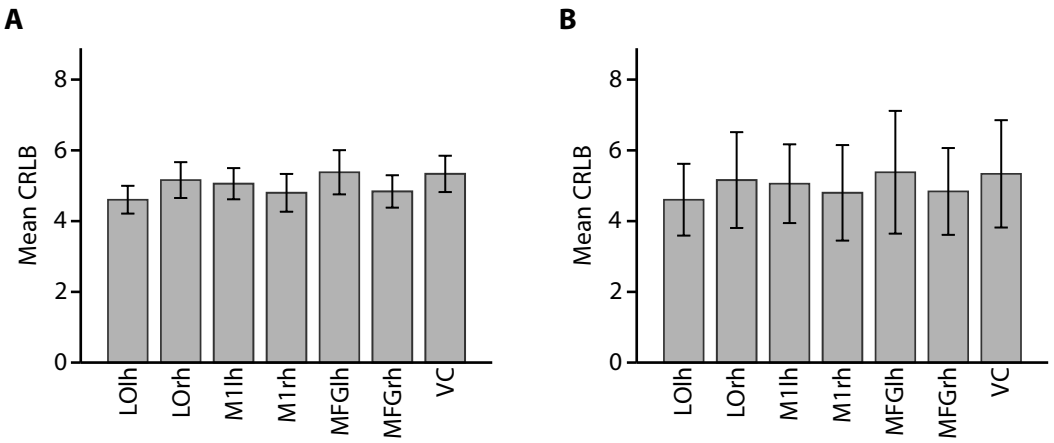

Figure A.5: Cramér-Rao lower bounds by region of interest. Mean CRLB calculations (n = 210) by ROI; LO=lateral occipital, M1=motor cortex, MFG=mid frontal gyrus, VC=early visual cortex, lh=left hand, rh=right hand. (**A**) bars are 95% confidence intervals. (**B**) bars are one standard deviation.

The mean GABA+ measurement for the ROIs was 1.35 ±0.19 (SD), the range was 1.08. The mean CRLB for the ROIs was 5.04 ±1.37 (SD), the range was 7.62. As the distribution of these values for the ROIs had small, overlapping standard deviation bars, we decided to group the ROIs together. This meant that any findings from the analysis would not be restricted to a particular brain region.

We split the data for the 210 MEGA-PRESS acquisition into 16 time courses in the same way that was described for **Figure A.3**. The first data set represented the data collected during the first 57.6 s, the second data set was collected over the first 115.2 s (i.e. it included the first data set in the average) and so forth until the 16th data set that was an average of all the data collected during the scan, and which took 921.6 s (15 min, 21.6 s). In this way each data set simulated the effect of running the same experiment 16 times, with each set being collected over a longer scan duration.

A.3 Results

In order to assess the simulated time course we analysed the following quality metrics; Q metric, signal to noise ratio and Cramér-Rao lower bounds. We also quantified the GABA+ as a function of time and correlated the longest duration scan data against each time point.

A.3.1 Q Metric

The first metric we looked at for characterising the quality of the spectra was the Tarquin Q metric (M. Wilson et al., 2011). This is defined as the standard deviation of the frequency domain residual between 0.2 ppm and 4.0 ppm, divided by the standard deviation of the spectral noise and is a measure of fit accuracy of the model line. A value of 1 is meant to indicate a perfect fit, with lower values indicating overfitting. The definition of the metric meant that random noise added to the fit would lead to an improvement (lowering) of the Q value. We therefore used this metric to characterise the decreasing noise levels that coincide with increasing numbers of averages.

This is demonstrated in **Figure A.6**, which showed a linear increase in Q with each addi-

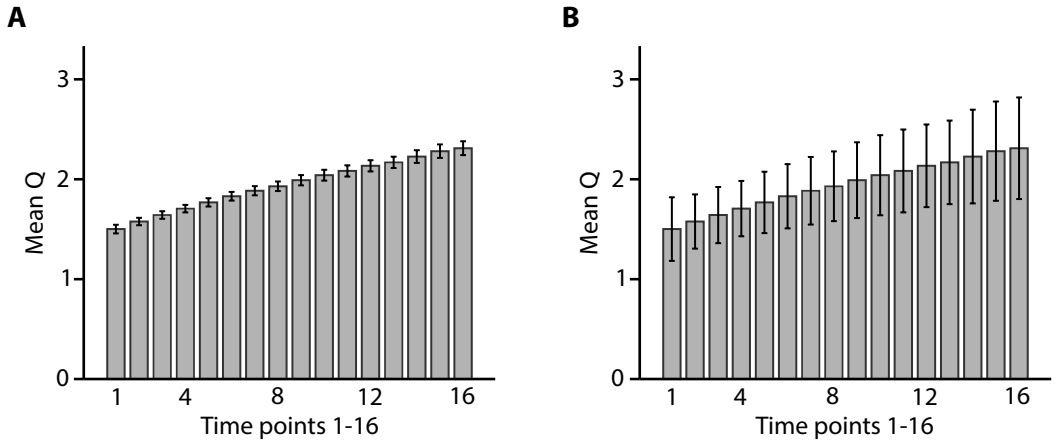

Figure A.6: Time course Q metric. Mean Q metric for cumulative averaged acquisitions (n=210). Leftmost bar is the first 32 samples (16 phase cycles of edit OFF and 16 phase cycles of edit ON), each subsequent bar adds another 32 samples so that the rightmost bar is derived from 512 samples. (**A**) bars are 95% confidence intervals. (**B**) bars are one standard deviation.

tional 32 samples that were added to the average. This chart should sound a note of caution when using the Q metric to compare spectra. Lower values (down to unity) should indicate better fits, but not in the case where random noise differs such as the case where spectra have been acquired with different numbers of averages. The Q metric would be appropriate in cases where the spectra were acquired with the same number of averages, in such cases lower Q values could be interpreted as indicating a better fit of the model. For this analysis we instead noted the implied reduction in noise that increasing Q values indicated.

A.3.2 Signal to Noise Ratio

The next metric we analysed was the signal to noise ratio (SNR). As expected, increasing the number of samples led to an increase in SNR (**Figure A.7**). Time point 4 represented a scan of 3 min 50.4 s, this was 25% of the duration of the longest scan at 15 min 21.6 s. However, its SNR of 26.7 ±4.69(SD) was 68% of the SNR for the longest time point, which was SNR = 39.15 ±7.43(SD). To put this into context, a recent paper looked at GABA quality and set the removal criteria for poor spectra at SNR < 3 (Riese et al., 2015). Even with the

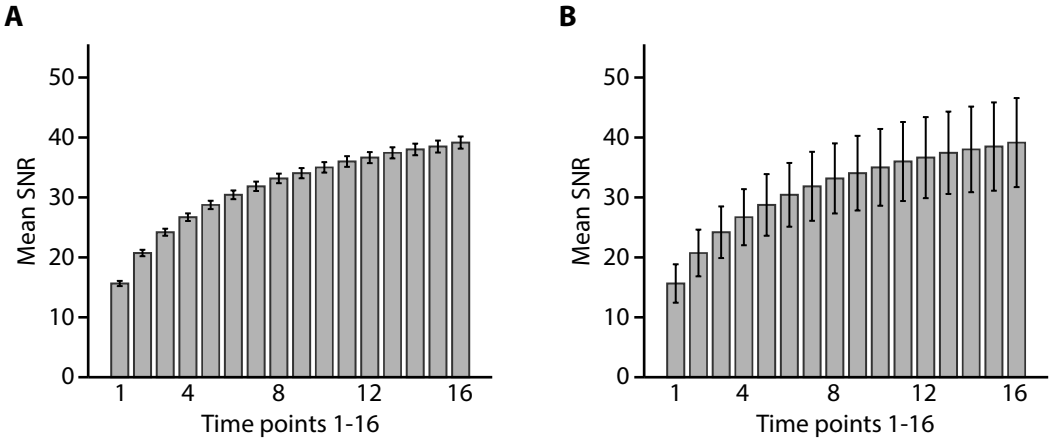

Figure A.7: Time course, signal to noise ratio. Mean SNR metric for cumulative averaged acquisitions (n=210). Leftmost bar is the first 32 samples (16 phase cycles of edit OFF and 16 phase cycles of edit ON), each subsequent bar adds another 32 samples so that the rightmost bar is derived from 512 samples. (**A**) bars are 95% confidence intervals. (**B**) bars are one standard deviation.

shortest time point in these data, the mean SNR was comfortably above this threshold and this could be achieved with a scan time of approximately one minute (57.6 s).

A.3.3 Cramér-Rao Lower Bounds

We also investigated the time course of the Cramér-Rao lower bounds (**Figure A.8**). These are metrics that are typically used to indicate the accuracy of the model fit to the data in MRS quantitation software. The values are expressed as %SD and a cut off value is chosen to indicate the level of accuracy that is acceptable and above which, spectra might be discarded as being too poor. The value varied in the literature, for example some researchers used a value of 30 (Mangia et al., 2006; Hall, Stephenson, Price, & Morris, 2014) and others used a value of 20 (Ganji et al., 2012; Riese et al., 2015; Northoff et al., 2007; Gasparovic et al., 2006). We adopted the more conservative cut off value of 20 to indicate poor quality spectra, with lower values indicating higher quality. We plotted the mean CRLB values for GABA across time points to measure the improving effect that increasing samples had.

Tarquin quantitated GABA as two peaks around 3 ppm and if a fit model quantitated an

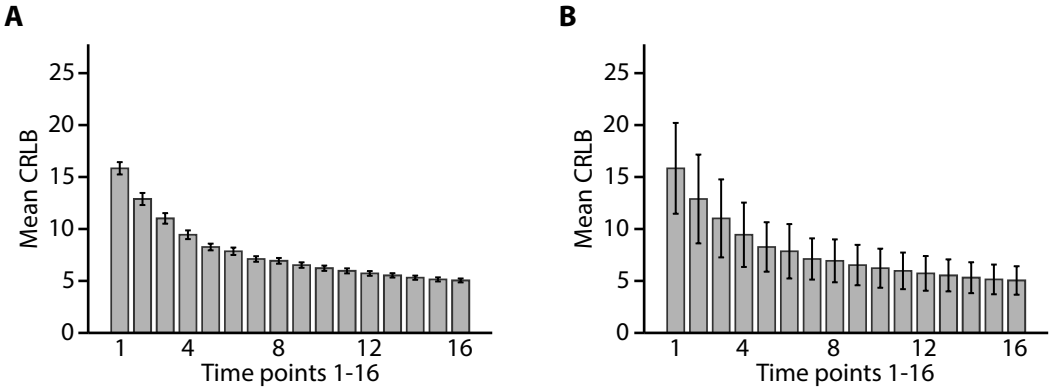

Figure A.8: Time course Cramér-Rao lower bounds (CRLB). Mean CRLB metric for cumulative averaged acquisitions (n=210). Leftmost bar is the first 32 samples (16 phase cycles of edit OFF and 16 phase cycles of edit ON), each subsequent bar adds another 32 samples so that the rightmost bar is derived from 512 samples. (**A**) bars are 95% confidence intervals. (**B**) bars are one standard deviation.

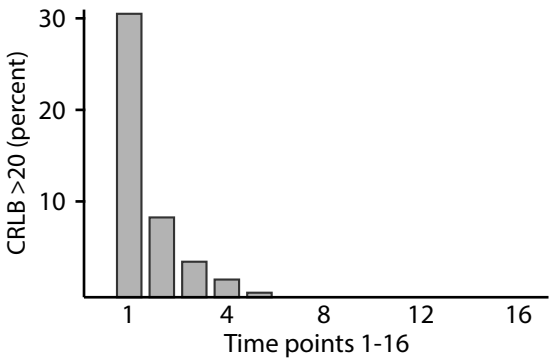

Figure A.9: CRLB exclusion criteria set to 20. Percentage of spectra whose CRLB was greater than 20 (n=210). Leftmost bar is the first 32 samples (16 phase cycles of edit OFF and 16 phase cycles of edit ON), each subsequent bar adds another 32 samples so that the rightmost bar is derived from 512 samples. Percentages with CRLB greater than 20 reduced exponentially through the first five time points (30.5%, 8.6%, 3.8%, 1.9%, 0.5%), after which there were no more cases of CRLB values above 20.

individual peak as very low, which was possible given the unreliable appearance of doublets in the raw data, then the CRLB values would become very high (they were reported as infinity where the quantitation was zero). This had a distorting effect on the mean values, therefore any CRLB values above 21 were recoded to the value 21. The mean CRLB values pointed to reliably fitted spectra (**Figure A.8A**), the first 32 samples averaged 15.84 ±4.37(SD). Using the first 25% of the acquisitions lowered the mean CRLB value to 9.44 ±3.1(SD) and this was further reduced to 5.04 ±1.37(SD) when all 512 samples were used.

Increasing the number of averages has an improving effect on the mean CRLB values. However we were also interested in the effect that the number of averages had on the absolute cutoff values. We therefore calculated the percentage of spectra whose CRLB value was above 20 (**Figure A.9**). According to our cutoff definition, these spectra would have failed to have met our quality criteria and should therefore be removed from subsequent analysis. The percentages of spectra that failed the quality criteria reduced exponentially for the first five time points, after which there were no further cases of CRLB values above 20.

A.3.4 GABA Quantification

The quality metrics are important in that they point to the reliability of the metabolite measurements. We were particularly interested on the effect that the number of acquisitions had on the actual quantification of GABA. We plotted the mean values per time point in **Fig-**

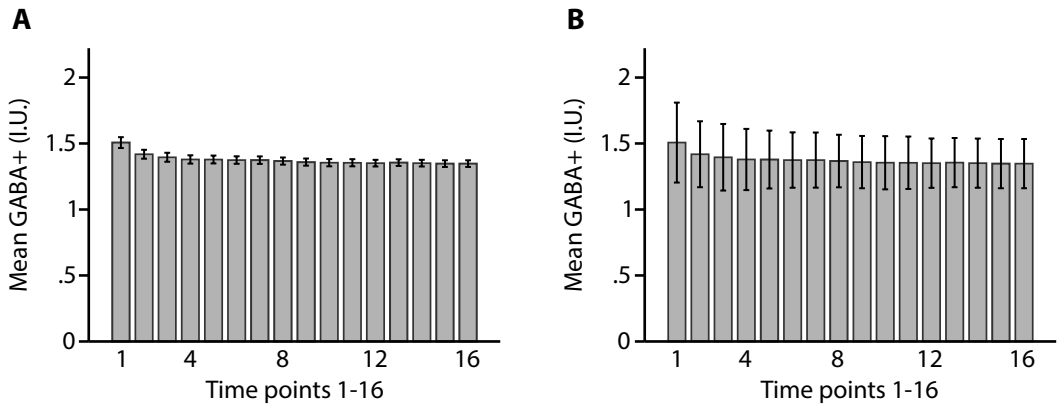

Figure A.10: GABA+ quantification. Mean GABA+ metric for cumulative averaged acquisitions (n=210). Leftmost bar is the first 32 samples (16 phase cycles of edit OFF and 16 phase cycles of edit ON), each subsequent bar adds another 32 samples so that the rightmost bar is derived from 512 samples. (**A**) bars are 95% confidence intervals. (**B**) bars are one standard deviation.

ure A.10. This showed a gradual reduction in GABA quantification as a function of the number of averages. We conducted a linear regression analysis; this found that for every 57.6 s (or approximately each minute) of acquisition time the mean GABA measurement decreased by 0.006 arbitrary units, $F(1,3358)=63.6$, $p=<0.001$. The 95% confidence intervals for the slope were -0.008 and -0.005, which led us to conclude that the effect was indeed small. We speculated that the higher values that accompanied fewer acquisitions were probably due to the additional noise being modelled as part of the GABA signal. Although the effect was small, we then wished to a ascertain whether the measurements were linearly scaled as a function of noise. If this was the case then this would mean that a case could be made for using shorter acquisitions times because the absolute values are less important than the reliability of the measurements when comparing measurements made under identical experimental conditions. In other words, if each measurement made using a scan time of five minutes was exactly 5% higher than one acquired using a scan time of ten minutes we could use either value in a correlation study, where GABA metabolite quantities are rarely expressed in anything other than arbitrary units anyway. The experiment described here was a simulation of multiple acquisi-

tions and is not really suitable for testing this hypothesis as longer acquisitions included scans from shorter ones. That being said, we plotted each time point against the last one to get an idea of how the data in the simulation correlated (**Figures A.11** and **A.12**).

For these data we noted that effect sizes of $R^2 = 0.645$ for the fourth time point (230.4 s), which increased to $R^2 = 0.779$ for the eighth time point, half way through the total scan time (460.8 s). All correlations were significant at the p=<0.05 level.

A.4 Discussion

This experiment investigated the feasibility of reducing the scan time for MEGA-PRESS experiments from a typical scan time of 15 min using a simulation of shorter scan durations based on splitting the time course of acquisitions. We investigated the GABA signals from four regions of interest (lateral occipital, motor cortex, mid frontal gyrus and visual cortex) for 210 acquisitions. We concluded that the quantitation and CRLB values for these acquisitions were similar enough to warrant analysing them all as a group rather than splitting the data by ROI. This was intended to make any findings applicable to MEGA-PRESS measurements generally and not restricted to a particular brain region.

It is known that with low concentration metabolites like GABA, more acquisitions will improve spectral quality. However, this analysis was intended to investigate whether shorter acquisitions could be made with acceptable, rather than optimal, quality. We investigated the Q metric, which had the disadvantage that the calculation becomes skewed by additional noise in the spectra, but has the advantage that it is a metric specific for the GABA peaks in the edited MEGA-PRESS experiment, as apposed to whole spectrum metrics. We showed that although noise was reduced throughout the time course of the experiment, as inferred by the increased Q value, the overlap in standard deviation bars indicated that the values were

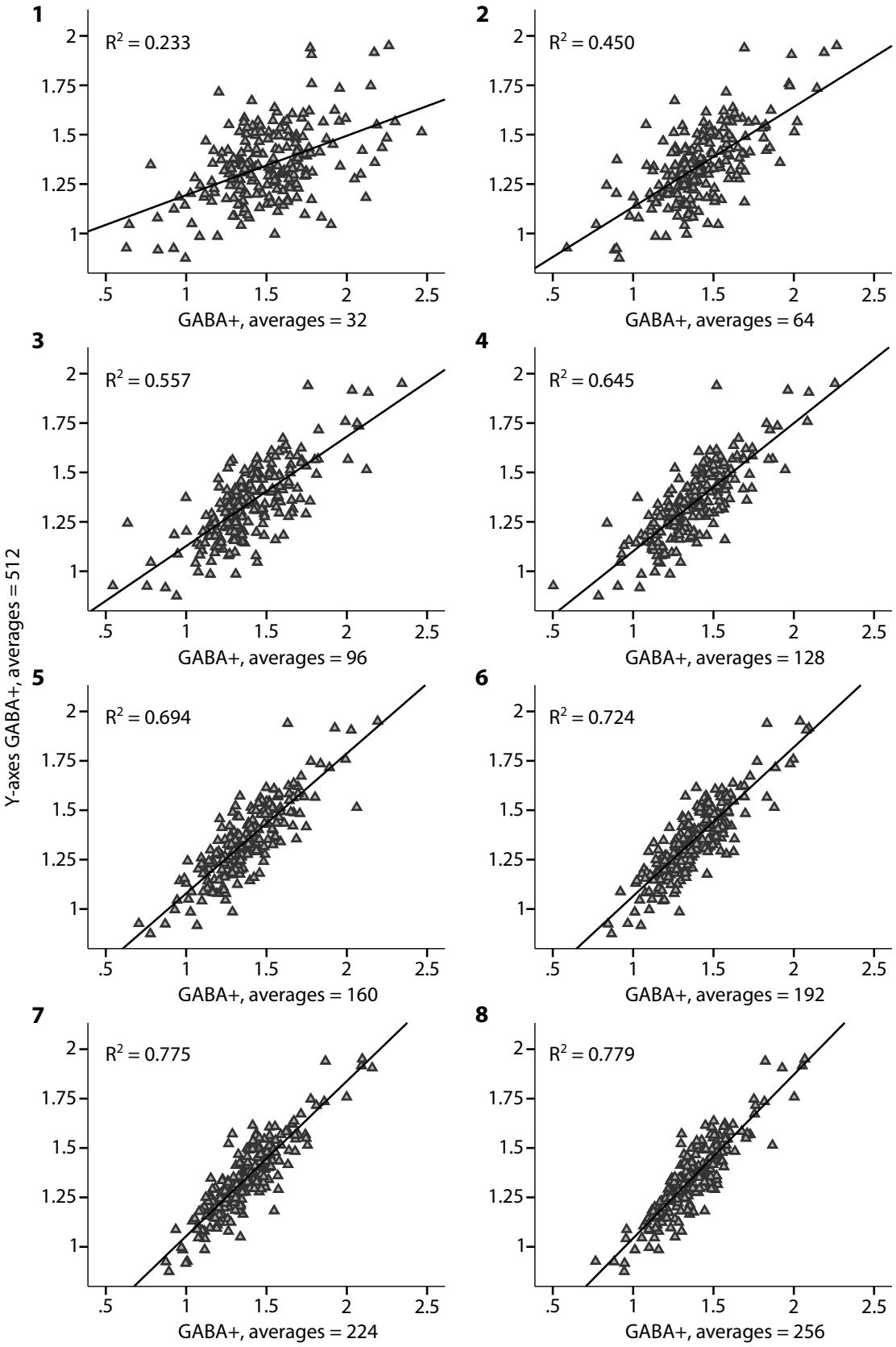

Figure A.11: Correlations, GABA+, 512 samples versus 32 to 256 samples. Plot (**1**) shows the correlation obtained from 512 samples versus 32 samples (16 edit OFF and 16 edit ON). Each subsequent numbered plot adds the next 32 samples to the x-axis averages.

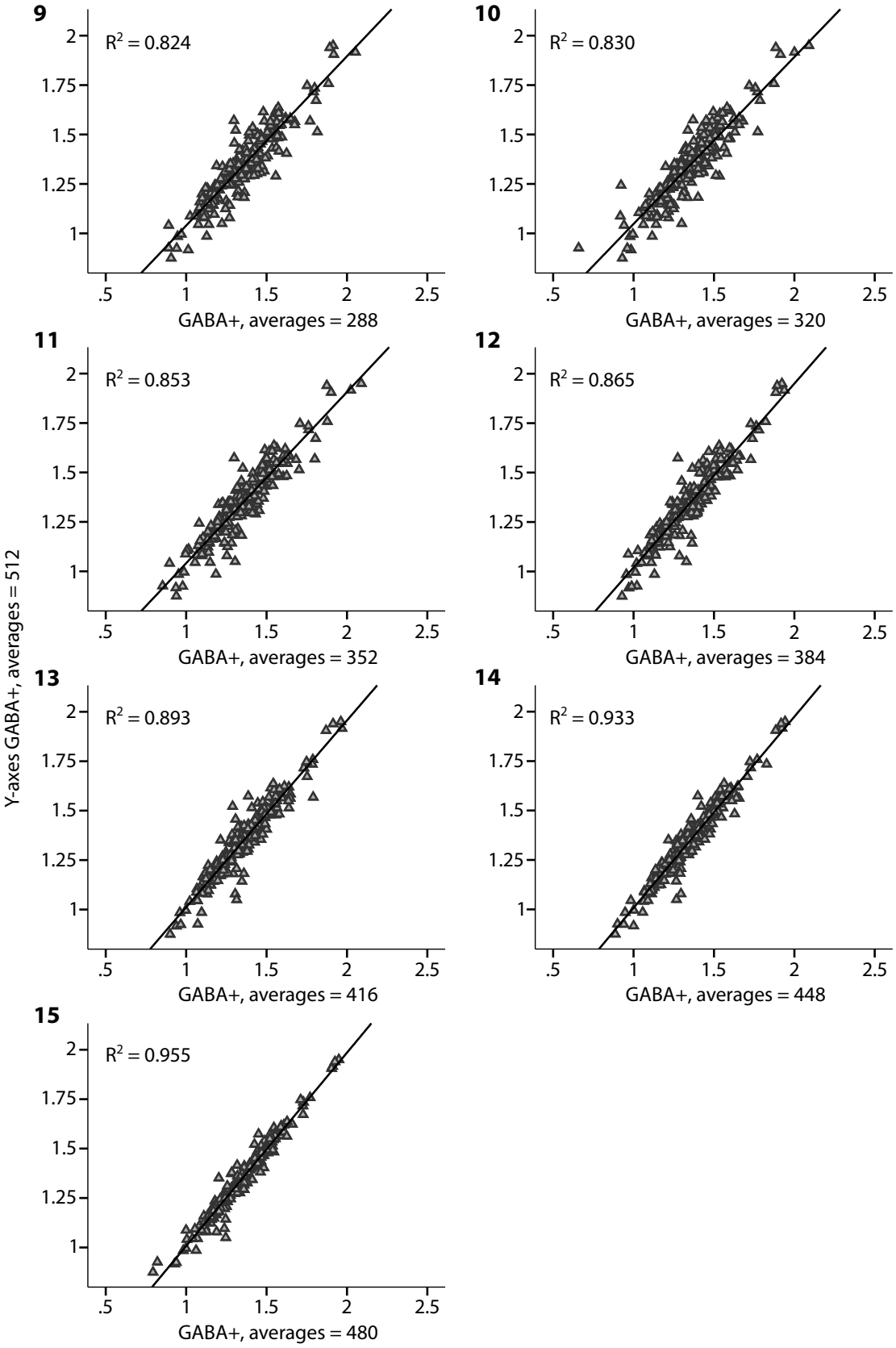

Figure A.12: Correlations, GABA+, 512 samples versus 288 to 480 samples. Plot (**9**) shows the correlation obtained from 512 samples versus 288 samples (16 edit OFF and 16 edit ON). Each subsequent numbered plot adds the next 32 samples to the x-axis averages.

not improved by much. We would characterise the change of Q value as a function of time as steady and linear.

Signal to noise ratio (SNR) is a common metric for characterising spectral quality. The analysis for SNR showed a more exponential type of increase for the first 25% of time points (approximately 4 min), which then became more linear. There was again overlap of the standard deviation bars from this time point forward and we concluded that using a scan time of less than 4 min would lead to spectra with 68% of the SNR of a 15 min scan. The actual mean SNR values for this time point were 26.7 ±4.69 and we concluded that this represented an acceptable value that represented good quality spectra.

We also looked at the Cramér-Rao lower bounds (CRLB) for the acquisitions. These lowered, or improved, in an analogous way to the increases seen in the SNR. That is they reduced steeply for the first 25% of time points before reducing steadily and linearly throughout the simulation. Overlap of the standard deviation range again indicated that a scan duration of approximately four minutes gave a CRLB value of less than half (9.44 ±3.1) of that commonly used as a cut-off value used in the field to indicate poor spectra. More importantly, we noted that scan durations of approximately 5 min (288 s) led to CRLB values that were lower than our exclusion criteria for all 210 acquisitions.

In addition to the quality metrics we also wanted to characterise the effect of shorter acquisition times had on the actual quantitation values of GABA+. We noted a small systematic decrease in measured quantity, which would mean slightly overestimated values for shorter acquisition times. We also correlated each time point against the cumulatively averaged 15 min scans. This showed significant correlations (all $p < .05$) for each time point's GABA+ quantitation values, with strong effects (r values >.6) from scan durations of approximately 4 min. We concluded therefore that reduced duration scans made very little difference to the quan-

titated GABA+ values, particularly for use in correlative studies where the absolute values are less important.

We concluded from the analysis that acquisition times shorter than 15 min might be appropriate for MEGA-PRESS experiments. The evidence from this section pointed to acquisition times as short as 230.4 s (3 min, 50.4 s), which produced acceptable data. However, these data were simulated rather than actually acquired in separate duration scans. Further validation of the shorter acquisition scans, with GABA measurements taken over a range of acquisition times, would be necessary before this conclusion could be confidently asserted. That being said, the evidence from this section indicated that shorter acquisition times were at least feasible and the experiments described here did nothing to negate the hypothesis that shorter acquisition times could be employed in further experiments. We think that this would be particularly useful for experiments where the aim was to investigate the time course of GABA, for example where a reduction of GABA was hypothesised during an experiment as a function of task mediated inhibitory processing.

B

VISUAL LEARNING PILOT STUDIES

In this appendix we document our investigations into psychophysics experiments that formed the preparations for the experiments described in **Chapter 5: Time Course of Training Difficulty Mediated Visual Learning** and **Chapter 7: GABA Versus Coarse and Fine Visual Learning**. Our aim for these investigations was to produce paradigms that elicited dissociable learning in the participants, through the manipulation of experimental parameters. The parameters that we planned to manipulate were those for the stimulus images (spiral angle and image signal), the length of sessions and the arrangement of test and training runs. As this appendix forms a record of our early investigations into visual learning paradigms, we present the pilot studies in the form of an edited lab book.

B.1 Introduction

The very first experiment that we ran had spiral angles of 30° versus 60°, noise levels of 50% versus 0%, two test runs and eight training runs of 120 stimulus images per run. Subsequent experiments were defined by changes made to any of these parameters. For example, in the second experiment we added a noise condition of 80% and in later experiments we manipulated the frequency of testing. As these pilots were attempts to investigate the parameters, we

will present them sequentially in the order that they were conceived. This is intended to show how we decided on the parameters for each new experiment. We used the results from each pilot to inform the next experiment rather than parametrically altering each variable, which would have necessitated many more pilots than we had the resources to complete.

B.2 Materials and Methods

The experiments described in this appendix were all variations of radial and concentric dot pattern classification tasks. We were interested in exploring the parameters to produce tasks where participants found it easier or more difficult to discriminate the shapes. We were also interested in the time course of learning for these paradigms and so experimented with experiment duration, for example we varied the length of runs and sessions throughout the pilot studies.

B.2.1 Stimulus Presentation

We manipulated the spiral angles and noise levels of dot patterns to produce radial and concentric shapes that were more discriminable (*Easy*) or less discriminable (*Hard*). A full description of the procedure is detailed elsewhere in this thesis (e.g. the methods sections of **Chapters 5, 6 and 7**), so for brevity we will omit this here and refer the reader to **Section 7.2.2**. In that section we explain how manipulating the spiral angle and noise levels effect the stimuli to produce the various experimental conditions, for example *Easy* or *Hard*. Samples of the type of stimuli that we use in the experiments are provided in **Figures 5.2 and 7.2** (in **Chapters 5 and 7**).

One parameter that we kept constant throughout all of the experiments was the stimulus presentation time, which was 200 ms. We wished to keep the presentation time short for two reasons: Firstly, we wanted the subjects to base their decisions on global features and

Table B.1: Stimuli presentation times. A selection of studies with similar stimulus parameters to those we planned to use.

Time (ms)	Stimuli	Reference
167	Glass patterns	H. R. Wilson & Wilkinson, 1998
300	Gabor fields	Altmann et al., 2003
332	Glass patterns	Ostwald et al., 2008
200	Glass patterns	Li et al., 2009
200	Glass patterns	Zhang, Meeson, Welchman, & Kourtzi, 2010
200	Gabor fields	Zhang & Kourtzi, 2010
200	Gabor fields	Kourtzi, 2010
300	Glass patterns	Mayhew & Kourtzi, 2013

limit scrutiny of local features. Secondly, we planned the experiments to make them compatible with fMRI experiments, where the duration of the stimuli presentations needs to be controlled with regard to the scan repetition time (TR). In fMRI experiments the TR is typically 1.5–2 s, so sufficient time for subject response needs to be factored in to the timing of the stimulus presentations. The short duration of the stimulus presentation has the advantage that it reduces the opportunity for eye movement, which is another consideration for fMRI experiments. We consulted literature for similar dot pattern paradigms and noted presentation times of 167–332 ms (**Table B.1**), with 200 ms being the most common value.

We reasoned that 200 ms would be suitable for our experiments as it is short enough to meet the constraints of fMRI and has been shown to evoke learning in experiments that had similarities to those that we were planning. By fixing the same presentation time for all experiments meant that we had one less parameter to manipulate and therefore reduced the complexity of the setup.

We presented all stimuli on a 21-inch CRT monitor (resolution 1280×1024 pixels, 85 Hz frame rate) in low light conditions. We fixed the viewing distance at 47 cm with a chin rest. We generated and presented the stimulus images using Matlab (The MathWorks, Inc., Natick, Massachusetts, USA) and Psychtoolbox version 3 (Brainard, 1997; Pelli, 1997).

From the participants perspective the experiments consisted of stimulus presentations (trials) that the subjects were tasked to classify as one of two types of shape. The stimulus presentations were organised in blocks of between 60 and 120 images. Each block was defined as either a training block or a test block. In training blocks audible feedback was provided for incorrect responses, no feedback was provided in test blocks. We varied both the number of blocks and the frequency of testing (test blocks) in different experiments.

B.2.2 Performance Evaluation

A typical session for the experiments described in these pilot studies involves approximately 1000 stimulus presentations, which the participants were tasked to categorise as a particular pattern. The sessions were presented sequentially and arranged in separate blocks with forced breaks in between. Some sessions were run over several days. This meant that there were potentially many ways that the performance could be evaluated. For example, performance could be grouped into arbitrarily sized bins according time, or metrics could be used to characterise performance gains across or within sessions. Performance could be evaluated in terms of the percentage of correct responses, or weighted to account for bias by using techniques such as d-prime (*d'*).

We began our pilots by concentrating on simple metrics and straightforward groupings. For example, in **Figure B.1** we have a sample chart that shows the performance of a single subject across one session. The performance is evaluated using a percent correct measure. We track bias informally by recording the percentage of responses for a given experimental condition. The sample chart represents the classification accuracy of two conditions, *radial* and *concentric*. Therefore a non biased observer should have equal numbers of responses to each condition, as there are equal numbers of *radial* and *concentric* presentations in each

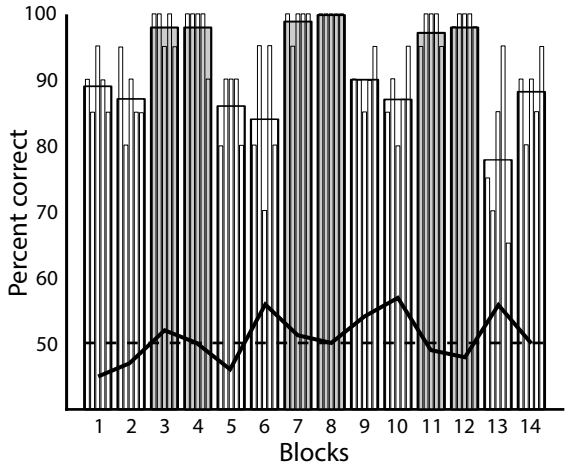

Figure B.1: Sample pilot study performance measures. This chart is representative of the type of chart we used to investigate learning performance in a session. Each run has been divided into five bins that show the percent correct metric for five time points within each block. The percent of responses that the subject answered 'radial' is indicated by the lower black line, which can be compared with the 50% line (dotted).

block. By plotting the percent of *radial* responses for each block, we can track bias as it will show as deviations from the (unbiased) 50% line.

We also presented our results averaged over sessions and participants and calculated various learning indices to produce charts such as the ones in **Figure B.2**.

Although there are many different types of analysis that could be used to characterise performance in psychophysics experiments we wished to keep our metrics as simple as possible. This suited the exploratory nature of the pilots. By standardising the measurements that we used in each pilot we were able to compare each iteration rapidly with those that preceded them. For these reasons we decided to represent performance in the pilot study tasks as the

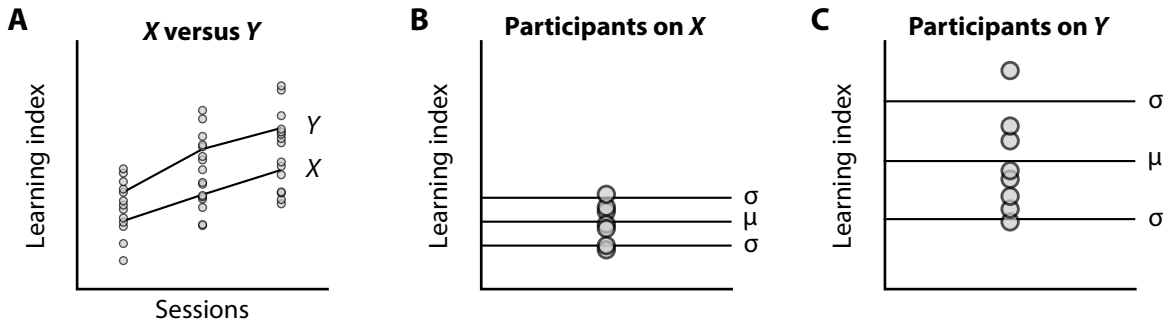

Figure B.2: Sample pilot study average performance measures. These charts are representative of the type of charts we used to investigate performance averaged over sessions or experiments. **(A)** Comparing two hypothetical conditions *X* and *Y* across three sessions. Lines indicate mean performance and circles represent individual participant scores on a (unspecified) learning metric. **(B)** Individual participants' performance for condition *X*, lines indicate statistics such as mean and standard deviation. **(C)** Contrasting performance for condition *Y*.

percentage of correct classifications in each run. We defined the *Percent Correct per Block (PCB)* metric as in **Equation 6.1** (see **Section 6.2.2: Behavioural Indexes**) to give the mean correct response scores for each block.

We also recorded the response time for each trial so that we could determine whether this changed over the course of the experiments. We expected that participants might become quicker with practice on the tasks, but we also considered that speed of response on correct trials might be another indicator of learning performance.

B.2.3 Participants

All observers were screened prior to participating in the experiments. The screening protocol involved a visual acuity test and a questionnaire for contraindications for the experiments. We defined the contraindications as poor vision, elevated alcohol, medication, or caffeine levels (self reported) or prior experience of the stimuli. We also included contraindications for fMRI experiments, such as metal contamination and history of epilepsy. These were included in case we extended the behavioural pilots to magnetic resonance imaging or spectroscopy studies. New participants were recruited for each pilot study (none were used on more than one pilot, although some took part in multi-sessions for the same study). The mean age of the participants was 21 and there was an approximate gender split of 50/50. All participants gave written, informed consent to take part and were paid for each session they completed. The studies were approved by the University of Birmingham ethics committee.

B.3 Visual Learning Pilot Experiments

We designed the pilot studies to investigate the parameters of Glass pattern experiments so that we could optimise settings to evoke dissociable learning performance. We present them in the order that they were run so that the reader might follow the reasoning that led to the

experimental setup described in **Chapters 5, 6 and 7**. To facilitate this we present the work as an edited lab book with a standard structure for each subsection (*Aims:, Design, Results* and *Conclusions*).

Exploratory Pilot

The first pilot that we ran was was used to get some general ideas about how varying parameters like spiral angle and image noise might influence performance in discriminating radial and concentric patterns. The participants were researchers involved in psychophysics research, including the author. This was the only pilot that was not completed by participants who were agnostic to the stimuli and research goals for the experiments. For this reason we refer to this experiment as the *Exploratory Pilot* to indicate that it was used to gain some insight into the participants' experience of the tasks.

Aims: We hypothesised that spiral angles that were closer together (e.g. 30° versus 60°) would be more difficult to discriminate than those that were further apart (e.g. 0° versus 90°). We also assumed that patterns with higher signal, that is those with less randomly oriented noise dots, would be easier to distinguish compared to those with lower signal. To test this we designed a stimulus space that included closer and wider spiral angles and two levels of signal. What we wanted to find out from running this pilot was how the spiral angles and noise levels influenced performance between the pre-training and post-training test blocks.

Design: We arranged the sequence of the experiment in blocks of 120 stimulus images per block (**Figure B.3: A**). We decided to use 120 images per block as this number has 16 factors and so is flexible for testing multiple conditions within a single block. We estimated that in a self-paced experiment, participants would complete each trial within 2 seconds and this lead

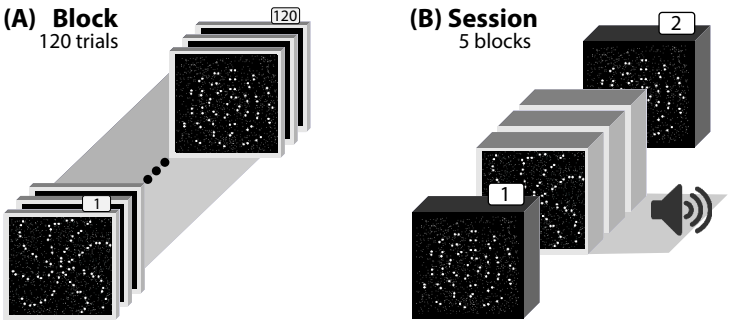

Figure B.3: ***Exploratory Pilot* design.** Each block **(A)** consisted of 120 trials. The session **(B)** consisted of two test blocks (dark, numbered boxes) and three training blocks (lighter boxes with audio icon).

to a block duration time of approximately 4 minutes. We thought that this duration would not be too fatiguing for the participants, whilst still providing sufficient data for us to quantify any performance improvements.

The arrangement of blocks for our first experiment had a test block, followed by three training blocks and a final test block (**Figure B.3: B**). This is a common way of arranging psychophysics experiment, with the first test block representing the pre-training base performance and the last test block representing the post-training learning effect. The training blocks were different from the test blocks as the training blocks had audible error beeps for each incorrect trial.

The stimuli consisted of radial and concentric dot patterns and we set the spiral angles to 0°, 30°, 60° and 90° spiral angles. We set the signal levels to 50% and 100% to give a total of four conditions for the experiment. Other experimental parameters are as detailed in **Table B.2**.

Table B.2: ***Exploratory Pilot* design.** Parameters for the *Exploratory Pilot*: **N** = number of participants, **Images** = number of images per block, **Blocks** = number of blocks per session, **Radial** = radial pattern spiral angle(s) in degrees, **Concentric** = concentric pattern spiral angle(s) in degrees, **Signal** = percent of signal dots, **Sessions** = number of sessions.

	N	Images	Blocks	Radial	Concentric	Signal	Sessions
Test	2	120	2	0 & 30	60 & 90	50 & 100	1
Train	2	120	3	0 & 30	60 & 90	50 & 100	1

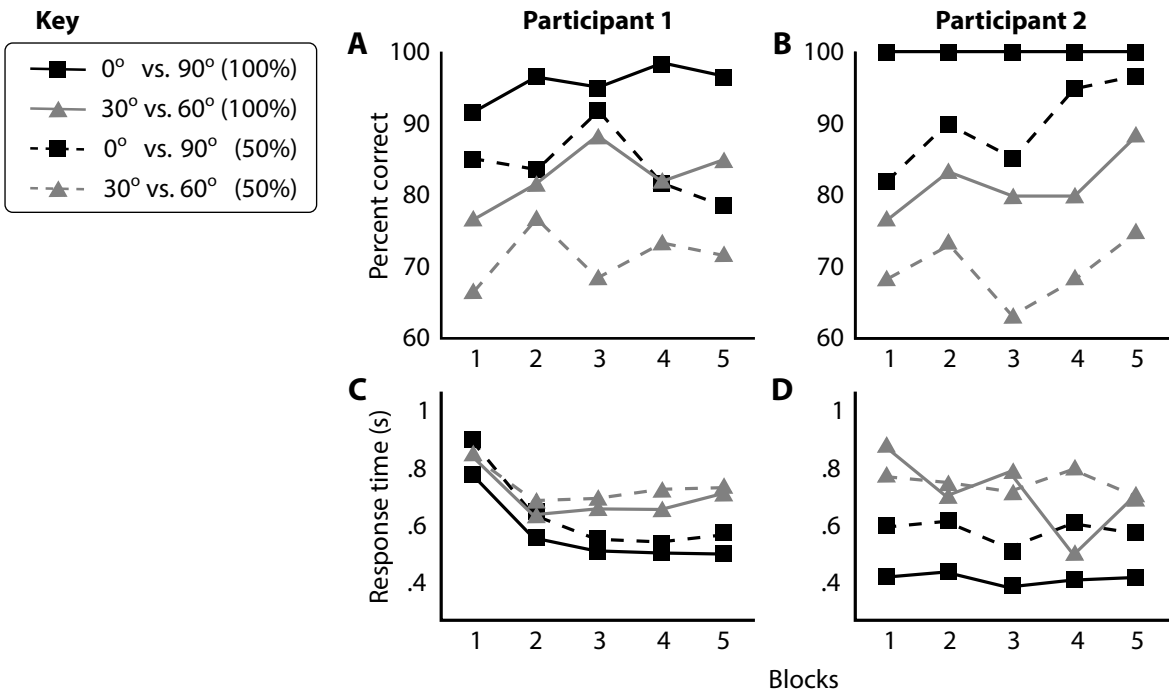

Figure B.4: *Exploratory Pilot* results. (A) and **(B)** *Percent Correct per Block (PCB)* in four conditions, based on spiral angles and signal percentage. The *x*-axes are blocks within the session. Test blocks are numbered 1 and 5, training blocks are numbered 2–4. **(C)** and **(D)** are the response times in seconds for the four conditions.

Results: We plotted the *Percent Correct per Block (PCB)* according to the four conditions for both participants (**Figure B.4: A,B**). We also plotted the mean response time by block (**Figure B.4: C,D**).

Conclusions: The results showed that bigger differences in spiral angle led to higher performance and higher signal images were easier to discriminate than lower signal images. This is intuitively obvious and completely expected. Results in the post-training block (run number 5) were generally higher than in the pre-training block (run number 1) and we interpreted this to indicate that learning had occurred during the training blocks (runs 2–4). The response times looked like they might be correlated with the performance, with faster responses for the more discriminable stimuli. However we did not use any statistical metrics on this data as the sample size was small. A further caveat to add about these results are that the participants

might be considered more practised than typical.

We concluded from these results that the 30° versus 60° spiral angles might be suitable for further pilot experiments. The performance on the 0° versus 90° angles indicated that this was probably too easy to discriminate as performance was above 80% correct before training in both the high and lower signal conditions. We wished to quantify performance improvement for the shape discrimination pilots and so preferred parameters that resulted in lower pre-training performance than those we measured for the 0° versus 90° conditions. From this perspective, all of the initial performance (i.e. *PCB* on the first run) was probably higher than we would like as higher initial performance leaves less room for improvement. After considering the results from this pilot, we decided to make subsequent experiments more difficult. We could do this by either narrowing the spiral angles, which would make the shapes less discriminable or by increasing the image noise.

Pilot 1

In this study we dropped the 0° versus 90° condition that featured in the *Exploratory Pilot* and lowered the signal in an attempt to make the tasks more difficult. This study used participants who were agnostic to the stimuli and were not connected to the research goals of our group. We increased the number of participants on this study and made the task longer by adding five more training runs.

Aims: Our aims for *Pilot 1* were to explore trends in visual learning over a single session of approximately one hour's duration.

Design: The main difference in the design of *Pilot 1* to the previous *Exploratory Pilot* was the addition of extra training runs. The extra training blocks were inserted between the pre-

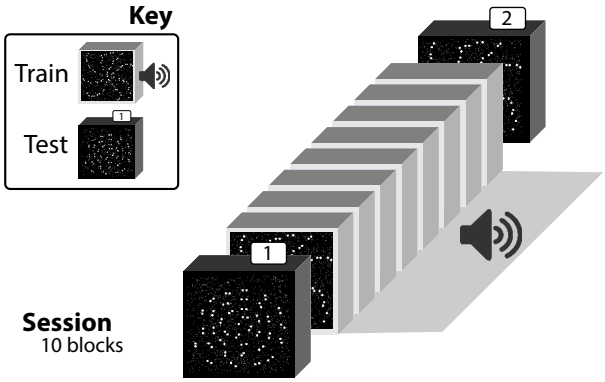

Figure B.5: *Pilot 1* design. A session consisted of two test blocks (darker boxes with number swatches) and eight training blocks (lighter boxes with audio icon).

training and post-training test blocks, as before (**Figure B.5**).

In *Pilot 1* we trained and tested participants to distinguish between two spiral angles (30° versus 60°). In addition, we manipulated the signal level of the trials on 2 levels: 50% and 100% during training runs and 45% and 95% during testing blocks.

Table B.3: *Pilot 1* design. Parameters for *Pilot 1*: **N** = number of participants, **Images** = number of images per block, **Blocks** = number of blocks per session, **Radial** = radial pattern spiral angle(s) in degrees, **Concentric** = concentric pattern spiral angle(s) in degrees, **Signal** = percent of signal dots, **Sessions** = number of sessions. Bold numbers represent changes from the previous pilot parameters.

	N	Images	Blocks	Radial	Concentric	Signal	Sessions
Test	5	120	2	**30**	**60**	**45 & 90**	1
Train	5	120	**8**	**30**	**60**	50 & 100	1

The parameters for the experiment are listed in **Table B.3**. Where a parameter is changed from the previous *Exploratory Pilot*, we have emboldened the number to help identify the changes. In **Table B.3** the parameters changed were the number of training blocks, the radial and concentric spiral angles (for test and training) and the signal percentages (for the test blocks). We lowered the signal by 5% in the testing blocks.

Results: We calculated the average *Percent Correct per Block (PCB)* for each run of the experiment and split the results according to the high and low signal conditions (**Figure B.6: A**). We plotted the mean response time, which we calculated for correct responses only (**Figure B.6: B**).

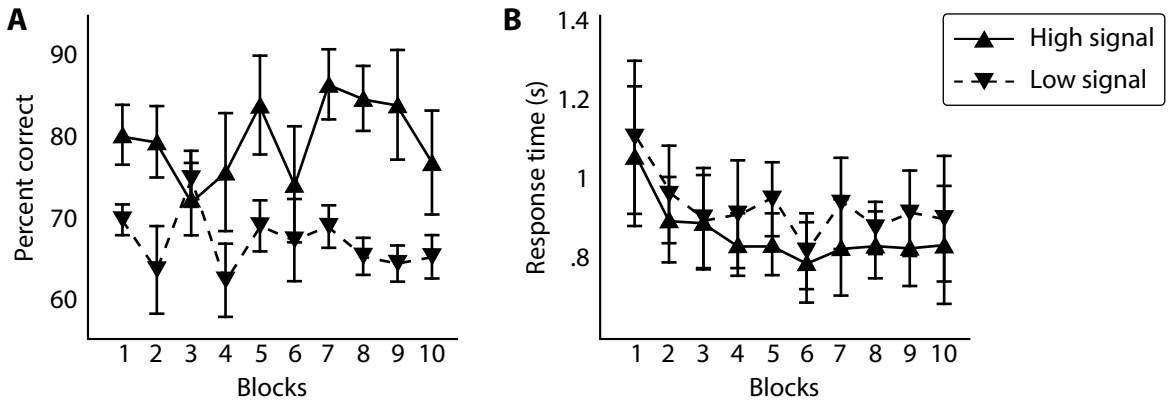

Figure B.6: *Pilot 1* results. (A) *Percent Correct per Block (PCB)* for high and low signal conditions. **(B)** Response time for correct responses for high and low signal conditions. Error bars are standard error.

Conclusions: The starting performance for the task was high in both signal conditions: It was $\approx$ 70% in the low signal condition and $\approx$ 80% in the high signal condition. There was no evidence that the training runs evoked a learning effect as the final performance on the last test run (block 10) had not improved from the starting performance.

The response time decreased by approximately 100 ms from block one to block two, although the variability has high as shown by the size of the error bars. We did not discern a decreasing trend in response times for subjects on this paradigm.

The lack of a discernible learning effect for these parameters, suggested to us that we needed to rethink the parameters for the next pilot study. In particular we wanted to investigate parameters that might show some learning transfer from the training blocks to the final test block.

Pilot 2A

We were beginning to formulate a hypothesis that training on more discriminable tasks might transfer to less discriminable tasks. This led us to try setting parameters that would make the training runs more discriminable (*Easy*) and the test runs less discriminable (*Hard*).

Aims: Our aims for *Pilot 2A* were to see if training on *Easy* tasks transferred to learning on *Hard* tasks.

Design: The arrangement of blocks on *Pilot 2A* was the same as in *Pilot 1* (see **Figure B.5**). We set the signal level to 80% for all training runs in order to make the training runs more discriminable. We tested the participants images with signal of 80% and 50%, with the lower signal representing the *Hard* condition (**Table B.4**).

Table B.4: *Pilot 2A* design. Parameters for *Pilot 2A*: **N** = number of participants, **Images** = number of images per block, **Blocks** = number of blocks per session, **Radial** = radial pattern spiral angle(s) in degrees, **Concentric** = concentric pattern spiral angle(s) in degrees, **Signal** = percent of signal dots, **Sessions** = number of sessions. Bold numbers represent changes from *Pilot 1* parameters.

	N	Images	Blocks	Radial	Concentric	Signal	Sessions
Test	4	120	2	30	60	**50 & 80**	1
Train	4	120	8	30	60	**80**	1

Results: We plotted the *Percent Correct per Block* and response times for the high and low signal (*Easy* and *Hard* conditions), see **Figure B.7**.

Conclusions: We were most interested in the performance on the *Hard* condition, which was represented in **Figure B.7A** as the low signal *PCB* in blocks one and ten. The performance was only marginally higher (with overlap of the error bars) in the post-training block compared with the pre-training block. The performance on the *Easy* condition showed a similar lack of improvement throughout the session. We concluded that altering the signal level to make

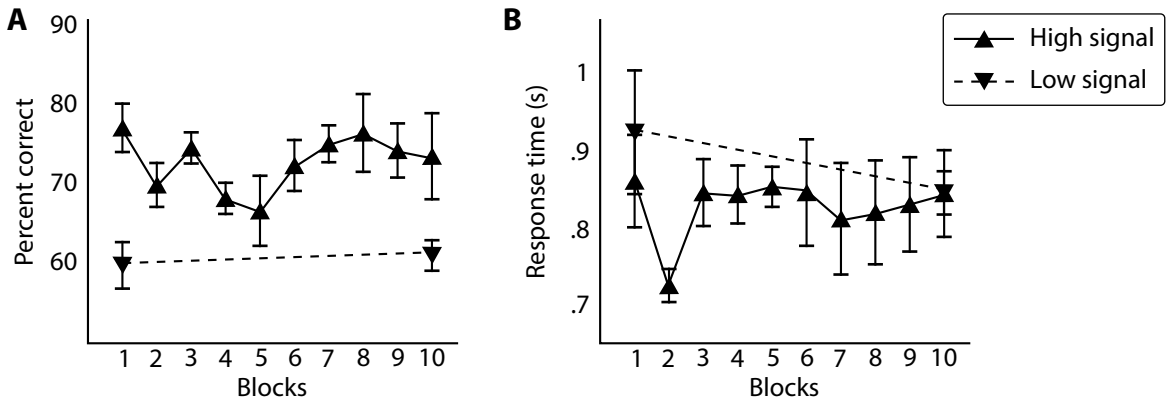

Figure B.7: *Pilot 2A* results. (A) *Percent Correct per Block (PCB)* for high and low signal conditions. **(B)** Response time for correct responses for high and low signal conditions. Error bars are standard error.

Easy training conditions did not evoke a learning effect. Response time of approximately 1 s were recorded across the session with no discernible overall improvement.

Pilot 2B

The results from *Pilot 2A* led us to consider that we should try varying the spiral angle, rather than the signal level to produce the *Easy* versus *Hard* conditions.

Aims: Our aims for *Pilot 2B* were still to see if *Easy* training transferred to a *Hard* task, but this time we would vary the spiral angle to produce the conditions.

Design: The arrangement of blocks was the same as in *Pilot 1* (**Figure B.5**). The *Easy* training condition was defined by discriminable spiral angles of 10° versus 80° and in the *Hard* condition the angles were set to 30° versus 60°. For this paradigm we keep the signal level

Table B.5: *Pilot 2B* design. Parameters for *Pilot 2B*: **N** = number of participants, **Images** = number of images per block, **Blocks** = number of blocks per session, **Radial** = radial pattern spiral angle(s) in degrees, **Concentric** = concentric pattern spiral angle(s) in degrees, **Signal** = percent of signal dots, **Sessions** = number of sessions. Bold numbers represent changes from pilot 2A parameters.

	N	Images	Blocks	Radial	Concentric	Signal	Sessions
Test	5	120	2	**10 & 30**	**60 & 80**	**50**	1
Train	5	120	8	**10**	**80**	**50**	1

constant at 50% for every trial (**Table B.5**.).

Results: We plotted the *Percent Correct per Block* and response times for the *Easy* and *Hard* conditions, as in **Figure B.8**.

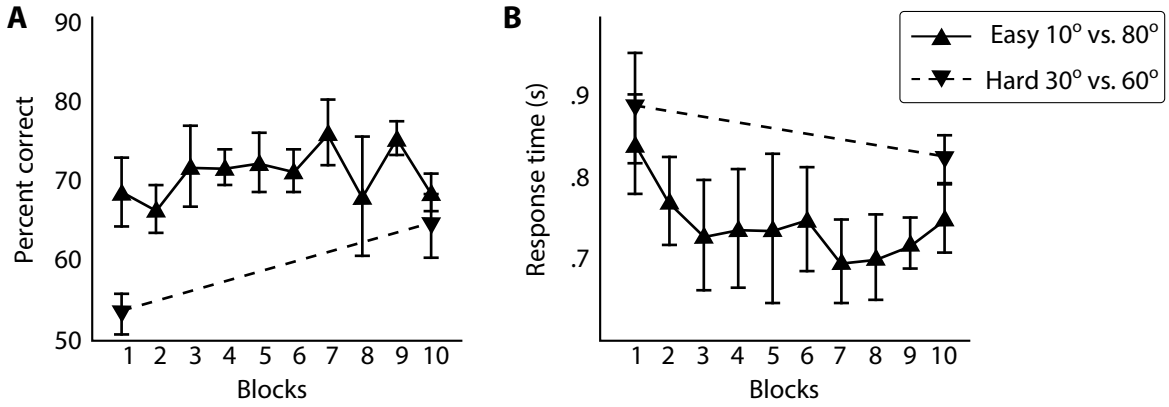

Figure B.8: *Pilot 2B* results. (A) *Percent Correct per Block (PCB)* for high and low signal conditions. **(B)** Response time for correct responses for high and low signal conditions. Error bars are standard error.

Conclusions: Performance improved in the *Hard* condition, from $\approx$ 55% in the pre-training block to $\approx$ 65% in the post-training block. We interpreted this to represent a transfer learning effect from the *Easy* training. Response times were on average approximately 200 ms quicker than *Pilot 2A*, although they started at a similar duration in the first block.

Pilot 3

The previous experiment (*Pilot 2B*) showed a potential learning transfer effect from an *Easy* training condition to a *Hard* test condition. We designed *Pilot 3* to probe this finding further.

Aims: We wished to investigate the time course for the learning transfer that we inferred from the results in *Pilot 2B*. One way to do this is to increase the frequency of testing. Another idea we wished to test was whether making the training conditions easier than in *Pilot 2B* would elevate the learning effect.

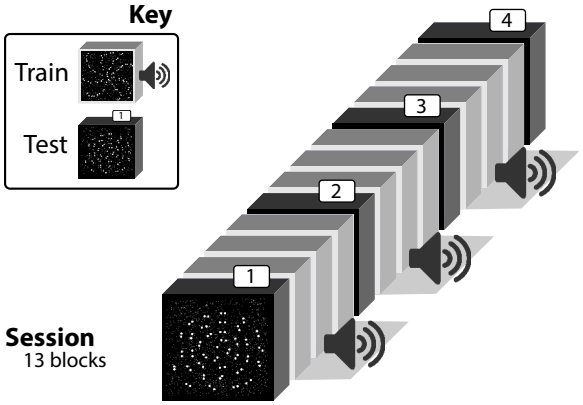

Figure B.9: *Pilot 3* design. A session consisted of four test blocks (dark, numbered boxes), including two 'mini' tests and nine training blocks (lighter boxes with audio icon).

Design: The main change to the design of *Pilot 3*, compared to our previous studies was the addition of two 'mini' tests, which we interleaved with the training blocks. These additional test runs had 60 stimulus images instead of 120, which was the number of stimuli in the other runs (**Figure B.9**).

A further change we made to the experimental design was to increase the signal of the *Easy* training images from 50% to 70% (**Table B.6**).

Table B.6: *Pilot 3* design. Parameters for *Pilot 3*: **N** = number of participants, **Images** = number of images per block, **Blocks** = number of blocks per session, **Radial** = radial pattern spiral angle(s) in degrees, **Concentric** = concentric pattern spiral angle(s) in degrees, **Signal** = percent of signal dots, **Sessions** = number of sessions. Bold numbers represent changes from pilot 2B parameters.

	N	Images	Blocks	Radial	Concentric	Signal	Sessions
Test	1	**60 & 120**	**4**	10 & 30	60 & 80	**50 & 70**	1
Train	1	120	**9**	10	80	**70**	1

Results: We plotted the *Percent Correct per Block* and response times for the *Easy* and *Hard* conditions, as in **Figure B.10**.

Conclusions: The results for *Pilot 3* did not show a learning effect between the pre-training and post-training test runs (blocks 1 & 13). There was arguably some evidence of learning during the *Easy* training blocks, as performance rose from 80% to 90% through the course of the experiment. Response times were higher on the test runs for this paradigm. As the

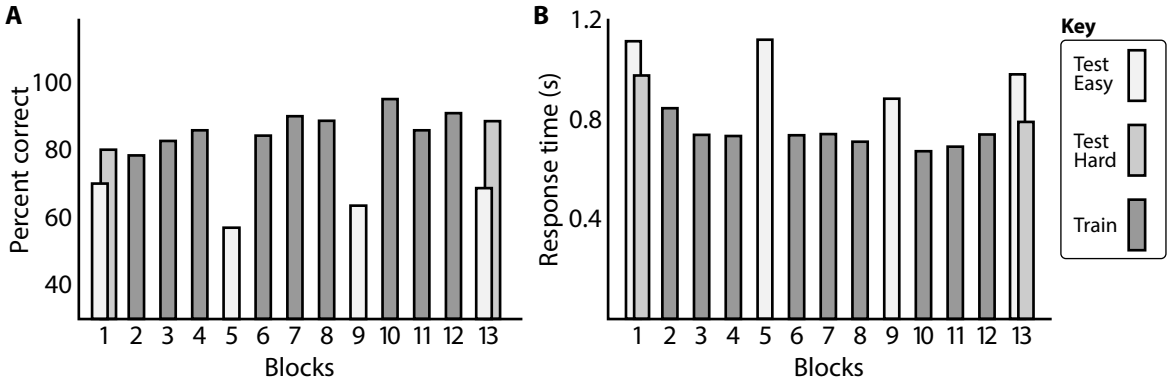

Figure B.10: *Pilot 3* results. (A) *Percent Correct per Block*. **(B)** Response time in seconds. The pre-training test (block 1) and the post-training test (block 13) contained *Easy* and *Hard* testing conditions.

training tasks had been made easier, we attributed the slower response times as an effect of the bigger difference between training and testing conditions. The baseline performance (i.e. the untrained *PCB* in block one) was higher than we were expecting at $\approx$ 70%. This caused us to make further changes to the design as we wished to avoid a paradigm where participants had high initial performance (as this would leave less room for improvement for any training transfer effects).

Pilot 3A

To address the problem of high starting performance that we observed in *Pilot 3* we increased the noise levels in the images.

Aims: The aims were similar to the previous study (*Pilot 3*), but we increased the testing frequency.

Design: The main change to the design was an additional 'mini' test (**Figure B.11**). This brought the total of test blocks to five (from four) and meant that there were two training blocks between each test. In *Pilot 3* the training blocks were run as groups of three consecutive runs.

An additional parameter change we introduced was to reduce the signal level of the 10°

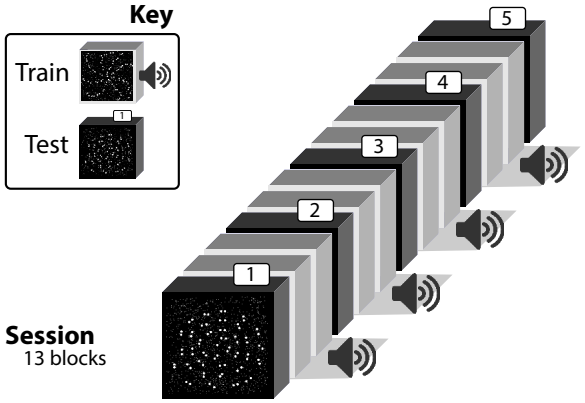

Figure B.11: *Pilot 3A* design. A session consisted of five test blocks (dark, numbered boxes), including three 'mini' tests and eight training blocks (lighter boxes with audio icon).

versus 80° images in the test runs from 70% to 50% (**Table B.7**).

Table B.7: *Pilot 3A* design. Parameters for *Pilot 3A*: **N** = number of participants, **Images** = number of images per block, **Blocks** = number of blocks per session, **Radial** = radial pattern spiral angle(s) in degrees, **Concentric** = concentric pattern spiral angle(s) in degrees, **Signal** = percent of signal dots, **Sessions** = number of sessions. Bold numbers represent changes from *Pilot 3* parameters.

	N	Images	Blocks	Radial	Concentric	Signal	Sessions
Test	5	60 & 120	**5**	10 & 30	60 & 80	**50**	1
Train	5	120	**8**	10	80	70	1

Results: We plotted the *Percent Correct per Block* and response times for the *Easy* and *Hard* conditions, as in **Figure B.12**.

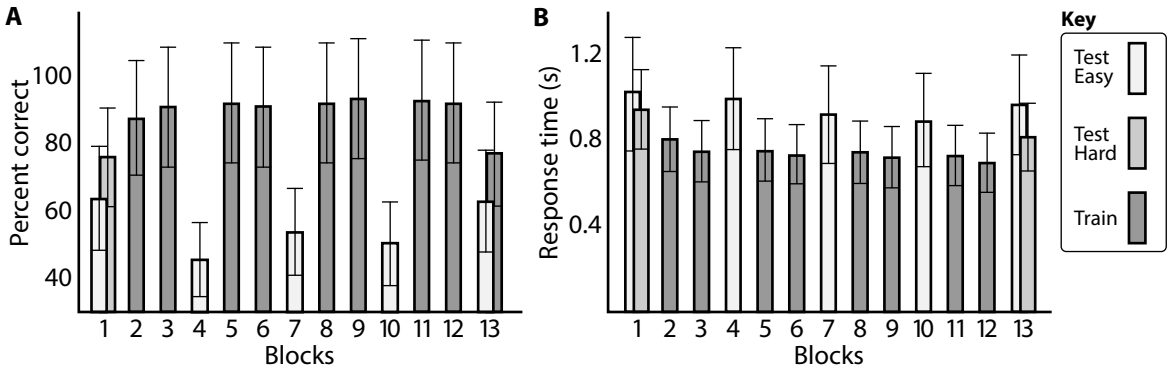

Figure B.12: *Pilot 3A results.* (A) *Percent Correct per Block.* **(B)** Response time in seconds. The pre-training test (block 1) and the post-training test (block 13) contained *Easy* and *Hard* testing conditions. Error bars are standard error.

Conclusions We did not discern a learning effect for this paradigm, although we did note that the initial starting performance was lower than in *Pilot 3*. The response times were fairly flat throughout the experiment, averaging at approximately 0.8 s per trial.

Pilot 3B

Aims: We sought to investigate the result of lowering the signal level (in order to make the training and testing more difficult) as we hypothesised that this might evoke a learning transfer effect that was absent in the previous pilot.

Design: The design for *Pilot 3B* was the same as the previous study (*Pilot 3A*, **Figure B.11**). We dropped the 10° versus 80° spiral angles for the test conditions and changed the signal levels in both the test and training blocks (**Table B.8**).

Table B.8: *Pilot 3B* design. Parameters for *Pilot 3B*: **N** = number of participants, **Images** = number of images per block, **Blocks** = number of blocks per session, **Radial** = radial pattern spiral angle(s) in degrees, **Concentric** = concentric pattern spiral angle(s) in degrees, **Signal** = percent of signal dots, **Sessions** = number of sessions. Bold numbers represent changes from *Pilot 3A* parameters.

	N	**Images**	**Blocks**	**Radial**	**Concentric**	**Signal**	**Sessions**
Test	7	60 & 120	5	**30**	**60**	**60**	1
Train	7	120	8	10	80	**50**	1

Results: We plotted the *Percent Correct per Block* and response times for the *Easy* and *Hard* conditions (**Figure B.13**).

Conclusions The test results increased from $\approx$ 55% to $\approx$ 70% during the experiment. The low pre-training scores were just above chance, which was the score that we were aiming for in these pilot experiments. The performance in the additional 'mini' tests were consistent with the idea that transfer of learning from the *Easy* training to the *Hard* testing was occurring throughout the experiment, as performance in most test runs was higher than the previous

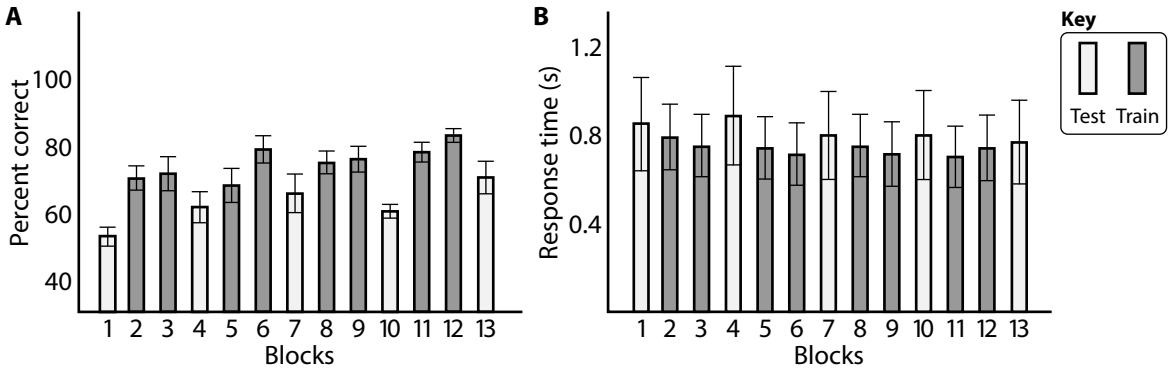

Figure B.13: *Pilot 3B* results. (A) *Percent Correct per Block*. **(B)** Response time in seconds. Error bars are standard error.

test block. We observed similar response times to *Pilot 3A*.

Pilot 3C

Aims: To verify that the results we found in the previous study were the result of learning transfer from the *Easy* training conditions. We decided to test the effect of only using *Hard* conditions in both the training and test blocks.

Design: The design was the same as that in **Figure B.11**. We changed the spiral angles in the training blocks to 30° versus 60°, so that only *Hard* conditions were tested (**Table B.9**). The signal was set to 60% in both test and training blocks.

Table B.9: *Pilot 3C* design. Parameters for *Pilot 3C*: **N** = number of participants, **Images** = number of images per block, **Blocks** = number of blocks per session, **Radial** = radial pattern spiral angle(s) in degrees, **Concentric** = concentric pattern spiral angle(s) in degrees, **Signal** = percent of signal dots, **Sessions** = number of sessions. Bold numbers represent changes from *Pilot 3B* parameters.

	N	Images	Blocks	Radial	Concentric	Signal	Sessions
Test	5	60 & 120	5	30	60	60	1
Train	5	120	8	**30**	**60**	**60**	1

Results: We plotted the *Percent Correct per Block* and response times for the *Easy* and *Hard* conditions, as in **Figure B.14**.

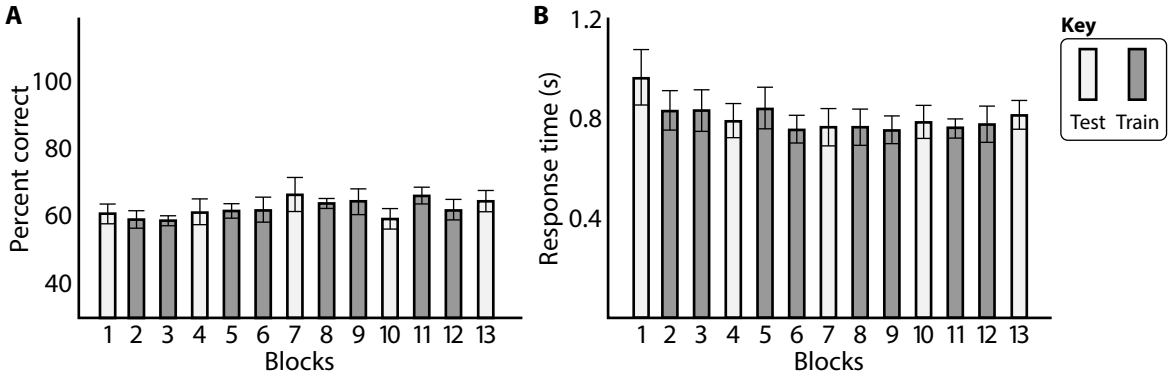

Figure B.14: *Pilot 3C* results. (A) *Percent Correct per Block*. **(N)** Response time in seconds. Error bars are standard error.

Conclusions: The parameter settings for *Pilot 3C* did not produce a learning effect as shown by the flat trend of the *Percent Correct per Block*. We interpreted this as showing that the increase in performance that we saw in *Pilot 3B* was likely to be connected to the *Easy* training as we did not observe the same effect with the *Hard* training in *Pilot 3C*. Response times were similar to the other pilot studies that we have described so far.

Pilot 3BS

Aims: We were interested to see the result of running *Pilot 3B* (i.e. the previous study) over more sessions.

Design: The design for *Pilot 3BS* was identical to *Pilot 3B* (see **Figure B.11**, which also shared the same arrangement of test and training blocks). The parameters for the experiment are listed in **Table B.10**. The only difference to the parameters for *Pilot 3BS*, compared to *Pilot*

Table B.10: *Pilot 3BS* design. Parameters for *Pilot 3BS*: **N** = number of participants, **Images** = number of images per block, **Blocks** = number of blocks per session, **Radial** = radial pattern spiral angle(s) in degrees, **Concentric** = concentric pattern spiral angle(s) in degrees, **Signal** = percent of signal dots, **Sessions** = number of sessions. The only difference to the parameters for *Pilot 3BS*, compared to *Pilot 3B* was the number of sessions, which increased to four.

	N	Images	Blocks	Radial	Concentric	Signal	Sessions
Test	1	60 & 120	5	30	60	60	**4**
Train	1	120	8	10	80	50	**4**

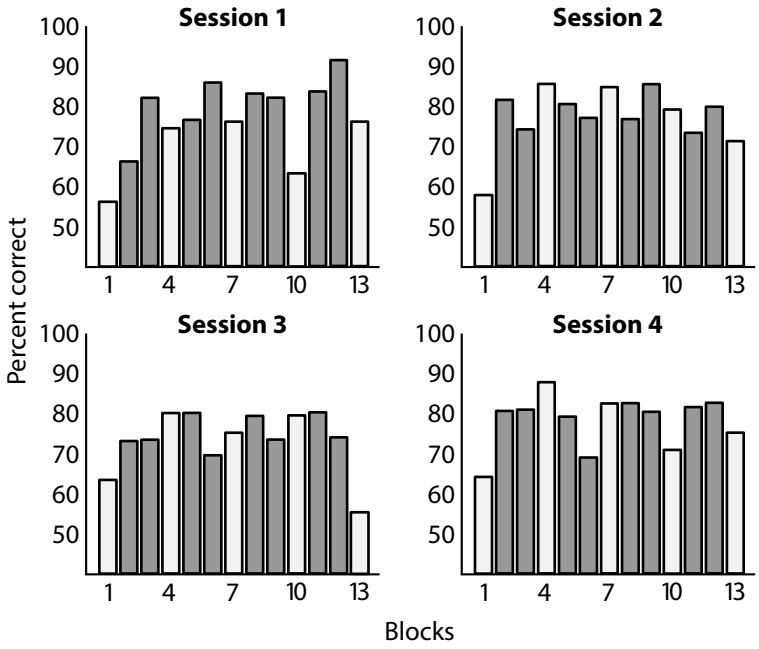

Figure B.15: *Pilot 3BS* results. *Percent Correct per Block* over the four sessions. The *x*-axes are block numbers. Test blocks are indicated by lighter shaded bars, training blocks (with audio feedback) are shown as darker shaded bars.

3B, was the number of sessions, which we increased to four.

Results: We plotted the *Percent Correct per Block* and response times for the four sessions in **Figure B.15**.

Conclusions: We only tested one participant on this pilot study, so we need to be cautious when drawing conclusions from the results. However, we did note that within-session improvement did seem to occur in most sessions. We also noted that performance in the first block did not appreciably increase between sessions. This led us to consider investigating learning across greater timescales than the single sessions that had characterised our designs so far.

Pilot 3CS

Aims: We were interested in seeing the result of running *Pilot 3C* over more sessions.

Design: The design for *Pilot 3CS* was identical to *Pilot 3C* (see **Figure B.11**, which also shared the same arrangement of test and training blocks). The parameters for the experiment are

Table B.11: *Pilot 3CS* design. Parameters for *Pilot 3CS*: **N** = number of participants, **Images** = number of images per block, **Blocks** = number of blocks per session, **Radial** = radial pattern spiral angle(s) in degrees, **Concentric** = concentric pattern spiral angle(s) in degrees, **Signal** = percent of signal dots, **Sessions** = number of sessions. Bold numbers represent changes from *Pilot 3C* parameters.

	N	Images	Blocks	Radial	Concentric	Signal	Sessions
Test	4	60 & 120	5	30	60	60	**4**
Train	4	120	8	30	60	60	**4**

listed in **Table B.11**, these are identical to the parameters for *Pilot 3C* except that the number of sessions increased to four.

Results: We plotted the *Percent Correct per Block* in **Figure B.16** and response times in **Figure B.17** for the four sessions.

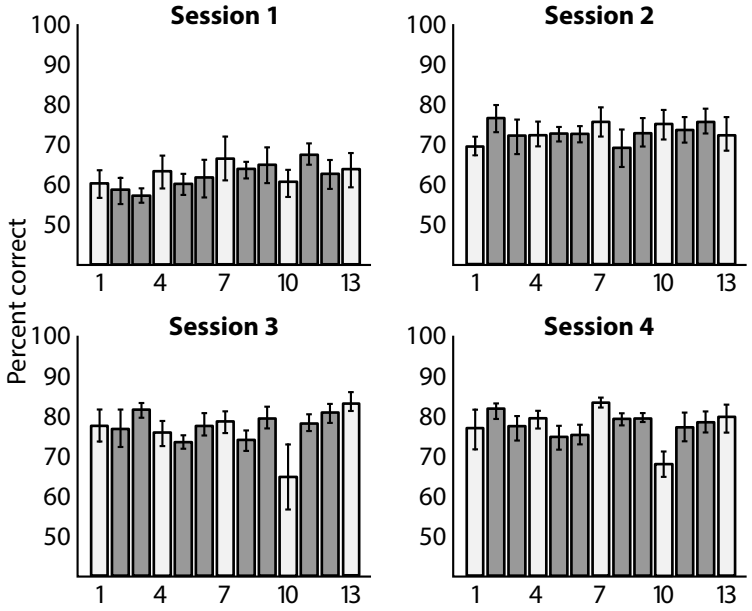

Figure B.16: *Pilot 3CS* results, percent correct. *Percent Correct per Block* over four sessions. The *x*-axes are block numbers. Test blocks are indicated by lighter shaded bars, training blocks (with audio feedback) are shown as darker shaded bars. Error bars are standard error.

Conclusions: In all sessions the performance seemed static across the test runs, as was the case in the previous experiment (*Pilot 3C*). However, the starting performance, as measured by the *Percent Correct per Block* in the first run, went from $\approx$ 60% in the first session to $\approx$ 70% in the second session and $\approx$ 78% in the third session. The fourth session had similar performance to the third session. We concluded from these results that this *Hard* training paradigm

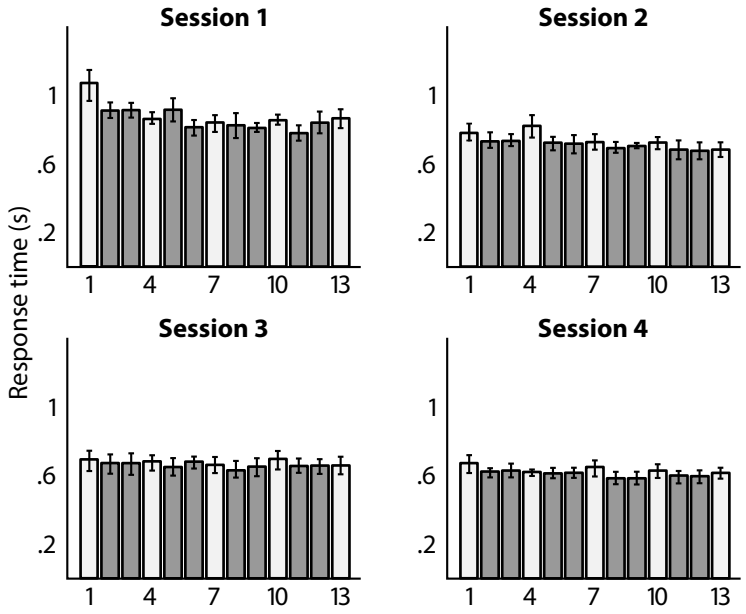

Figure B.17: *Pilot 3CS* results, response time. Response time over four sessions. The *x*-axes are block numbers. Test blocks are indicated by lighter shaded bars, training blocks (with audio feedback) are shown as darker shaded bars. Error bars are standard error.

was evoking a learning effect, but that the effect manifested itself as a between-session performance improvement. This was different to the previous within-session learning that we saw in *Pilot 3B*. We felt that these results vindicated the multi session design that we had been experimenting with for the last two pilot studies. We also observed a steady decrease in response time over the sessions (approximately 200 ms).

Pilot 3D

Aims: We wished to investigate the effect of *Easy* training, to compare with *Pilot 3C*, which was a *Hard* training study.

Design: The design for *Pilot 3D* had the same arrangement of test and training blocks as **Figure B.11**. We set the signal to 50% in both the test and training blocks, but the main difference from *Pilot 3C* was the spiral angles for the training runs. We set them to 10° versus 80° to create an *Easy* training paradigm to contrast the *Hard* training angles of 30° versus 60° from *Pilot 3C*. The parameters for *Pilot 3D* are listed in **Table B.12**.

Table B.12: *Pilot 3D* design. Parameters for *Pilot 3D*: **N** = number of participants, **Images** = number of images per block, **Blocks** = number of blocks per session, **Radial** = radial pattern spiral angle(s) in degrees, **Concentric** = concentric pattern spiral angle(s) in degrees, **Signal** = percent of signal dots, **Sessions** = number of sessions. Bold numbers represent changes from *Pilot 3C* parameters.

	N	Images	Blocks	Radial	Concentric	Signal	Sessions
Test	3	60 & 120	5	30	60	**50**	1
Train	3	120	8	**10**	**80**	**50**	1

Results: We plotted the *Percent Correct per Block* and response times for this study (**Figure B.18: A,B**). We also plotted the results for a single participant, whose performance was elevated compared to the mean results (**Figure B.18: C,D**).

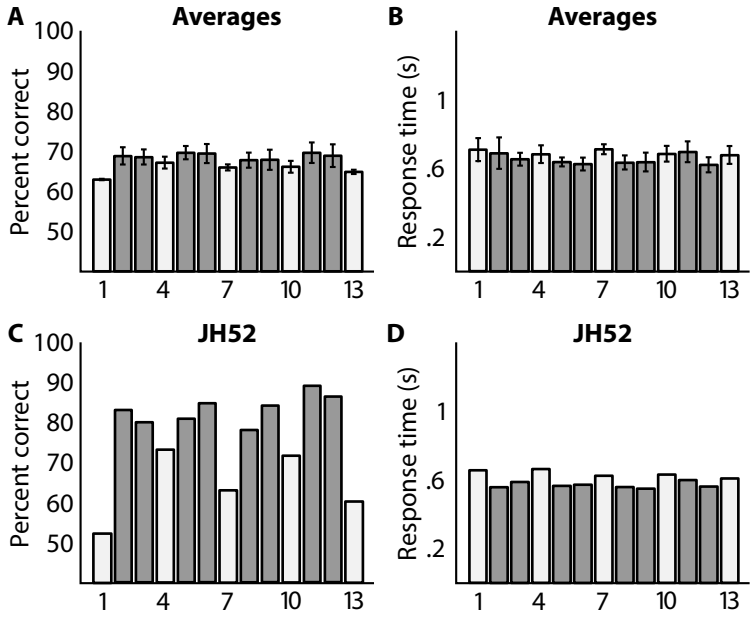

Figure B.18: *Pilot 3D* results. (A) Average *Percent Correct per Block* and **(B)** response time for all participants. **(C)** and **(D)** are the results for a single participant (JH52). The *x*-axes are block numbers. Test blocks are indicated by lighter shaded bars, training blocks (with audio feedback) are shown as darker shaded bars. Error bars are standard error.

Conclusions: When we investigated the *Percent Correct per Block* in the testing runs, we noted an increase in performance of approximately 5% from the first test block to the last. In the test blocks in between the first and last (runs 4, 7 and 10), the participants scored higher results ($PCB \approx 59\%$). These results seemed to suggest that there was little improvement in performance overall. However, the size of the error bars indicated that there was larger variation in the participants' performance for the runs 2–12. We therefore looked more closely at the individual participant results to compare them with the average results.

The performance of one participant (JH52) was higher than the other two (**Figure B.18: C**). We ascertained from JH52 that he was very practiced at performing psychophysics experiments, although like all the other participants he was not familiar with Glass pattern stimuli. The *PCB* of JH52 on test block four was approximately 74%, which showed a large performance increase from the untrained score of $\approx$ 52%. Taken in isolation, JH52's performance could be interpreted to represent a learning transfer effect from the easy training paradigm. Taken in the round, we interpreted JH52's results to represent outlier performance, which skewed the overall average scores. This sounded a note of caution about the potential for misinterpretation of results with small sample sizes.

One thing that we observed in the performance of all the participants was a drop for the last test block compared to previous test runs. This lead us to consider that the participants may have found the length of the experiment to cause fatigue, which might explain the apparent lowering of performance towards the end.

Pilot 3E

Aims: Our aims for *Pilot 3E* were to run another *Easy* training study, but this time over three sessions.

Design: The arrangement of each session's test and training blocks in *Pilot 3E* was the same that it has been for all the studies since *Pilot 3A* (see **Figure B.11**).

Table B.13: *Pilot 3E* design. Parameters for *Pilot 3E*: **N** = number of participants, **Images** = number of images per block, **Blocks** = number of blocks per session, **Radial** = radial pattern spiral angle(s) in degrees, **Concentric** = concentric pattern spiral angle(s) in degrees, **Signal** = percent of signal dots, **Sessions** = number of sessions. Bold numbers represent changes from *Pilot 3D* parameters.

	N	Images	Blocks	Radial	Concentric	Signal	Sessions
Test	4	**60**	5	30	60	50	**3**
Train	4	120	8	10	80	50	**3**

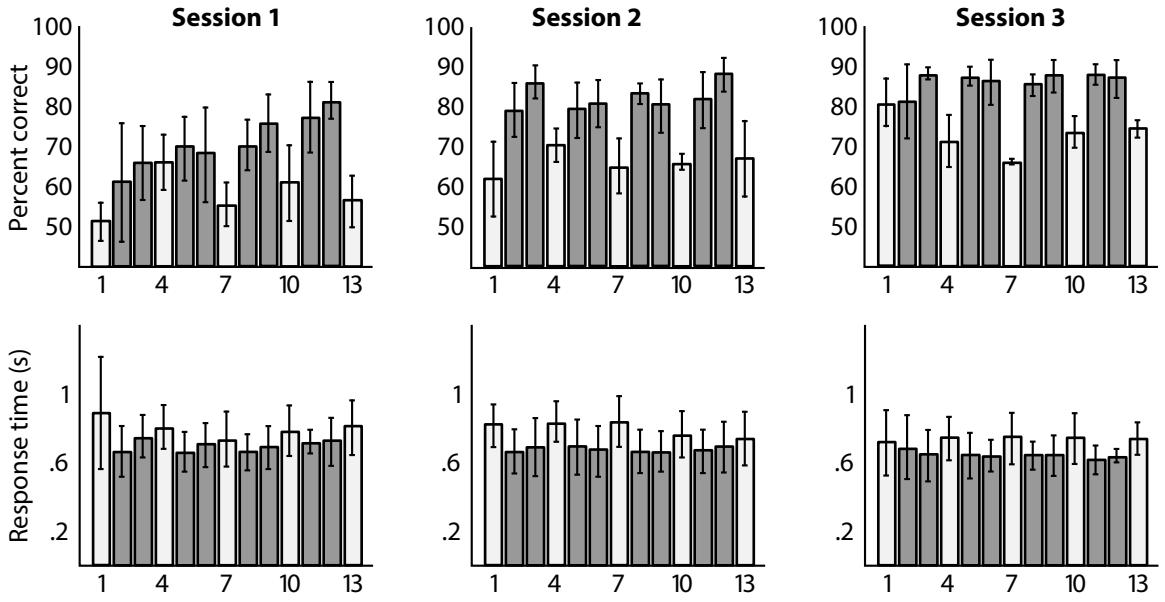

Figure B.19: *Pilot 3E* results. *Percent Correct per Block* and response time over three sessions, conducted on subsequent days. The *x*-axes are block numbers. Test blocks are indicated by lighter shaded bars, training blocks (with audio feedback) are shown as darker shaded bars. Error bars are standard error.

A change that we made was to reduce the number of trials in the test runs (**Table B.13**). We did this to try to address the drop in performance that we noticed at the end of *Pilot 3D*. *Pilot 3E* was another multi-session experiment (this time there were three sessions).

Results: We plotted the *Percent Correct per Block (PCB)* and response times for the three sessions (**Figure B.19**).

Conclusions: The results showed that there was no within session learning for this protocol, but there did seem to be across session learning evoked by the *Easy* training paradigm. *Percent Correct per Block* on the first run of each session was $\approx$ 50%, $\approx$ 60% and $\approx$ 80% respectively. Response times were fairly static at approximately 0.8 ms per trial.

Pilot 3F

Aims: We sought to replicate the *Easy* training, across session improvement that we saw in *Pilot 3E*, with some fine tuning of the signal.

Table B.14: *Pilot 3F* design. Parameters for *Pilot 3F*: **N** = number of participants, **Images** = number of images per block, **Blocks** = number of blocks per session, **Radial** = radial pattern spiral angle(s) in degrees, **Concentric** = concentric pattern spiral angle(s) in degrees, **Signal** = percent of signal dots, **Sessions** = number of sessions. Bold numbers represent changes from *Pilot 3E* parameters.

	N	Images	Blocks	Radial	Concentric	Signal	Sessions
Test	3	60	5	30	60	**60**	3
Train	3	120	8	10	80	**60**	3

Design: The arrangement of training and test blocks for *Pilot 3F* was the same as **Figure B.11**, except that *Pilot 3F* was to be conducted over three sessions. A change to the parameters that we made for *Pilot 3F* compared to *Pilot 3E* was to increase the signal in the stimulus images (**Table B.14**).

Results: We plotted the *Percent Correct per Block* and response times for the three sessions (**Figure B.20**).

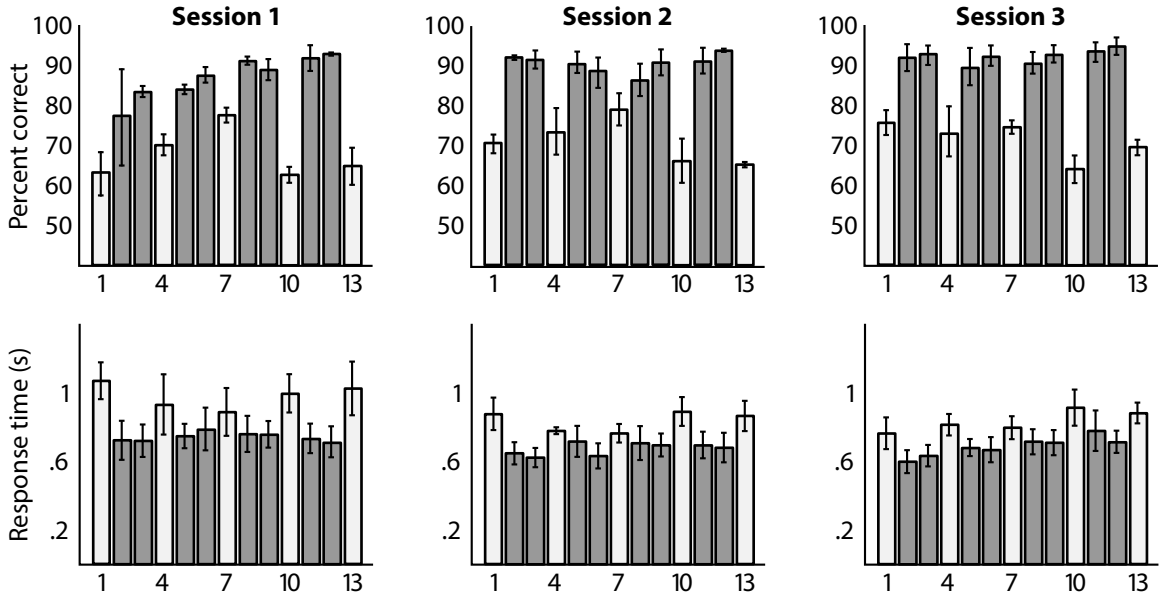

Figure B.20: *Pilot 3F* results. *Percent Correct per Block* and response time over three sessions, conducted on subsequent days. The *x*-axes are block numbers. Test blocks are indicated by lighter shaded bars, training blocks (with audio feedback) are shown as darker shaded bars. Error bars are standard error.

Conclusions: The results showed the across session learning improvement that we observed in the previous *Easy* training study (*Pilot 3E*). We also noted across session improvement with first run *Percent Correct per Block* scores of ≈ 65%, ≈ 70% and ≈ 75%. Interestingly, the improvement was lower than on the previous pilot, which had a lower signal percentage in the images. We also noted that there seemed to be within-session improvement in the first three testing blocks of sessions one and two. This improvement was not sustained for the last two test blocks, which had a similar *PCB* scores as the first test block.

Pilot 4A

Aims: This study was conceived as a further investigation into the *Easy* training paradigm, but where we increased the frequency of testing.

Design: In the studies that we had conducted so far, we were generally more interested in the test results rather than the training results. This was particularly so in the case of *Easy* training paradigms, where the performance in training runs was usually high. We therefore redesigned the experiment so that we had more testing blocks, while at the same time reducing the overall length of the experiment. In the design for *Pilot 4A* (**Figure B.21**) we had six test blocks and four training blocks, which we interleaved in pairs. The previous study (*Pilot 3F*) had five test blocks and eight training blocks.

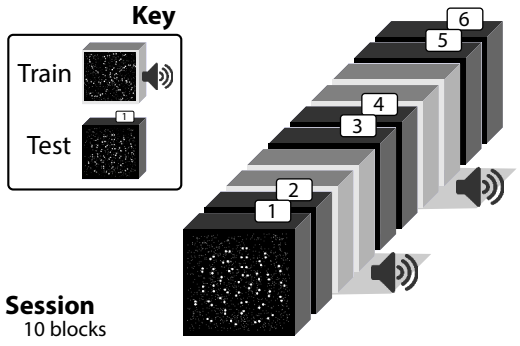

Figure B.21: *Pilot 4A* design. A session consisted of six test blocks (dark, numbered boxes) and four training blocks (lighter boxes with audio icon).

Table B.15: *Pilot 4A* design. Parameters for *Pilot 4A*: **N** = number of participants, **Images** = number of images per block, **Blocks** = number of blocks per session, **Radial** = radial pattern spiral angle(s) in degrees, **Concentric** = concentric pattern spiral angle(s) in degrees, **Signal** = percent of signal dots, **Sessions** = number of sessions. Bold numbers represent changes from *Pilot 3F* parameters.

	N	Images	Blocks	Radial	Concentric	Signal	Sessions
Test	3	**100**	**6**	30	60	60	3
Train	3	**100**	**4**	10	80	60	3

We set the number of trials in each test and training block to 100. In our previous pilot studies we had generally used 120 trial per block and also introduced 'mini' tests comprising 60 trials. The reasons for using 120 trials per block were so that we could test many different conditions at once if we wished (as discussed in **Section B.3**). We no longer needed this requirement and wished to shorten the duration of the experiment. We therefore reduced the number of trials per block to 100, which simplified the calculations for the *Percent Correct per Block* metric. These changed parameters doubled the number of test trials compared to *Pilot 3F*, from 300 to 600. The overall number of trials per session was reduced from 1260 to 1000. The parameters for *Pilot 4A* are listed in **Table B.15**.

Results: We plotted the *Percent Correct per Block* for each session (**Figure B.22**) and fitted a curve to the results from the test blocks using a nonlinear least-squares data fitting algorithm. The algorithm was the Matlab (The MathWorks, Inc., Natick, Massachusetts) function `lsqnonlin`.

We plotted the *Percent Correct per Block* and the response times for combined pairs of adjacent blocks (**Figure B.23**). This simulated the effect of an altered design with five blocks (three testing and two training), with double the number of stimulus presentations in each block. We presented the data in paired groups to see if this made the patterns of performance any clearer.

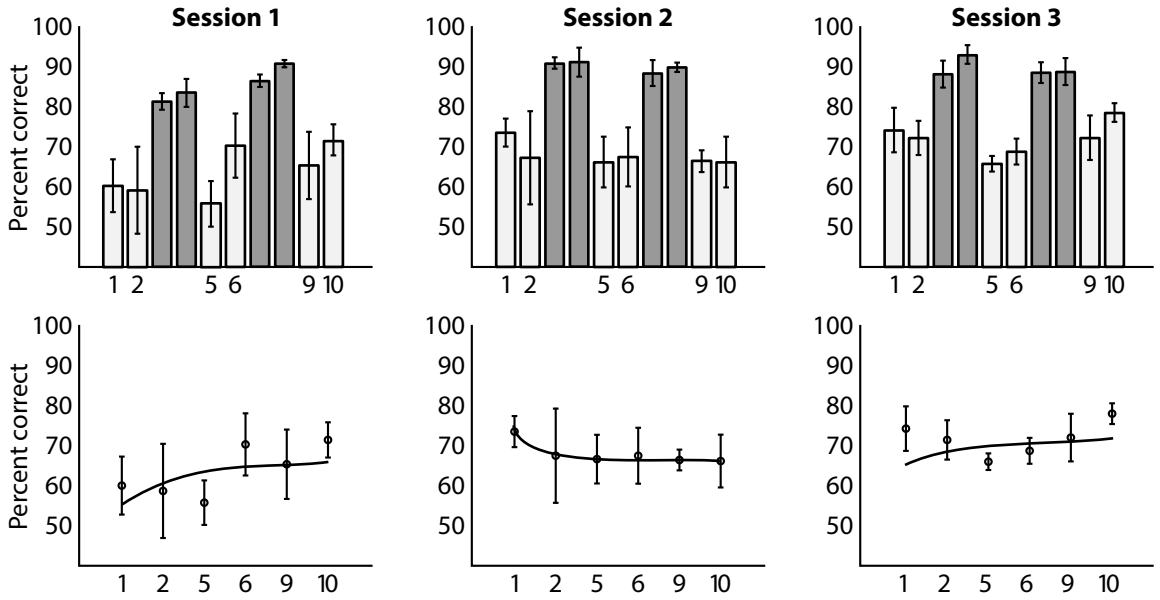

Figure B.22: *Pilot 4A* results. Average *Percent Correct per Block* per session. The *x*-axes are block numbers. Test blocks are indicated by lighter shaded bars, training blocks (with audio feedback) are shown as darker shaded bars. The upper figures show the test and training runs, as in previous figures. The lower figures show the test blocks fitted with a nonlinear least-squares data fitting algorithm. Error bars are standard error.

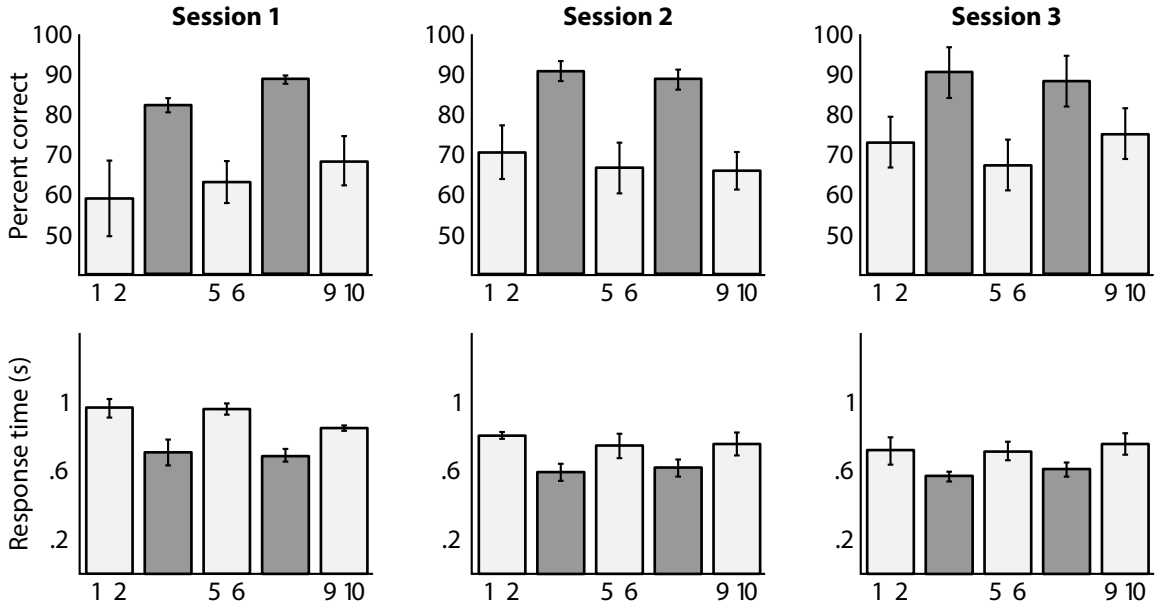

Figure B.23: *Pilot 4A* paired results. *Percent Correct per Block* (upper figures) and response time (lower figures) over three sessions, grouped by pairs of test and training blocks. The *x*-axes are block numbers. Test blocks are indicated by lighter shaded bars, training blocks (with audio feedback) are shown as darker shaded bars. Error bars are standard error.

Conclusions: The results suggested a possible across-session learning effect, as performance at the start of session two and three was higher than performance at the end of session one and two, respectively. The between-session improvement was more pronounced for session two to three, rather than session one to two. The nonlinear least-squares curves accentuated the between-session performance differences for session one and two, but diminished the improvement from session two to three. There was arguably a within-session learning effect for session one, which we had not expected for the *Easy* training. The improving trend in session one was clearer in the paired charts (**Figure B.23**) than the non paired charts (**Figure B.22**). Although there was considerable overlap of the error bars, which caused us to be cautious in reading too much into this observation. Response times decreased marginally, as we have observed in the other studies.

Pilot 4B

Aims: For *Pilot 4B* we wished to investigate the performance of a *Hard* training learning pilot to compare it with the *Easy* training study of *Pilot 4A*.

Design: The arrangement of test and training blocks was kept identical to that of *Pilot 4A* (**Figure B.21**). The only difference in experimental parameters, compared to *Pilot 4A*, were the spiral angles for the training blocks. These were changed to 30° versus 60° to make the discrimination more difficult than the 10° versus 80° angles in *Pilot 4A* (**Table B.16**).

Table B.16: Pilot 4B design. Parameters for *Pilot 4B*: **N** = number of participants, **Images** = number of images per block, **Blocks** = number of blocks per session, **Radial** = radial pattern spiral angle(s) in degrees, **Concentric** = concentric pattern spiral angle(s) in degrees, **Signal** = percent of signal dots, **Sessions** = number of sessions. Bold numbers represent changes from *Pilot 4A* parameters.

	N	Images	Blocks	Radial	Concentric	Signal	Sessions
Test	3	100	6	30	60	60	3
Train	3	100	4	**30**	**60**	60	3

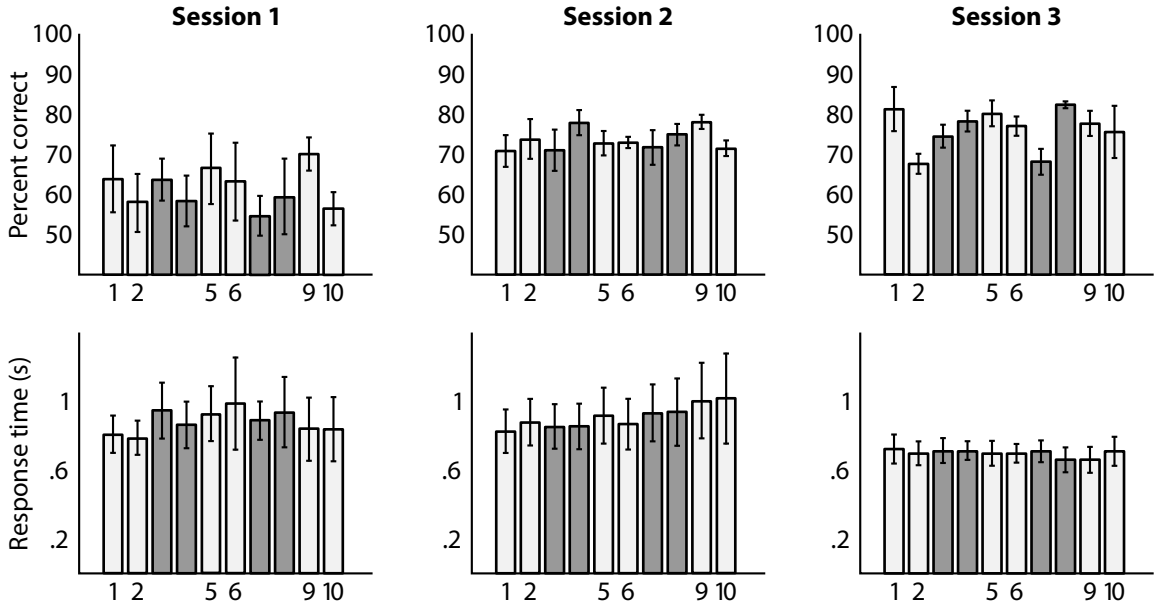

Figure B.24: *Pilot 4B* results. *Percent Correct per Block* and response time over three sessions, conducted on subsequent days. The *x*-axes are block numbers. Test blocks are indicated by lighter shaded bars, training blocks (with audio feedback) are shown as darker shaded bars. Error bars are standard error.

Results: As in previous pilot studies, we plotted the *Percent Correct per Block* and response times for *Pilot 4B* (**Figure B.24**).

Conclusions: The starting performance on this paradigm was greater than 60%, which suggested that the experiment was still not difficult enough. We noted that the performance on the last test block in each session was lower than that in the previous run. We hypothesised that this might be an indication of fatigue, despite our efforts to shorten the duration of the sessions. We also speculated that this drop in performance might be obscuring any within-session learning, which is what we had anticipated from this paradigm. The response times dropped marginally over the course of the experiment, which was a consistent feature throughout the studies.

B.4 Discussion

We observed some performance improvements for both within and across sessions in some of our studies. Moreover, the parameter changes that we experimented with suggested that *Easy* versus *Hard* training evoked different types of learning (within and across session), rather than just different magnitudes of learning effect. This was most noticeable when comparing the results of the multisession studies of *Pilot 3BS* versus *Pilot 3CS*. We observed a within-session improvement for *Pilot 3BS*, which was an *Easy* training paradigm. The results from *Pilot 3CS* suggested an across session learning from the *Hard* training experiment. The results from these pilot studies were to inform the methodological basis for the *Easy* versus *Hard* training experiments of **Chapter 5: Time Course of Training Difficulty Mediated Visual Learning**.

For most of the pilot studies described in this appendix we kept the image signal constant at approximately 50–60%. Where we varied the signal, we did so to make tasks either more *Easy* or *Hard*. One thing that we considered when we reviewed all of the results at the end of the pilot studies was that changes in the signal level might alter the character of the experiments themselves, rather than just the difficulty levels. By reducing the signal levels, we hypothesised that we might be creating the conditions for detection experiments, as apposed to discrimination studies that resulted from changes made to spiral angles. With detection experiments the task is to detect a condition that is obscured by noise, whereas in discrimination experiments it is to make fine discriminatory judgements between similar conditions in the absence of noise. We investigated the distinction between detection versus discrimination experiments in **Chapter 7: GABA Versus Coarse and Fine Visual Learning**.

We found that response time, as measured on correct responses, was not a revealing metric for characterising learning. The mean response time (RT) for *Pilots 1–3C* was approximately

0.75 s and the RT for *Pilots 3BS–4B* was approximately 0.65 s. In each of the pilot studies there was a reduction of approximately 100–200 ms over the length of a session, but we felt that this could be explained by familiarity with the paradigm as much as with learning effect. The differences between response times for learned and pre-training performance were too small to be used as accurate predictors of performance. We therefore suspended the response time analysis on further experiments so that we could better concentrate on the percent correct measures.

Throughout the pilot studies we had used the *Percent Correct per Block* metric as the main way that we evaluated performance. We found that by consistently using a simple (intuitively understandable) metric we were able to rapidly assess and alter our experimental designs. Where we tried more complicated metrics, for example the nonlinear least squares approach of *Pilot 4A*, we found that the results were less interpretable as they required additional assumptions to explain the same findings. As our ultimate goals were to investigate correlations between GABA concentrations and performance metrics, we decided that in future we would use simple metrics if they continued to show a clear pattern of performance improvement.

The focus for this appendix was to describe the sequence of experiments that lead to the *Easy* versus *Hard* training experiments of **Chapter 5: Time Course of Training Difficulty Mediated Visual Learning** and the detection versus discrimination experiments in **Chapter 7: GABA Versus Coarse and Fine Visual Learning**. We considered the pilot studies successful, in that we felt we had laid the foundations for more detailed studies into *Easy* versus *Hard* training and visual discrimination versus detection tasks. We felt confident from these preliminary findings that such studies might show dissociable learning effects, particularly with the interleaved test and training protocol that we developed.

C

CODE LISTINGS

This appendix contains code fragments to illustrate the approaches and solutions investigated in **Chapters 3: MEGA-PRESS Acquisition** and **4: Post-Acquisition Processing**.

Listing C.1: Combining MEGA-PRESS FIDs. Matlab function that converts time domain signals to frequency domain spectra and combines them. Line broadening and ppm scale calculations are demonstrated in this script.

```
function fids = get_fid_rows(file)
    lambda = 1; % line broadening parameter
    spar = [file '.SPAR'];
    sdat = [file '.SDAT'];
    [time_sig, paras] = read_philips(spar, sdat);
    zfill = 1;
    ref = 4.7; % water
    freq_scale=(-paras.fs/2:paras.fs/(paras.samples*zfill):paras.fs/2 ...
        - paras.fs/(paras.samples*zfill)).';
    fids.ppm_scale=(-freq_scale/paras.t_freq)*10^6+ref;
    t = 0:1/paras.fs:(paras.samples/paras.fs-1/paras.fs); % t for time
    exp_fn = exp(-lambda*t); % exponential function for line broadening
    exp_fn_resized = repmat(exp_fn',1,paras.rows/2);
    % reshape the data into rows samples x rows (eg 2048x32)
    data_rows = reshape(time_sig,paras.samples,paras.rows);
    % odd rows, time domain
    edit_on = data_rows(:,1:2:paras.rows);
    edit_on_exp = edit_on.*exp_fn_resized;
    fids.edit_on_fft = fft(edit_on_exp);
    fids.edit_on_real_fftshift = real(fftshift(fft(edit_on_exp)));
    % even rows
    edit_off = data_rows(:,2:2:paras.rows);
    edit_off_exp = edit_off .* exp_fn_resized;
    fids.edit_off_fft = fft(edit_off_exp);
    fids.edit_off_real_fftshift = real(fftshift(fft(edit_off_exp)));
    combined = edit_on + edit_off; % eg 2048 x 16
    combined_exp = combined .* exp_fn_resized; % apply exp funct
    fids.combined_fft = fft(combined_exp);
```

```
    fids.combined_real_fftshift = real(fftshift(fft(combined_exp)));
    fids.rows = paras.rows;
end
```

Listing C.2: Automatic phasing. Example of conversion from time domain FID to frequency domain, for automatic phasing. Assumes that FIDs have been read into a Matlab structure (`fids`), `autophase_adg` is a wrapper function for the phasing algorithm. The phase-zero and phase-one components are retrieved with this code.

```
% read td from SDAT, SPAR
fids = get_fids([the_path, the_file]);
fids_water = get_fids([the_path, the_water_file]);
% convert TD_ON to FD_ON
on_fd = fftshift(fft(fids.edit_on_td));
% convert TD_OFF to FD_OFF
off_fd = fftshift(fft(fids.edit_off_td));
% FD_OFF_phased = autophase(FD_OFF)
off_ps = NaN(size(off_fd));
for idx = 1:size(off_fd,2)
  [off_ps(:,idx), off_p0(:,idx), off_p1(:,idx)] = ...
    autophase_adg(off_fd(:,idx));
end

on_ps = NaN(size(on_fd));
for idx = 1:size(on_fd,2)
  [on_ps(:,idx), on_p0(:,idx), on_p1(:,idx)] = ...
    autophase_adg(on_fd(:,idx));
end
```

Listing C.3: Visualising subspectral misalignment. Matlab function that creates animated plots to characterise the shift in the subspectral components of MEGA-PRESS acquisitions. The parameter `fids` contains frequency domain data for the edit ON and edit OFF acquisitions.

```
function plot_fids_simultaneously(fids)
  delay=1; % set to 1 for 1sec pause between individual fids
  figure
  gaba_ppm = 3.0; % position on ppm scale where we identify GABA
  naa_ppm = 2.0; % position of NAA
  inv_pulse = 1.9; % position of inversion pulse
  offset_size = 0.2; % arbitrary offset to identify width of metabolite
      peaks on plots
  % find indexes for NAA peak
  idx_naa = find(fids.ppm_scale >= (naa_ppm - offset_size) & ...
    fids.ppm_scale <= (naa_ppm + offset_size));
  naa_lb = min(idx_naa); % NAA lower bound (to identify NAA peak for
      phasing)
  naa_ub = max(idx_naa); % NAA upper bound
  % find indexes for GABA peak
  idx_gaba = find(fids.ppm_scale >= (gaba_ppm - offset_size) & ...
    fids.ppm_scale <= (gaba_ppm + offset_size));
  gaba_lb = min(idx_gaba); % GABA lower bound
  gaba_ub = max(idx_gaba); % GABA upper bound
  idx_x_scale = find(fids.ppm_scale >= (inv_pulse - offset_size) & ...
    fids.ppm_scale <= (gaba_ppm + 4*offset_size));
  x_lb = min(idx_x_scale);
```

```
x_ub = max(idx_x_scale);
x_lim = [inv_pulse - offset_size, gaba_ppm + 4*offset_size];
min_y = min(min(fids.combined_fd(x_lb:x_ub,:)));
max_y = max(max(fids.combined_fd(x_lb:x_ub,:)));
% plot the edit ON and OFF at 3ppm
x_lim = [gaba_ppm - offset_size, gaba_ppm + offset_size];
%subplot(4,4,[11 12]);
hold on
set(gca, 'xlim', x_lim);
set(gca,'xDir','reverse');
x = fids.ppm_scale(gaba_lb:gaba_ub);
min_y_on = min(min(fids.edit_on_fd(gaba_lb:gaba_ub,:)));
max_y_on = max(max(fids.edit_on_fd(gaba_lb:gaba_ub,:)));
min_y_off = min(min(fids.edit_off_fd(gaba_lb:gaba_ub,:)));
max_y_off = max(max(fids.edit_off_fd(gaba_lb:gaba_ub,:)));
min_y = min(min_y_on, min_y_off);
max_y = max(max_y_on, max_y_off);
set(gca, 'ylim', [min_y, max_y]);
for idx=1:fids.rows/2
  y_on = fids.edit_on_fd(gaba_lb:gaba_ub,idx);
  plot(x, y_on, 'Linewidth', 1, 'Color', 'r' );
  y_off = fids.edit_off_fd(gaba_lb:gaba_ub,idx);
  plot(x, y_off, 'Linewidth', 1, 'Color', 'r' );
  pause(delay)
  % overwrite in blue
  plot(x, y_on, 'Linewidth', 1, 'Color', 'b' );
  plot(x, y_off, 'Linewidth', 1, 'Color', 'b' );
end
% plot the mean with a red line
pause(delay)
y_mean_on = mean(fids.edit_on_fd(gaba_lb:gaba_ub,:),2);
err_on = std(fids.edit_on_fd(gaba_lb:gaba_ub,:),0,2);
mean_err_on = mean(err_on);
y_mean_off = mean(fids.edit_off_fd(gaba_lb:gaba_ub,:),2);
err_off = std(fids.edit_off_fd(gaba_lb:gaba_ub,:),0,2);
mean_err_off = mean(err_off);

plot(x, y_mean_on+err_on, 'Linewidth', 2, 'LineStyle', '--', 'Color', '
    k');
plot(x, y_mean_on-err_on, 'Linewidth', 2, 'LineStyle', '--', 'Color', '
    k');
plot(x, y_mean_on, 'Linewidth', 2, 'Color', 'r' );
plot(x, y_mean_off+err_off, 'Linewidth', 2, 'LineStyle', '--', 'Color',
     'k');
plot(x, y_mean_off-err_off, 'Linewidth', 2, 'LineStyle', '--', 'Color',
     'k');
plot(x, y_mean_off, 'Linewidth', 2, 'Color', 'r' );
line([gaba_ppm, gaba_ppm], [min_y, max_y], 'LineWidth', 1, 'Color', 'k'
    )
title(['Edit␣ON,␣mean␣std=' num2str(mean_err_on) ...
  '␣Edit␣OFF,␣mean␣std␣=' num2str(mean_err_off)])
hold off

file_name = [fids.OUTPUT_PATH, fids.subj_id, '_', fids.voxel, '_var'];
set(gcf,'PaperPositionMode','auto')
% without tiff 174KB
print('-depsc', '-r150', file_name);
```

```
  close
end
```

Listing C.4: Peak identification. Matlab fragment that demonstrates creatine peak identification as an offset to the NAA peak.

```
ex_naa_plus_1_dot_01 = naa_ppms + 1.01; % expected ppm for Cr
win_size_Cr = 0.1; % smaller window as we have used prior k of naa peak

% find indexes for Cr window (diff to NAA where we just had one index)
for idx = 1:length(ex_naa_plus_1_dot_01)
  idx_Cr(:,idx) = find(fids.ppm_scale <= (ex_naa_plus_1_dot_01(idx) +
      win_size_Cr) & ...
    fids.ppm_scale >= (ex_naa_plus_1_dot_01(idx) - win_size_Cr));
  Cr_lb(idx) = min(idx_Cr(:,idx)); % Cr window lower bound
  Cr_ub(idx) = max(idx_Cr(:,idx)); % Cr window upper bound
end
```

Listing C.5: Weighted average. Matlab fragment that demonstrates weighted average peak identification.

```
% get a vector based on weighted average
for idx = 1:size(off_ps,2)
  % OFF
  [sort_vals_Cr_off(idx,:), sort_idxs_Cr_off(idx,:)] = ...
    sort(real(off_ps(Cr_lb(idx):Cr_ub(idx),idx)),'descend');
  a_off=sort_idxs_Cr_off(idx, 1:num_points);
  w_off=sort_vals_Cr_off(idx, 1:num_points);
  idx_mid_Cr_peaks_ps_off(idx) = round(sum( a_off .* w_off) ./ sum( w_off
      ));
  idx_mid_Cr_peaks_ps_off(idx) = ...
    idx_mid_Cr_peaks_ps_off(idx) + Cr_lb(idx) -1;
  % ON
  [sort_vals_Cr_on(idx,:), sort_idxs_Cr_on(idx,:)] = ...
    sort(real(on_ps(Cr_lb(idx):Cr_ub(idx),idx)),'descend');
  a_on=sort_idxs_Cr_on(idx, 1:num_points);
  w_on=sort_vals_Cr_on(idx, 1:num_points);
  idx_mid_Cr_peaks_ps_on(idx) = round(sum( a_on .* w_on) ./ sum( w_on ));
  idx_mid_Cr_peaks_ps_on(idx) = ...
    idx_mid_Cr_peaks_ps_on(idx) + Cr_lb(idx) -1;
end
```

Listing C.6: Calculating the signal to noise ratio for the GABA peaks. Python script that demonstrates the GABA SNR calculation; the maximum value from the peaks between 2.8 ppm and 3.2 ppm was divided by the root mean square of the noise from the range -2 ppm to zero ppm.

```
gaba_data = 0.0
gaba_data_max = 0.0
for idx in range(idx_3pt2ppm,idx_2pt8ppm):
  gaba_data = float(reader[idx][idx_data])
  if (gaba_data > gaba_data_max):
    gaba_data_max = gaba_data

noise_squared = 0.0
for idx in range(idx_0ppm,idx_minus2ppm):
```

```
    gaba_data = float(reader[idx][idx_data])
    noise_squared += math.pow(gaba_data,2)

mean_noise_squared = noise_squared / num_data_pts_noise
rms_noise = math.sqrt(mean_noise_squared)

gaba_snrPA = gaba_data_max / rms_noise
```

Listing C.7: Scanner coordinates. Python script that demonstrates the retrieval of offset and angulation information from DICOM and XML files.

```
"""
gets position and angulation info from DICOM or XML
"""
import os, subprocess
from xml.dom.minidom import parseString

idx_dir = 0
idx_file_name = 1
idx_dcm = 2
idx_dir_cos = 3
idx_dir_cos_corr = 4
idx_pos = 5
idx_pos_corr = 6

def get_dir_cos_rc(theFile):
    """
    row and column direction cosines are in the DICOM files
    """
    if theFile.endswith('xml'):
        xml_file = open(theFile, 'r')
        data = xml_file.read()
        xml_file.close()
        dom = parseString(data)
        dc_DOM = dom.getElementsByTagName('ImageOrientationPatient')[0].
            getElementsByTagName('value')[0:6]
        dir_cos = []
        for dc in dc_DOM:
            # cast to float
            dir_cos.append(float(dc.firstChild.data))
        return dir_cos
    if theFile.endswith('dcm'):
        command = ( 'dcmdump +L -s +P 0020,0037 ' + theFile + ' | awk \'{
            print$3}\' | tr -d \"[]\" | tr \"\\\\\" \"\" ')
        #return command
        p = subprocess.Popen(command, bufsize=2048, shell=True, stdin=
            subprocess.PIPE, stdout=subprocess.PIPE, close_fds=True)
        p.wait()
        #print p.communicate()[0]
        dc_dcmdump = p.communicate()[0]
        dc_dcmdump = dc_dcmdump.rsplit()
        dir_cos = []
        for dc in dc_dcmdump:
            dir_cos.append(float(dc))
        return dir_cos
```

Listing C.8: Slice direction cosines. Python function that demonstrates the calculation of the slice direction cosines from the row and column direction cosines.

```
def get_dir_cos_s(rc):
    """
    calculates slice direction cosines from row and column direction
        cosines
    rc consists of floats and will have 6 values, x, y & z for row and col
    """
    rx=rc[0]; ry=rc[1]; rz=rc[2]; cx=rc[3]; cy=rc[4]; cz=rc[5]
    sx = ry * cz - rz * cy
    sy = rz * cx - rx * cz
    sz = rx * cy - ry * cx
    return [sx, sy, sz]
```

Listing C.9: MRI synthesis. Python function that wraps the `mri_vol_synth` function to create a synthesised MRI volume.

```
def get_cmd_mri_volsynth(mrs_vals):
    """
    creates a terminal command to create a synthesised mri volume
    """
    cras_x = str(mrs_vals[idx_pos_corr][0])
    cras_y = str(mrs_vals[idx_pos_corr][1])
    cras_z = str(mrs_vals[idx_pos_corr][2])
    rx = str(mrs_vals[idx_dir_cos_corr][0])
    ry = str(mrs_vals[idx_dir_cos_corr][1])
    rz = str(mrs_vals[idx_dir_cos_corr][2])
    cx = str(mrs_vals[idx_dir_cos_corr][3])
    cy = str(mrs_vals[idx_dir_cos_corr][4])
    cz = str(mrs_vals[idx_dir_cos_corr][5])
    sx = str(mrs_vals[idx_dir_cos_corr][6])
    sy = str(mrs_vals[idx_dir_cos_corr][7])
    sz = str(mrs_vals[idx_dir_cos_corr][8])
    fn_nii = mrs_vals[idx_file_name]
    fn_nii = os.path.join(mrs_vals[idx_dir], fn_nii)

    command = ('mri_volsynth␣--dim␣30␣30␣30␣1␣--pdf␣const␣--c_ras␣' +
          cras_x + '␣' + cras_y + '␣' + cras_z +
          '␣--cdircos␣' + cx + '␣' + cy + '␣' + cz +
          '␣--rdircos␣' + rx + '␣' + ry + '␣' + rz +
          '␣--sdircos␣' + sx + '␣' + sy + '␣' + sz +
          '␣--o␣' + fn_nii)
    return command, fn_nii
```

Listing C.10: Scanner to NifTI conversion. Python function that demonstrates the conversion of one co-ordinate frame to another.

```
def get_corrected_dir_cos(dc):
    """
    niftii files expect a different co-ordinate frame than the scanner
    """
    dc_rx=dc[0]; dc_ry=dc[1]; dc_rz=dc[2];
    dc_cx=dc[3]; dc_cy=dc[4]; dc_cz=dc[5];
    dc_sx=dc[6]; dc_sy=dc[7]; dc_sz=dc[8];
```

```
  rx = (-dc_rx) # x = -x
  ry = (-dc_ry) # y = -y
  rz = dc_rz # z doesn't change

  cx = (-dc_cx)
  cy = (-dc_cy)
  cz = dc_cz

  sx = (-dc_sx)
  sy = (-dc_sy)
  sz = dc_sz

  return [rx, ry, rz, cx, cy, cz, sx, sy, sz]
```

Listing C.11: Registration matrices. Python functions used to create registration matrices and makes use of the Freesurfer tool `tkregister2`.

```
#!/usr/bin/python
"""
create registration matrices from MRS volumes (synthesised MRI) to
Freesurfer anatomical.  Uses tkregister2.
Same session uses regheader, across session manual alignment using T2
as an intermediate volume.

For same session registration matrix:
  dat_name = os.path.join(os.path.dirname(mri_volnii), dat)
  command = reg_same_session(subject, mri_volnii, dat_name)
  os.system(command)
To produce an nii file from a T2 dicom use:
  command = t2_dcm_2_nii(t2_dir)
  os.system(command)
For T2 to anatomical (will require manual registration):
  save the registration afterwards
For different session use the intermediate (T2) image and reg
  save the ...int.dat
"""
import os

def reg_same_session(subject, moveable, dat_name):
  """
  register same session MRS and anatomical:
    dat_name = os.path.join(os.path.dirname(mri_volnii), dat)
    command = reg_same_session(subject, mri_volnii, dat_name)
    os.system(command)
  """
  command = ('tkregister2 --s ' + subject + ' --mov ' + moveable + ' --
      regheader --reg ' + dat_name + ' --noedit ')
  return command

def reg_t2_to_anatomical(subject, moveable, dat_name):
  """
  register t2 to anatomical (different sessions)
  """
  command = ('tkregister2 --s ' + subject + ' --mov ' + moveable + ' --
      regheader --reg ' + dat_name + ' --surf')
  return command
```

```
def reg_diff_sessions(subject, moveable, int, int_dat, dat_name):
    """
    register different session MRS and anatomical (use intermediate reg):
    """
    # use int vol from manual T2 registration
    command = ('tkregister2 --s ' + subject + ' --mov ' + moveable + ' --
        int ' + int + ' ' + int_dat + ' --reg ' + dat_name + ' --fmov 100 ')
    return command

def t2_dcm_2_nii(path_to_dcm):
    """
    call dcm2nii with appropriate parameters to produce an nii file from
        the T2 DICOM
      t2_dir = ...
      command = t2_dcm_2_nii(t2_dir)
    """
    command = ('/Applications/osx/dcm2nii -i n -d n -p n -v y -x n -o ' +
        path_to_dcm + ' ' + path_to_dcm + '/*')
    return command
```

Listing C.12: Calculating tissue proportions. Python fragment that wraps the function `mri_compute_volume_fractions`.

```
def create_segmentations(reg_matrix, mrs_vol, output_file_name_prefix):
    command = ('mri_compute_volume_fractions ' + reg_matrix + ' ' + mrs_vol
        + ' ' + output_file_name_prefix)
    return command
```

D

MEGA-PRESS PARAMETERS

This sample exam card details the parameter settings that were used in all *in vivo* MEGA-PRESS experiments for this project.

Table D.1: Sample exam card. The parameters for a typical MEGA-PRESS experiment as used in the experiments for this project.

Parameter Name	Value
Nucleus =	"H1"
Coil selection =	"SENSE-Head-8"
element selection =	"SENSE"
connection =	"d"
Dual coil =	"no"
VOI orientation =	"sagittal"
VOI size AP (mm) =	30
RL (mm) =	30
FH (mm) =	30
Samples =	2048
Spectral BW (Hz) =	2150
Ang. AP (deg) =	0
RL (deg) =	0
FH (deg) =	0
VOI offc. AP (P=+mm) =	40.9492989
RL (L=+mm) =	36.6866379
FH (H=+mm) =	24.2860928
VOI ang. AP (deg) =	21.4503765
RL (deg) =	-0.0441694073
FH (deg) =	40.84758
Chem. shift Dir AP =	"A"
Chem. shift Dir LR =	"L"

Continued on next page...

Table D.1 Sample exam card. *Continued from previous page.*

Parameter Name	Value
Chem. shift Dir FH =	"F"
Large table movement =	"no"
REST slabs =	0
Patient position =	"head first"
orientation =	"supine"
Scan type =	"Spectroscopy"
Scan mode =	"SV"
technique =	"ECHO"
VOI selection =	"volume"
method =	"PRESS"
Gradient Spoiling =	"no"
Fast Imaging mode =	"none"
Echo acquisition =	"half"
TE =	"user defined"
(ms) =	68
Flip angle (deg) =	90
RF pulse set =	"normal"
TR =	"user defined"
(ms) =	1800
Shim =	"PB-auto"
PB order =	"second"
Water suppression =	"VAPOR"
window (Hz) =	140
WS prescan =	"no"
BASING pulse =	"MEGA basic"
pulse dur (ms) =	15
water freq (ppm) =	4.67999983
pulse freq1 (ppm) =	1.89999998
pulse freq2 (ppm) =	8.46000004
flip angle (deg) =	180
frequency offset =	"default"
Fat suppression =	"no"
Grad. rev. offres. supp. =	"no"
Research prepulse =	"no"
Pre-saturation =	"no"
SAR mode =	"high"
B1 mode =	"default"
PNS mode =	"moderate"
Gradient mode =	"maximum"
SofTone mode =	"no"
Cardiac synchronization =	"no"
Respiratory compensation =	"no"
Startup acquisitions =	0
NSA =	16
Phase cycles =	16
Frequency stabilization =	"yes"
Parameter series =	"no"
Manual start =	"no"
Dynamic study =	"individual"
dyn scans =	32
dyn scan times =	"shortest"
dummy scans =	0

Continued on next page...

Table D.1 Sample exam card. *Continued from previous page.*

Parameter Name	**Value**
prospect. motion corr. =	"no"
Arterial Spin labeling =	"no"
Preparation phases =	"auto"
Manual Offset Freq. =	"no"
Receiver optimization =	"ON"
Spectral correction =	"no"
Reference tissue =	"White matter"
PlanScan metabolite =	"user defined"
chemical shift (PPM) =	2.45000005
Shifted metabolite displayed =	"none"
Preset window contrast =	"soft"
Save raw data =	"yes"
Hardcopy protocol =	"no"
Elliptical k-space shutter =	"default"
IF_info_seperator =	0
Total scan duration =	"15:21.6"
Rel. signal level (%) =	100
Act. TR/TE (ms) =	"1800 / 68"
Dyn. scan time =	"00:28.8"
Min. TR/TE (ms) =	"1790 / 64"
Spectral resolution (Hz/point) =	1.04980469
Readout duration (ms) =	952.558105
SAR / head =	"< 9 % / 0.3 W/kg"
Whole body / level =	"0.0 W/kg / normal"
B1 rms [uT] =	0.705540895
PNS / level =	"63 % / normal"
Sound Pressure Level (dB) =	0

E

POST-ACQUISITION SUPPLEMENTARY

This appendix contains supplementary figures for **Chapter 4: Post-Acquisition Processing**.

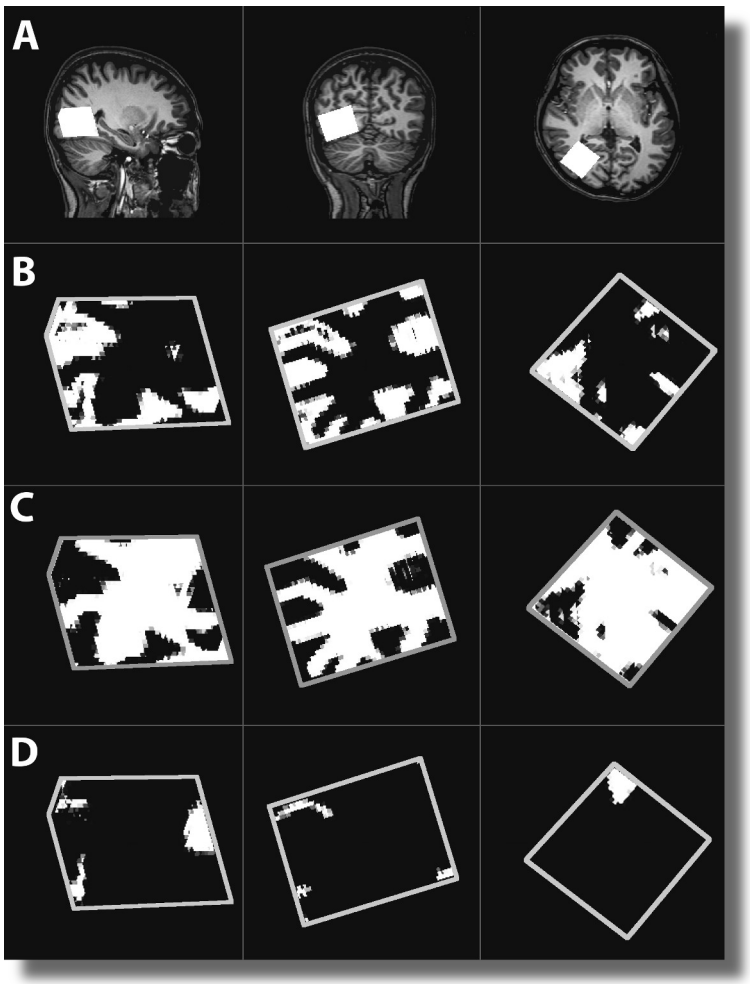

Figure E.1: Monochrome segmented MRS acquisition. This figure represents a grey scale version of **Figure 4.17**, which is suitable for monochrome printing purposes.
(**A**) Visualisation of the simulated fMRI as a proxy for the MRS acquisition (white filled shapes). These sample images (sagittal, coronal and axial) are of a lateral occipital acquisition taken in the left hemisphere.
(**B**) Grey matter segmentation images corresponding with the MRS acquisition. Lighter pixels indicate higher probability that the voxel is identified as GM.
(**C**) White matter segmentation images. Lighter pixels indicate higher probability that the voxel is identified as WM.
(**D**) Cerebrospinal fluid segmentation images. Lighter pixels indicate higher probability that the voxel is identified as CSF.

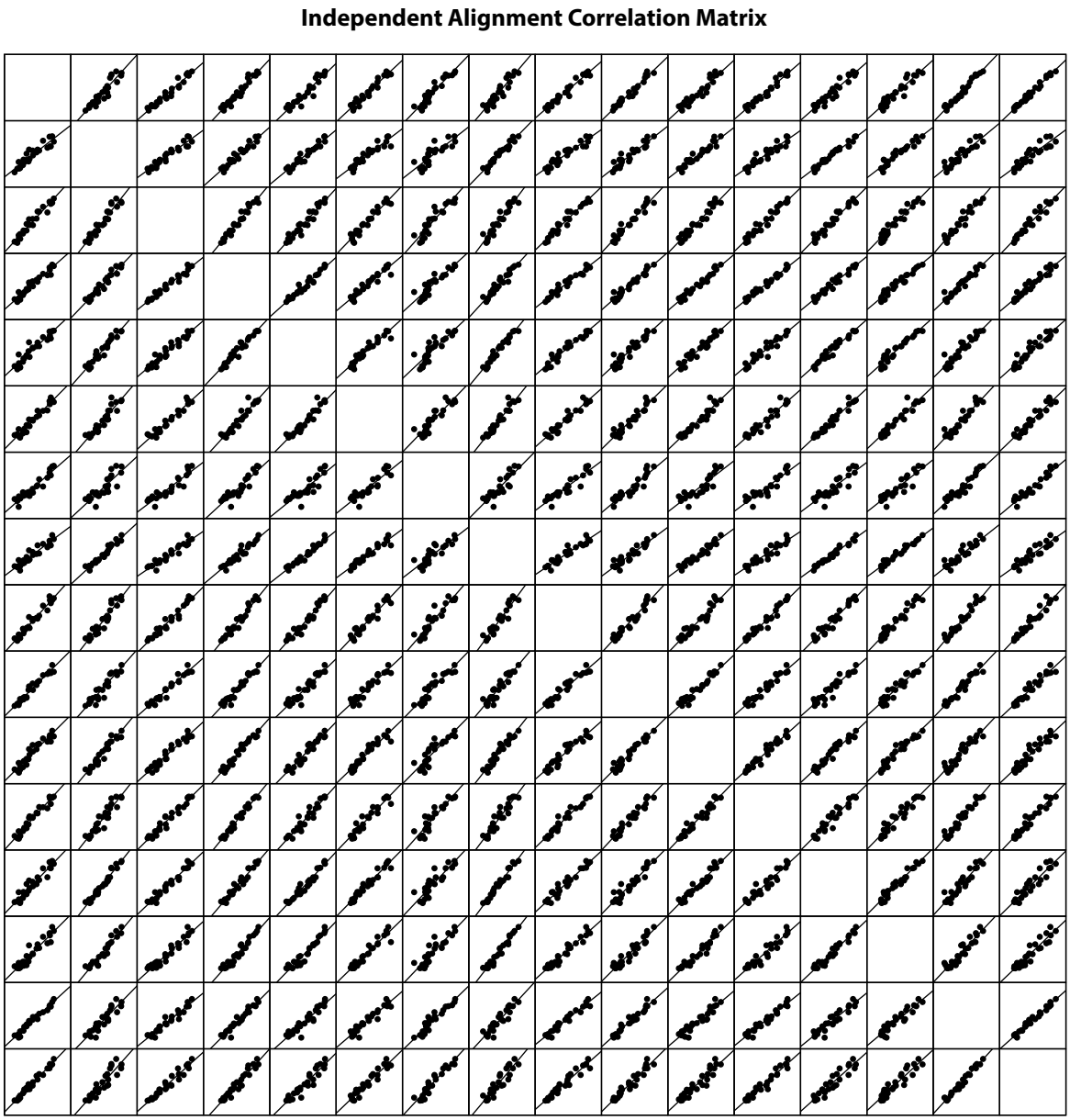

Figure E.2: Independent alignment correlation matrix. This plot shows the correlations for the spectra from **Figure 4.9E**. The correlation coefficient for this data was $r = 0.96$ ($p < 0.01$), which demonstrates an improvement compared with the paired alignment in **Figure E.3**.

Figure E.3: Paired alignment correlation matrix. This plot shows the correlations for the spectra from **Figure 4.9B**. The correlation coefficient for this data was $r = 0.82$ ($p < 0.01$), which demonstrates a weaker correlation compared with the independent alignment in **Figure E.2**.

REFERENCES

Aberg, K. C., & Herzog, M. H. (2012). Different types of feedback change decision criterion and sensitivity differently in perceptual learning. *Jounal of Vision*, *12(3)*, 1–11.

Ahissar, M. (2001). Perceptual training: A tool for both modifying the brain and exploring it. *Proceedings of the National Academy of Sciences of the USA*, *98*, 11842–11843.

Ahissar, M., & Hochstein, S. (1996). Learning pop-out detection: Specificities to stimulus characteristics. *Vision Research*, *36(21)*, 3487–3500.

Ahissar, M., & Hochstein, S. (1997). Task difficulty and the specificity of perceptual learning. *Nature*, *387*, 401–406.

Ahissar, M., & Hochstein, S. (2004). The reverse hierarchy theory of visual perceptual learning. *Trends in Cognitive Sciences*, *8(10)*, 457–464.

Alger, J. R. (2010). Quantitative proton magnetic resonance spectroscopy and spectroscopic imaging of the brain: A didactic review. *Topics in Magnetic Resonance Imaging*, *21*, 115–128.

Altmann, C. F., Bülthoff, H. H., & Kourtzi, Z. (2003). Perceptual organization of local elements into global shapes in the human visual cortex. *Current Biology*, *13*(4), 342–349.

Angulo, M. C., Le Meur, K., Kozlov, A. S., Charpak, S., & Audinat, E. (2008). GABA, a forgotten gliotransmitter. *Progress in Neurobiology*, *86*, 297–303.

Aufhaus, E., Weber-Fahr, W., Sack, M., Tunc-Skarka, N., Oberthuer, G., Hoerst, M., … Ende, G. (2013). Absence of changes in GABA concentrations with age and gender in the human anterior cingulate cortex: a MEGA-PRESS study with symmetric editing pulse frequencies for macromolecule suppression. *Magnetic Resonance in Medicine*, *69*(2), 317–320.

Azevedo, F. A. C., Carvalho, L. R. B., Grinberg, L. T., Farfel, J., Ferretti, R. E. L., Leite, R. E. P., … Herculano-Houzel, S. (2009). Equal numbers of neuronal and nonneuronal cells make the human brain an isometrically scaled-up primate brain. *The Journal of Comparative Neurology*, *513*(5), 532–541.

Bachtiar, V., & Stagg, C. J. (2014). The role of inhibition in human motor cortical plasticity. *Neuroscience*, *278*(0), 93–104.

Ball, K., & Sekuler, R. (1987). Direction-specific improvement in motion discrimination. *Vision Research*, *27*, 953–965.

Bhagwagar, Z., Wylezinska, M., Jezzard, P., Evans, J., Ashworth, F., Sule, A., … Cowen, P. J. (2007). Reduction in occipital cortex γ-aminobutyric acid concentrations in medication-free recovered unipolar depressed and bipolar subjects. *Biological Psychiatry*, *61*(6), 806–812.

Bhattacharyya, P. K., Phillips, M. D., Stone, L. A., & Lowe, M. J. (2011). In-vivo MRS measurement of gray-matter and white-matter GABA concentration in sensorimotor cortex using a motion-controlled MEGA-PRESS sequence. *Magnetic Resonance Imaging*, *29(3)*, 374–379.

Blaus, B. (2014). *Medical gallery of Blausen Medical.* Retrieved August 2017, from `https://upload.wikimedia.org/wikipedia/commons/thumb/b/bb/Blausen_0102_Brain_Motor&Sensory_(flipped).png`

Blicher, J. U., Near, J., Næss-Schmidt, E., Stagg, C. J., Johansen-Berg, H., Nielsen, J. F., … Ho, Y.-C. L. (2014). GABA levels are decreased after stroke and GABA changes during rehabilitation correlate with motor improvement. *Neurorehabilitation and Neural Repair*, *1*, 1–9.

Blüml, S., & Panigraphy, A. (2013). *MR spectroscopy of pediatric brain disorders*. Berlin, Germany: Springer Science.

Bogner, W., Gruber, S., Doelken, M., Stadlbauer, A., Ganslandt, O., Boettcher, U., … Hammen, T. (2010). In vivo quantification of intracerebral GABA by single-voxel ^{1}H-MRS - How reproducible are the results? *European Journal of Radiology*, *73*(3), 526–531.

Boy, F., Evans, J., Edden, R. A. E., Singh, K. D., Hussain, M., & Sumner, P. (2010). Individual differences in subconscious motor control predicted by GABA. *Current Biology*, *20*, 1779–1785.

Brainard, D. H. (1997). The Psychophysics Toolbox. *Spatial Vision*, *10*, 443–446.

Brown, M. A., & Semelka, R. C. (2010). *MRI: Basic principles and applications*. John Wiley & Sons, Ltd.

Bruce, V., Green, P. R., & Georgeson, M. A. (2003). *Visual perception: Physiology, psychology and ecology* (Fourth ed.). Psychology Press, Hove.

Chen, L., Weng, Z., Goh, L., & Garland, M. (2002). An efficient algorithm for automatic phase correction of NMR spectra based on entropy minimization. *Journal of Magnetic Resonance*, *158*, 164–168.

Choi, C., Bhardwaj, P. P., Kalra, S., Casault, C. A., Yasmin, U. S., Allen, P. S., & Coupland, N. J. (2007). Measurement of GABA and contaminants in gray and white matter in human brain in vivo. *Magnetic Resonance in Medicine*, *58*(1), 27–33.

Choi, I.-Y., Lee, S.-P., Merkle, H., & Shen, J. (2006). In vivo detection of gray and white matter differences in GABA concentration in the human brain. *Neuroimage*, *33*, 85–93.

Cossart, R., Bernard, C., & Ben-Ari, Y. (2005). Multiple facets of GABAergic neurons and synapses: multiple fates of GABA signalling in epilepsies. *Trends in Neurosciences*, *28*(2), 108–115.

Dager, S. R., Oskin, N. M., Richards, T. L., & Posse, S. (2008). Research applications of magnetic resonance spectroscopy (MRS) to investigate psychiatric disorders. *Topics in Magnetic Resonance Imaging*, *19(2)*, 81–96.

Dale, A. M., Fischl, B., & Sereno, M. I. (1999). Cortical surface-based analysis. *Neuroimage*, *9*, 179–194.

Desimone, R. (1998). Visual attention mediated by biased competition in extrastriate visual cortex. *Philosophical Transactions of the Royal Society*, *353*, 1245–1255.

De Valois, K. K. (1977). Spatial frequency adaptation can enhance contrast sensitivity. *Vision Research*, *17*(9), 1057–1065.

Donahue, M. J., Near, J., Blicher, J. U., & Jezzard, P. (2010). Baseline GABA concentration and fMRI response. *NeuroImage*, *53(2)*, 392–398.

Dosher, B. A., & Lu, Z.-L. (1999). Mechanisms of perceptual learning. *Vision Research*, *39*, 3197–3221.

Duarte, J. M. N., Lei, H., Mlynárik, V., & Gruetter, R. (2012). The neurochemical profile quantified by in vivo ^{1}H NMR spectroscopy. *Neuroimage*, *61*(2), 342–362.

Duncan, J. (2001). An adaptive coding model of neural function in prefrontal cortex. *Nature Reviews Neuroscience*, *2*(11), 820–829.

Duncan, J., Papademetris, X., Yang, J., Jackowski, M., Zeng, X., & Staib, L. H. (2004). Geometric strategies for neuroanatomic analysis from MRI. *NeuroImage*, *23*(2004), 34–45.

Dwyer, D. M., Hodder, K. I., & Honey, R. C. (2004). Perceptual learning in humans: Roles of preexposure schedule, feedback, and discrimination assay. *The Quarterly Journal of Experimental Psychology*, *57B(3)*, 245–259.

Edden, R. A. E., & Barker, P. B. (2007). Spatial effects in the dectection of γ-aminobutyric acid improved sensitivity at high fields using inner volume saturation. *Magnetic Resonance in Medicine*, *58*, 1276–1282.

Edden, R. A. E., Intrapiromkul, J., Zhu, H., Cheng, Y., & Barker, P. B. (2012). Measuring T_2 in vivo with J-difference editing: application to GABA at 3 Tesla. *Journal of Magnetic Resonance Imaging*, *35*(1), 229–

234.

Edden, R. A. E., Muthukumaraswamy, S. D., Freeman, T. C. A., & Singh, K. D. (2009). Orientation discrimination performance is predicted by GABA concentration and gamma oscillation frequency in human primary visual cortex. *The Journal of Neuroscience*, *29(50)*, 15721–15726.

Edden, R. A. E., Puts, N. A. J., & Barker, P. B. (2012). Macromolecule-suppressed GABA-edited magnetic resonance spectroscopy at 3T. *Magnetic Resonance in Medicine*, *68(3)*, 657–661.

Edden, R. A. E., Puts, N. A. J., Harris, A. D., Barker, P. B., & Evans, J. (2014). Gannet: A batch-processing tool for the quantitative analysis of gamma-aminobutyric acid-edited MR spectroscopy spectra. *Journal of Magnetic Resonance Imaging*, *40*, 1445–1452.

Edwards, J. D., Ross, L. A., Wadley, V. G., Clay, O. J., Crowe, M., Roenker, D. L., & Ball, K. K. (2006). The useful field of view test: Normative data for older adults. *Archives of Clinical Neuropsychology*, *21*(4), 275–286.

Ernst, T., Kreis, R., & Ross, B. D. (1993). Absolute quantitation of water and metabolites in the human brain. I. compartments and water. *Journal of Magnetic Resonance, Series B*, *102*(1), 1–8.

Evans, C. J., McGonigle, D. J., & Edden, R. A. E. (2010). Diurnal stability of γ-aminobutyric acid concentration in visual and sensorimotor cortex. *Journal of Magnetic Resonance Imaging*, *31*, 204–209.

Evans, C. J., Puts, N. A. J., Robson, S. E., Boy, F., McGonigle, D. J., Sumner, P., … Edden, R. A. E. (2012). Frequency (mis-)alignment and subtraction artefacts in GABA spectroscopy. In *BC-ISMRM 18th meeting.* University of Cambridge: International Society for Magnetic Resonance in Medicine.

Evans, C. J., Puts, N. A. J., Robson, S. E., Boy, F., McGonigle, D. J., Sumner, P., … Edden, R. A. E. (2013). Subtraction artifacts and frequency (mis-)alignment in J-difference GABA editing. *Journal of Magnetic Resonance Imaging*, *38*(4), 970–975.

Fahle, M. (2004). Perceptual learning: a case for early selection. *Journal of Vision*, *4*, 879–890.

Fahle, M., & Edelman, S. (1993). Long-term learning in vernier acuity: effects of stimulus orientation, range and of feedback. *Vision Research*, *33*, 397–412.

Fields, R. D. (2008). White matter in learning, cognition and psychiatric disorders. *Trends in Neurosciences*, *31*(7), 361–370.

Fine, I., & Jacobs, R. A. (2002). Comparing perceptual learning tasks: a review. *Journal of Vision*, *2*, 190–203.

Fiorentini, A., & Berardi, N. (1980). Perceptual learning specific for orientation and spatial frequency. *Nature*, *287*, 43–44.

Fischl, B., Salat, D. H., Busa, E., Albert, M., Dieterich, M., Haselgrove, C., … Dale, A. M. (2002). Whole brain segmentation: Automated labeling of neuroanatomical structures in the human brain. *Neuron*, *33*(3), 341–355.

Floyer-Lea, A., Wylezinska, M., Kincses, T., & Matthews, P. M. (2006). Rapid modulation of GABA concentration in human sensorimotor cortex during motor learning. *Journal of Neurophysiology*, *95*(3), 1639–1644.

Foerster, B. R., Pomper, M. G., Callaghan, B. C., Petrou, M., Edden, R. A. E., Mohamed, M. A., … Feldman, E. L. (2013). An imbalance between excitatory and inhibitory neurotransmitters in amyotrophic lateral sclerosis revealed by use of 3-T proton magnetic resonance spectroscopy. *JAMA Neurology*, *70*(8), 1009–1016.

Fox, P. T., & Raichle, M. E. (1986). Focal physiological uncoupling of cerebral blood flow and oxidative metabolism during somatosensory stimulation in human subjects. *Proceedings of the National Academy of Sciences of the United States of America*, *83*, 1140–1144.

Fox, P. T., Raichle, M. E., Mintun, M. A., & Dence, C. (1988). Nonoxidative glucose consumption during focal physiologic neural activity. *Science*, *241*, 462–464.

Frackowiak, R. S. J., Friston, K. J., Frith, C. D., Dolan, R. J., & Mazziotta, J. C. (Eds.). (1997). *Human brain function*. Academic Press USA.

Furmanski, C. S., & Engel, S. A. (2000). Perceptual learning in object recognition: object specificity and size invariance. *Vision Research*, *40*, 473–484.

Ganji, S. K., Banerjee, A., Patel, A. M., Zhao, Y. D., Dimitrov, I. E., Browning, J. D., … Choi, C. (2012). T_2 measurement of J-coupled metabolites in the human brain at 3T. *NMR in Biomedicine*, *25*(4), 523–529.

Gao, F., Edden, R. A. E., Li, M., Puts, N. A. J., Wang, G., Liu, C., … Barker, P. B. (2013). Edited magnetic resonance spectroscopy detects an age-related decline in brain GABA levels. *NeuroImage*, *78*, 75–82.

Garcia, A., Kuai, S.-G., & Kourtzi, Z. (2013). Differences in the time course of learning for hard compared to easy training. *Frontiers in Psychology*, *4*, 1–8.

Gasparovic, C., Song, T., Devier, D., Bockholt, H. J., Caprihan, A., Mullins, P. G., … Morrison, L. A. (2006). Use of tissue water as a concentration reference for proton spectroscopic imaging. *Magnetic Resonance in Medicine*, *55*(6), 1219–1226.

Gibson, E. J. (1969). *Principles of perceptual learning.* New York: Appleton-Century-Crofts.

Gilbert, C. D., & Li, W. (2013). Top-down influences on visual processing. *Nature Reviews Neuroscience*, *14*, 350-363.

Gilbert, C. D., Li, W., & Piëch, V. (2009). Perceptual learning and adult cortical plasticity. *The Journal of Physiology*, *587*(12), 2743–2751.

Glass, L. (1969). Moiré effect from random dots. *Nature*, *223*, 578–580.

Golcu, D., & Gilbert, C. D. (2009). Perceptual learning of object shape. *Journal of Neuroscience*, *29*, 13621–13629.

Goto, N., Yoshimura, R., Moriya, J., Kakeda, S., Hayashi, K., Ueda, N., … Nakamura, J. (2010). Critical examination of a correlation between brain gamma-aminobutyric acid (GABA) concentrations and a personality trait of extroversion in healthy volunteers as measured by a 3 Tesla proton magnetic resonance spectroscopy study. *Psychiatry Research: Neuroimaging*, *182*, 53–57.

Govindaraju, V., Young, K., & Maudsley, A. A. (2000). Proton NMR chemical shifts and coupling constants for brain metabolites. *NMR in Biomedicine*, *13*, 129–153.

Hall, E. L., Stephenson, M. C., Price, D., & Morris, P. G. (2014). Methodology for improved detection of low concentration metabolites in MRS: Optimised combination of signals from multi-element coil arrays. *NeuroImage*, *86*(0), 35–42.

Harris, A. D., Glaubitz, B., Near, J., Evans, C. J., Puts, N. A., Schmidt-Wilcke, T., … Edden, R. A. (2014). Impact of frequency drift on gamma-aminobutyric acid-edited MR spectroscopy. *Magnetic Resonance in Medicine*, *72*, 941–948.

Harris, A. D., Puts, N. A., & Edden, R. A. (2015). Tissue correction for GABA-edited MRS: Considerations of voxel composition, tissue segmentation, and tissue relaxations. *Journal of Magnetic Resonance Imaging*, *42*, 1431–1440.

Heekeren, H. R., Marrett, S., Bandettini., P. A., & Ungerleider, G. (2004). A general mechanism for perceptual decision-making in the human brain. *Nature*, *431*, 859–862.

Herzog, M. H., & Fahle, M. (1997). The role of feedback in learning a vernier discrimination task. *Vision Research*, *37(15)*, 2133–2141.

Hetherington, H. P., Newcomer, B., & Pan, J. (1998). Measurements of human cerebral GABA at 4.1T using numerically optimised editing pulses. *Magnetic Resonance in Medicine*, *39*, 6–10.

Hubel, D. H. (1988). *Eye, brain and vision.* New York: Scientific American Library.

Jansen, J. F. A., Backes, W. H., Nicolay, K., & Kooi, M. E. (2006). ^{1}H MR spectroscopy of the brain: Absolute quantification of metabolites. *Radiology*, *240*(2), 318–332.

Jenkinson, M., Bannister, P. R., Brady, J. M., & Smith, S. M. (2002). Improved optimisation for the robust and accurate linear registration and motion correction of brain images. *NeuroImage*, *17(2)*, 825–841.

Jenkinson, M., Beckmann, C. F., Behrens, T. E., Woolrich, M. W., & Smith, S. M. (2012). FSL. *Neuroimage*, *62*(2), 782–790.

Jensen, J. E., deB. Frederick, B., & Renshaw, P. F. (2005). Grey and white matter GABA level differences in the human brain using two-dimensional, J-resolved spectroscopic imaging. *NMR in Biomedicine*, *18*, 570–576.

Jeter, P. E., Dosher, B. A., Petrov, A., & Lu, Z. L. (2009). Task precision at transfer determines specificity of perceptual learning. *Journal of Vision*, *9(3)*, 11–13.

Jung, R. E., Gasparovic, C., Chavez, R. S., Caprihan, A., Barrow, R., & Yeo, R. A. (2009). Imaging intelligence with proton magnetic resonance spectroscopy. *Intelligence*, *37*(2), 192–198.

Jung, R. E., Gasparovic, C., Chavez, R. S., Flores, R. A., Smith, S. M., Caprihan, A., & Yeo, R. A. (2009). Biochemical support for the "threshold" theory of creativity: A magnetic resonance spectroscopy study. *Journal of Neuroscience*, *29*(16), 5319–5325.

Jung, R. E., Haier, R. J., Yeo, R. A., Rowland, L., Petropoulos, H., Levine, A. S., … Brooks, W. M. (2005). Sex differences in N-acetylaspartate correlates of general intelligence: An ^{1}H-MRS study of normal human brain. *Neuroimage*, *26*(3), 965–972.

Kaiser, L. G., Young, K., & Matson, G. B. (2007). Elimination of spatial interference in PRESS-localized editing spectroscopy. *Magnetic Resonance in Medicine*, *58*, 813–818.

Kaiser, L. G., Young, K., Meyerhoff, D. J., Mueller, S. G., & Matson, G. B. (2008). A detailed analysis of localized J-difference GABA editing: theoretical and experimental study at 4 T. *NMR in Biomedicine*, *21*, 22–32.

Kandel, E. R. (Ed.). (2013). *Principles of neural science* (5th ed.). McGraw-Hill.

Karni, A., & Sagi, D. (1991). Where practice makes perfect in texture discrimination: Evidence for primary visual cortex plasticity. *Proceedings of the National Academy of Sciences of the United States of America*, *88*, 4966–4970.

Karni, A., & Sagi, D. (1993). The time course of learning a visual skill. *Nature*, *365*, 250–252.

Karni, A., Tanne, D., Rubenstein, B. S., Askenasy, J. J. M., & Sagi, D. (1994). Dependence on REM sleep of overnight improvement of a perceptual skill. *Science*, *265*, 679–682.

Keltner, J. R., Wald, L. L., Frederick, B. D., & Renshaw, P. F. (1997). In vivo detection of GABA in human brain using a localized double-quantum filter technique. *Magnetic Resonance in Medicine*, *37*, 366–371.

Kherlopian, A. R., Song, T., Duan, Q., Neimark, M. A., Po, M. J., Gohagan, J. K., & Laine, A. F. (2008). A review of imaging techniques for systems biology. *BMC Systems Biology*, *2*, 74.

Kourtzi, Z. (2010). Visual learning for perceptual and categorical decisions in the human brain. *Vision Research*, *50*, 433–440.

Kourtzi, Z., Betts, L. R., Sarkheil, P., & Welchman, A. E. (2005). Distributed neural plasticity for shape learning in the human visual cortex. *PLoS Biology*, *3*(7), e204.

Kourtzi, Z., & DiCarlo, J. J. (2006). Learning and neural plasticity in visual object recognition. *Current Opinion in Neurobiology*, *16*(2), 152–158. (Cognitive neuroscience)

Kourtzi, Z., & Kanwisher, N. (2000). Cortical regions involved in perceiving object shape. *The Journal of Neuroscience*, *20*(9), 3310–3318.

Kreis, R., Ernst, T., & Ross, B. D. (1993). Absolute quantitation of water and metabolites in the human brain. II. metabolite concentrations. *Journal of Magnetic Resonance, Series B*, *102*(1), 9–19.

Krupa, K., & Bekiesińska-Figatowska, M. (2015). Artifacts in magnetic resonance imaging. *Polish Journal of Radiology*, *80*, 93–106.

Li, S., Mayhew, S. D., & Kourtzi, Z. (2009). Learning shapes the representation of behavioral choice in the human brain. *Neuron*, *62*, 441–452.

Liu, J., Lu, Z.-L., & Dosher, B. A. (2010). Augmented Hebbian reweighting: Interactions between feedback and training accuracy in perceptual learning. *Journal of Vision*, *10*, 1–14.

Liu, J., Lu, Z.-L., & Dosher, B. A. (2012). Mixed training at high and low accuracy levels leads to perceptual learning without feedback. *Vision Research*, *61*, 15–24.

Liu, Z. (1999). Perceptual learning in motion discrimination that generalizes across motion directions. *Proceedings of the National Academy of Sciences of the United States of America*, *96*, 14085–14087.

Liu, Z., & Weinshall, D. (2000). Mechanisms of generalization in perceptual learning. *Vision Research*, *40*, 97–109.

Logothetis, N. K. (2010). The neural basis of the blood-oxygen-level-dependent functional magnetic resonance imaging signal. *Philosophical Transactions of the Royal Society*, *357*, 1003–1037.

Logothetis, N. K., Pauls, J., Augath, M., Trinath, T., & Oeltermann, A. (2001). Neurophysiological investigation of the basis of the fMRI signal. *Nature*, *412*, 150–157.

Lu, Z. L., Chu, W., & Dosher, B. A. (2006). Perceptual learning of motion direction discrimination in fovea: separable mechanisms. *Vision Research*, *46*, 2315–2327.

Luck, S. J., & Vogel, E. K. (1997). The capacity of visual working memory for features and conjunctions. *Nature*, *390*(6657), 279–281.

Mangia, S., Tkáč, I., Gruetter, R., Moortele, P.-F. V. D., Giovec, F., Maravigliad, B., & Uğurbil, K. (2006). Sensitivity of single-voxel ^{1}H-MRS in investigating the metabolism of the activated human visual cortex at 7 T. *Magnetic Resonance Imaging*, *24*, 343–348.

Matthews, N., Liu, Z., Geesaman, B. J., & Qian, N. (1999). Perceptual learning on orientation and direction discrimination. *Vision Research*, *39*, 3692–3701.

Mayhew, S. D., & Kourtzi, Z. (2013). Dissociable circuits for visual shape learning in the young and aging human brain. *Frontiers in Human Neuroscience*, *7*, 1–15.

McLean, M. A., Busza, A. L., Wald, L. L., Simister, R. J., Barker, G. J., & Williams, S. R. (2002). In vivo GABA+ measurement at 1.5T using a PRESS-localized double quantum filter. *Magnetic Resonance in Medicine*, *48*(2), 233–241.

Mednick, S., Nakayama, K., & Stickgold, R. (2003). Sleep-dependent learning: a nap is as good as a night. *Nature Neuroscience*, *6(7)*, 697–698.

Menon, R. S. (2001). Imaging function in the working brain with fMRI. *Current Opinion in Neurobiology*, *11*, 630–636.

Mescher, M., Merkle, H., Kirsch, J., Garwood, M., & Gruetter, R. (1998). Simultaneous in vivo spectral editing and water suppression. *NMR in Biomedicine*, *11*, 266–272.

Michels, L., Martin, E., Klaver, P., Edden, R. A. E., Zelaya, F., Lythgoe, D. J., … O'Gorman, R. L. (2012). Frontal GABA levels change during working memory. *PloS One*, *7*(4), e31933.

Miller, B. T., & D'Esposito, M. (2005). Searching for the top in top-down control. *Neuron*, *48*(4), 535–538.

Miller, E. K., & Cohen, J. D. (2001). An integrative theory of prefrontal cortex function. *Annual Review of Neuroscience*, *24*, 167–202.

Morgan, P. T., Pace-Schott, E. F., Mason, G. F., Forselius, E., Fasula, M., Valentine, G. W., & Sanacora, G. (2012). Cortical GABA levels in primary insomnia. *Sleep*, *35*(6), 807–814.

Mullins, P. G., Chen, H., Xu, J., Caprihan, A., & Gasparovic, C. (2008). Comparative reliability of proton spectroscopy techniques designed to improve detection of J-coupled metabolites. *Magnetic Resonance in Medicine*, *60*, 964–969.

Mullins, P. G., McGonigle, D. J., O'Gorman, R. L., Puts, N. A. J., Vidyasagar, R., Evans, C. J., & Edden, R. A. E. (2014). Current practice in the use of MEGA-PRESS spectroscopy for the detection of GABA. *Neuroimage*, *86*(0), 43–52.

Mumuni, A., McLean, J., Brennan, D., Lopez, R., Waiter, G., Cavanagh, J., & Condon, B. (2012). Comparison of the BOLD responses of brain tissue water and creatine during a sustatined visual stimulation. In *BC-ISMRM 18th meeting.*

Muthukumaraswamy, S. D., Edden, R. A. E., Jones, D. K., Swettenham, J. B., & Singh, K. D. (2009). Resting GABA concentration predicts peak gamma frequency and fMRI amplitude in response to visual stimulation in humans. *Proceedings of the National Academy of Sciences of the USA*, *106*(20), 8356–8361.

Muthukumaraswamy, S. D., Evans, C. J., Edden, R. A. E., Wise, R. G., & Singh, K. D. (2012). Individual variability in the shape and amplitude of the BOLD-HRF correlates with endogenous GABAergic inhibition. *Human Brain Mapping*, *33*(2), 455–465.

Northoff, G., Walter, M., Schulte, R. F., Beck, J., Dydak, U., Henning, A., … Boesiger, P. (2007). GABA con-

centrations in the human anterior cingulate cortex predict negative BOLD responses in fMRI. *Nature Neuroscience*, *10(12)*, 1515–1517.

Ogawa, S., Lee, T. M., Kay, A. R., & Tank, D. W. (1990). Brain magnetic resonance imaging with contrast dependent on blood oxygenation. *Proceedings of the National Academy of Sciences of the United States of America*, *87*, 9868–9872.

O'Gorman, R. L., Michels, L., Edden, R. A. E., Murdoch, J. B., & Martin, E. (2011). In vivo detection of GABA and glutamate with MEGA-PRESS: Reproducibility and gender effects. *Journal of Magnetic Resonance Imaging*, *33*, 1262–1267.

Ostwald, D., Lam, J. M., Li, S., & Kourtzi, Z. (2008). Neural coding of global form in the human visual cortex. *Journal of Neurophysiology*, *99*(5), 2456–2469.

Ozturk, A., Degaonkar, M., Matson, M. A., Wells, C. T., Mahone, E. M., & Horska, A. (2009). Proton MR spectroscopy correlates of frontal lobe function in healthy children. *American Journal of Neuroradiology*, *30*(7), 1308–1314.

Parrish, T. B., Gitelman, D. R., LaBar, K. S., & Mesulam, M. M. (2000). Impact of signal-to-noise on functional MRI. *Magnetic Resonance in Medicine*, *44(6)*, 925–932.

Pelli, D. G. (1997). The VideoToolbox software for visual psychophysics: Transforming numbers into movies. *Spatial Vision*, *10*, 437–442.

Pernet, C., Franceries, X., Basan, S., Cassol, E., Démonet, J., & Celsis, P. (2004). Anatomy and time course of discrimination and categorization processes in vision: an fMRI study. *NeuroImage*, *22*(4), 1563–1577.

Petroff, O. A., Spencer, D. D., Alger, J., & Prichard, J. W. (1989). High-field proton magnetic resonance spectroscopy of human cerebrum obtained during surgery for epilepsy. *Neurology*, *39*, 1197–1202.

Petrov, A. A., Dosher, B. A., & Lu, Z.-L. (2005). The dynamics of perceptual learning: An incremental reweighting model. *Psychological Review*, *112(4)*, 715–743.

Pfleiderer, B., Ohrmann, P., Suslow, T., Wolgast, M., Gerlach, A. L., Heindel, W., & Michael, N. (2004). N-acetylaspartate levels of left frontal cortex are associated with verbal intelligence in women but not in men: a proton magnetic resonance spectroscopy study. *Neuroscience*, *123*(4), 1053–1058.

Poldrack, R. A., Desmond, J. E., Glover, G. H., & Gabrieli, J. D. (1998). The neural basis of visual skill learning: an fMRI study of mirror reading. *Cereb Cortex*, *8*(1), 1–10.

Pouwels, P. J. W., & Frahm, T. (1998). Regional metabolite concentrations in human brain as determined by quantitative localized proton MRS. *Magnetic Resonance in Medicine*, *39*, 53–60.

Provencher, S. W. (2001). Automatic quantitation of localized in vivo ^{1}H spectra with LCModel. *NMR in Biomedicine*, *14(4)*, 260–264.

Puts, N. A. J., Barker, P. B., & Edden, R. A. E. (2013). Measuring the longitudinal relaxation time of GABA in vivo at 3 Tesla. *J Magn Reson Imaging*, *37*(4), 999–1003.

Puts, N. A. J., & Edden, R. A. E. (2012). In vivo magnetic resonance spectroscopy of GABA: a methodological review. *Progress in Nuclear Magnetic Resonance Spectroscopy*, *60*, 29–41.

Puts, N. A. J., Edden, R. A. E., Evans, C. J., McGlone, F., & McGonigle, D. J. (2011). Regionally specific human GABA concentration correlates with tactile discrimination thresholds. *The Journal of Neuroscience*, *31(46)*, 16556–16560.

Ramachandran, V. S., & Braddick, O. (1973). Orientation-specific learning in stereopsis. *Perception*, *2*(3), 371–376.

Reynolds, G., Wilson, M., Peet, A., & Arvanitis, T. N. (2006). An algorithm for the automated quantitation of metabolites in in vitro NMR signals. *Magnetic Resonance in Medicine*, *56*, 1211–1219.

Riese, F., Gietl, A., Zölch, N., Henning, A., O'Gorman, R., Kälin, A. M., … Michels, L. (2015). Posterior cingulate γ-aminobutyric acid and glutamate+glutamine are reduced in amnestic mild cognitive impairment and are unrelated to APOE genotype. *Neurobiology of Aging*, *36*(1), 53–59.

Ritsner, M. S., & Gottesman, I. I. (2009). *The handbook of neuropsychiatric biomarkers, endophenotypes and*

genes. Springer Science.

Robson, S. E., Muthukumaraswamy, S. D., Sumner, P., Evans, C. J., & Singh. (2012). Dependence of GABA and gamma frequency on V1 area and thickness. In *BC-ISMRM 18th meeting*.

Roelfsema, P. R. (2006). Cortical algorithms for perceptual grouping. *Annual Review of Neuroscience*, *29*, 203–227.

Roelfsema, P. R., & van Ooyen, A. (2005). Attention-gated reinforcement learning of internal representations for classification. *Neural Computation*, *17*(10), 2176–2214.

Rothman, D. L., Petroff, O. A. C., Behar, K. L., & Mattson, R. H. (1993). Localized ^{1}H-NMR measurements of gamma-aminobutyric acid in human brain in vivo. *Proceedings of the National Academy of Sciences of the United States of America*, *90*, 5662–5666.

Rowland, L. M., Kontson, K., West, J. T., Zhu, H., Edden, R. A. E., Holcomb, H. H., & Barker, P. B. (2012). MRS study of glutamate, GABA and NAAG in schizophrenia. *Schizophrenia Research*, *136*, S294. (Abstracts of the 3rd Biennial Schizophrenia International Research Conference)

Rubin, N., Nakayama, K., & Shapley, R. (1997). Abrupt learning and retinal size specificity in illusory-contour perception. *Current Biology*, *7*, 461–467.

Sagi, D. (2011). Perceptual learning in vision research. *Vision Research*, *51*, 1552–1566.

Sanacora, G., Gueorguieva, R., & Yu-Te, W. (2004). Subtype-specific alterations of γ-aminobutyric acid and glutamate in patients with major depression. *Archives of General Psychiatry*, *61*(7), 705–13.

Sandberg, K., Blicher, J. U., Dong, M. Y., Rees, G., Near, J., & Kanai, R. (2013). Occipital GABA correlates with cognitive failures in daily life. *Neuroimage*, *87*, 55–60.

Schwarzkopf, D. S., Zhang, J., & Kourtzi, Z. (2009). Flexible learning of natural statistics in the human brain. *Journal of Neurophysiology*, *102*(3), 1854–1867.

Seitz, A. R., Nanez, J. E. S., Holloway, S., Tsushima, Y., & Watanabe, T. (2006). Two cases requiring external reinforcement in perceptual learning. *Journal of Vision*, *6*, 966–973.

Shattuck, D. W., Sandor-Leahy, S. R., Schaper, K. A., Rottenberg, D. A., & Leahy, R. M. (2001). Magnetic resonance image tissue classification using a partial volume model. *NeuroImage*, *13*(5), 856–876.

Shaw, A., Brealy, J., Richardson, H., Muthukumaraswamy, S. D., Edden, R. A. E., Evans, C. J., … Keedwell, P. A. (2013). Marked reductions in visual evoked responses but not γ-aminobutyric acid concentrations or γ-band measures in remitted depression. *Biological Psychiatry*, *73*(7), 691–698.

Shiu, L. P., & Pashler, H. (1992). Improvement in line orientation discrimination is retinally local but dependent on cognitive set. *Perception and Psychophysics*, *52*, 582–588.

Sigman, M., Pan, H., Yang, Y., Stern, E., Silbersweig, D., & Gilbert, C. D. (2005). Top-down reorganization of activity in the visual pathway after learning a shape identification task. *Neuron*, *46*(5), 823–835.

Splettstoesser, T. (2015). *Synapse image*. Retrieved August 2017, from `https://upload.wikimedia.org/wikipedia/commons/thumb/d/d7/SynapseSchematic_lines.svg`

Stagg, C., & Rothman, D. (Eds.). (2014). *Magnetic resonance spectroscopy*. Elsevier Academic Press.

Stagg, C. J. (2014). Magnetic resonance spectroscopy as a tool to study the role of GABA in motor-cortical plasticity. *NeuroImage*, *86*(0), 19–27.

Stagg, C. J., Bachtiar, V., Amadi, U., Gudberg, C. A., Ilie, A. S., Sampaio-Baptista, C., … Johansen-Berg, H. (2014). Local GABA concentration is related to network-level resting functional connectivity. *eLife*, *3*, e01465.

Stagg, C. J., Bachtiar, V., & Johansen-Berg, H. (2011a). The role of GABA in human motor learning. *Current Biology*, *21*, 480–484.

Stagg, C. J., Bachtiar, V., & Johansen-Berg, H. (2011b). What are we measuring with GABA magnetic resonance spectroscopy? *Communicative & Integrative Biology*, *4*(5), 573–575.

Stagg, C. J., Wylezinska, M., Matthews, P. M., Johansen-Berg, H., Jezzard, P., Rothwell, J. C., & Bestmann, S. (2009). Neurochemical effects of theta burst stimulation as assessed by magnetic resonance spectroscopy.

Journal of Neurophysiology, *101*(6), 2872–2877.

Stanisz, G. J., Odrobina, E. E., Pun, J., Escaravage, M., Graham, S. J., Bronskill, M. J., & Henkelman, R. M. (2005). T_1, T_2 relaxation and magnetization transfer in tissue at 3T. *Magnetic Resonance in Medicine*, *54*(3), 507–512.

Stefan, D., Di Cesare, F., Andrasescu, A., Popa, E., Lazariev, A., Vescovo, E., … Graveron-Demilly, D. (2009). Quantitation of magnetic resonance spectroscopy signals: the jMRUI software package. *Measurement Science and Technology*, *20*(10), 104035–104044.

Sumner, P., Edden, R. A. E., Bompas, A., Evans, C. J., & Singh, K. D. (2010). More GABA, less distraction: a neurochemical predictor of motor decision speed. *Nature Neuroscience*, *13(7)*, 825–827.

Talairach, J., & Tournoux, P. (1988). *Co-planar stereotaxic atlas of the human brain*. Germany: Thieme.

Terpstra, M., Ugurbil, K., & Gruetter, R. (2002). Direct in vivo measurement of human cerebral GABA concentration using MEGA-editing at 7 Tesla. *Magnetic Resonance in Medicine*, *47*, 1009–1012.

Vogels, R., Sary, G., Dupont, P., & Orban, G. A. (2002). Human brain regions involved in visual categorization. *NeuroImage*, *16*(2), 401–414.

Waddell, K. W., Avison, M. J., Joers, J. M., & Gore, J. C. (2007). A practical guide to robust detection of GABA in human brain by J-difference spectroscopy at 3 Tesla using a standard volume coil. *Magnetic Resonance Imaging*, *25(7)*, 1032–1038.

Waddell, K. W., Zanjanipour, P., Pradhan, S., Xu, L., Welch, E. B., Joers, J. M., … Gore, J. C. (2010). Anterior cingulate and cerebellar GABA and Glu correlations measured by ^{1}H J-difference spectroscopy. *Magnetic Resonance Imaging*, *29*, 19–24.

Wang, Y., & Li, S.-J. (1998). Differentiation of metabolic concentrations between gray matter and white matter of human brain by in vivo ^{1}H magnetic resonance spectroscopy. *Magnetic Resonance in Medicine*, *39*, 28–33.

Webb, S. (Ed.). (1988). *The physics of medical imaging*. Taylor and Francis, New York.

Weisstein, E. W. (2017, February). *Gaussian function*. Retrieved 12/02/2017, from `http://mathworld.wolfram.com/GaussianFunction.html`

Wiebking, C., Duncan, N. W., Tiret, B., Hayes, D. J., Marjanska, M., Doyon, J., … Northoff, G. (2014). GABA in the insula - a predictor of the neural response to interoceptive awareness. *Neuroimage*, *86*(0), 10–18.

Willard, S. S., & Koochekpour, S. (2013). Glutamate, glutamate receptors, and downstream signaling pathways. *International Journal of Biological Sciences*, *9*(9), 948–959.

Wilson, H. R., & Wilkinson, F. (1998). Detection of global structure in Glass patterns: implications for form vision. *Vision Research*, *38*, 2933–2947.

Wilson, M., Reynolds, G., Kauppinen, R. A., Arvanitis, T. N., & Peet, A. C. (2011). A constrained least-squares approach to the automated quantitation of in vivo ^{1}H magnetic resonance spectroscopy data. *Magnetic Resonance in Medicine*, *65*, 1–12.

Wylezinska, M., Mathews, P., & Jezzard, P. (2003). Quantitation of GABA in human brain using MEGA-PRESS editing and LCM analysis. *Proceeding of the International Society of Magnetic Resonance in Medicine*, *11*, 1997.

Yamamoto, T., Isobe, T., Akutsu, H., Masumoto, T., Ando, H., Sato, E., … Matsumura, A. (2015). Influence of echo time in quantitative proton MR spectroscopy using LCModel. *Magnetic Resonance Imaging*, *33*(5), 644–648.

Yoon, J. H., Maddock, R. J., Rokem, A., Silver, M. A., Minzenberg, M. J., Ragland, J. D., & Carter, C. S. (2010). GABA concentration is reduced in visual cortex in schizophrenia and correlates with orientation-specific surround suppression. *The Journal of Neuroscience*, *30*(10), 3777–3781.

Yotsumoto, Y., Sasaki, Y., Chan, P., Vasios, C. E., Bonmassar, G., Ito, N., … Shimojo, T. (2009). Location-specific cortical activation changes during sleep after training for perceptual learning. *Current Biology*, *19*, 1278–1282.

Zhang, J., & Kourtzi, Z. (2010). Learning-dependent plasticity with and without training in the human brain.

Proceedings of the National Academy of Sciences of the USA, *107(30)*, 13503–13508.

Zhang, J., Meeson, A., Welchman, A. E., & Kourtzi, Z. (2010). Learning alters the tuning of functional magnetic resonance imaging patterns for visual forms. *The Journal of Neuroscience*, *30(42)*, 14127–14133.

Zhu, H., Edden, R. A. E., Ouwerkerk, R., & Barker, P. B. (2011). High resolution spectroscopic imaging of GABA at 3 Tesla. *Magnetic Resonance in Medicine*, *65*, 603–609.